

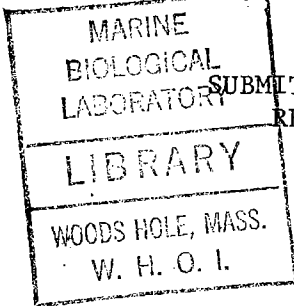
GC
7.1
H12
1976

THE SENSITIVITY AND PREDICTABILITY
OF MESOSCALE EDDIES IN AN
IDEALIZED MODEL OCEAN

by

DALE B. HAIDVOGEL

S. B. Massachusetts Institute of Technology
(1971)



SUBMITTED IN PARTIAL FULFILLMENT OF THE
REQUIREMENTS FOR THE DEGREE OF
DOCTOR OF PHILOSOPHY

at the

MASSACHUSETTS INSTITUTE OF TECHNOLOGY

and the

WOODS HOLE OCEANOGRAPHIC INSTITUTION

April, 1976

Signature of Author..... *Dale B. Haidvogel*

Joint Program in Oceanography, Massachusetts
Institute of Technology-Woods Hole Oceanographic
Institution, and Department of Earth and Planetary
Sciences, and Department of Meteorology, Massachu-
setts Institute of Technology, April, 1976

Certified by..... *Robert C Beardsley*

Thesis Supervisor

Accepted by..... *M. Edmond*

Chairman, Joint Oceanography Committee in the Earth
Sciences, Massachusetts Institute of Technology-
Woods Hole Oceanographic Institution

THE SENSITIVITY AND PREDICTABILITY OF MESOSCALE EDDIES
IN AN IDEALIZED MODEL OCEAN

by

DALE B. HAIDVOGEL

Submitted to the Massachusetts Institute of
Technology - Woods Hole Oceanographic Institution
Joint Program in Oceanography on April 26, 1976, in
partial fulfillment of the requirements for the
degree of Doctor of Philosophy.

ABSTRACT

Two numerical applications of two-level quasigeostrophic theory are used to investigate the interrelationships of the mean and mesoscale eddy fields in a closed-basin ocean model. The resulting techniques provide a more accurate description of the local dynamics, origins, and parametric dependences of the eddies than that available in previous modelling studies.

First, we propose a novel and highly efficient quasigeostrophic closed-domain model which has among its advantages a heightened resolution in the boundary layer regions. The pseudospectral method, employing an orthogonal expansion in Fourier and Chebyshev functions, relies upon a discrete Green's function technique capable of satisfying to spectral accuracy rather arbitrary boundary conditions on the eastern and western (continental) walls. Using this formulation, a series of four primary numerical experiments tests the sensitivity of wind-driven single and double-gyred eddying circulations to a transition from free-slip to no-slip boundary conditions. These comparisons indicate that, in the absence of topography, no-slip boundaries act primarily to diffuse vorticity more efficiently. The interior transport fields are thus reduced by as much as 50%, but left qualitatively unchanged. In effect, once having separated from the western wall, the internal jet has no knowledge, apart from its characteristic flow speed, of the details of the boundary layer structure.

Next, we develop a linearized stability theory to analyze the local dynamic processes responsible for the eddy fields observed in these idealized models. Given two-dimensional (x, z) velocity profiles of arbitrary horizontal orientation, the resulting eigenfunction problems are solved to predict a variety of eddy properties: growth rate, length and time scales, spatial distribution, and energy fluxes. This simple methodology accurately reproduces many of the eddy statistics of the fully nonlinear fields; for instance, growth rates of 10-100 days predicted for the growing waves by the stability analysis are consistent with observed model behavior and have been

1977-05-10

confirmed independently by a perturbation growth test. Local energetic considerations indicate that the eddy motions arise in distinct and recognizable regions of barotropic and baroclinic activity. The baroclinic instabilities depend sensitively on the vertical shear which must exceed $O(5 \text{ cm sec}^{-1})$ across the thermocline to induce eddy growth. As little as a 10% reduction in $|u_z|$, however, severely suppresses the cascade of mean potential energy to the eddy field. In comparison, the barotropic energy conversion process scales with the horizontal velocity shear, $|u_y|$, whose threshold values for instability, $O(2 \times 10^{-6} \text{ sec}^{-1})$, is undoubtedly geophysically realizable. A simple scatter diagram of $|u_y|$ versus $|u_z|$ for all the unstable modes studied shows a clear separation between the regions of barotropic and baroclinic instability. While the existence of baroclinic modes can be deduced from either time mean or instantaneous flow profiles, barotropic modes cannot be predicted from mean circulation profiles (in which the averaging process reduces the effective horizontal shears).

Finally, we conduct a separate set of stability experiments on analytically generated jet profiles. The resulting unstable modes align with the upper level velocity maxima and, although highly sensitive to local shear amplitude, depend much less strongly on jet separation and width. Thus, the spatial and temporal variability of the mesoscale statistics monitored in the nonlinear eddy simulations can be attributed almost entirely to time-dependent variations in local shear strength. While these results have been obtained in the absence of topography and in an idealized system, they yet have strong implications for the importance of the mid-ocean and boundary layer regions as possible eddy generation sites.

Thesis Supervisor: Robert C. Beardsley

Title: Lecturer, Massachusetts Institute of Technology
 Research Scientist, Woods Hole Oceanographic Institution

ACKNOWLEDGEMENTS

The author would certainly be remiss in failing to recognize the support - moral, technical, and financial - given him during the course of this work. Though the manuscript has benefited from the continued interest and influence of many people, the largest debt of gratitude is certainly due to Dr. Robert C. Beardsley of the Woods Hole Oceanographic Institution and Dr. William R. Holland of the National Center for Atmospheric Research (NCAR); both have contributed the encouragement, criticism, and inspiration which have, at times, been necessary for the successful continuation of these studies. Special appreciation must also be expressed to Dr. Francis P. Bretherton of NCAR who originally suggested the importance of the localized stability problems, to Dr. John E. Hart of the Massachusetts Institute of Technology (MIT) for his critical reading of the manuscript, and to Prof. Steven A. Orszag of MIT under whose tutelage the mysteries of the spectral method gradually became clear. Last, but far from least, the author wishes to acknowledge the help given by Ms. Barbara Wysochansky in the preparation of the early drafts of this manuscript. This research has been made possible by National Science Foundation grant OCE74-03001 A03, formerly DES73-00528, and the National Science Foundation funded National Center for Atmospheric Research whose facilities, scientists, and staff must all be thanked for their major contribution to the completion of this project.

TABLE OF CONTENTS

ABSTRACT.....	2
ACKNOWLEDGEMENTS.....	4
TABLE OF CONTENTS.....	5
I. Introduction.....	7
I.1 Evidence for an energetic and dynamically active eddy field.....	8
I.2 The preliminary results of numerical eddy simulations.....	10
I.3 A global eddy modelling strategy.....	13
II. Formulation of the Quasigeostrophic Model.....	15
II.1 The potential vorticity equation.....	17
II.2 Conservation principles.....	24
II.3 Vertical discretization and the resulting system of equations.....	25
II.4 The mean field equations.....	30
III. Numerical Solution Techniques.....	34
III.1 Lateral boundary conditions and choice of the expansion series.....	36
III.2 The decoupled equations.....	42
III.3 Solution technique - free-slip boundaries.....	45
III.4 Solution technique - no-slip boundaries.....	49
IV. Eddy Sensitivity to Western Boundary Layer Structure.....	52
IV.1 Experiment 1.....	54
IV.2 Experiment 1R.....	78
IV.3 Experiment 2.....	87
IV.4 Experiment 2R.....	95
V. A Linearized Stability Analysis.....	110
V.1 The stability of parallel flows above topography.....	111
V.2 The predictions of linearized stability theory.....	116
VI. The Local Properties of the Unstable Modes and the Prediction of Eddy Statistics.....	118
VI.1 A stability analysis of experiment 1.....	120
VI.2 A stability analysis of experiment 1R.....	150

VI.3	A stability analysis of experiment 2.....	153
VI.4	A stability analysis of experiment 2R.....	176
VI.5	Generalized properties of the baroclinic mode.....	192
VI.6	Generalized properties of the barotropic mode.....	216
VII	Conclusions.....	221
Appendix A	Fast sine/cosine transforms.....	229
Appendix B	Some properties of Chebyshev series.....	233
Appendix C	A modified Adams-Bashforth method.....	235
Appendix D	Constructing pseudospectral analogues of Arakawa conservative schemes.....	236
REFERENCES.....		241
BIOGRAPHY.....		245

(I) Introduction

There is a long history of attempts, both theoretical and numerical, to model and predict ocean circulation features. The earliest studies, those of Sverdrup (1947), Stommel (1948), and Munk (1950), for instance, began by investigating the combined roles of wind stress, planetary vorticity, and frictional effects in determining the large-scale flow. Some of the mean properties of the western boundary current and the associated broad return flow were thereby deduced from these early linear models.¹ Except for the free inertial solutions of Fofonoff (1954) and Charney (1955), however, the inclusion of first-order nonlinear effects awaited the advent of the numerical model as a recognized tool in the simulation of geophysical flows. The first numerical experiments, carried out by Bryan (1963) and Veronis (1966), were simple extensions of the original Stommel and Munk frictional theories to include significant nonlinearity, a more complete dynamic formulation than was tractable analytically. In a barotropic system, the corresponding results incorporated features of both frictional and inertial boundary layers; flows intensified towards the west (beta effect) and north (inertial effect). In addition, an inertial recirculation adjacent to the western boundary current developed which could be made unstable for suitable parameters and boundary conditions (Bryan, 1963; Blandford, 1971). More complicated dynamical formulations, including the effects of topography and baroclinicity, were soon shown to reproduce the qualitative features of the mean large-scale ocean circulation rather well (Holland, 1966 and 1973).

¹For an overview of the theories of the wind-driven ocean, see Robinson (1963).

(I.1) Evidence for an energetic and dynamically active eddy field

These early analytic and numerical models fail because they resolve only the grossest dynamical scales of the ocean circulation and treat subgridscale motion as a turbulent, dissipative field. Such a representation does not take account of the possibility of mean flows driven by smaller scale, time-varying motions, a mechanism of some importance in the maintenance of the atmospheric general circulation (Starr, 1968). In fact, observational evidence collected over the past decade reveals a rather energetic and well organized mesoscale field which may actually support, rather than inhibit, the mean circulation of the ocean. Swallow and Crease first documented the presence of the eddies in what had been believed to be a relatively quiescent deep mid-ocean environment (Crease, 1962). Recent field data confirm the persistent and ubiquitous existence of an eddy field in not only the North Atlantic (Koshlyakov and Grachev, 1973; Gould, Schmitz, and Wunsch, 1974), but in the Pacific Ocean as well (Bernstein and White, 1975); the preferred spatial and temporal scales of these motions are typically 100 km and 15-25 days respectively. These measurements suggest that the mesoscale may contribute substantially to the local maintenance of the mid-ocean mean circulation.

Theoreticians soon identified several dynamic processes which might populate the mid-ocean with eddies of the observed characteristics. For instance, meandering of the Gulf Stream can result in the shedding of cyclonic rings whose effects can be felt well into the oceanic interior. Using the historical records summarized by Parker (1971), Flierl (1975b)

has shown that ring spindown and subsequent wave radiation may drive a mid-ocean velocity field of several centimeters per second. Eddies can also arise directly in the mid-ocean through the agency of baroclinic instability which acts to convert the potential energy of the large-scale flow into eddy kinetic energy at the radius of deformation. The potential energy field of the world's oceans is quite sufficient to account for the eddies in this manner (Gill, Green, and Simmons, 1974). In fact, the growth time scales for infinitesimal baroclinic eddies can be as short as 50 days for rather modest values of the ambient vertical shear (Robinson and McWilliams, 1974). Finally, interaction of the mean circulation with topography may play an important role in sustaining the baroclinic eddy field both in the intense western boundary layer (and its seaward extension) where topographic variabilities can very often destabilize the mean circulation and induce meandering and energy radiation into the interior (Orlanski, 1969), and in the open ocean where topographic scattering maintains the baroclinicity of the eddy field against the forces of two-dimensional turbulence (Rhines, 1975). A complete dynamical treatment of these instability processes and the accompanying eddy-mean flow interactions hinged upon the formulation of more sophisticated analytic and numerical models which took explicit account of the dynamic consequences of an active mesoscale.

(I.2) The preliminary results of numerical eddy simulations

Two distinct but related approaches have been adopted in an attempt to numerically simulate mesoscale eddy behavior. The simplest, and that yielding the most easily interpretable results, is the so-called process model in which local dynamic processes are studied in a periodic, unforced domain. Starting from some initial circulation, the dynamic equations are integrated forward in time and the evolution of the field statistics monitored. Perhaps the most convincing comparison of model results to a collection of field data has been made in this way by Bretherton and Owens whose multileveled quasigeostrophic regional model accurately simulates the mesoscale statistics of the MODE-I region (Owens, 1975). At the same time, related analytic and numerical studies reveal a great deal of the generalized nonlinear behavior of waves and turbulence, for example, the fundamental instability of a baroclinic Rossby wave (Kim, 1975), the halting of the two-dimensional cascade of energy towards low wavenumber, barotropic currents by wave radiation and topographic scattering (Rhines, 1975), and the evolution of a two-dimensional turbulent field above topography towards a state of minimum enstrophy characterized, on a beta-plane, by predominantly westward flow (Bretherton and Haidvogel, 1976). Since these models rely heavily on the powerful Fourier expansion technique, they have the advantage of predicting the spectral as well as the physical space energy transfers occurring during these nonlinear interactions.

A second type of model attempts to simulate an entire oceanic gyre

rather than just a localized mid-ocean region. Consequently, in addition to a turbulent eddy field these models include idealized representations of the intense western boundary current and associated (often unstable) westward return flow. Such an isolated gyre is necessarily enclosed by impermeable walls, thus complicating both the boundary conditions and the numerical techniques that must be applied to solve the problem. In contrast to the spindown experiments mentioned above, the fluid is spunup from rest to an equilibrium state by some hypothesized distribution of wind stresses. The presence of a driven mean flow complicates the interpretation, especially the spectral transfer properties, of the closed-basin simulations. The results do indicate, however, that for certain parameter ranges, mesoscale eddies can spontaneously appear during the spinup phase (Holland and Lin, 1975a). Following this initial period of instability the model generally settles into an oscillatory equilibrium in which the eddy streamfunction and energy fields, superimposed on the steady, large-scale flow, vary periodically. At this stage, the finite-amplitude eddies contribute substantially to the mean dynamic balances. For instance, in the absence of vertical momentum transport, only the Reynolds stresses induced by the eddies can sustain a nonzero mean flow at the lower levels. Although model behavior varies considerably with the values of the environmental parameters, the predictions of these closed-basin simulations - including eddy space and time scales, phase speeds, and source and sink regions - can closely correspond to observed mesoscale statistics (Holland and Lin, 1975b). With the addition to

these preliminary models of continentality, bottom topography, and a less coarse vertical decomposition, dynamically accurate eddy general circulation models for the world's oceans may be realizable in the near future.

(I.3) A global eddy modelling strategy

One of the most important limitations of these closed-basin models is their sensitivity to small parametric changes. Thus, even given a perfect physical model, we would still have to examine its response throughout a multidimensional space of unknown parameters and boundary conditions; that is, the model must be "tuned". This is perhaps a straightforward, but nontrivial, task. The large block of computer resources needed to run even a single nonlinear eddy simulation effectively limits the number of such runs that we can realistically envision. Though essentially a trial-and-error approach, this simple but costly methodology has nevertheless formed a basis for much of our modelling of global eddy behavior.

This investigation addresses two separate problems central to the issue of model sensitivity and predictability. First, we derive and construct a highly accurate two-level quasigeostrophic closed-basin model in which the boundary constraints on the eastern and western walls may be arbitrarily specified (Chapters II and III). With this model, we make a preliminary evaluation of the effects of lateral boundary conditions on eddy generation (Chapter IV). Second, we devise a procedure by which the energetic balances of the local mean flows and accompanying eddies can be explored. The method, based on a linearized stability theory, predicts eddy features such as growth rate, finite amplitude spatial and temporal structure, and mean to eddy energy conversions given velocity profiles for the upper and lower layer flows (Chapter V). The predictions of the linearized stability analysis compare favorably

with the fully nonlinear results over a large range of parameters (Chapter VI). In addition to their diagnostic capabilities, such stability analyses can be used as an exploratory tool in parametric ranges where fully nonlinear simulations are unavailable. Consideration of the local stability properties of simple mean flows also allows us to generalize about the signatures of barotropic and baroclinic eddy generation regions. Of particular interest is a determination of the mean flow features that induce wave growth, and the energy flux quantities that may locally identify energy sources and sinks for the mesoscale eddy field.

(II) Formulation of the Quasigeostrophic Model

An accurate numerical simulation of the dynamics of mesoscale eddies in a suitably large domain requires very fine spatial and temporal resolution, and consequently a high degree of numerical sophistication. To insure that such simulations be economically feasible, however, a viable model can retain only the most essential physical processes. With such a simplification in mind, we will first ignore the irregularity of the continental boundaries. The planar representation of these boundaries does not disturb the fundamental dynamics of the enclosed fluid, although qualitative mean flow features may be lost. Rectilinear coastlines also facilitate the implementation of efficient numerical techniques, as we will see. Similarly, we replace the upper bounding surface by a rigid lid in the traditional manner. The concomitant filtering of surface gravity waves relaxes the restrictive Courant-Friedrichs-Lewy (CFL) condition on the magnitude of the time step permissible during the numerical integration of the hydrodynamical equations. The remaining bounding surface, the ocean bottom, must be treated more explicitly, thereby preserving the well known effects of topography on the strength and stability of oceanic circulations (Orlanski and Cox, 1973; Holland, 1973). The necessity of the retention of an idealized baroclinic structure arises as a consequence not only of the highly stratified nature of the mid-ocean environment, but of our anticipation that a cascade of available potential energy into baroclinically unstable waves will be one of the eddy generation mechanisms. The effects of the sphericity of the earth will be

adequately modelled by adopting the conventional mid-latitude β -plane approximation

$$f = f_0 + \beta y = f_0 (1 + Ly/a \tan \Theta_0)$$

where f_0 is the local value of the Coriolis parameter at some central latitude, Θ_0 ; a the mean radius of the earth; and L the horizontal basin dimension. Nonlinearity is presumably also important in conjunction with the dynamics of planetary waves in directing energy transfers between differing scales of motion (Rhines, 1973). Finally, the approach to statistical equilibrium will require the inclusion of some dissipation though its correct parameterization remains a matter of considerable uncertainty.

(II.1) The potential vorticity equation

As have many in the past, we will make a quasigeostrophic approximation to the full equations of motion. This formulation incorporates all the essential physical and environmental factors mentioned in the previous section and, fortunately, accords well with observations made in the mid-ocean (Gould, Schmitz, and Wunsch, 1974; Bryden, 1975). Take the local cartesian variables x' , y' , and z' (positive upwards) as the eastward, northward, and vertical coordinate directions; u' , v' , and w' the corresponding components of the vector velocity \underline{u}' ; and $(-H + h(x', y'))$ the total depth measured downwards from the rigid sea surface ($z' = 0$). The idealized fluid system, contained between impermeable vertical walls at $x'=0$, x_0 and $y'=0$, y_0 , obeys the equations of fluid motion

$$\begin{aligned} \frac{du'}{dt'} + u' \nabla u' + w' \frac{du'}{dz'} - f v' &= -\frac{1}{\rho_0} \frac{dp'}{dx'} + K_H \nabla^2 u' + K_V \frac{d^2 u'}{dz'^2} \\ \frac{dv'}{dt'} + u' \nabla v' + w' \frac{dv'}{dz'} + f u' &= -\frac{1}{\rho_0} \frac{dp'}{dy'} + K_H \nabla^2 v' + K_V \frac{d^2 v'}{dz'^2} \\ \frac{dw'}{dt'} + u' \nabla w' + w' \frac{dw'}{dz'} &= -\frac{1}{\rho_0} \frac{dp'}{dz'} - \frac{\rho' g}{\rho_0} \\ \frac{dp'}{dt'} + u' \nabla \rho' + w' \frac{d\rho'}{dz'} &= 0 \\ \frac{du'}{dx'} + \frac{dv'}{dy'} + \frac{dw'}{dz'} &= 0 \end{aligned}$$

where ∇ denotes the horizontal gradient operator, ∇^2 the two-dimensional Laplacian, and K_H and K_V the horizontal and vertical

coefficients of eddy diffusivity.¹ Note also the traditional and Boussinesq approximations. Decompose the density field such that

$$\rho' = \rho_0 + \rho'_1(z') + \rho'_2(x', y', z', t')$$

where

$$\rho_0 > \rho'_1 > \rho'_2.$$

Similarly,

$$p' = p'_1(z') + p'_2(x', y', z', t')$$

where

$$p'_{1z'} = -g(\rho_0 + \rho'_1).$$

Together, these field assumptions define the mean hydrostatic states and the deviations therefrom. Choosing the non-dimensionalization

$$t' = (f_0 \omega)^{-1} t$$

$$(x', y') = L(x, y)$$

$$z' = H z$$

$$(u', v') = V(u, v)$$

$$\omega' = (V \delta) \omega$$

$$\delta = H/L$$

$$f = f_0(1 + \alpha y)$$

$$\alpha = \beta L / f_0$$

¹The corresponding terms are therefore assumed to adequately model the subgrid-scale turbulent diffusion of momentum. Other such formulations in current use are the fourth-order frictional mechanisms of the process models (Rhines; Bretherton and Owens), and cascade models deduced from simple turbulence arguments (Leith; Holloway).

$$\rho' = \left(\rho_0 f_0 \frac{LV}{gH} \right) \rho$$

and
$$P_2' = (\rho_0 f_0 LV) P,$$

the equations can be rewritten

$$\epsilon \frac{Du}{Dt} - (1 + \alpha y) v = -P_x + E_H \nabla^2 u + E_V u_{zz}$$

$$\epsilon \frac{Dv}{Dt} + (1 + \alpha y) u = -P_y + E_H \nabla^2 v + E_V v_{zz}$$

$$\epsilon \delta^2 \frac{Dw}{Dt} = -P_z - \rho_2$$

$$\epsilon \frac{D\rho}{Dt} - Bw = 0$$

$$u_x + v_y + w_z = 0$$

where
$$\frac{D}{Dt} = \left(\frac{\omega}{\epsilon} \right) \frac{d}{dt} + \underline{u} \cdot \nabla + \omega \frac{d}{dz}.$$

The nondimensional parameters are then

$$\epsilon = V / f_0 L = \text{Rossby number}$$

$$\tau^2 = -g \rho_1' / \rho_0 f_0^2 = N^2 / f_0^2$$

$$B = (\tau \delta)^2 = \text{Burger number}$$

$$E_H = K_H / f_0 L^2 = \text{horizontal Ekman number}$$

and $E_v = K_v / f_0 H^2 = \text{vertical Ekman number.}$

Quasigeostrophy is insured by setting

$$\begin{pmatrix} u \\ v \\ w \\ p \\ \rho \end{pmatrix} = \begin{pmatrix} {}^0u \\ {}^0v \\ {}^0w \\ {}^0p \\ {}^0\rho \end{pmatrix} + \epsilon \begin{pmatrix} {}^1u \\ {}^1v \\ {}^1w \\ {}^1p \\ {}^1\rho \end{pmatrix} + O(\epsilon^2)$$

and adopting the parametric ordering

- (i) $O(\epsilon) < \epsilon/B \ll O(1)$
 (ii) $\alpha y \approx \delta \approx \omega \leq O(\epsilon)$
 and (iii) $\frac{E_v^{1/2}}{\epsilon} \approx \frac{E_H}{\epsilon} \leq O(\epsilon).$

Physically, statement (i) is equivalent to the requirement that the thermocline in a two-layer model not intersect the surface; (ii) demands that the domain have small lateral scales compared to variations in f (and even smaller vertical dimensions), and that the motions be characterized by the advective time scale; lastly, (iii) restricts frictional action to lateral boundary layers of thickness $\omega_F = (E_H/\alpha)^{1/3}$.

Under these conditions, the lowest order balances become

$$\begin{aligned} - {}^0\sigma &= - {}^0p_x \\ {}^0u &= - {}^0p_y \\ {}^0p_z &= - {}^0\rho \\ {}^0\omega &= 0 \\ {}^0u_x + {}^0\sigma_y + {}^0\omega_z &= {}^0u_x + {}^0\sigma_y = 0. \end{aligned}$$

To lowest order the fields are geostrophic and hydrostatic, an approximation consistent with the results of the MODE-I field experiment (Bryden, 1975). To next order

$$\begin{aligned} \frac{d}{dt}({}^0u) - {}^1v - (\alpha y/\epsilon) {}^0v &= -{}^1p_x + (\epsilon_H/\epsilon) \nabla^2({}^0u) \\ \frac{d}{dt}({}^0v) + {}^1u + (\alpha y/\epsilon) {}^0u &= -{}^1p_y + (\epsilon_H/\epsilon) \nabla^2({}^0v) \\ {}^1p_z &= -{}^1\rho \end{aligned} \tag{2.1}$$

$${}^1u_x + {}^1v_y + {}^1\omega_z = 0$$

$$\frac{d}{dt}({}^0\rho) - \mathcal{B}({}^1\omega) = 0$$

where $\frac{d}{dt} = \left(\frac{\omega}{\epsilon}\right) \frac{d}{dt} + {}^0\mathbf{x} \cdot \nabla$.

Equivalently, the vorticity equation may be written as

$$\frac{d}{dt}({}^0\zeta) - {}^1\omega_z + (\alpha/\epsilon) {}^0v - (\epsilon_H/\epsilon) \nabla^2({}^0\zeta) = O(\epsilon + \delta + \alpha y + \epsilon_H + \omega)$$

where the error in this formulation, represented by the right-hand side, is assumed to be everywhere small. Though this may be the case in the mid-ocean environment, the approximations leading to the quasigeostrophic potential vorticity equation are less accurate in the narrow inertiofrictional boundary layers where the scaling arguments break down. (Recent numerical results suggest that this oversimplified treatment of the boundary layers does in fact run into trouble during the spinup of a stratified fluid model; however, the steady or oscillatory equilibrium attained subsequent to the spinup period seems to be relatively insensitive to whether primitive or quasigeostrophic dynamics

are used.) Returning to dimensional form and dropping the prime notation

$$\frac{dS}{dt} + \beta \frac{d\psi}{dx} = f_0 \omega_z + K_H \nabla^2 S \quad (2.2)$$

where the streamfunction, ψ , and vorticity, ζ , assume their standard definitions

$$\psi = \int \frac{v}{f_0} dy$$

and

$$\zeta = \partial_x v - \partial_y u = \nabla^2 \psi.$$

The statement of the problem is completed by specifying an appropriate set of boundary conditions. At $z=0$, we assume the existence of a known wind stress, $\tau(x, y, t)$, while along the bottom the normal component of velocity vanishes. In analogy to the well known homogeneous spinup problem, we anticipate the action of thin Ekman boundary layers at the upper and lower surfaces. These must exist so as to adjust the interior flow to the prescribed boundary conditions. The boundary layers may be turbulent, but the net suction velocities into the interior are assumed to be related to a constant Ekman veering (independent of the interior flow); hence, the equivalent constraints on the interior assume the dimensional form

$$(i) \quad \omega_0 = \omega(z=0) = \frac{\hat{k} \cdot \nabla \times \tau}{\rho_0 f_0} = T/f_0 \quad (2.3)$$

$$\text{and } (ii) \quad \omega_B = \omega(z=-H+h) = \left\{ \frac{1}{2} \nabla^2 h + K_E S \right\}_{z=-H+h} \quad (2.4)$$

where

$$K_E = (K_v / 2f_0)^{1/2}.$$

In the horizontal,

$$(iii) \quad \psi = 0 \quad \begin{array}{l} x = 0, x_0 \\ y = 0, y_0 \end{array} \quad (2.5)$$

to disallow flow through the impermeable boundaries.

(II.2) Conservation principles

A fluid system conforming to the above dynamics quasiconserves both vorticity and energy. Applying the vector identities

$$\begin{aligned} \text{(i)} \quad \psi (\nabla \psi \cdot \nabla \eta) &= \nabla \cdot (\nabla \psi \eta) - \eta (\nabla \psi \cdot \nabla \psi) - \psi \eta (\nabla \cdot \nabla \psi) \\ &= \nabla \cdot (\nabla \psi \eta) \end{aligned}$$

$$\text{and (ii)} \quad \psi \nabla^2 \psi_t = \nabla \cdot (\psi \nabla \psi_t) - \left\{ \frac{(\nabla \psi)^2}{2} \right\}_t$$

where η is an arbitrary scalar function, equation 2.2 can be integrated to yield

$$\frac{d}{dt} \iiint \psi \, dV = K_H \iiint \nabla^2 \psi \, dV + \iint \{ T - f_0 K_E \psi \} \, dx \, dy$$

$$\begin{aligned} \text{and} \quad \frac{d}{dt} \iiint \left\{ \frac{(\nabla \psi)^2}{2} + \frac{f_0^2 (\psi_z)^2}{2N^2} \right\} \, dV &= -K_H \iiint \psi \nabla^2 \psi \, dV \\ &\quad - \iint \left\{ \psi T \Big|_{z=0} - f_0 K_E \psi \Big|_{z=-H+h} \right\} \, dx \, dy \end{aligned}$$

where use has been made of the dimensional form of (2.1). Note that in a closed basin the global integral of the advective terms vanishes. Identifying the quantities $\frac{(\nabla \psi)^2}{2}$ and $\frac{f_0^2 (\psi_z)^2}{2N^2}$ with the kinetic and potential energy densities respectively, these equalities demonstrate that both the integrated vorticity and energy density are conserved in the absence of wind stress and viscous forces. In a similar fashion, other quadratic invariants, such as enstrophy, can be shown to exist.

(II.3) Vertical discretization and the resulting system of equations

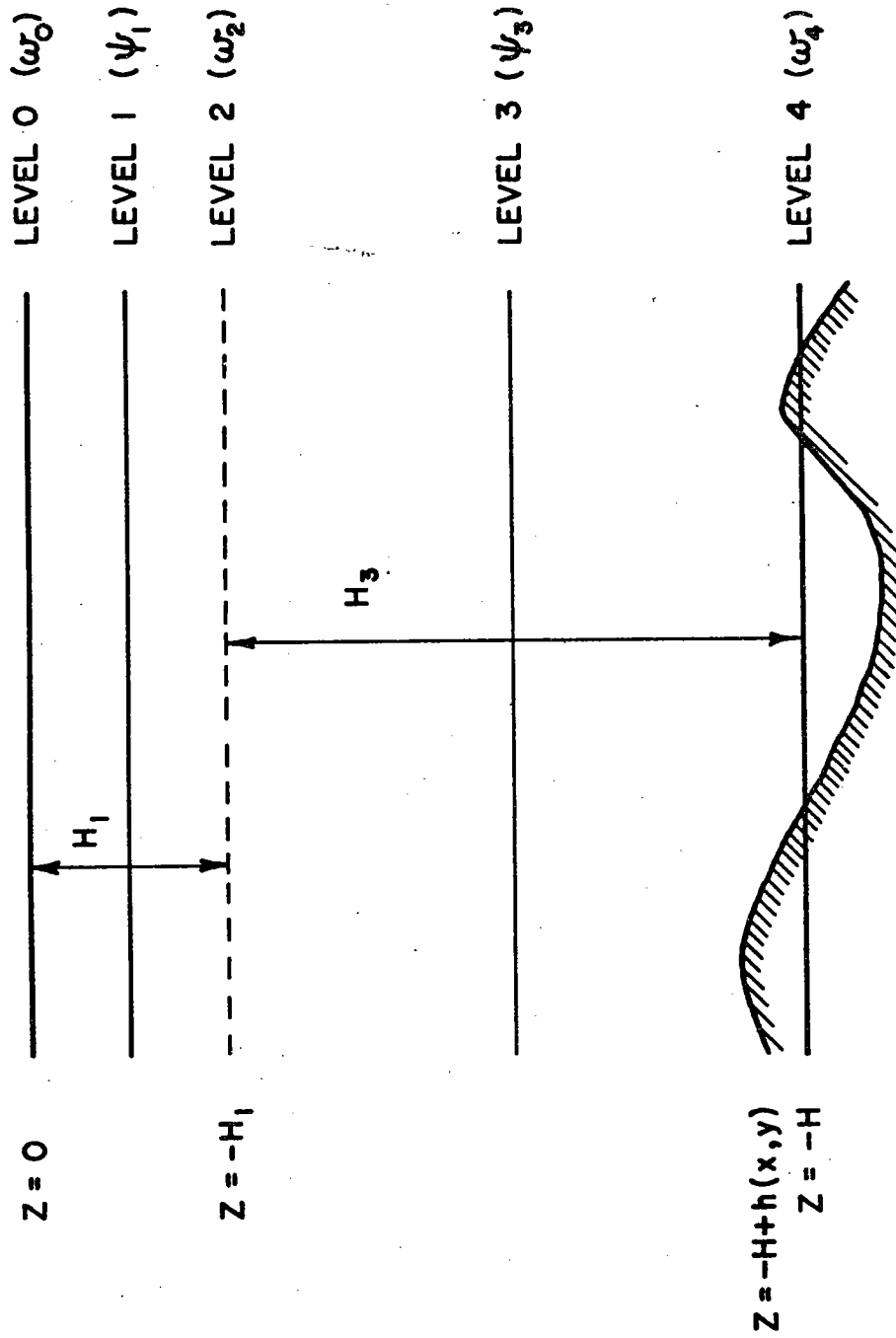
The importance of baroclinicity has already been mentioned.

Fortunately, observational evidence suggests that the physical responses we seek may be adequately modelled by a very coarse vertical decomposition. In fact, we choose to retain only two degrees of freedom in the vertical dimension, a discretization entirely analogous to the assumption of two immiscible fluid layers in stable stratification. In a meteorological context, such two-level models have been known for some time to retain many of the essential features of the baroclinic instability processes observed in continuous systems (Phillips, 1951). This formulation also agrees moderately well with the actual mid-ocean situation in which the upper and lower weakly stratified layers are separated by the highly stable thermocline, and relies on the observed dominance of the barotropic and first baroclinic modes in the mid-ocean environment during the MODE experiment (Gould, Schmitz and Wunsch, 1974). Since both these modes are uniquely recoverable from a two-level model (Flierl, 1975a), such a scheme, while offering the convenience of being simple, yet retains a high degree of dynamic similarity to the real ocean.

Diagrammatically, the vertical grid system is shown in Figure 1. Assuming we know the fields of ψ (and hence ξ) at two nonuniformly spaced levels in the vertical, second-order finite-difference approximations to equation 2.2 at levels 1 and 3 yield

$$\frac{d_1}{dt}(\xi_1) + \beta \frac{d\psi_1}{dx} = K_{1H} \nabla^2 \xi_1 + f_0 \left\{ \frac{\omega_0 - \omega_2}{H_1} \right\} \quad (2.6)$$

Figure 1: Vertical discretization of the continuous problem.



and
$$\frac{d_3}{dt} (\xi_3) + \beta \frac{d^2 \xi_3}{dx^2} = K_{3H} \nabla^2 \xi_3 + f_0 \left\{ \frac{\omega_2 - \omega_4}{H_3} \right\} \quad (2.7)$$

where subscripts denote a given reference level. Note that the equations are coupled through the vertical velocity at level 2, a level taken to correspond to that of the main thermocline in the open ocean. Using (2.1) in dimensional form and the upper and lower boundary conditions 2.3 and 2.4, the coupling can be made more explicit; that is,

$$\frac{d_1}{dt} (\xi_1 + f) + F_1 \frac{d_2}{dt} (\eta_3 - \eta_1) = K_{1H} \nabla^2 \xi_1 + \tau/H_1$$

and
$$\frac{d_3}{dt} (\xi_3 + f) - F_3 \frac{d_2}{dt} (\eta_3 - \eta_1) = K_{3H} \nabla^2 \xi_3 - K_B \xi_4 - (f_0/H_3) \alpha_4 \cdot \nabla h$$

where
$$F_i = \alpha f_0^2 / N^2 H_i H_i \quad (i=1,3)$$

and
$$K_B = (K_V f_0 / 2 H_3^2)^{1/2}$$
.

The Rossby radius of deformation, R_d , in this formulation becomes

$$R_d = (F_1 + F_3)^{-1/2} = (\alpha f_0^2 / N^2 H_1 H_3)^{-1/2}$$

The problem is closed by making the approximations

(i)
$$\alpha_4 \cdot \nabla h = \alpha_3 \cdot \nabla h \quad K_B \xi_4 = K_B \xi_3$$

(ii)
$$K_{1H} = K_{3H} = K_H$$

and (iii)
$$\alpha_2 = (1 - \frac{H_1}{H}) \alpha_1 + (\frac{H_1}{H}) \alpha_3$$

which equate the independent variables at level 2 to a linear combination of those at levels 1 and 3, and the bottom velocity to that at

level 3. Note also that the coefficient of eddy diffusivity is now strictly constant. Finally,

$$\left\{ \frac{d}{dt} + J(\psi_1, \quad) \right\} \left\{ \nabla^2 \psi_1 + f + F_1(\psi_3 - \psi_1) \right\} = K_H \nabla^4 \psi_1 + \frac{T_H}{H} \quad (2.8)$$

and

$$\left\{ \frac{d}{dt} + J(\psi_3, \quad) \right\} \left\{ \nabla^2 \psi_3 + f - F_3(\psi_3 - \psi_1) \right\} = K_H \nabla^4 \psi_3 - K_B \nabla^2 \psi_3 - \left(\frac{f_0}{H_3} \right) J(\psi_3, h). \quad (2.9)$$

The only estimate of the mean stratification enters through the parameters F_1 and F_3 which each contain a factor of $N^2 = \frac{-g}{\rho_0} \frac{d\rho}{dz}$ evaluated at level 2. In practice, the value of the Brunt-Vaisala frequency is not a thermocline (that is a point) value, but some mean stratification representative of the entire water column lying between levels 1 and 3. Subject to some appropriate horizontal discretization and the boundary conditions 2.5, these coupled equations can be solved for ψ_1 and ψ_3 . The numerical details are reserved for Chapter III.

(II.4) The mean field equations

In anticipation of solutions which exhibit both mean and time-dependent features, consider the usual decomposition of the streamfunction into mean and perturbation fields

$$\psi_i = \bar{\psi}_i + \psi_i' \quad (i=1,3)$$

where

$$\bar{\psi}_i = \frac{1}{t_0} \int_0^{t_0} \psi_i dt$$

and by definition

$$\overline{\psi_i'} = 0$$

and can be realized from numerical or observational data if $t_0 \gg \tau_F$, the integral scale for the eddy field. The vorticity and vertical velocity fields may be similarly decomposed. Insofar as we wish to approximate an average over an ensemble of realizations, these operations are assumed to commute with both spatial and temporal differential operators. Given these definitions, the equivalent mean field analogues of (2.6) and (2.7) are

$$\begin{aligned} \frac{d\bar{\psi}_1}{dt} = 0 &= H_1 \bar{u}_1 \cdot \nabla \bar{\psi}_1 + H_1 \overline{u_1' \cdot \nabla \psi_1'} + H_1 \beta \bar{\psi}_1 \\ &\quad - H_1 K_H \nabla^2 \bar{\psi}_1 - \bar{T} + f_0 \bar{\omega}_2 \end{aligned} \quad (2.11)$$

and

$$\begin{aligned} \frac{d\bar{\psi}_3}{dt} = 0 &= H_3 \bar{u}_3 \cdot \nabla \bar{\psi}_3 + H_3 \overline{u_3' \cdot \nabla \psi_3'} + H_3 \beta \bar{\psi}_3 \\ &\quad - H_3 K_H \nabla^2 \bar{\psi}_3 + H_3 K_B \bar{\psi}_3 + f_0 \bar{u}_3 \cdot \nabla h - f_0 \bar{\omega}_2. \end{aligned} \quad (2.12)$$

The mean vorticity dynamics are then seen to arise from a local balance of advective, Reynolds stress, and planetary vorticity effects, lateral and bottom viscous dissipation, wind forcing, and the stretching of

vortex lines due to the vertical motions induced at the level of the thermocline (level 2) and at the bottom (level 4).

Defining the mean and eddy energy densities as

$$\begin{aligned} \bar{K}_i &= H_i \frac{(\nabla \bar{\psi}_i)^2}{2} \\ K'_i &= H_i \frac{(\nabla \psi'_i)^2}{2} \end{aligned} \quad (2.10)$$

$$\bar{P} = c (\bar{\psi}_3 - \bar{\psi}_1)^2 = c \bar{\chi}^2 \quad c = \frac{f_0^2}{N^2 H}$$

and
$$P' = c \overline{(\psi'_3 - \psi'_1)^2} = c \overline{\chi'^2}$$

equations 2.1, 2.6, and 2.7 combine to give the mean energetic balances

$$\begin{aligned} \frac{d}{dt} (\bar{K}_1) &= 0 = H_1 \nabla \cdot \left\{ \bar{\psi}_1 \bar{\rho}_1 \bar{u}_1 + f \bar{\psi}_1 \bar{u}_1 + \bar{\psi}_1 \overline{u'_1 \rho'_1} \right\} \\ &+ \langle \bar{P} \rightarrow \bar{K}_1 \rangle + \langle \bar{W} \rightarrow \bar{K}_1 \rangle + \langle K'_1 \rightarrow \bar{K}_1 \rangle - \langle \bar{K}_1 \rightarrow D_H \rangle \end{aligned} \quad (2.13)$$

$$\begin{aligned} \frac{d}{dt} (\bar{K}_3) &= 0 = H_3 \nabla \cdot \left\{ \bar{\psi}_3 \bar{\rho}_3 \bar{u}_3 + f \bar{\psi}_3 \bar{u}_3 + \bar{\psi}_3 \overline{u'_3 \rho'_3} + \frac{f_2}{H_3} \bar{\psi}_3 h \bar{u}_3 \right\} \\ &+ \langle \bar{P} \rightarrow \bar{K}_3 \rangle + \langle K'_3 \rightarrow \bar{K}_3 \rangle - \langle \bar{K}_3 \rightarrow D_H \rangle - \langle \bar{K}_3 \rightarrow D_B \rangle \end{aligned} \quad (2.14)$$

and
$$\begin{aligned} \frac{d}{dt} (\bar{P}) &= 0 = -2c \nabla \cdot \left\{ \bar{u}_2 \left(\frac{\bar{\chi}^2}{2} \right) + \bar{\chi} \overline{u'_2 \chi'} \right\} \\ &- \langle \bar{P} \rightarrow \bar{K}_1 \rangle - \langle \bar{P} \rightarrow \bar{K}_3 \rangle + \langle P' \rightarrow \bar{P} \rangle \end{aligned} \quad (2.15)$$

where $\langle \bar{P} \rightarrow \bar{K}_1 \rangle = f_0 \bar{\psi}_1 \bar{w}_2$

$$\langle \bar{P} \rightarrow \bar{K}_3 \rangle = -f_0 \bar{\psi}_3 \bar{w}_2$$

$$\langle K'_i \rightarrow \bar{K}_i \rangle = - \overline{u'_i \rho'_i} \cdot \nabla \bar{\psi}_i \quad (i=1,3)$$

$$\langle P' \rightarrow \bar{P} \rangle = 2c \overline{u'_2 \chi'} \cdot \nabla \bar{\chi}$$

$$\langle \bar{K}_i \rightarrow D_H \rangle = H_i K_H \bar{\psi}_i \nabla^2 \bar{\psi}_i \quad (i=1,3)$$

$$\langle \bar{K}_3 \rightarrow D_B \rangle = -H_3 K_B \bar{\psi}_3 \bar{S}_3$$

and $\langle \bar{W} \rightarrow \bar{K}_1 \rangle = -f_0 \bar{\psi}_1 \bar{T}$.

The eddy energy balances can be cast in a similar form:

$$\frac{d}{dt} (K'_1) = 0 = H_1 \nabla \cdot \left\{ \bar{u}_1 \overline{\psi'_1 S'_1} + \bar{S}_1 \overline{u'_1 \psi'_1} + \overline{u'_1 \psi'_1 S'_1} + f \overline{\psi'_1 u'_1} \right\} + \langle P' \rightarrow K'_1 \rangle - \langle K'_1 \rightarrow \bar{K}_1 \rangle + \langle W' \rightarrow K'_1 \rangle - \langle \bar{K}_1 \rightarrow D_H \rangle \quad (2.16)$$

$$\frac{d}{dt} (K'_3) = 0 = H_3 \nabla \cdot \left\{ \bar{u}_3 \overline{\psi'_3 S'_3} + \bar{S}_3 \overline{u'_3 \psi'_3} + \overline{u'_3 \psi'_3 S'_3} + f \overline{\psi'_3 u'_3} \right\} + \langle P' \rightarrow K'_3 \rangle - \langle K'_3 \rightarrow \bar{K}_3 \rangle - \langle K'_3 \rightarrow D_H \rangle - \langle K'_3 \rightarrow D_B \rangle \quad (2.17)$$

and $\frac{d}{dt} (P') = 0 = -2c \left\{ \bar{u}_2 \overline{\left(\frac{\chi'^2}{2} \right)} + \overline{u'_2 \left(\frac{\chi'^2}{2} \right)} - \bar{\chi} \overline{u'_2 \chi'} \right\} - \langle P' \rightarrow K'_1 \rangle - \langle P' \rightarrow K'_3 \rangle - \langle P' \rightarrow \bar{P} \rangle \quad (2.18)$

where

$$\langle P' \rightarrow K'_1 \rangle = f_0 \overline{\psi'_1 \omega'_2}$$

$$\langle P' \rightarrow K'_3 \rangle = -f_0 \overline{\psi'_3 \omega'_2}$$

$$\langle K'_i \rightarrow D_H \rangle = -H_i K_H \overline{\psi'_i \nabla^2 S'_i} \quad (i=1,3)$$

$$\langle K'_3 \rightarrow D_B \rangle = H_3 K_B \overline{\psi'_3 S'_3}$$

and $\langle W' \rightarrow K'_1 \rangle = -f_0 \overline{\psi'_1 T'}$.

Ignoring the advective terms which do not contribute to the global energetics, the remaining terms reflect the transfers of energy between the components of kinetic and potential energy. Also represented are the sources and sinks of energy arising from the mechanical action of the wind at the sea surface ($\langle \bar{W} \rightarrow \bar{K}_1 \rangle$), lateral dissipation ($\langle \bar{K}_i \rightarrow D_H \rangle$), and bottom drag effects ($\langle \bar{K}_3 \rightarrow D_B \rangle$). A summation of (2.13) through (2.18) readily shows that quasiconservation of mean total energy is

maintained in this vertically quantized version of the original continuous problem. As in the case of a double-layered fluid model, the components of mean potential energy as defined in (2.10) are interpretable precisely in terms of the concept of available potential energy (Lorenz, 1955). Under our assumptions, the lowest order (unavailable) potential energy corresponds to a state of no motion, $\psi_i \equiv 0$, and is of little dynamical significance.

(III) Numerical Solution Techniques

Because we have restricted our attention to a rectangular domain, equations 2.8 and 2.9 can be integrated via pseudospectral approximation, a variant of the Galerkin (spectral) method which is highly efficient in simulating incompressible flows within simple geometries (Orszag, 1971a). Both techniques use truncated spectral series to approximate the primary variables and their derivatives, which can be accurately evaluated in the spectral domain; however, pseudospectral approximation imposes the governing differential equations at selected collocation points in physical space, whereas the Galerkin procedure distributes the error more uniformly by making the error in the (discretized) differential equation orthogonal to the expansion functions (Orszag, 1972). In comparison to the more traditional finite-difference techniques, spectral and pseudospectral methods possess several advantages, most notably that they are not subject to first-differencing (phase), second-differencing, or incompressibility errors (Orszag, 1971b). Moreover, if a problem has an infinitely differentiable solution, then spectral and pseudospectral approximation with an N term spectral series converge faster than any power of $(1/N)$ as $N \rightarrow \infty$.¹ Since spectral schemes are also efficiently implementable via fast transform methods, they offer substantial gains in accuracy over finite-difference techniques. On the other hand, spectral and pseudospectral methods seem to be equally accurate in the simulation of

¹Such series are said to possess "infinite" order accuracy in analogy to simple finite-difference schemes whose error decreases as some finite power of Δs , the mesh size (Orszag, 1971b).

many geophysical turbulence problems despite aliasing "errors" in the pseudospectral approach (Fox and Orszag, 1973). For these reasons, and because of its twofold advantage in efficiency, pseudospectral prediction is preferred in most applications, as indeed it will be here.

(III.1) Lateral boundary conditions and choice of the expansion series

In order to completely specify the problem, conditions on the lateral boundaries must be chosen in addition to (2.5). For our problem, in which both inflow and outflow have been ignored, the eastern and western boundaries will be modelled either as "slippery" or "rigid" surfaces; that is, flows tangential to the lateral walls either suffer no frictional retardation whatsoever, in which case

$$(\psi_i)_{xx} = 0 \quad x=0, x_0 \quad (i=1,3) \quad (3.1)$$

or are allowed no slippage at all, whereby ψ must vanish and

$$(\psi_i)_x = 0 \quad x=0, x_0 \quad (i=1,3). \quad (3.2)$$

The northern and southern walls are thought of as the boundaries between adjacent oceanic gyres that exchange neither mass nor momentum; hence,

$$(\psi_i)_{yy} = 0 \quad y=0, y_0 \quad (i=1,3) \quad (3.3)$$

will be assumed to hold in all cases.

We have yet to choose an appropriate set of horizontal expansion functions. Clearly, the suitability of a particular series depends critically on the choice of boundary conditions. If, for instance, our domain were periodic, a two-dimensional Fourier series would be convenient. Let us suppose first that the constraints (3.1) and (3.3), as well as (2.5), apply. Then, not only the streamfunction, ψ , but the vorticity, $\zeta = \nabla^2 \psi$, must vanish on all four walls. A convenient expansion for this behavior might be

$$\psi_i(x, y) = \sum_{n=0}^N \sum_{m=0}^M a_{inm} \sin(kx) \sin(ly) \quad (3.4)$$

where $k = \frac{n\pi}{x_0}$

and $l = \frac{m\pi}{y_0}$

identically satisfy the boundary conditions. This series is again implementable via the fast Fourier transform (FFT) algorithm. Unfortunately, this series representation fails due to the presence of the planetary vorticity term. In particular, $\beta \frac{\partial \psi}{\partial x}$ must formally be a truncated series of cosine functions. These, in turn, can be asymptotically represented by an equivalent sine expansion, but not without the appearance of a Gibbs effect near $x = 0, x_0$ where the summation of sine modes vanishes and cannot model a nonzero first derivative field. In this sense, $\psi \propto \sin(kx)$ is not a "natural" expansion for a problem in which β is nonzero; even for an initial field completely describable by (3.4), non-sinusoidal terms are immediately generated in the x direction. Physically, this can be most easily visualized in the Munk model of the wind-driven ocean circulation (Munk, 1950) in which lateral viscous stresses ($K_H \nabla^2 \psi$) arise to balance the planetary vorticity effect in the western boundary layer region. The maximum diffusion of vorticity occurs at $x = 0$ and clearly cannot be simulated by $\psi \propto \sin(kx)$. Note, however, that sinusoidal expansion of ψ in the y direction suffers no such defect since all dynamical terms can be exactly represented as a north-south sine series. This antisymmetry about $y=y_0$ together with the constrain that ψ be real, makes it possible to utilize highly efficient fast Fourier sine transforms (FFST) which

require approximately one quarter the number of operations of a conventional FFT on the same array (Appendix A). (In addition, we have used machine language programming for all fast Fourier transforms, thereby increasing efficiency by a factor of two over the comparable FORTRAN codes.)

Now suppose that the streamfunction fields satisfy (3.2) and (3.3). Since the boundary conditions along the northern and southern extremities remain unchanged, a FFST can again be applied in the y direction. As we approach the eastern and western walls, however, frictional effects must bring the flow to rest. Such a boundary layer velocity profile clearly cannot be represented in general by an expansion of the type (3.4). This consideration, together with that mentioned in connection with the planetary vorticity effect, dictates that we choose an extremely flexible expansion in the x direction. We therefore let

$$\psi_i(\hat{x}, y) = \sum_{n=0}^N \sum_{m=0}^M a_{inm} T_n(\hat{x}) \sin(\frac{m}{M} \pi y) \quad (3.5)$$

where $\hat{x} = (2x - x_0) / x_0$, and $T_n(\hat{x}) = T_n(\cos \theta) = \cos(n\theta)$ is the Chebyshev polynomial of degree n, a function of the linearly stretched coordinate \hat{x} . If we now choose the collocation points

$$(\hat{x}_p, y_b) = \left\{ \cos\left(\frac{\pi p}{N}\right), \frac{q y_0}{M} \right\},$$

then

$$\psi_i(\hat{x}_p, y_b) = \sum_{n=0}^N \sum_{m=0}^M a_{inm} \cos\left\{\frac{\pi p n}{N}\right\} \sin\left\{\frac{\pi q m}{M}\right\}.$$

In other words, a series in $T_n(\hat{x})$ is identical to a cosine transform on a nonuniformly stretched grid of points. This equivalence

underscores two important numerical advantages of the Chebyshev technique, namely,

- (i) a Chebyshev expansion can be implemented using a fast Fourier cosine transform (FFCT, Appendix A), and
- (ii) the nonuniformly spaced collocation points \hat{x}_p are more densely packed near $\hat{x} = \pm 1$, thereby insuring increased resolution at the western and eastern walls where the most highly structured flows are anticipated (Table 1).

A more detailed account of the solution technique is given in the following sections.

Table 1: The location and separation of the equivalent collocation points (N_C) for a 32-term Chebyshev expansion in a 1000 km domain.

N_c	x (km)	Δx (km)
0	0.0	2.4
1	2.4	7.2
2	9.6	11.9
3	21.5	17.1
4	38.6	20.4
5	59.0	25.3
6	84.3	29.2
7	113.5	32.9
8	146.4	36.4
9	182.8	39.4
10	222.2	42.1
11	264.3	44.4
12	308.7	46.2
13	354.9	47.6
14	402.5	48.5
15	451.0	49.0
16	500.0	

N_c	x (km)	Δx (km)
17	549.0	48.5
18	597.5	47.6
19	645.1	46.2
20	691.3	44.4
21	735.7	42.1
22	777.8	39.4
23	817.2	36.4
24	853.6	32.9
25	886.5	29.2
26	915.7	25.3
27	941.0	20.4
28	961.9	17.1
29	978.5	11.9
30	990.4	7.2
31	997.6	2.4
32	1000.0	

(III.2) The decoupled equations

The equations to be solved are (2.8) and (2.9), subject to some suitable expansion of the time derivative terms. In order to treat the diffusion terms semi-implicitly, we use the modified Adams-Bashforth scheme described in Appendix C. Under this second-order approximation, the dynamic equations become, in the usual notation,

$$\begin{aligned} & \left[-\left(\frac{\Delta t K_H}{2}\right) \nabla^2 \xi_1 + \xi_1 + F_1(\psi_3 - \psi_1) \right]^{k+1} = \\ & \left[\xi_1 + F_1(\psi_3 - \psi_1) \right]^k + \left(\frac{3\Delta t}{2}\right) \xi_1^k + \left(\frac{\Delta t}{2}\right) (\eta_1^k - \xi_1^{k-1}) = R_1(x, y) \end{aligned}$$

$$\begin{aligned} \text{and} \quad & \left[-\left(\frac{\Delta t K_H}{2}\right) \nabla^2 \xi_3 + \xi_3 - F_3(\psi_3 - \psi_1) \right]^{k+1} = \\ & \left[\xi_3 - F_3(\psi_3 - \psi_1) \right]^k + \left(\frac{3\Delta t}{2}\right) \xi_3^k + \left(\frac{\Delta t}{2}\right) (\eta_3^k - \xi_3^{k-1}) = R_3(x, y) \end{aligned}$$

$$\text{where} \quad \xi_1^k = -J \left\{ \psi_1, \xi_1 + f + F_1 \psi_3 \right\}^k + T_{H_1}^k$$

$$\xi_3^k = -J \left\{ \psi_3, \xi_3 + f + F_3 \psi_1 + \left(\frac{f_3}{H_3}\right) h \right\}^k - K_B \xi_3^k$$

$$\text{and} \quad \eta_i^k = K_H \nabla^4 \psi_i^k \quad (i=1, 3).$$

To further simplify the numerical analysis, we decouple the equations by isolating the equivalent barotropic and baroclinic modal equations in the new variables

$$\phi_1 = \psi_1 + \left(\frac{H_3}{H_1}\right) \psi_3$$

$$\text{and} \quad \phi_3 = \psi_1 - \psi_3.$$

Stability considerations dictate that the resulting uncoupled fourth-order equations be solved in a two-step procedure when using the tau method to be described shortly. Therefore, the resulting equations take the form

$$\begin{aligned} \left[\nabla^2 \mathcal{H}_1 - \left(\frac{\partial}{\partial t} K_H \right) \mathcal{H}_1 \right]^{k+1} &= R_1 + (H_3/H_1) R_3 \\ \nabla^2 \varphi_1^{k+1} &= - \left(\frac{\partial}{\partial t} K_H \right) \mathcal{H}_1^{k+1} \end{aligned}$$

$$\begin{aligned} \text{and} \quad \left[\nabla^2 \mathcal{H}_3 + G \mathcal{H}_3 \right]^{k+1} &= R_1 - R_3 \\ \left[\nabla^2 \varphi_3 - \left(\frac{\partial}{\partial t} K_H + G \right) \varphi_3 \right]^{k+1} &= - \left(\frac{\partial}{\partial t} K_H \right) \mathcal{H}_3^{k+1} \end{aligned}$$

$$\text{where} \quad G = \left\{ -1 + \left[1 - \frac{4f_0^2 \Delta t K_H}{N^2 H_1 H_3} \right]^{1/2} \right\} / \Delta t K_H .$$

In analogy to (3.5), we expand the independent variables as

$$\varphi_i(\hat{x}, y) = \sum_{n=0}^N \sum_{m=0}^M a_{inm} T_n(\hat{x}) \sin(ly)$$

$$\text{and} \quad \mathcal{H}_i(\hat{x}, y) = \sum_{n=0}^N \sum_{m=0}^M b_{inm} T_n(\hat{x}) \sin(ly) .$$

Since the R_i are defined at previous time levels and hence presumed known, the sine expansion in the north-south direction decouples the y-dependence from the problem. In n-m (wavenumber) space, reached by a simultaneous FFST in y and a FFCT in x, the problem may be solved independently for each mode number m in the truncated y expansion. For m fixed, the equations reduce to the following

$$\left[b_1'' - \left(\frac{2}{\Delta t K_H} + l^2 \right) b_1 \right]_{nm}^{k+1} = \left[R_1 + \left(H_3/H_1 \right) R_3 \right]_{nm} \quad 0 \leq n \leq N \quad (3.6a)$$

$$\left[a_1'' - l^2 a_1 \right]_{nm}^{k+1} = - \left(\frac{2}{\Delta t K_H} \right) b_{1nm}^{k+1} \quad 0 \leq n \leq N \quad (3.6b)$$

$$\left[b_3'' + (G - l^2) b_3 \right]_{nm}^{k+1} = \left[R_1 - R_3 \right]_{nm} \quad 0 \leq n \leq N \quad (3.7a)$$

$$\left[a_3'' - \left(\frac{2}{\Delta t K_H} + G + l^2 \right) a_3 \right]_{nm}^{k+1} = - \left(\frac{2}{\Delta t K_H} \right) b_{3nm}^{k+1} \quad 0 \leq n \leq N \quad (3.7b)$$

where a double prime refers to a coefficient in a second derivative series (Appendix B).

(III.3) Solution technique - free-slip boundaries

We now outline the method of solution for a system entirely enclosed by free-slip boundaries, a constraint which together with the requirement of no normal flow through the boundaries, implies that

$$\psi_i = \xi_i = 0 \quad (i=1,3) \text{ on } \hat{x}=\pm 1 - \text{equations 2.5 and 3.1.}$$

Note that no further regard need be paid to the northern and southern walls, since the expansion in $\sin(\ell y)$ identically satisfies the free-slip constraints at $y=0, y_0$. The solution technique we adopt has been alluded to in the previous section; it is an approximation called the tau method, and consists merely of neglecting the two highest order dynamic equations in each of 3.6a, 3.6b, 3.7a, and 3.7b. The remaining equations are then supplemented by eight boundary conditions to close the system. Rewriting the boundary conditions in terms of their Chebyshev series equivalents (Appendix B), the final problem becomes, for fixed m ,

$$\left[b_i'' - \left(\frac{\alpha^2}{\Delta t K_H} + \ell^2 \right) b_i \right]_{nm}^{k+1} = \left[R_1 + \left(\frac{H_3}{H_1} \right) R_3 \right]_{nm} \quad 0 \leq n \leq N-2$$

$$\sum_{\substack{n=0 \\ n \text{ even}}}^N b_{1nm}^{k+1} = \sum_{\substack{n=0 \\ n \text{ odd}}}^N b_{1nm}^{k+1} = 0$$

$$\left[a_i'' - \ell^2 a_i \right]_{nm}^{k+1} = - \left(\frac{\alpha^2}{\Delta t K_H} \right) b_{1nm}^{k+1} \quad 0 \leq n \leq N-2$$

$$\sum_{\substack{n=0 \\ n \text{ even}}}^N a_{1nm}^{k+1} = \sum_{\substack{n=0 \\ n \text{ odd}}}^N a_{1nm}^{k+1} = 0$$

$$\text{and } [b_3'' + (G - l^2)b_3]_{nm}^{k+1} = [R_1 - R_3]_{nm} \quad 0 \leq n \leq N-2 \quad (3.8a)$$

$$\sum_{\substack{n=0 \\ n \text{ even}}}^N b_{3nm}^{k+1} = \sum_{\substack{n=0 \\ n \text{ odd}}}^N b_{3nm}^{k+1} = 0 \quad (3.8b)$$

$$\left[a_3'' - \left(\frac{2}{\Delta t K_H} + G + l^2 \right) a_3 \right]_{nm}^{k+1} = - \left(\frac{2}{\Delta t K_H} \right) b_{3nm}^{k+1} \quad 0 \leq n \leq N-2$$

$$\sum_{\substack{n=0 \\ n \text{ even}}}^N a_{3nm}^{k+1} = \sum_{\substack{n=0 \\ n \text{ odd}}}^N a_{3nm}^{k+1} = 0$$

By expanding a_i'' and b_i'' in terms of the equivalent a_i and b_i series expansions (Appendix B, equation b.2), the resulting upper diagonal matrix equations are repeatedly solved via standard matrix inversion techniques for each mode number m in the discrete north-south expansion. A pair of inverse Fourier transforms (IFFST and IFFCT) then yields φ_{ipq}^{k+1} and ρ_{ipq}^{k+1} ($i=1,3$) from which the state of the system at $t = (k+1)\Delta t$ is exactly known.

It has been brought to our attention that an even more efficient matrix solution technique exists. Consider equations b.4 and b.5 of Appendix B. These expressions show that, rather than using the cumbersome series representation for a_i'' and b_i'' , we can write the second derivative terms in a much more compact form. For example, we can expand (3.8a) according to (b.4) and (b.5) to get the following series of relations:

$$[b_{3n}'' + (G - l^2)b_{3n}]_m^{k+1} = [R_{1m} - R_{3m}]_m,$$

$$\left[b_{3n}'' + \left(\frac{G - l^2}{2n} \right) \{ c_{n-1} b'_{3,n-1} - b'_{3,n+1} \} \right]_m^{k+1} = [R_{1m} - R_{3m}]_m,$$

$$\left[b_{3n}'' + \frac{(G-l^2)c_{n-1}}{4n(n-1)} \{ c_{n-2} b_{3,n-2}'' - b_{3n}'' \} - \frac{(G-l^2)}{4n(n+1)} \{ c_n b_{3n}'' - b_{3,n+2}'' \} \right]_m^{k+1} = [R_{1n} - R_{3n}]_m,$$

$$\left[\left\{ \frac{G-l^2}{4n(n+1)} \right\} b_{3,n+2}'' + \left\{ 1 - \frac{(G-l^2)c_{n-1}}{4n(n-1)} - \frac{(G-l^2)c_n}{4n(n+1)} \right\} b_{3n}'' + \left\{ \frac{(G-l^2)c_{n-1}c_{n-2}}{4n(n-1)} \right\} b_{3,n-2}'' \right]_m^{k+1} = [R_{1n} - R_{3n}]_m,$$

or, finally,

$$\left[\left\{ \frac{1}{4n(n+1)} \right\} b_{3,n+2} + \left\{ \frac{1}{G-l^2} - \frac{c_{n-1}}{4n(n-1)} - \frac{c_n}{4n(n+1)} \right\} b_{3n} + \left\{ \frac{c_{n-1}c_{n-2}}{4n(n-1)} \right\} b_{3,n-2} \right]_m^{k+1} = \left\{ \frac{[R_{1,n+2} - R_{3,n+2}]_m}{4n(n+1)(G-l^2)} \right\} - \left\{ \frac{c_{n-1}}{4n(n-1)} - \frac{c_n}{4n(n+1)} \right\} \frac{[R_{1n} - R_{3n}]_m}{(G-l^2)} + \left\{ \frac{c_{n-1}c_{n-2}}{4n(n-1)} \right\} \frac{[R_{1,n-2} - R_{3,n-2}]_m}{(G-l^2)} \quad (3.8c)$$

Thus, for fixed m , the equation for mode n can be written in terms of the known quantities R_i ($i=1,3$) and the unknown coefficients $b_{3,n+2}$, $b_{3,n}$, and $b_{3,n-2}$. Together with the boundary conditions 3.8b, the dynamic equations in the new representation 3.8c clearly decouple into two independent problems, one for n even and another for n odd. In addition, since the equation for the n^{th} mode involves only modes $n+2$, n , and $n-2$, the matrix equations are tridiagonal and diagonally dominant (except for the boundary condition which involves the sum of the b_3 coefficients). Matrices of this form (as opposed to the more general upper diagonal matrices considered above), can be inverted more efficiently and with less round off error. In its future applications, the

pseudospectral model will be modified to take advantage of this tri-diagonality.

As in finite difference schemes, care should perhaps be taken to quasi- conserve such quadratic quantities as energy and entropy. In analogy to the well known Arakawa schemes (Arakawa, 1966), there exist a set of equivalent forms for pseudospectral nonlinear operators that can be shown to approximate the desired conservative properties (Appendix D). For instance, it is quite easy to prove that one such energy preserving form is

$$[J(\psi, \eta)]_{pq}^k = \left[\frac{d}{dy} (\eta \frac{dy}{dx}) - \frac{d}{dx} (\eta \frac{dy}{dy}) \right]_{pq}^k$$

with η an arbitrary scalar function. This form has been used throughout except in the case of the planetary vorticity terms, $J(\psi_i, f)$, which are given their correct pointwise values, $\beta \psi_i$, $i = 1, 3$.¹ Note also a further advantage of the pseudospectral technique, namely, both the advective terms and the boundary conditions are implemented to infinite order accuracy. As we shall see, this is not only true for rather simple boundary constraints, as in the case of free-slip walls, but also when more complicated conditions must be imposed.

¹This points out the choice that must be made in all spectral β -plane models. The planetary vorticity term may be included in one of two ways: as $J(\psi_i, f)$ which though identically conservative may not be pointwise equal to $\beta \psi_i / dx$, or as $\beta \psi_i / dx$ which though locally correct is not globally conservative. These differences arise from the properties of the pseudospectral technique and the implicit assumption, valid only in the limit of infinite resolution, that $f = f_0 + \beta y$ can be exactly expanded in analogy to (2.5) in a Chebyshev-sine series.

(III.4) Solution technique - no-slip boundaries

Retaining the free-slip conditions on $y = 0, y_0$, let us modify those on the eastern and western walls to disallow slippage along $\hat{x} = \pm 1$. Referring to Appendix B, this requirement (equation 3.2) can be compactly restated in terms of the Chebyshev coefficients:

$$\sum_{\substack{n=0 \\ n \text{ even}}}^N n^2 a_{1nm} = \sum_{\substack{n=0 \\ n \text{ odd}}}^N n^2 a_{1nm} = 0 \quad (3.9a)$$

and

$$\sum_{\substack{n=0 \\ n \text{ even}}}^N n^2 a_{3nm} = \sum_{\substack{n=0 \\ n \text{ odd}}}^N n^2 a_{3nm} = 0 \quad (3.9b)$$

(m fixed).

In addition, we once again require $\psi_i = 0$ ($i = 1, 3$) on $\hat{x} = \pm 1$.

To satisfy these somewhat more cumbersome conditions, we adopt what is best described as a discrete Green's function approach. This is necessitated by the fact that all four constraints are given in terms of the a_{inm} ; we have no conditions to apply on either of the Helmholtz equations for vorticity. We circumvent this problem by employing a two-step procedure in which we solve two related problems:

(Step I)

$$\left[p B_i'' - \left(\frac{\alpha}{\Delta t K_H} + \ell^2 \right) p B_i \right]_{nm}^{k+1} = \left[R_1 + \left(\frac{H_3}{H_1} \right) R_3 \right]_{nm} \quad 0 \leq n \leq N-2$$

$$\sum_{\substack{n=0 \\ n \text{ even}}}^N p B_{1nm}^{k+1} = \sum_{\substack{n=0 \\ n \text{ odd}}}^N p B_{1nm}^{k+1} = 0$$

$$\left[p A_i'' - \ell^2 p A_i \right]_{nm}^{k+1} = - \left(\frac{\alpha}{\Delta t K_H} \right) p B_{1nm}^{k+1} \quad 0 \leq n \leq N-2$$

$$\sum_{\substack{n=0 \\ n \text{ even}}}^N p A_{1nm}^{k+1} = \sum_{\substack{n=0 \\ n \text{ odd}}}^N p A_{1nm}^{k+1} = 0$$

$$\begin{aligned}
[\rho B_3'' + (G - \ell^2) \rho B_3]_{nm}^{k+1} &= [R_1 - R_3]_{nm} \quad 0 \leq n \leq N-2 \\
\sum_{\substack{n=0 \\ n \text{ even}}}^N \rho B_{3nm}^{k+1} &= \sum_{\substack{n=0 \\ n \text{ odd}}}^N \rho B_{3nm}^{k+1} = 0 \\
[\rho A_3'' - (\frac{2}{\Delta t K_H} + G + \ell^2) \rho A_3]_{nm}^{k+1} &= -(\frac{2}{\Delta t K_H}) \rho B_{3nm}^{k+1} \quad 0 \leq n \leq N-2 \\
\sum_{\substack{n=0 \\ n \text{ even}}}^N \rho A_{3nm}^{k+1} &= \sum_{\substack{n=0 \\ n \text{ odd}}}^N \rho A_{3nm}^{k+1} = 0
\end{aligned}$$

(Step II)

$$\begin{aligned}
[h B_1'' - (\frac{2}{\Delta t K_H} + \ell^2) h B_1]_{nm}^{k+1} &= 0 \quad 0 \leq n \leq N-2 \\
\sum_{\substack{n=0 \\ n \text{ even}}}^N h B_{1nm}^{k+1} &= \sum_{\substack{n=0 \\ n \text{ odd}}}^N h B_{1nm}^{k+1} = 1 \\
[h A_1'' - \ell^2 h A_1]_{nm}^{k+1} &= -(\frac{2}{\Delta t K_H}) h B_{1nm}^{k+1} \quad 0 \leq n \leq N-2 \\
\sum_{\substack{n=0 \\ n \text{ even}}}^N h A_{1nm}^{k+1} &= \sum_{\substack{n=0 \\ n \text{ odd}}}^N h A_{1nm}^{k+1} = 0 \\
[h B_3'' + (G - \ell^2) h B_3]_{nm}^{k+1} &= 0 \quad 0 \leq n \leq N-2 \\
\sum_{\substack{n=0 \\ n \text{ even}}}^N h B_{3nm}^{k+1} &= \sum_{\substack{n=0 \\ n \text{ odd}}}^N h B_{3nm}^{k+1} = 1 \\
[h A_3'' - (\frac{2}{\Delta t K_H} + G + \ell^2) h A_3]_{nm}^{k+1} &= -(\frac{2}{\Delta t K_H}) h B_{3nm}^{k+1} \quad 0 \leq n \leq N-2 \\
\sum_{\substack{n=0 \\ n \text{ even}}}^N h A_{3nm}^{k+1} &= \sum_{\substack{n=0 \\ n \text{ odd}}}^N h A_{3nm}^{k+1} = 0
\end{aligned}$$

Evidently, the first problem determines the particular solution we are seeking subject to $\nabla^2 \psi_i = 0$ ($i = 1, 3$) on $\hat{x} = \pm 1$. In the second step, we isolate an independent homogeneous solution by requiring

$$\sum_{\substack{n=0 \\ n \text{ even}}}^N h \beta_{inm}^{k+1} = \sum_{\substack{n=0 \\ n \text{ odd}}}^N h \beta_{inm}^{k+1} = 1 \quad (i=1,3).$$

We have yet to satisfy (3.8a,b); therefore, choose

$$\begin{aligned} a_{inm} &= p A_{inm} + \alpha_i (h A_{inm}) \\ \text{and} \\ b_{inm} &= p B_{inm} + \alpha_i (h B_{inm}) \end{aligned} \quad (i=1,3).$$

Needless to say, the free constraints α_1 and α_3 are chosen to satisfy 3.9a and 3.9b. (There are actually a total of four α 's, one pair for n even and another for n odd; since the odd and the even modes are not coupled, these problems are solved independently for maximum efficiency. At each time step then, we apply the Green's function technique $O(4M)$ times - twice for $i=1, 3$, twice for n odd and n even, and M times for $m=0, M$.) The problem is then solved.

Although this procedure appears to require twice as many matrix solutions as the scheme for a free-slip basin, this is in fact not the case. Step II does not depend on the state of the system at previous time levels and need be preprocessed only once at the beginning of a simulation. Conceptually, the scheme is somewhat more complicated, but the efficiency is negligibly affected, the only additional calculations being those required to fix α_1 and α_3 . As in the case of slippery walls, these calculations conserve energy in the absence of dissipation and time differencing errors (in the sense outlined in Appendix D).

(IV) Eddy Sensitivity to Western Boundary Layer Structure

The recent work of Holland and Lin (henceforth referred to as HL) exemplifies the prevailing eddy modelling strategy which is to investigate eddy behavior under a large range of frictional and topographic parameterizations, and driving and boundary conditions. The pseudo-spectral model developed in Chapter III has been designed to make such parametric studies and in particular to address the previously unanswered question of the sensitivity of mid-ocean eddy dynamics to changes in boundary layer structure. (Enhanced boundary layer flexibility makes the Chebyshev formulation particularly attractive for such studies.)

In order to make our comparisons, we will draw heavily on the results of two previous quasigeostrophic simulations conducted in basins bounded entirely by stress-free walls (HL, 1976). The former, henceforth to be referred to as experiment 1, or E1, is driven by a single-gyred wind stress distribution identical to that adopted originally by Stommel (1948), and the latter, experiment 2 (E2), incorporates a double-gyred stress in a basin of twice the north-south extent. For comparison, an analogous pair of experiments (E1R and E2R) have been performed which differ from their counterparts solely in that they are now bounded on the east and west by rigid (no-slip) walls. These sets of simulations allow us to deduce the effects of the western boundary layer on the stability of the mid-ocean environment.

It must be noted at the outset that our initial simulations have all been carried out in a flat-bottomed domain. This is, in itself, a

severe constraint on the system; topographic variations are well known to be responsible for destabilizing strong mean flows (Orlanski, 1969; Orlanski and Cox, 1973) and for impeding the two-dimensional cascade toward low-wavenumber, barotropic flows (Rhines, 1975). Thus, we acknowledge immediately that the physics of our model remains incomplete at this stage, essentially so that we may initially address the most tractable version of the boundary layer question. Our conclusions, therefore, must be tempered by a recognition that a primary dynamic mechanism may have been ignored. The introduction of an idealized topographic variation is being planned in a future set of experiments.

(IV.1) Experiment 1

The values of the model parameters for E1 (Table 2) have been chosen to coincide with those adopted by Holland and Lin for their primary finite-difference wind-driven ocean simulation. Since the results of this experiment have been so thoroughly studied, we select this experiment as our benchmark in two ways. In addition to the boundary layer comparison to be made shortly, the results and equilibrium statistics obtained for experiment 1 by HL serve as a test problem for the verification of the nonlinear pseudospectral model.¹ (Alternatively, we can regard the small differences between the predictions of the two formulations as an evaluation of the finite-difference model relative to the theoretically more accurate pseudospectral technique. Since that is not our present concern, such a comparison will be elaborated elsewhere.)

Briefly, the time-dependent model behavior in E1 has three distinct phases: spinup, onset of instability, and eventual statistical equilibrium. Thus, after a three-year spinup from a state of rest, HL noted that the resulting highly inertial circulation went spontaneously unstable, generating a field of mesoscale eddies of 340 kilometer (km) wavelength. After an additional, but shorter, period of integration, the mean and perturbation fields (Figure 2) settled into an oscillatory equilibrium characterized by a well defined periodicity of 57 days in both the pointwise streamfunction amplitude and the global energy

¹The linear version of the model has been tested against the known analytic solutions to the two-level versions of the Stommel and Munk frictional theories; the agreement was perfect in all cases.

Table 2: The environmental parameters, forcing functions, and boundary conditions adopted for the four primary simulations. In addition to the nondimensional groups mentioned in the text, we have included Re , W_I/L_x , and W_F/L_x ; these are the Reynolds number of the interior flow, and the relative widths of the inertial and frictional western boundary layers, respectively.

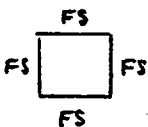
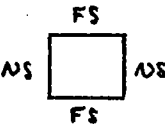
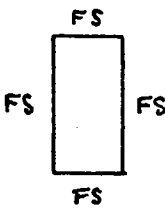
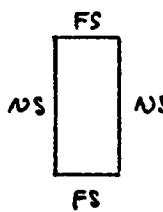
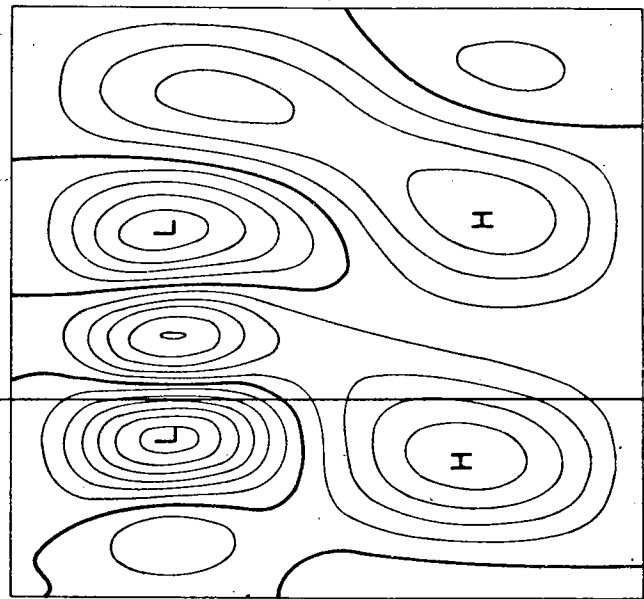
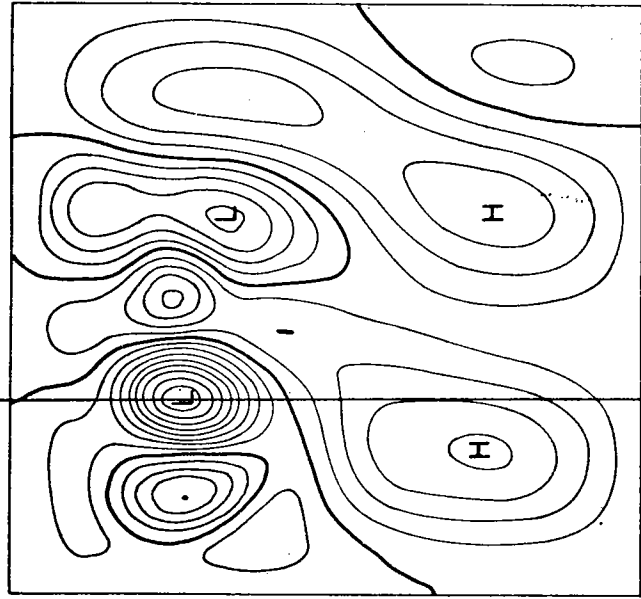
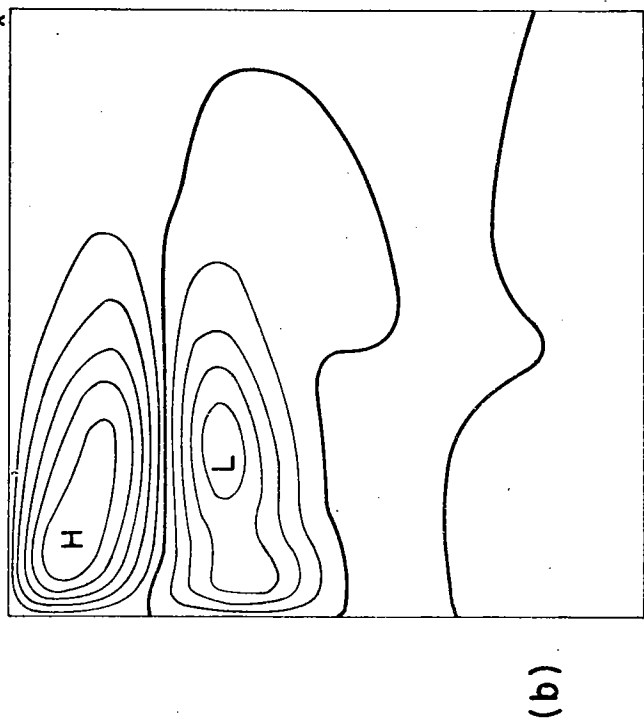
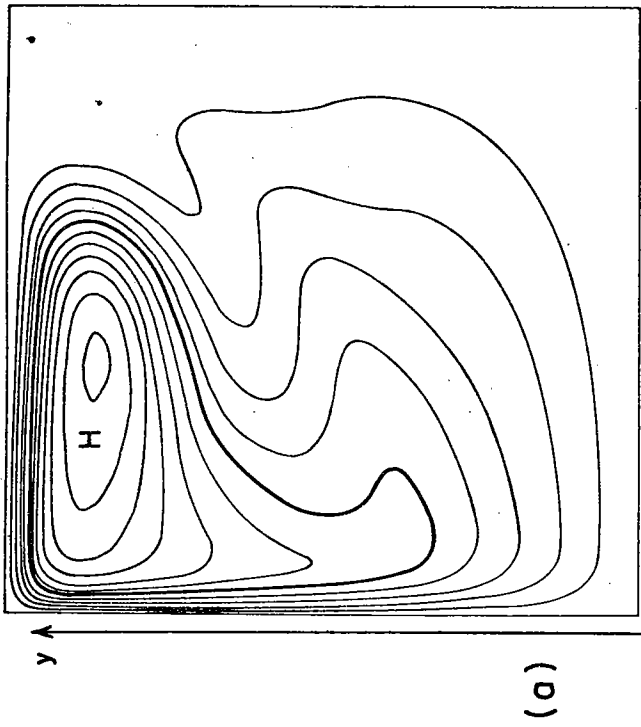
	E1	E1R	E2	E2R
L_x (cm)	1.0×10^8	1.0×10^8	1.0×10^8	1.0×10^8
L_y (cm)	1.0×10^8	1.0×10^8	2.0×10^8	2.0×10^8
H_1 (cm)	1.0×10^5	1.0×10^5	1.0×10^5	1.0×10^5
H_3 (cm)	4.0×10^5	4.0×10^5	4.0×10^5	4.0×10^5
f_o (sec ⁻¹)	8.3×10^{-5}	8.3×10^{-5}	9.3×10^{-5}	9.3×10^{-5}
β (cm sec) ⁻¹	2.0×10^{-13}	2.0×10^{-13}	2.0×10^{-13}	2.0×10^{-13}
N^2 (sec ⁻²)	8.0×10^{-6}	8.0×10^{-6}	8.0×10^{-6}	8.0×10^{-6}
R_d (cm)	4.8×10^6	4.8×10^6	4.3×10^6	4.3×10^6
K_H (cm ² sec ⁻¹)	3.3×10^6	3.3×10^6	1.0×10^6	1.0×10^6
K_B (sec ⁻¹)	0.0	0.0	0.0	0.0
$\hat{c}_x = c_x$ (dynes cm ⁻²)	$-\cos\left\{\frac{\pi y}{L_y}\right\}$	$-\cos\left\{\frac{\pi y}{L_y}\right\}$	$-\cos\left\{\frac{2\pi y}{L_y}\right\}$	$-\cos\left\{\frac{2\pi y}{L_y}\right\}$
boundary conditions				
	<p>FS = FREE-SLIP NS = NO-SLIP</p>			
numerical model	spectral 32x32	spectral 32x32	finite difference 50x50	spectral 32x64
$\varepsilon = \frac{v}{\frac{f_o L_x}{\beta}} = \frac{c_o}{\beta H_1 f_o L_x^2}$	6.8×10^{-5}	6.8×10^{-5}	5.4×10^{-5}	5.4×10^{-5}
$E_N = K_H / \beta L_x^2$	4.0×10^{-6}	4.0×10^{-6}	1.1×10^{-6}	1.1×10^{-6}
$Re = c_o / \beta H_1 K_H$	15	15	50	50
R_d / L_x	4.8×10^{-2}	4.8×10^{-2}	4.3×10^{-2}	4.3×10^{-2}
$\frac{\omega_T}{L_x} = \left(\frac{c_o}{H_1 L_x \beta^2}\right)^{1/2} / L_x$	1.6×10^{-2}	1.6×10^{-2}	1.6×10^{-2}	1.6×10^{-2}
$\frac{\omega_F}{L_x} = \left(\frac{K_H}{\beta}\right)^{1/3} / L_x$	2.6×10^{-2}	2.6×10^{-2}	1.7×10^{-2}	1.7×10^{-2}

Figure 2: Experiment 1 from Holland and Lin (1976).
(a) mean upper layer streamfunction (average over 600 days; contour intervals = 2.4 Sverdrups).
(b) mean lower layer streamfunction (average over 600 days; contour interval = 1.6 Sverdrups).
(c) instantaneous upper layer eddy streamfunction (contour interval = 0.8 Sverdrups).
(d) instantaneous lower layer eddy streamfunction (contour interval = 3.2 Sverdrups).
Lines have been drawn along $x = 320$ km to indicate the phase relationship between the upper and lower layer eddies. Lows (L) and highs (H) indicate cyclonic and anticyclonic flow respectively.



components. The set of equilibrium eddy statistics is summarized in Table 3.

In the manner of section (II.4), the mean field energies and the accompanying fluxes can be calculated and the global means of these quantities conveniently entered on a "six-box diagram". The energy budget resulting from the HL simulation appears in Figure 3. The global energetics indicate a predominant baroclinic cascade of mean potential energy to the equilibrium eddy field which maintains the meso-scale eddies in the presence of lateral dissipation. The primary energy transfer path is

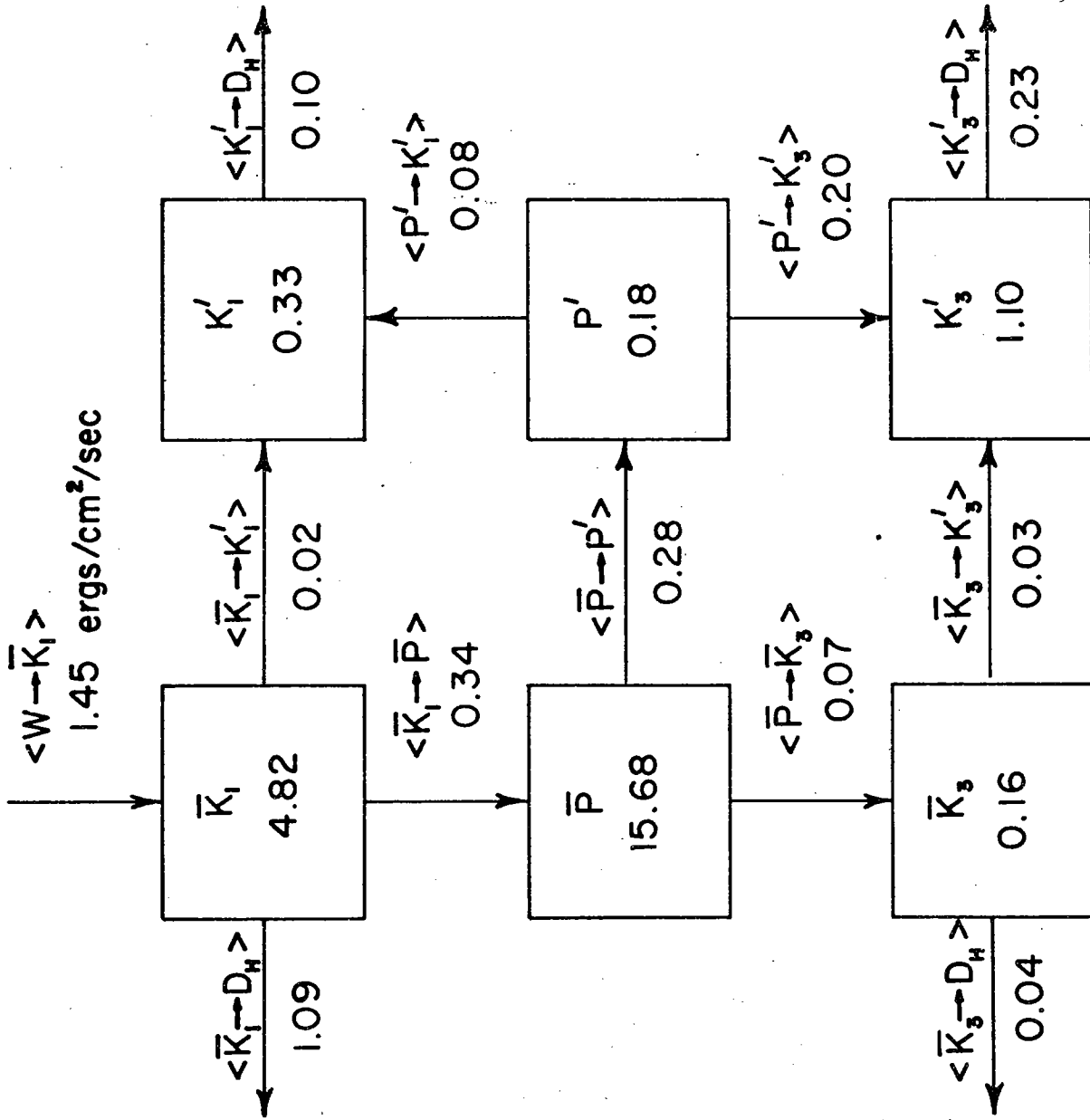
$$W \rightarrow \bar{K}_1 \rightarrow \bar{P} \rightarrow K'_3 \rightarrow D_H. \quad (\text{FP1})$$

In the localized region of intense baroclinic activity, confined to the intense westward return flow (Figure 2a, c), the upper and lower layer eddies bear the 90° phase relationship indicative of baroclinic instability (Robinson and McWilliams, 1974). Contouring the levels of the three mean eddy energy components also effectively demarcates the area of baroclinic activity (Figure 9). In the southern half basin, removed from the intense currents of the north, the eddies are nearly barotropic, thus confirming the efficiency of the trend towards barotropy observed by Rhines (1975) in flat-bottomed local eddy interaction simulations; only in the region of persistent energy cascade is the baroclinicity of the eddy field preserved. Finally, note the contribution of the Reynolds stresses to the maintenance of the mean flow field; this is most clear in the lower layer where forcing by the

Table 3: The equilibrium eddy statistics from the four primary simulations.

	E1 (Holland)	E1 (Haidvogel)	E1R	E2	E2R
wavelength (km)	340	380		400/680	360
period (days)	57	64		110/56	64/51
phase speed (cm sec ⁻¹)	7.0	6.8		4.2/13.9	8.9
global energy transfer	baroclinic (FP1)	baroclinic (FP1)	stable	barotropic (FP2)	mixed (FP3)

Figure 3: The experiment 1 global energy budget from Holland and Lin (1976). Energy fluxes are in $\text{ergs/cm}^2/\text{sec}$; energies in 10^6 ergs/cm^2 .



transient eddies is, in the absence of vertical momentum diffusion, the only mean flow generation mechanism.

When integrated from a state of rest with the same values of the environmental parameters chosen by HL, the pseudospectral model displays an identical behavior. Figure 4 shows the mean energy components as a function of time; the spinup, onset, and statistical equilibrium phases are again evident. The mean streamfunction fields and representative (instantaneous) eddy streamfunction fields are plotted in Figure 5. The similarity to the finite-difference results (Figure 2) is striking, if not for all intents and purposes exact. The eddy statistics collected from the pseudospectral simulation compare favorably to their finite difference analogues (Table 3) and the eddy phase relations noted above recur. As before, the equilibrium eddy field has well defined temporal as well as spatial features. The frequency spectra of the upper and lower layer streamfunction amplitude (Figure 6) shows the dominant periodicity to be 64 days (and its higher harmonics). An x-t diagram taken through the latitude of most active eddying displays a uniform phase propagation consistent with these scales (Figure 7).

Energetically, the primary cascade (FP1) occurs as in the HL model though a quantitative comparison of the finite-difference and pseudospectral models reveals some systematic differences in the predicted global energy budgets (Figures 3 and 8). The mean energy levels and fluxes are everywhere lower in the pseudospectral approximation, by as much as 50% in some of the smaller terms. The primary energy fluxes are uncertain to only 0(10%), however, and the pathway itself is

Figure 4: The experiment 1 globally averaged energy components as a function of time from the pseudospectral model.

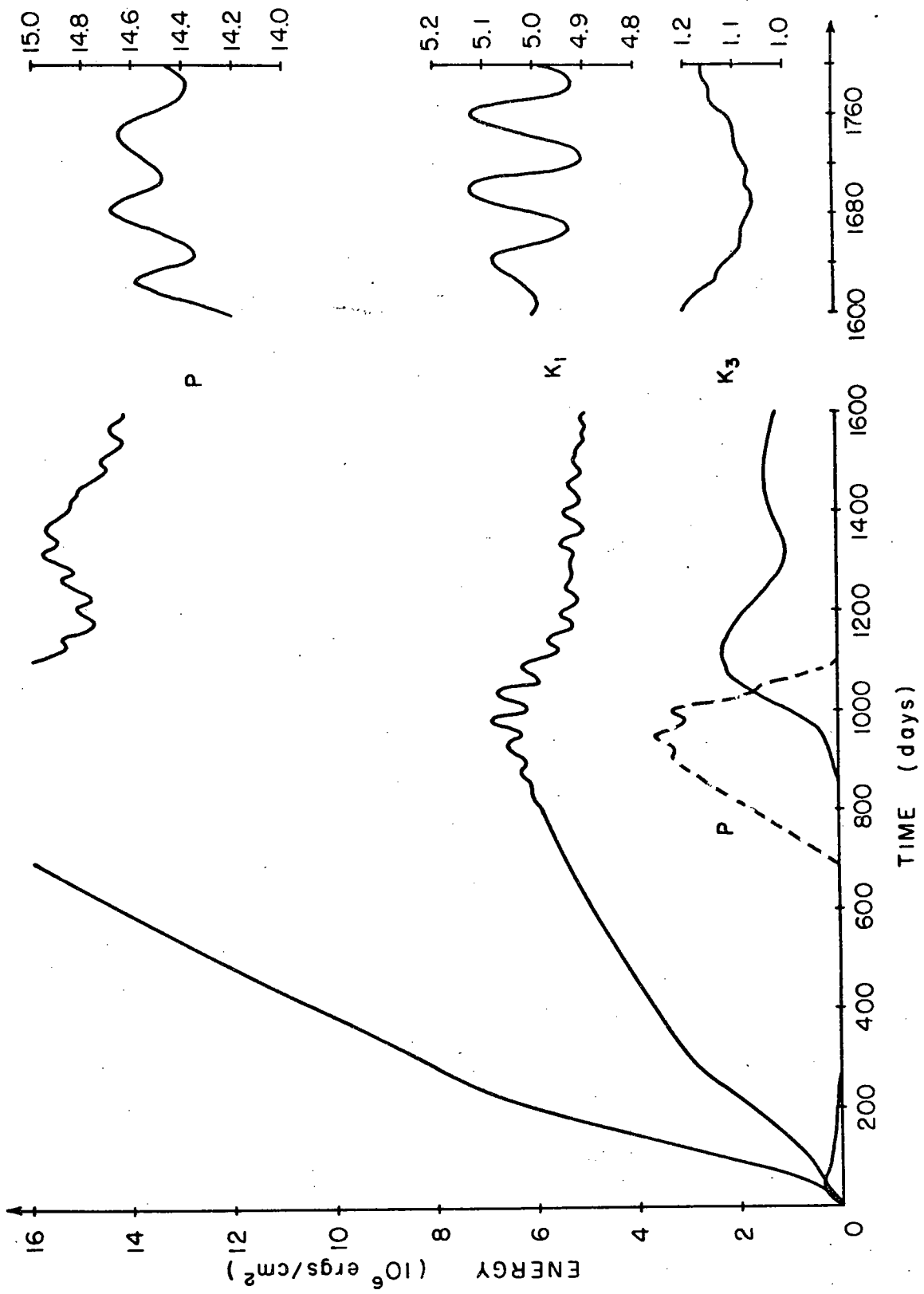
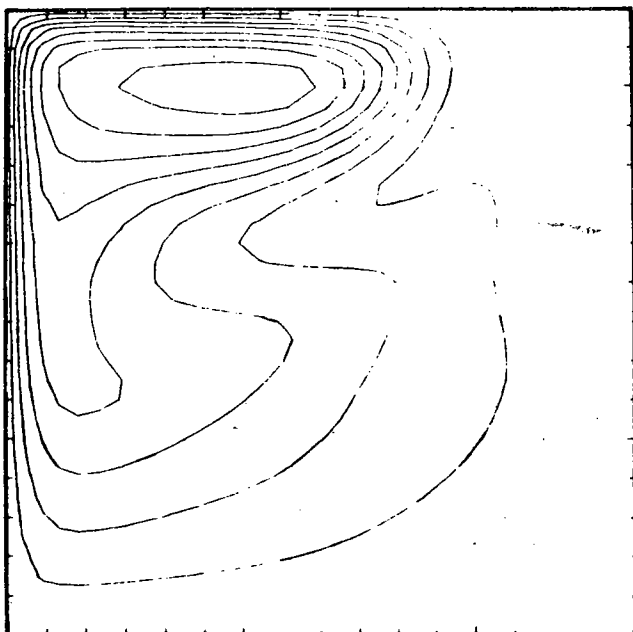


Figure 5: Experiment 1 from the pseudospectral model.

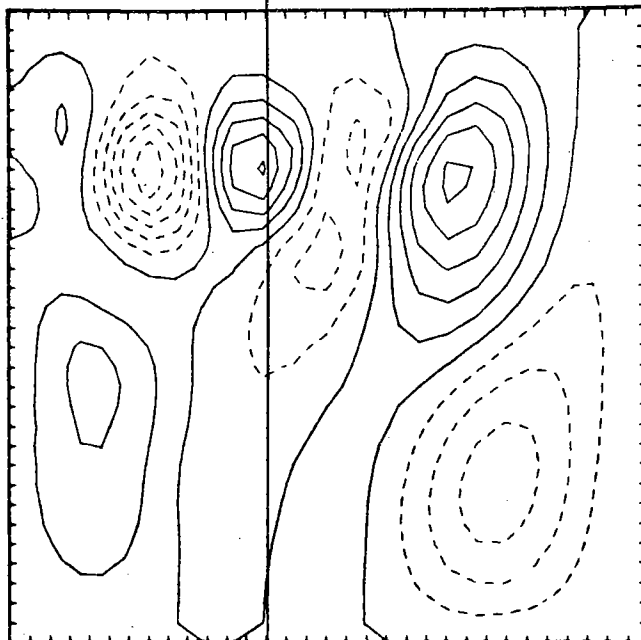
- (a) mean upper level streamfunction (average over 500 days; contour interval = 3.0 Sverdrups).
- (b) mean lower level streamfunction (average over 500 days; contour interval = 1.6 Sverdrups).
- (c) instantaneous upper level eddy streamfunction (contour interval = 1.0 Sverdrup).
- (d) instantaneous lower level eddy streamfunction (contour interval = 4.0 Sverdrups).

Lines have been drawn along $x = 430$ km to indicate the phase relationship between the upper and lower level eddies.

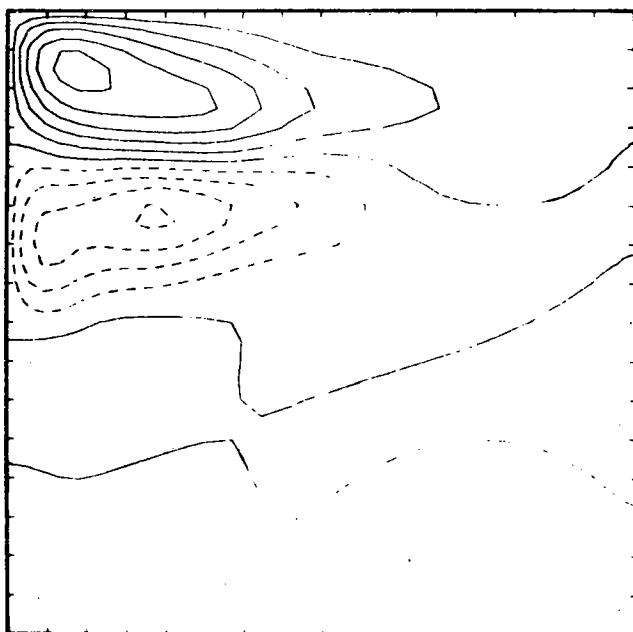
(a)



(c)



(b)



(d)

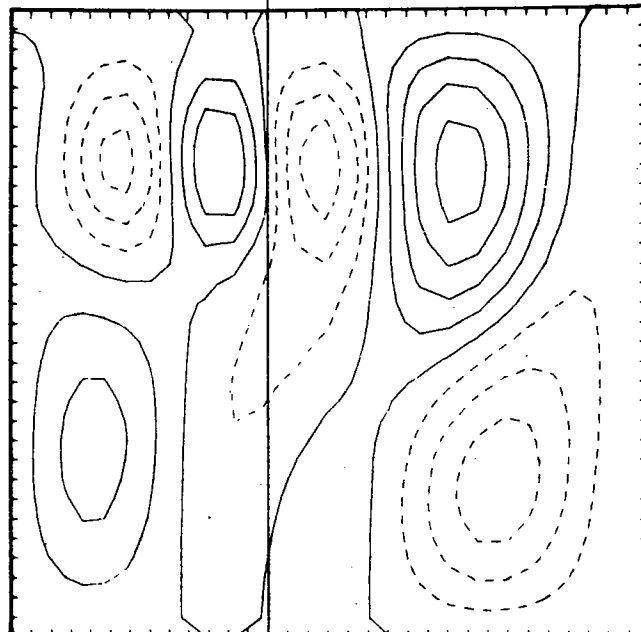


Figure 6: Composite frequency spectra for the upper and lower level streamfunction fields of experiment 1. The spectra have been obtained by averaging 25 separate frequency spectra of the streamfunction amplitude taken at 25 equally spaced points.

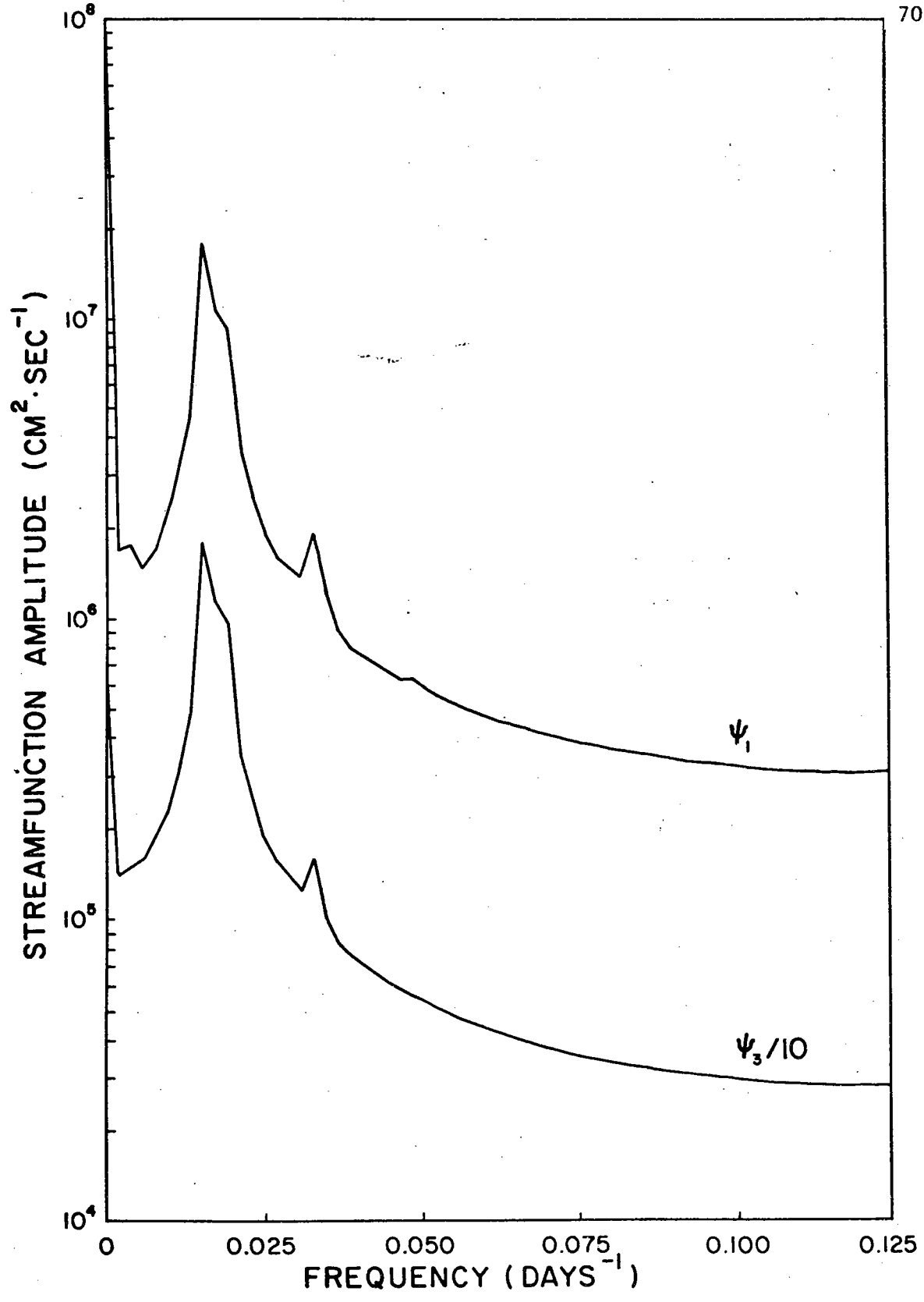
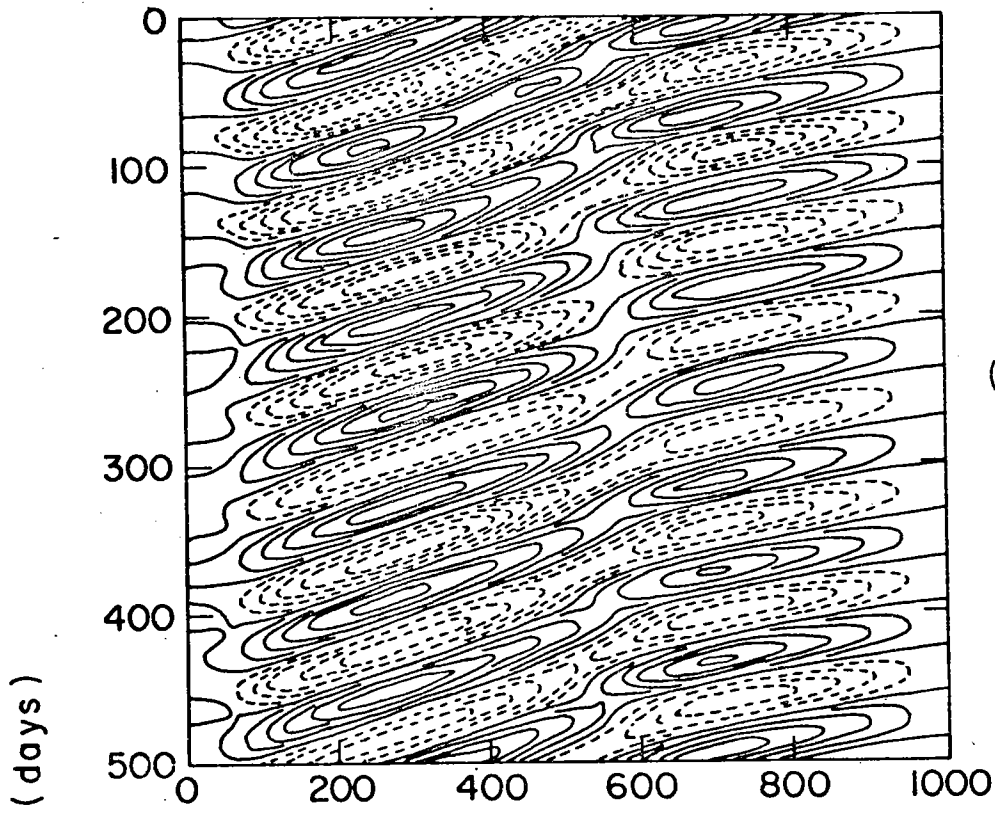
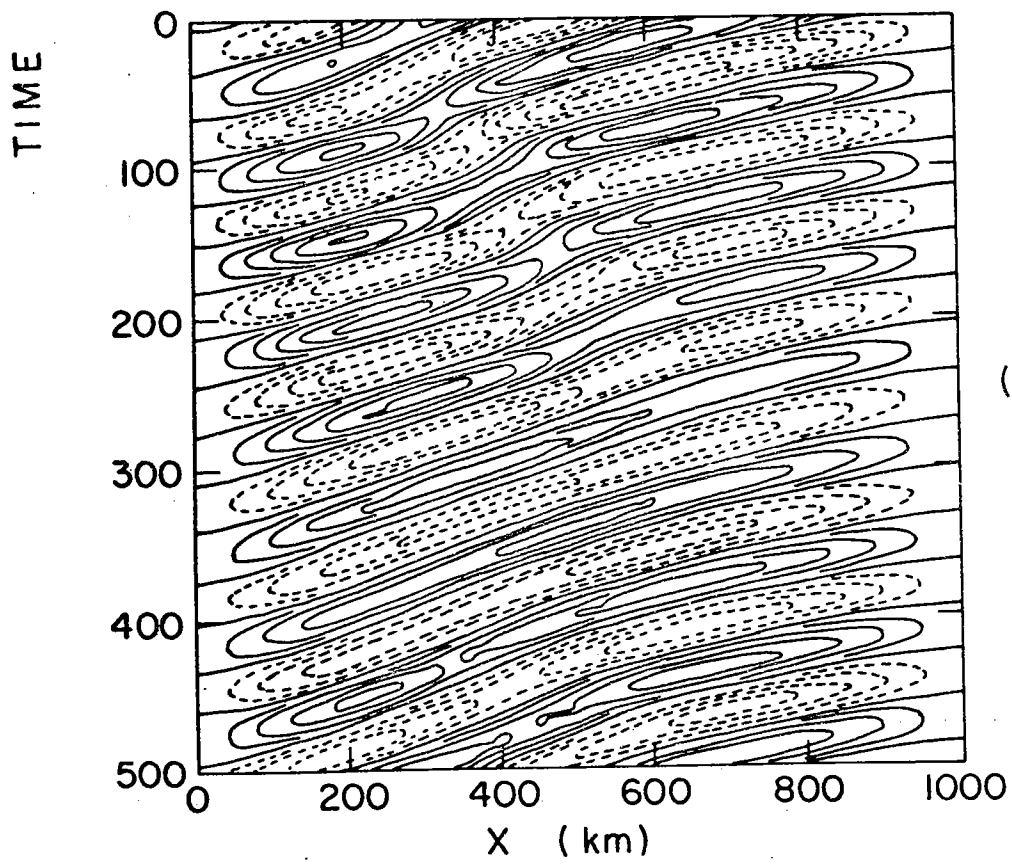


Figure 7: Experiment 1 x-t diagrams.
(a) upper level streamfunction.
(b) lower level streamfunction.
The profiles have been taken along the
latitude of most active eddying
($y = 750$ km).



(a)



(b)

Figure 8: The experiment 1 global energy budget according to the pseudospectral model. Energy fluxes are in $\text{ergs/cm}^2/\text{sec}$; energies in 10^6 ergs/cm^2 .

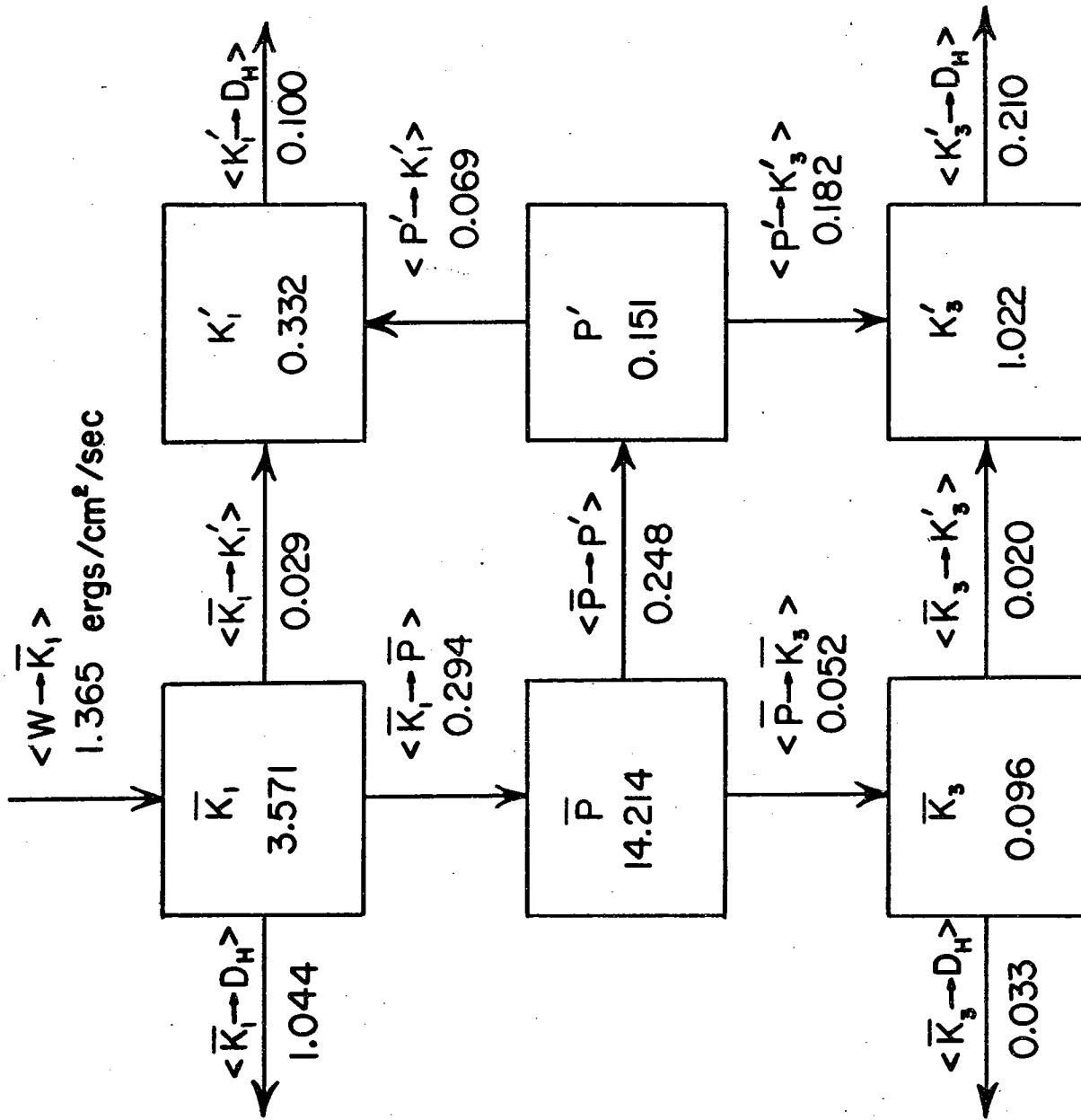
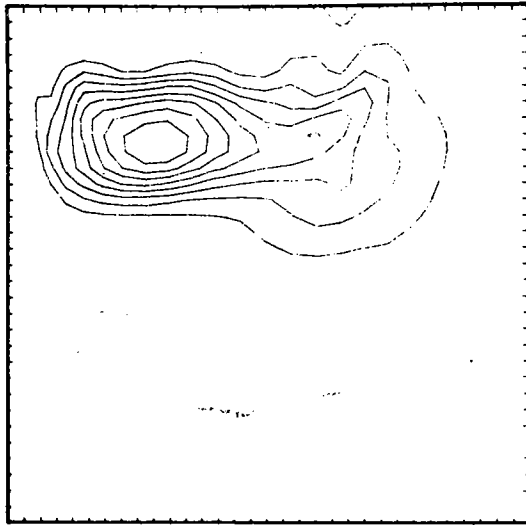
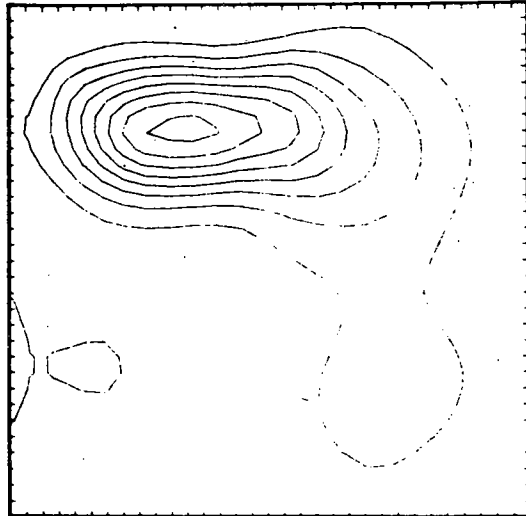


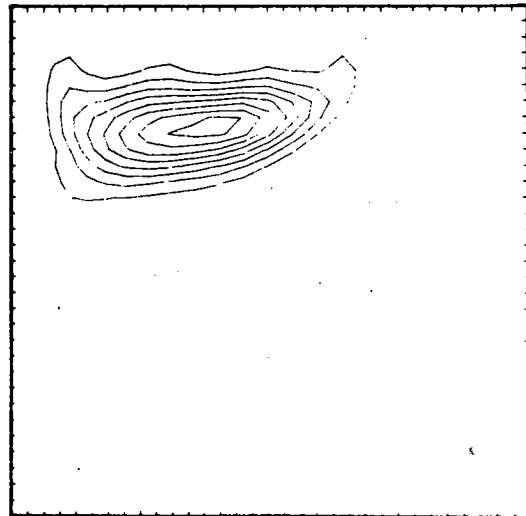
Figure 9: The experiment 1 mean eddy energy components.
(a) upper level eddy kinetic energy (contour interval = 0.3×10^6 ergs/cm²).
(b) lower level eddy kinetic energy (contour interval = 0.7×10^6 ergs/cm²).
(c) eddy potential energy (contour interval = 0.3×10^6 ergs/cm²).



(a)



(b)



(c)

unambiguous. Such errors as these are perhaps not unreasonable considering the modest physical differences between a two-layer model which takes account of the small variations in layer thickness due to undulations in the thermocline and our two-level formulation which does not, and the inherent dissimilarities between the finite-difference and pseudospectral methods. For our purposes here, however, the overall results are sufficiently similar to confirm the HL experimental findings and to validate the Chebyshev model, which we now extend to the no-slip analogue of experiment 1.

(IV.2) Experiment 1R

Starting from rest, the quasigeostrophic equations (2.8, 2.9) are integrated in time as has been described for E1 except for the imposition of rigid boundary conditions, equation 3.2, on the eastern and western walls. The spinup phase proceeds as before, taking approximately 1,000 days, but here the similarity ends. Instead of entering a period of rapid energy cascade from the mean field to a set of growing waves, E1R is stabilized by the effects of the rigid boundary and soon reaches a steady equilibrium circulation characterized by velocities confined to the upper level (Figures 10 and 11). (The absence of both instabilities and viscous coupling between the layers guarantees that the equilibrium flow at level 3 must vanish, although small amplitude transients do exist near $t = 0$; these are quickly damped by friction.) The energy flow diagram for E1R, Figure 12, demonstrates the resulting steadiness very well. Within the measurement error, energy input from the wind is just sufficient to drive the upper level circulation against the forces of lateral dissipation. No significant amount of energy leaks to any of the other components once the mean potential energy field has been established during the spinup phase. Thus, E1R follows a two-stage process - spinup followed by a rapid approach to steady flow. The mid-ocean eddy generation witnessed in E1 has apparently been suppressed by some direct or indirect action of the now modified dynamic balances near the western boundary.

In contrast to the rather strong differences in equilibrium behavior detailed above, the corresponding mean circulation patterns of

Figure 10: The experiment 1R globally averaged energy components as a function of time.

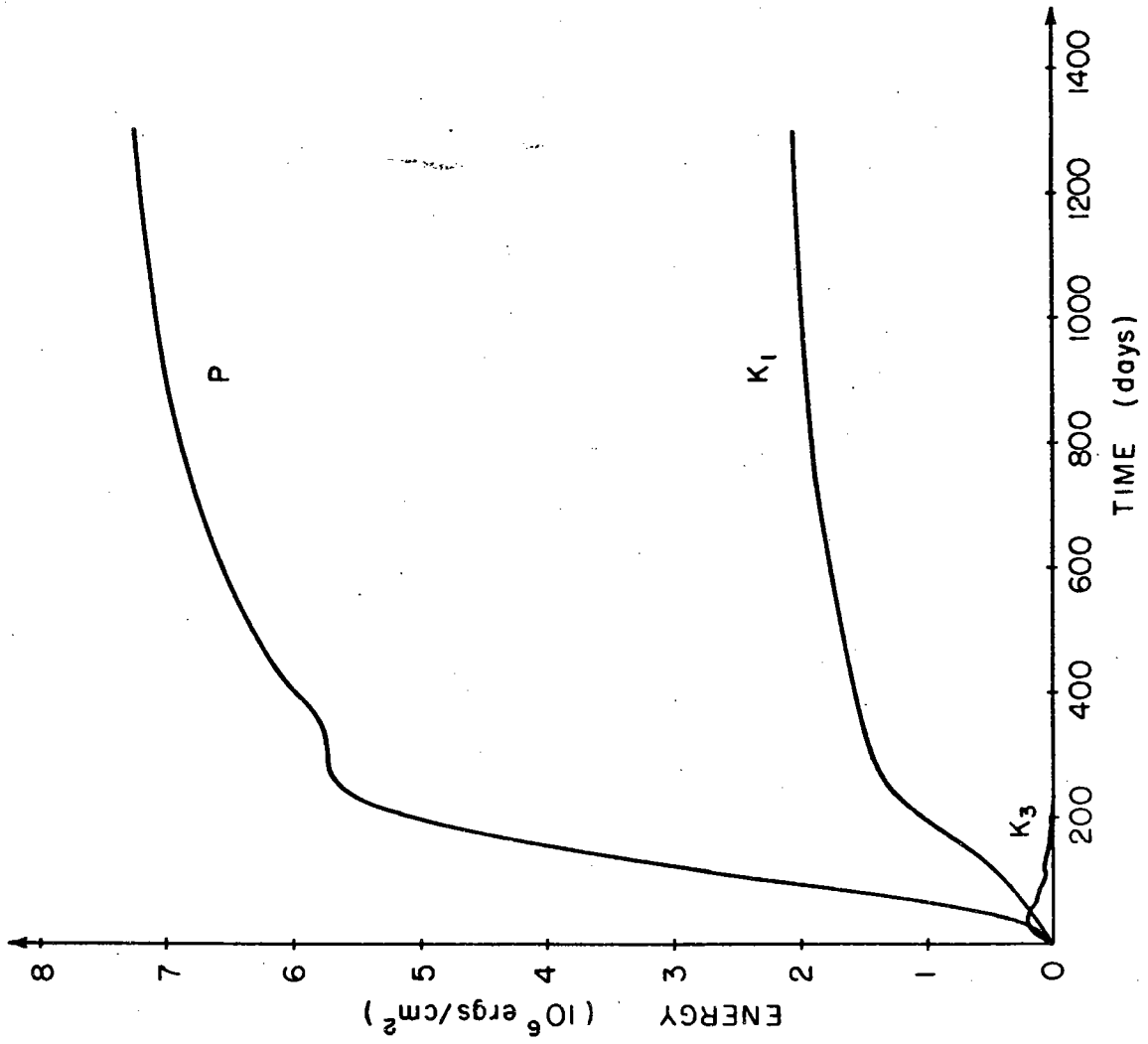


Figure 11: The experiment 1R equilibrium upper level stream-function (contour interval = 2.0 Sverdrups).

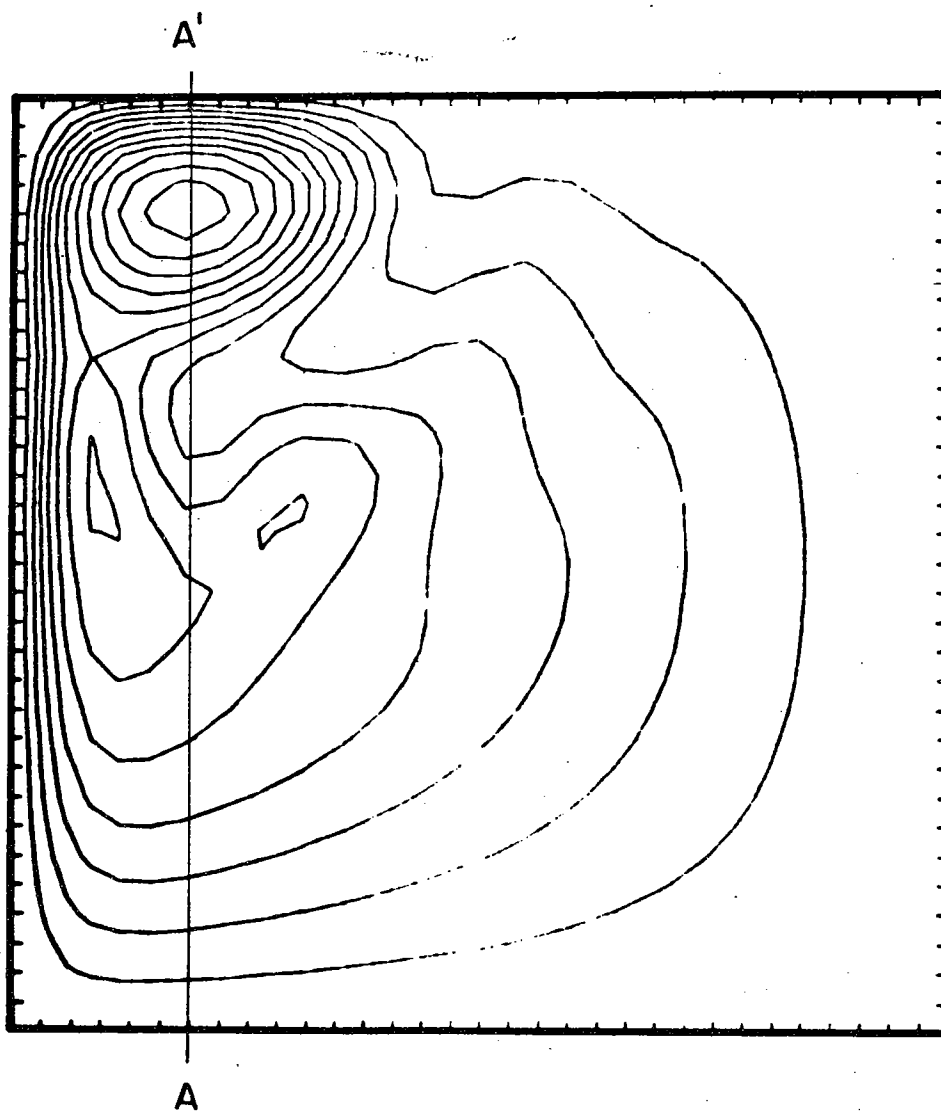
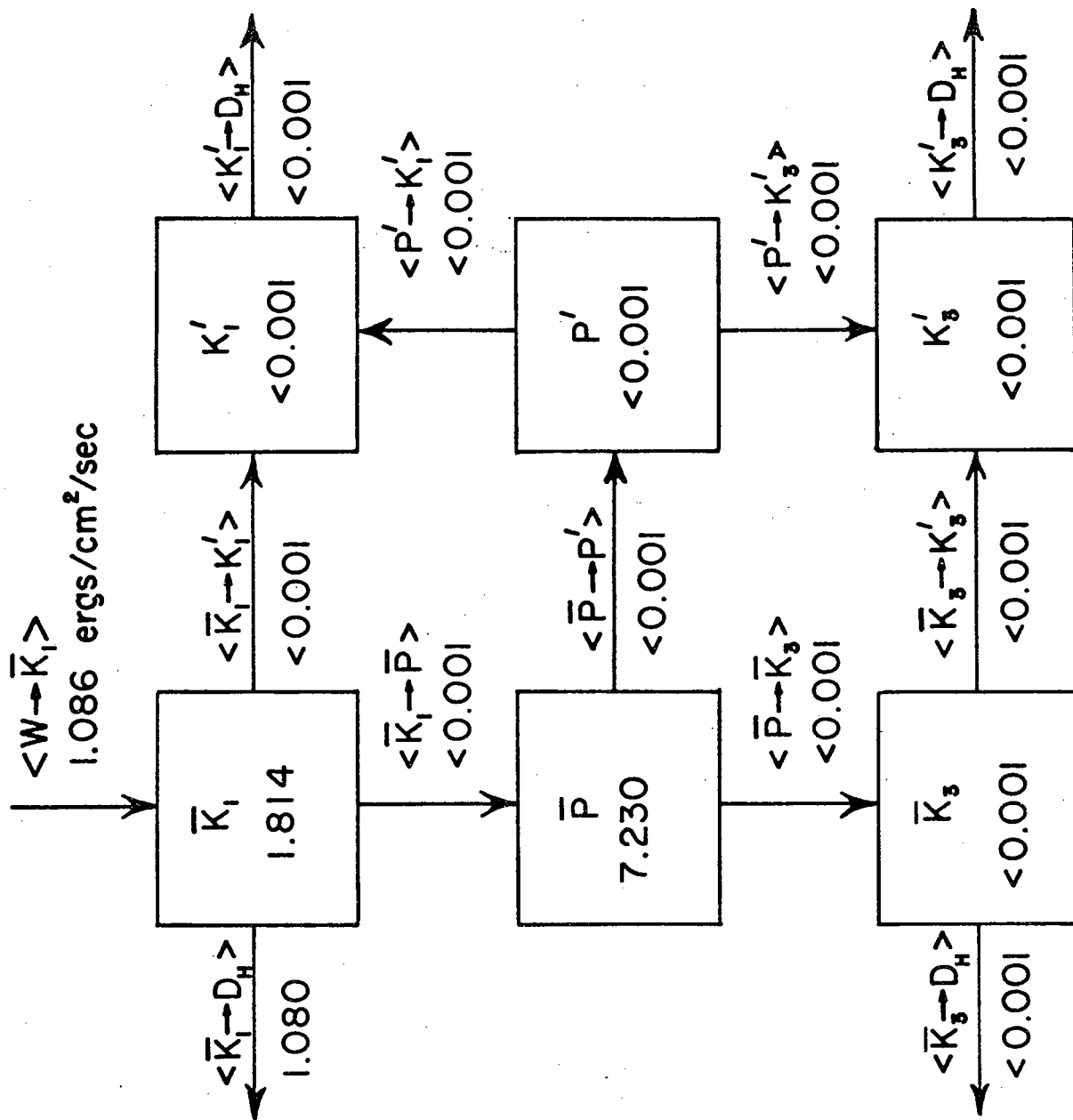


Figure 12: The experiment 1R global energy budget. Energy fluxes are in $\text{ergs/cm}^2/\text{sec}$; energies in 10^6 ergs/cm^2 .



E1 and E1R are qualitatively similar in many respects (Figures 5 and 11). The boundary layer scale thicknesses along the western and northern walls are comparable in both instances, as is the tendency towards smooth inertial recirculation after the separation of the northern boundary from the coast. The advent of the semi-rigid domain in E1R has, however, reduced the upper layer kinetic energy by a factor of two (Figures 8 and 12), although the boundary layer transport suffers by only 0(10%), a consequence of the Sverdrup balance over the bulk of the interior. The immediate effect of this weakening is a premature truncation, relative to E1, of the inertial boundary layer along the northern wall. Though delayed in E1, however, the redistribution of the boundary layer flow into the interior is no more abrupt in one experiment than the other. Boundary layer profiles taken through E1 and E1R - Figures 24 and 31 - establish this similarity, apart from a scaling factor, very nicely. The important point to be noted is that the adjustment from a no-slip to a free-slip vorticity profile is made very quickly once the circulation leaves the western boundary layer region and proceeds along the northern margin of the basin. A distance of only two or three frictional boundary layer widths (w_F) is sufficient for the flow profiles to lose any memory of the dynamics to which they were so lately subject. Of course, there has been an increased diffusive constraint placed upon the overall circulation. Rigid boundaries offer resistance to flow tangentially as well as normally and must a priori increase viscous effects. This is precisely the case in E1R where the regional influence of vorticity diffusion has been strengthened and the circulation greatly retarded. The interior flow senses the

details of the boundary layer vorticity balances only indirectly through the modified energy and transport levels dictated by the increased dissipation. We must once again remind ourselves, however, that the flat-bottomed assumption effectively precludes topographic instabilities associated with the western boundary layer. With appropriate topography, such instabilities can be quite generally induced in highly structured jets similar to those connected here with rigid boundary conditions (Orlanski and Cox, 1973) and might be supposed to enlarge the region over which the western boundary layer dynamics directly affects the interior. Thus, subject to this one restriction of vanishing topographic influence, the comparison of E1 and E1R supports the hypothesis that the immediate effect on the mid-ocean circulation of a rigid western wall - the dynamical consequences of rigidity along the eastern boundary are trivial in this case - is an increase in the local and global diffusive loss of vorticity and an attendant reduction in flow strength. If this conclusion is valid, it follows that the stability properties of the equilibrium states in E1 and E1R, in which the jet structure itself remains approximately invariant, are explicable primarily on the basis of the local amplitude of the mid-ocean circulation. In Chapter VI we will see that this is indeed an interpretation consistent with the stability properties of these flow fields.

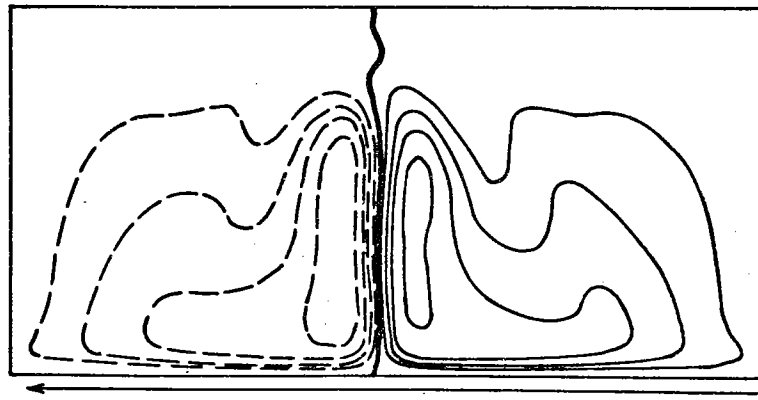
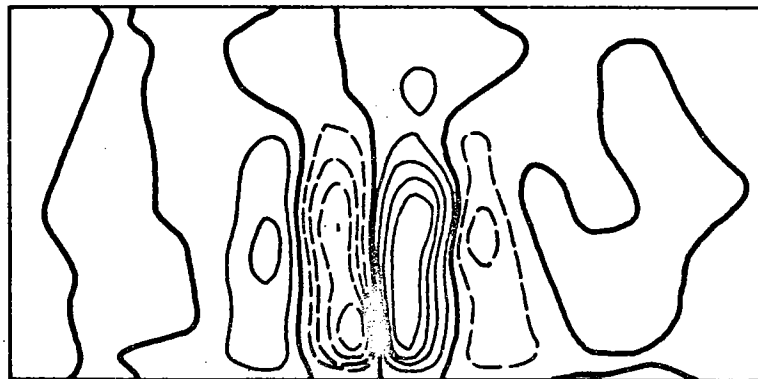
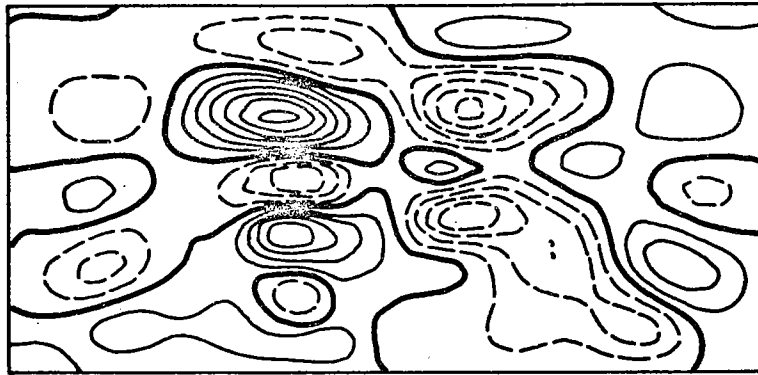
(IV.3) Experiment 2

In E1, the dominant, and as will be shown shortly the only, unstable energy transfer occurs in the westward flowing inertial recirculation. Though the localization of this instability conforms with the known vulnerability of westward flowing zonal currents (Robinson and McWilliams, 1974), this flow feature does not accord well with the observed circulation pattern of, say, the Gulf Stream to which this model might attempt to claim relevance. It would be more pleasing to observe instability in the eastward flowing region, not only because the Gulf Stream has a strong meandering eastward jet, but also because eddy interactions with an eastward current are more favorable for mean flow intensification (Rhines, 1975). Gulf Stream measurements (Webster, 1965) have indeed documented this behavior in some narrow regions adjacent to the coast; perhaps similar processes are at work in the mid-ocean extension of the stream as well. In an attempt to create a flow pattern at once more realistic and more susceptible to instability, HL have investigated the equilibria induced by double-gyred wind stresses. These can be thought of as the antisymmetric reflection of the classical single gyre about the northern latitude of the (1000 km x 1000 km) basin used in E1, thus creating a doubly sized domain (1000 km x 2000 km). In so doing, we relax the requirement that the eastward jet flow, at least initially, along a northern wall where the vorticity must vanish and allow the eastward flow to separate into the interior in a manner somewhat more analogous to the trajectory of the Gulf Stream (given that we have ignored continental and topographic variabilities).

An initial double gyre experiment (E2) has been carried out by HL as part of their own mesoscale studies; the authors have generously

made the following results available for inclusion here. The parametric values chosen for E2 (Table 2) are identical to those of E1 and E1R except for a slightly smaller Rossby radius of deformation, R_d , and lateral diffusivity, K_H . As before, integration proceeds from a state of rest using the HL finite-difference model which is enclosed, as in E1, entirely by free-slip walls. Since the relaxation of the constraint on the separated flow implies a greater range of admissible unstable response, it is not surprising that the three phases of flow development noted in E1 recur in E2. Onset of instability occurs after a long period of spinup during which the velocity field remains completely symmetric about the mid-latitude, and an oscillatory, but now more complicated, equilibrium follows in which this symmetry has been relaxed via the appearance of the unstable modes. Figure 13 documents the equilibrium fields that result. They were formed by an average over 1050 days of streamfunction fields taken at two-day intervals, a length of time barely sufficient to define a stable set of associated statistics. (There is some evidence that long time scale changes are indeed still going on after a cumulative time in excess of 10 years.) Even so, the mean flow patterns clearly differ from those of the single-gyred ocean; in particular, not only has the eastward flowing internal jet developed well defined meanders, but the westward redistribution of mass into the noninertial interior is broader and less intense. The nonzero lower level mean flow, comprised of two weak primary gyres underlying, and in the same sense as, the upper level circulation has again been driven by eddy-eddy interactions. Thus, the energy transfers taking place on the mesoscale not only tend to reduce local horizontal

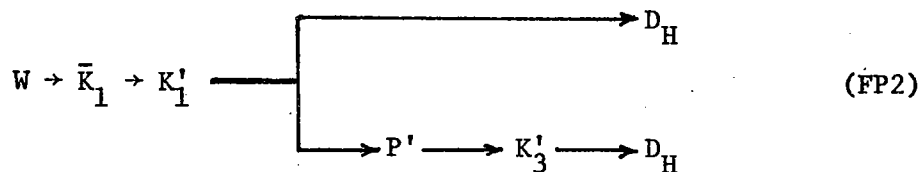
Figure 13: Experiment 2 (Holland and Lin, 1976).
(a) mean upper layer streamfunction (average over 1050 days; contour interval = 3.0 Sverdrups).
(b) mean lower layer streamfunction (average over 1050 days; contour interval = 3.6 Sverdrups).
(c) instantaneous upper layer eddy streamfunction (contour interval = 4.0 Sverdrups).
(d) instantaneous lower layer eddy streamfunction (contour interval = 8.0 Sverdrups).



shears (in the mean due to meandering) but also local vertical shears (in the mean due to lower layer current generation). We will return to this observation again upon consideration of the local stability properties of these flows.

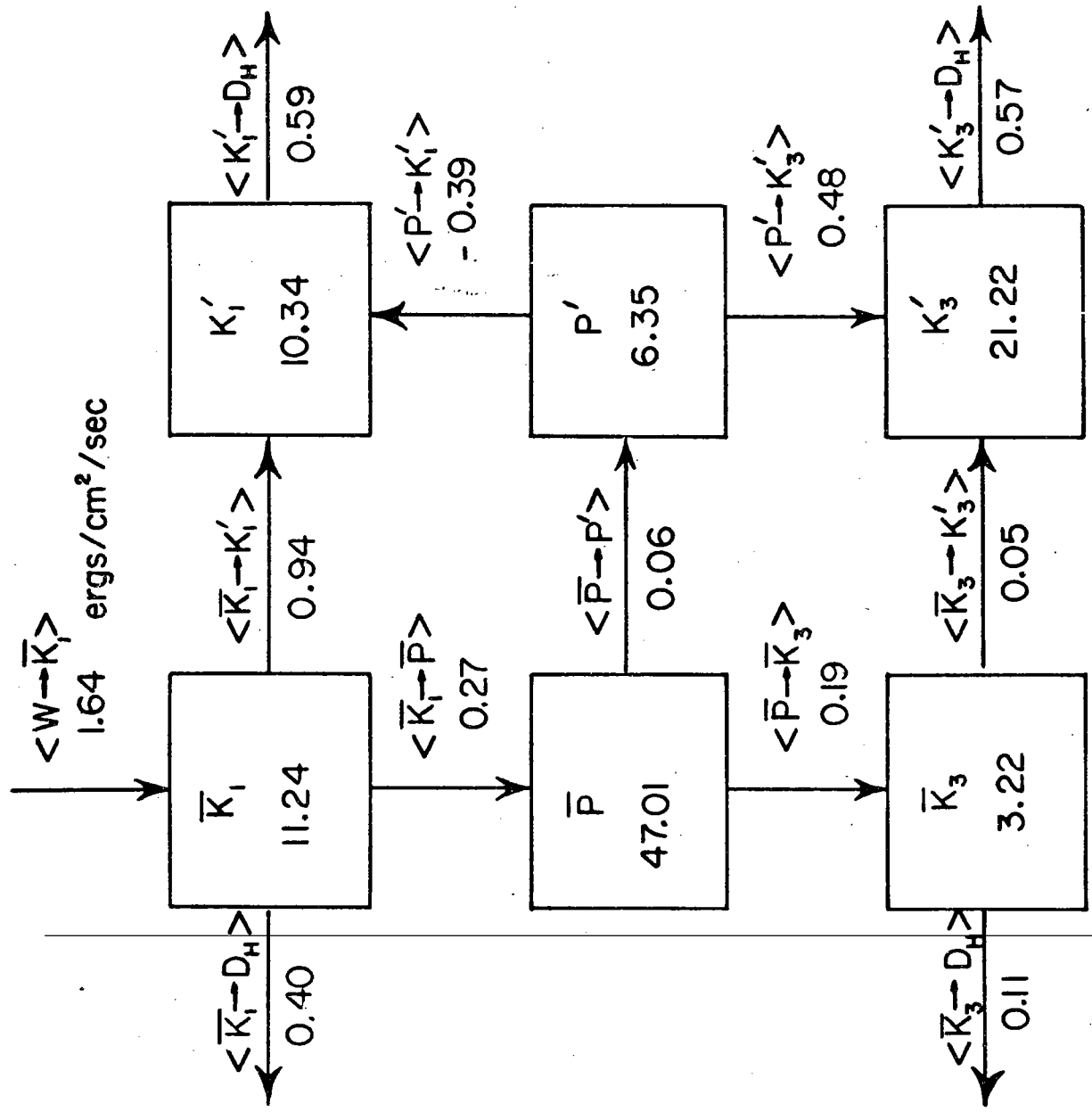
The instantaneous eddy fields of E2 (Figures 13c, d) are more incoherent than those noted in E1 though the mean eddy statistics (Table 3) differ very little from their E1 counterparts. The path of the eastward flowing jet is now the favored location for eddy production; indeed, the meandering of the stream occasionally sheds closed circulations which migrate for short distances before eventual reabsorption. The eddies embedded in the jet and its recirculation cannot be clearly characterized as barotropic or baroclinic; both types of instability are assumed (and will be demonstrated) to be locally active. The far field eddies, uninfluenced by local forcing, are highly barotropic as in E1.

A global estimate of the energy transfers - Figure 14 - reveals the dominance of an intense barotropic cascade of mean kinetic energy to the equilibrium eddy field; the barotropically unstable jet has the primary energy circuit



In E2, energy supplied to the eddies cascades from \bar{K}_1 to K'_1 , rather than from \bar{P} to P' as in E1. Note also that a greater fraction of the energy is lost directly to lateral dissipation of the mean upper level circulation in E1 (Figures 3 and 14) so that the equilibrium levels of

Figure 14: The experiment 2 global energy budget. Energy fluxes are in $\text{ergs/cm}^2/\text{sec}$; energies in 10^6 ergs/cm^2 .



eddy energy are correspondingly lower. Calculations in Chapter VI will verify that the instabilities at work in E2 are many times more vigorous than those in E1. Though barotropic instabilities are now active, the regions of concentrated westward return flow (one to the north, the other to the south) again exhibit baroclinic energy transfers; the mean potential to eddy potential energy transfer pathway (FP1) is undoubtedly locally operational even though it is dominated by the barotropic cascade in the global statistics. This observation underscores an important failing of a global energy budget: secondary (and sometimes even primary) instabilities may not be identifiable from a basin-wide analysis.

(IV.4) Experiment 2R

We now test the generality of the conclusions of section IV.2 by redoing E2 in a semirigid domain. The environmental parameters are listed in Table 2 for reference. For our tentative ideas to carry through to this double-gyred experiment, we expect the mean fields of E2R to be qualitatively similar to those of E2 but quantitatively reduced as a result of increased western boundary layer diffusion. The flow may be stabilized in consequence (as in E1R), resulting in a steady rather than an oscillatory equilibrium, but whether or not this is the case the final state of the system is predicted to be dependent only on the local amplitude of the interior calculation and not on direct boundary layer influences.

Figure 15 shows the time history of the mean energy components. Obviously, instability has occurred, as in E2, even though the mean fields (Figure 16) are substantially weakened as has been predicted on the basis of E1 and E1R. However, despite a boundary layer transport reduced by 50% relative to E2, the qualitative characteristics of both the upper level (wind-driven) and lower level (eddy-driven) circulations in E2R closely mimic the mean state in the free-slip experiment. Note that a 500-day statistical average is sufficient in E2R to produce a smooth mean flow field while a 1050-day time series was required in E2 where the meandering is more intense and less "clean". The instantaneous eddies in E2R are also more coherent than their counterparts in E2; Figure 16d is reminiscent of the E1 eddy patterns (which were observed to align with the westward flowing branch of the inertial

Figure 15: The experiment 2R globally averaged energy components as a function of time.

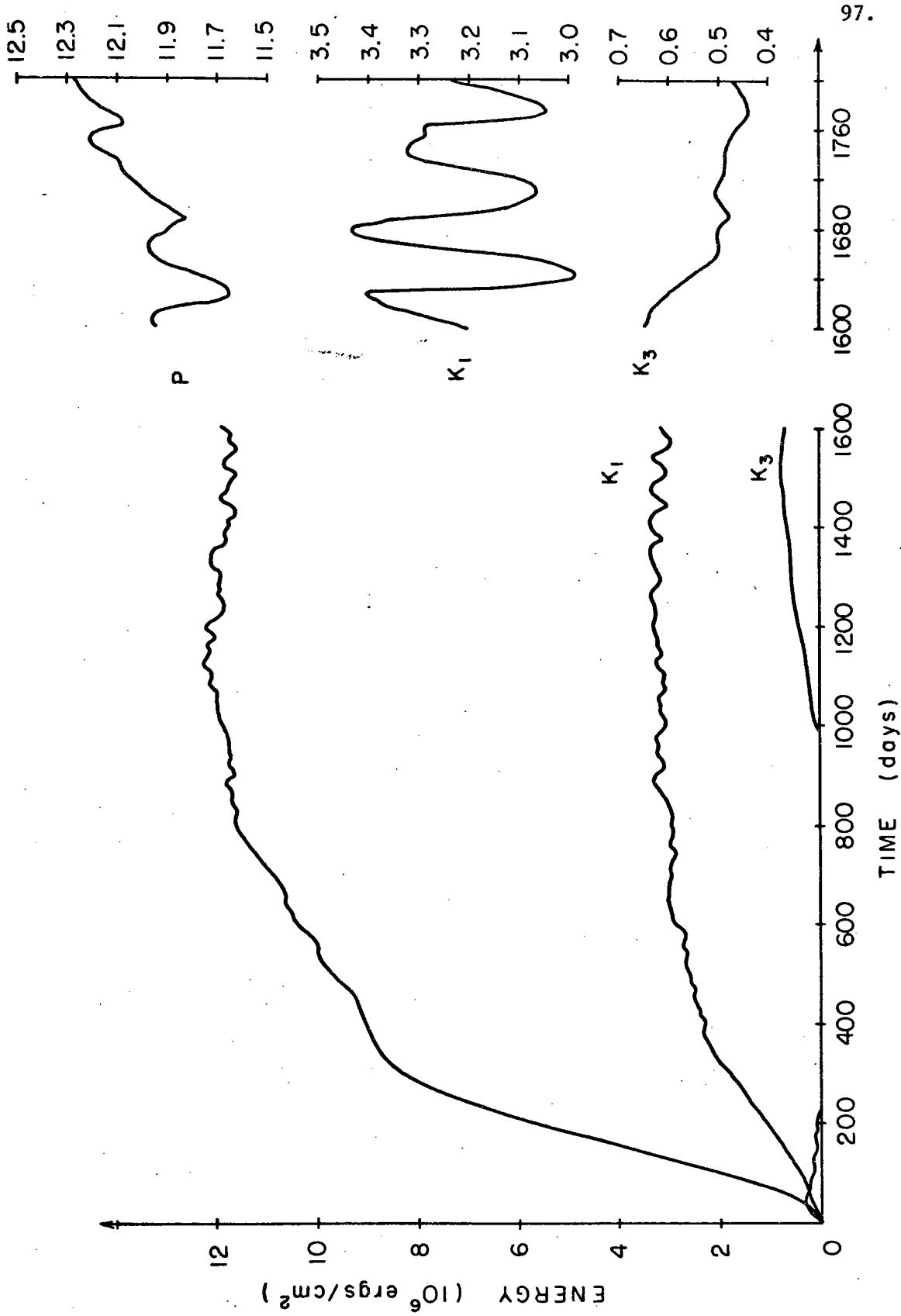
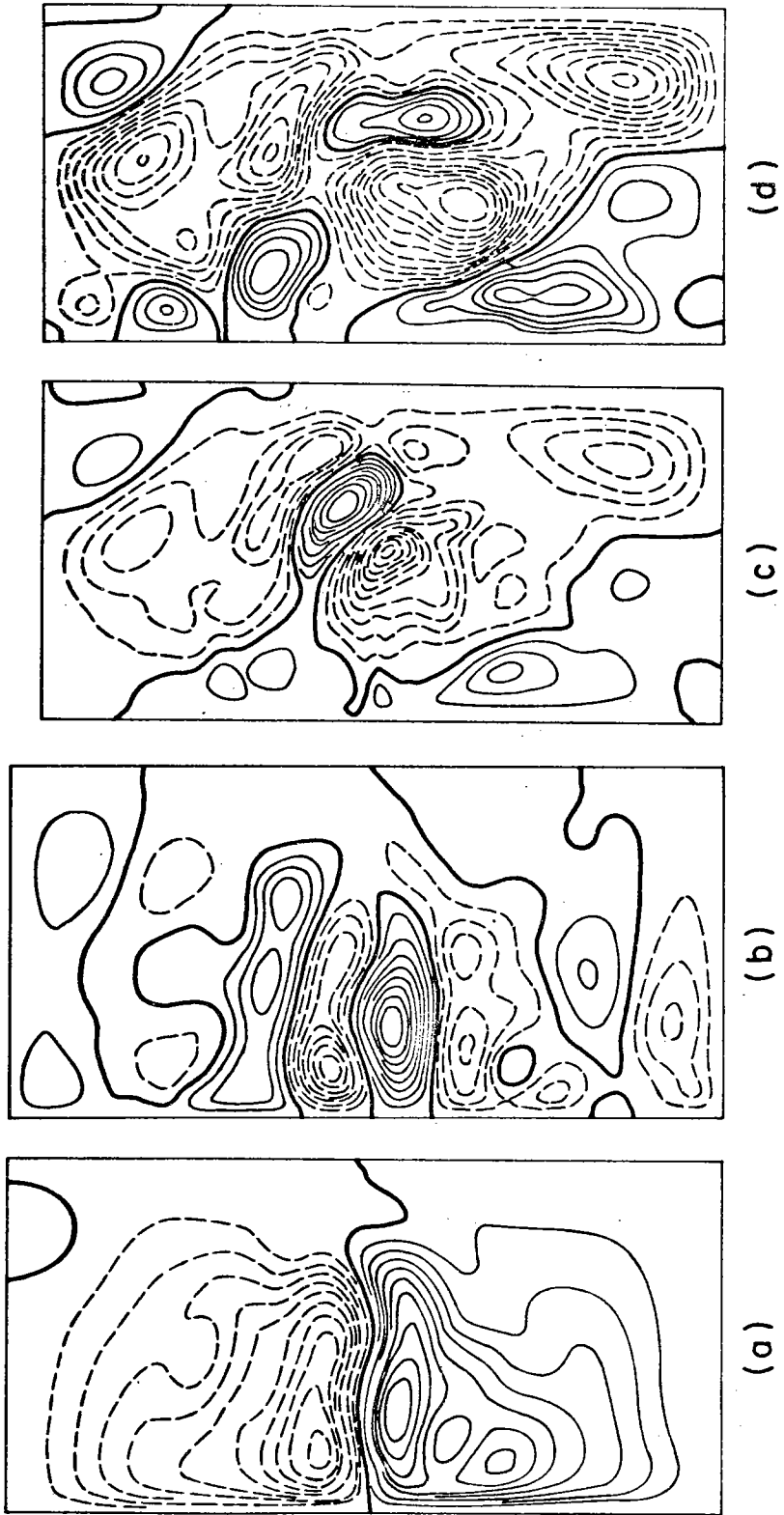


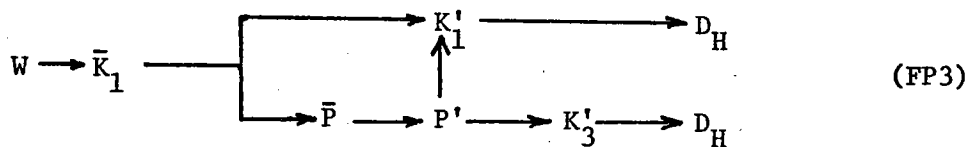
Figure 16: Experiment 2R.

- (a) mean upper level streamfunction (average over 500 days; contour interval = 4.0 Sverdrups).
- (b) mean lower level streamfunction (average over 500 days; contour interval = 1.6 Sverdrups).
- (c) instantaneous upper level eddy streamfunction (contour interval = 1.0 Sverdrup).
- (d) instantaneous lower level eddy streamfunction (contour interval = 4.0 Sverdrups).



circulation) and for good reason, as we shall see. Both instability processes are locally operative and consequently the frequency spectra of streamfunction amplitude (Figure 17) shows content in frequency bands that had been rather unenergetic in E1, for instance at 51 days and its higher harmonics, though the dominant contribution still occurs near a period of 64 days. Similarly, phase propagation is somewhat confused, though a characteristic phase speed can still be defined (Figure 18, Table 3).

In terms of energy fluxes, the rigid boundaries and consequent reduction in transport have been effective in suppressing the barotropic energy cascade relative to the baroclinic (compare Figures 14 and 19). Experiment 2R contains unstable modes of both types and the dominant energy flux path is a combination of FP1 and FP2



with both barotropic and baroclinic circuits active.¹ Contour plots of the mean perturbation energy components (Figure 20) illustrate the dual characteristic of the transfer processes at work in E2R. The eddy

¹Other experiments conducted by HL demonstrate that these flux pathways can be modified by selection of other viscous mechanisms. For instance, a small amount of a higher order vorticity diffusion ($K_4 \nabla^4 \zeta$) combined with a modest level of bottom drag ($K_0 \zeta$) can reroute the energy cascade by requiring that most energy be transferred vertically and lost through the bottom rather than laterally where it is lost in the boundary layers. This is in many ways a more preferable energy dissipation scheme in which the higher order viscosity selectively extracts the enstrophy cascaded to the highest wavenumbers while leaving the mesoscale relatively unaffected.

Figure 17: Composite frequency spectra for the upper and lower level streamfunction fields of experiment 2R. The spectra have been obtained by averaging 50 separate frequency spectra of the streamfunction amplitude taken at 50 equally spaced points.

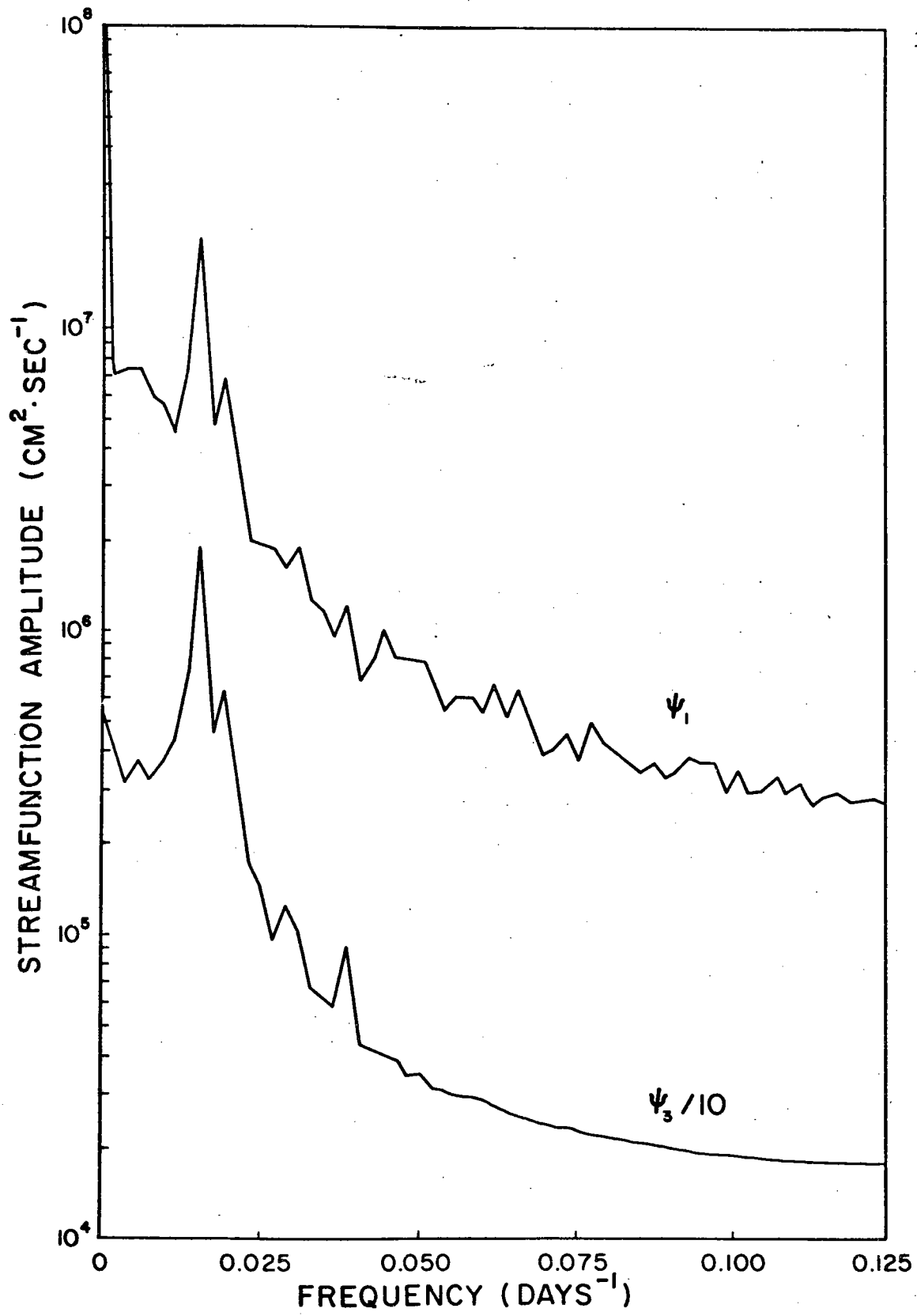


Figure 18: Experiment 2R x-t diagrams.
(a) upper level streamfunction.
(b) lower level streamfunction.
The profiles have been taken along $y = 1350$ km.

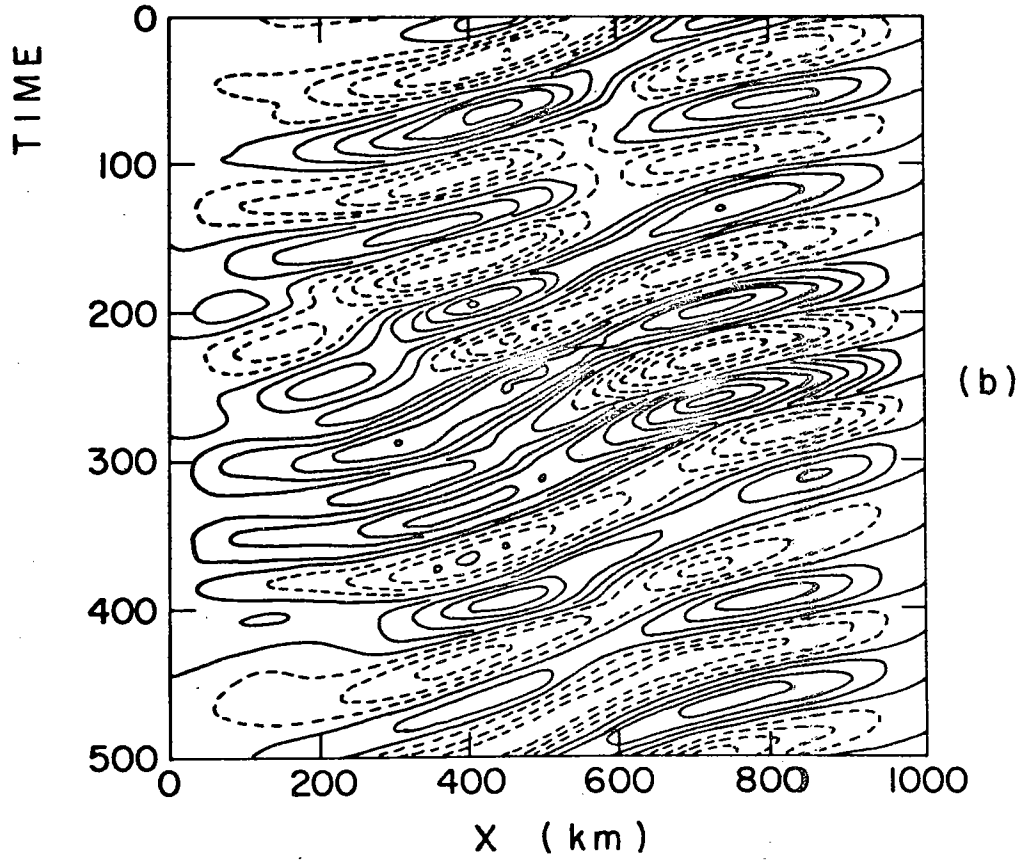
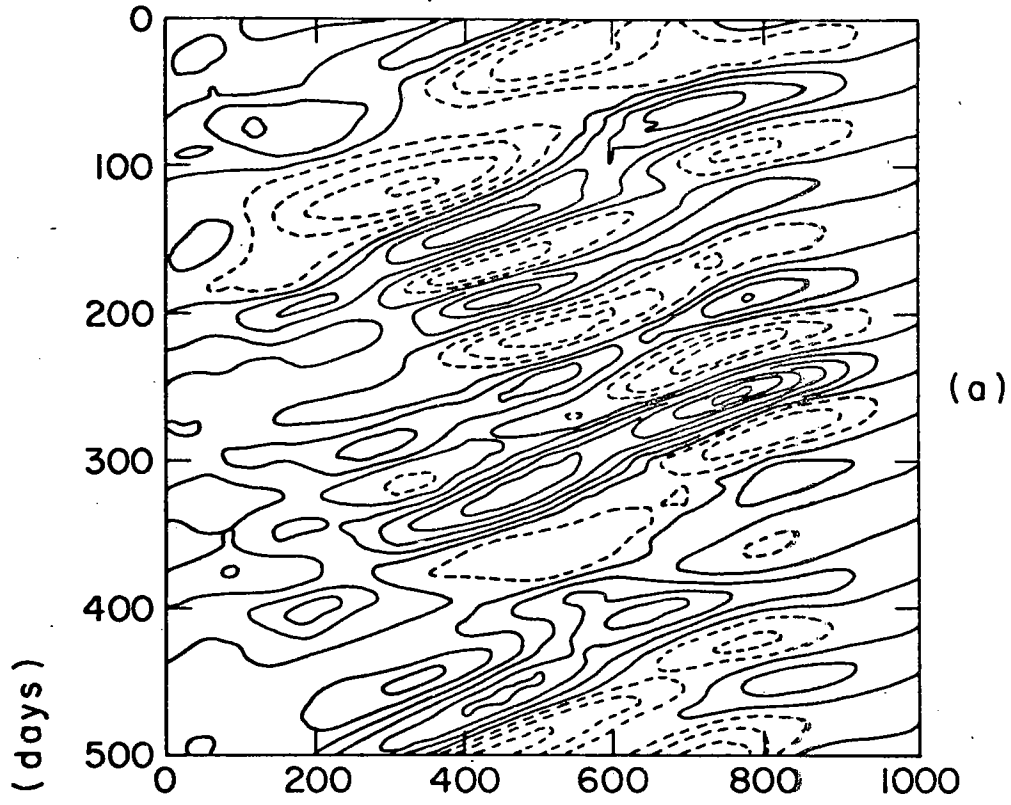


Figure 19: The experiment 2R global energy budget. Energy fluxes are in $\text{ergs/cm}^2/\text{sec}$; energies in 10^6 ergs/cm^2 .

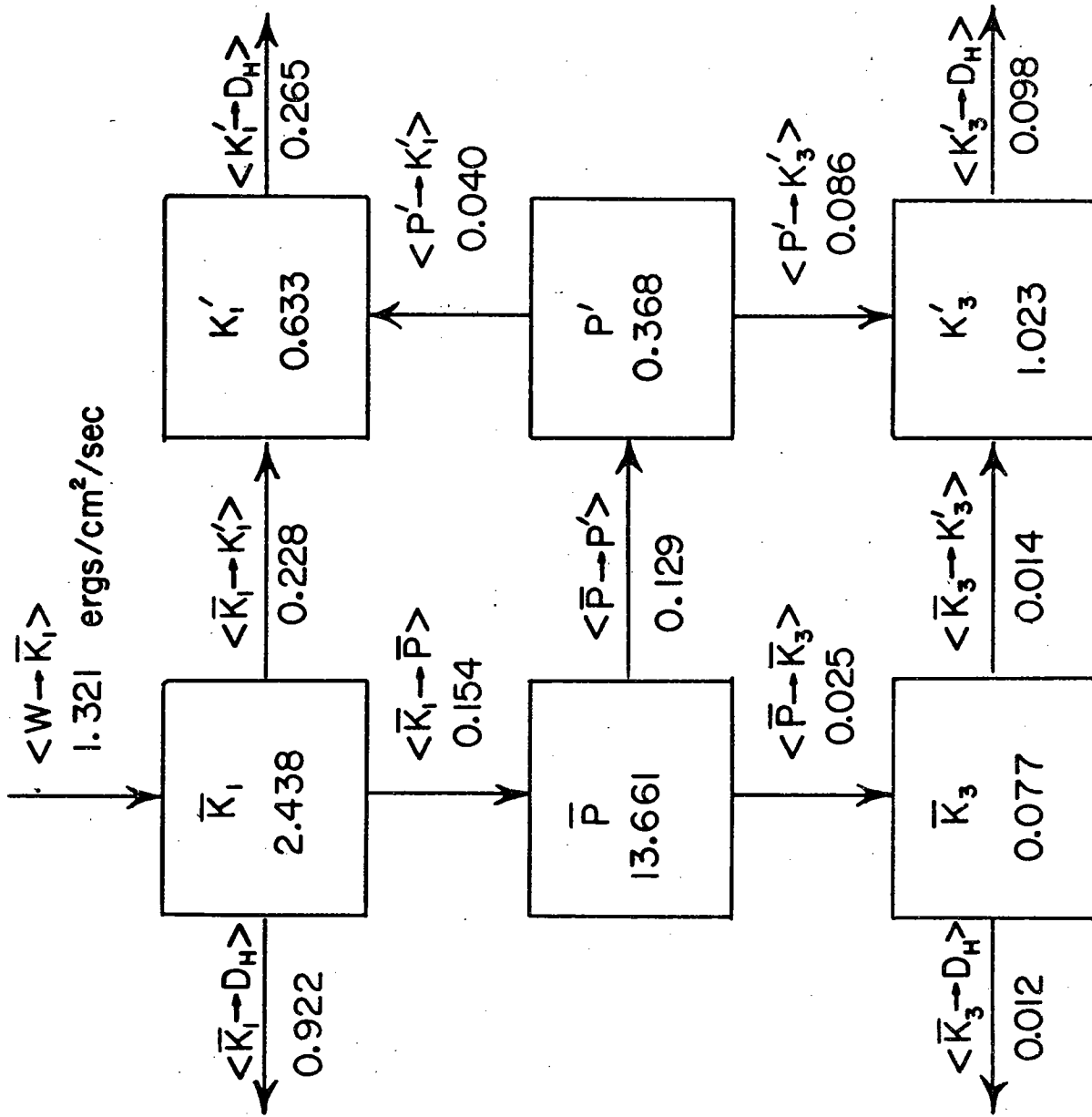
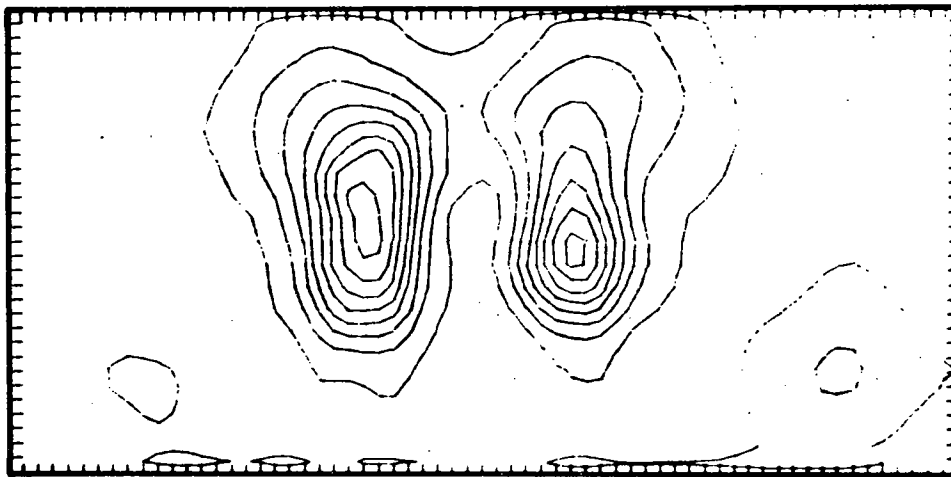


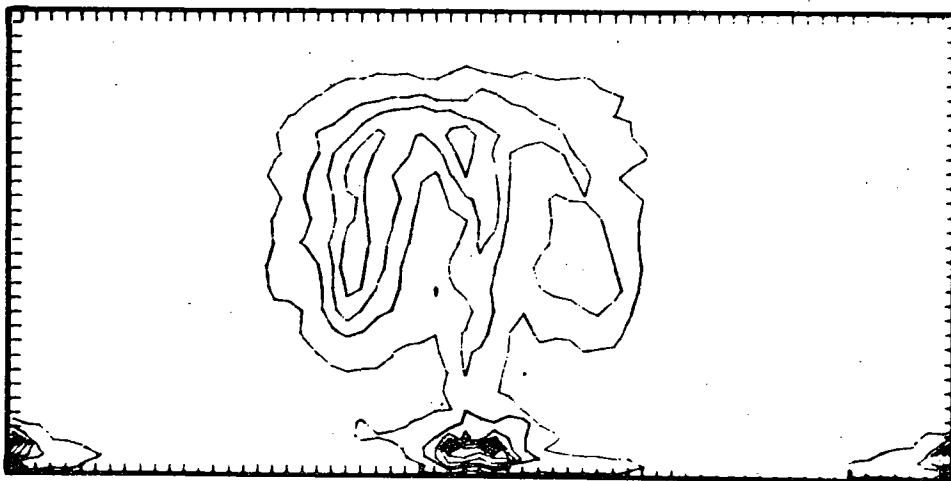
Figure 20: The experiment 2R mean eddy energy components.
(a) upper level eddy kinetic energy (contour interval = 0.8×10^6 ergs/cm²).
(b) lower level eddy kinetic energy (contour interval = 0.7×10^6 ergs/cm²).
(c) eddy potential energy (contour interval = 0.5×10^6 ergs/cm²).



(c)



(b)



(a)

energy, no longer confined primarily to either the eastward or westward flowing currents, has contributions in both regions in the case of K_1' (Figure 20a). The lower level eddy kinetic energy (K_3' , Figure 20b) is once again being fed exclusively by baroclinic activity in the two regions of westward recirculation and conforms nicely to the equivalent single-gyre results (Figure 9b).

Except for lower overall energy levels and the relatively more important contribution of baroclinic instability, the important features of the E2 equilibrium circulation recur in E2R despite the severe modification in boundary layer physics. Once separated by several boundary layer widths from the coast, the structure of the internal jet no longer depends on the boundary conditions on $x = 0$; for example, compare Figures 34 and 43. The eddies seem to be generated locally in intense mid-ocean regions of barotropic and baroclinic instability and their exact statistics are dependent on the western boundary layer only insofar as the overall amplitude of the idealized circulation is determined by frictional effects in the west. Especially in cases such as E2R where a mixture of modes exists, we can test this proposed dependence of eddy properties on the local environment only by a truly local analysis.¹ Such a theory is advanced in the next chapter.

¹ Another interesting test of these ideas would be to redo E1R and E2R with an increased wind stress. If our scaling hypothesis is at all valid, an appropriate strengthening of the forcing in E1R and E2R should quantitatively as well as qualitatively reproduce the results of E1 and E2, thus verifying the independence of the results of the explicit western boundary layer structure (for fixed W_I and W_F). Such tests have not been made due to computer resource limitations; however, the same conclusions arise during the course of the highly efficient stability analyses discussed in Chapter VI.

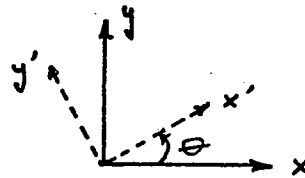
(V) A Linearized Stability Analysis

We are beginning to accumulate a growing number of numerical simulations upon which to base conclusions about eddy behavior under various parametric conditions. Hopefully, those in which eddies spontaneously appear display some basic instability having a counterpart in the world's oceans. In many of these experiments, highly localized regions of significant mean field/eddy interaction coincide with the intense boundary current after it separates from the western (or northern) wall; however, the mesoscale disturbances propagate out from these regions and ultimately modify the dynamics in other areas as well. The instantaneous and mean streamfunction fields available from these simulations represent, therefore, a picture of the integrated response of the system to some distribution in time and space of mesoscale energy sources and sinks. In some fortuitous cases, eddy behavior is rather easily understood on the basis of the associated global energy fluxes; in these instances, the eddies generally possess well defined space and time scales that stand out in the experimental results. Other simulations exist, however, in which the mesoscale response is much more confused, being a composite of several unstable modes, and for which more sensitive diagnostic tools are needed. This chapter proposes one such tool, based upon a quasisteady stability analysis of model flow profiles, whose advantages are simplicity and efficiency. Succeeding chapters will discuss and assess the feasibility of extending this simple idea to a more predictive use.

(V.1) The stability of parallel flows above topography

Consider an arbitrarily oriented coordinate system (x', y') which lies at an angle Θ to the coordinate frame (x, y) of Chapter II. Because there is no preferred direction, the equations are insensitive to such a coordinate rotation except for the β term which will, in general, be split in two components:

$$\begin{aligned} f &= f_0 + \beta y \\ &= f_0 + \beta_x x' + \beta_y y' \end{aligned}$$



where

$$\beta_x = \beta \sin \Theta$$

and

$$\beta_y = \beta \cos \Theta.$$

In these coordinates, we may then write the two-level quasigeostrophic equations as

$$\begin{aligned} \frac{d}{dt} [\nabla^2 \psi_1 + F_1(\psi_3 - \psi_1)] &= \left[\beta_x \frac{\partial \psi_1}{\partial y'} - \beta_y \frac{\partial \psi_1}{\partial x'} \right] \\ &\quad - J[\psi_1, \nabla^2 \psi_1 + F_1 \psi_3] + K_H \nabla^4 \psi_1 \end{aligned} \quad (5.1)$$

and

$$\begin{aligned} \frac{d}{dt} [\nabla^2 \psi_3 - F_3(\psi_3 - \psi_1)] &= \left[\beta_x \frac{\partial \psi_3}{\partial y'} - \beta_y \frac{\partial \psi_3}{\partial x'} \right] \\ &\quad - J[\psi_3, \nabla^2 \psi_3 + F_3 \psi_1 + \frac{f_0 h}{H_3}] + K_H \nabla^4 \psi_3 - K_B \nabla^2 \psi_3. \end{aligned}$$

The reduction of this problem to one horizontal dimension requires the assumption that the mean streamfunction of levels 1 and 3 be independent of time and of one coordinate, let us say x' . (This theory therefore automatically rules out certain classes of instabilities, most notably

the barotropic instability of Rossby waves (Lorenz, 1972) which cannot be adequately represented in terms of parallel flows.) Then, in the traditional manner, we may expand into mean and perturbation:

$$\begin{aligned}\psi_1 &= \bar{\psi}_1(y) + \lambda \Phi_1(x, y, t) + O(\lambda^2) \\ &= \bar{\psi}_1(y) + \text{Re } \lambda \phi_1(y, t) e^{ikx} + O(\lambda^2)\end{aligned}\tag{5.2}$$

and

$$\begin{aligned}\psi_3 &= \bar{\psi}_3(y) + \lambda \Phi_3(x, y, t) + O(\lambda^2) \\ &= \bar{\psi}_3(y) + \text{Re } \lambda \phi_3(y, t) e^{ikx} + O(\lambda^2)\end{aligned}$$

where λ is assumed small ($\lambda \ll 1$). Formally, the validity of this theory as a predictor of the properties of the growing waves requires that

- (i) the projection of the mean (finite-amplitude) velocity field onto the y' axis be small,
- (ii) the mean flow be quasisteady over many eddy periods, and
- (iii) the perturbation amplitude remain small.

The independence of the mean fields of the x' coordinate allows a wave-like solution in this direction; k is now a free parameter and represents the x wavenumber of the infinitesimal disturbance. As usual, we substitute (5.2) into (5.1) and linearize by neglecting terms proportional to $O(\lambda^2)$ or smaller. There results

$$\begin{aligned}\frac{d}{dt} [\phi_{1yy} - (F_1 + k^2)\phi_1 + F_1\phi_3] &= [\beta_x \phi_{1y} - ik\beta_y \phi_1] \\ &+ ik \bar{\psi}_{1y} [\phi_{1yy} - k^2\phi_1 + F_1\phi_3] \\ &- ik \phi_1 [\bar{\psi}_{1yy} + F_1\bar{\psi}_3]_y + K_H \nabla^4 \phi_1\end{aligned}\tag{5.3}$$

and

$$\begin{aligned}\frac{d}{dt} [\phi_{3yy} - (F_3 + k^2)\phi_3 + F_3\phi_1] &= [\beta_x \phi_{3y} - ik\beta_y \phi_3] \\ &+ ik \bar{\psi}_{3y} [\phi_{3yy} - k^2\phi_3 + F_3\phi_1] + K_H \nabla^4 \phi_3 \\ &- ik \phi_3 [\bar{\psi}_{3yy} + F_3\bar{\psi}_1 + \frac{f_0 h}{H_3}]_y - K_B [\phi_{3yy} - k^2\phi_3]\end{aligned}$$

where $\nabla^4 \phi_i = k^4 \phi_i - 2k^2 \phi_{i,yy} + \phi_{i,yyyy}$ ($i=1,3$)

and the primes for the rotated system have been dropped. Finally, we set $\phi_i \propto e^{\sigma t}$ and inquire for what complex values of $\sigma = \sigma_r + i\sigma_i$ solutions exist to these equations (subject to some appropriate boundary conditions on the ϕ_i). Equation 5.3 is not in the form of a standard eigenvalue problem; otherwise, the solution would be immediately available by any number of techniques. Fortunately, a little manipulation serves to reduce (5.3) to a more manageable form.

In general, this problem must be solved numerically on a discrete grid of points. Therefore, let us make a second-order finite-difference approximation to (5.3). Using a subscript j to denote the j^{th} gridpoint along our transect in the y direction, the discretized equations become

$$\begin{aligned} \frac{d}{dt} \left[\left(\frac{1}{\Delta y^2} \right) \phi_{1,j+1} - \left(\frac{2}{\Delta y^2} + F_1 + k^2 \right) \phi_{1,j} + \left(\frac{1}{\Delta y^2} \right) \phi_{1,j+1} + F_1 \phi_{1,j} \right] = \\ ik \left\{ -\beta_4 \phi_{1,j} + [\mathcal{A}_{1,y}]_j \left[\left(\frac{1}{\Delta y^2} \right) \phi_{1,j+1} - \left(\frac{2}{\Delta y^2} + k^2 \right) \phi_{1,j} + \left(\frac{1}{\Delta y^2} \right) \phi_{1,j+1} + F_1 \phi_{1,j} \right] \right. \\ \left. - [\phi_{1,j}] \left[\mathcal{A}_{1,yyy} + F_1 \mathcal{A}_{1,y} \right]_j \right\} \\ + \left\{ \left(\frac{\beta_x}{2\Delta y} \right) (\phi_{1,j+1} - \phi_{1,j-1}) + \left(\frac{K_H}{\Delta y^4} \right) [\phi_{1,j-2} - 4\phi_{1,j-1} + 6\phi_{1,j} - 4\phi_{1,j+1} + \phi_{1,j+2}] \right. \\ \left. - \left(\frac{\alpha k^2 K_H}{\Delta y^2} \right) [\phi_{1,j-1} - 2\phi_{1,j} + \phi_{1,j+1}] + k^4 K_H \phi_{1,j} \right\} \end{aligned} \quad (5.4a)$$

and

$$\begin{aligned} \frac{d}{dt} \left[\left(\frac{1}{\Delta y^2} \right) \phi_{3,j+1} - \left(\frac{2}{\Delta y^2} + F_3 + k^2 \right) \phi_{3,j} + \left(\frac{1}{\Delta y^2} \right) \phi_{3,j+1} + F_3 \phi_{3,j} \right] = \\ ik \left\{ -\beta_4 \phi_{3,j} + [\mathcal{A}_{3,y}]_j \left[\left(\frac{1}{\Delta y^2} \right) \phi_{3,j+1} - \left(\frac{2}{\Delta y^2} + k^2 \right) \phi_{3,j} + \left(\frac{1}{\Delta y^2} \right) \phi_{3,j+1} + F_3 \phi_{3,j} \right] \right. \\ \left. - [\phi_{3,j}] \left[\mathcal{A}_{3,yyy} + F_3 \mathcal{A}_{3,y} + \frac{s_0 h_1}{H_3} \right]_j \right\} \\ + \left\{ \left(\frac{\beta_x}{2\Delta y} \right) (\phi_{3,j+1} - \phi_{3,j-1}) + \left(\frac{K_H}{\Delta y^4} \right) [\phi_{3,j-2} - 4\phi_{3,j-1} + 6\phi_{3,j} - 4\phi_{3,j+1} + \phi_{3,j+2}] \right. \\ \left. - \left(\frac{\alpha k^2 K_H}{\Delta y^2} \right) [\phi_{3,j-1} - 2\phi_{3,j} + \phi_{3,j+1}] + k^4 K_H \phi_{3,j} \right. \\ \left. - K_B \left[\left(\frac{1}{\Delta y^2} \right) \phi_{3,j-1} - \left(\frac{2}{\Delta y^2} + k^2 \right) \phi_{3,j} + \left(\frac{1}{\Delta y^2} \right) \phi_{3,j+1} \right] \right\}. \end{aligned} \quad (5.4b)$$

To these equations we must add the finite-difference analogues of the chosen boundary conditions on ϕ_i . These need be specified because the highly differentiated terms - in this case, the viscous terms - cannot be evaluated on the boundaries unless some information is given on how ϕ behaves beyond its normal range. Suppose $j = 1$ is the first nonzero gridpoint; then, equation 5.4a calls for $\phi_{i,j=0}$, and $\phi_{i,j=-1}$ which are not yet known. Given a particular set of boundary conditions, however, they can be specified in terms of the interior points in the following manner. For a free-slip, impermeable wall

$$\begin{aligned} \phi_{i,j=0} &= 0 \\ \text{and } \phi_{i,j=-1} &= -\phi_{i,j=1} \end{aligned} \quad (i=1,3)$$

which arise as second-order approximations to the conditions $\zeta = \zeta_{yy} = 0$ on the boundary. Similarly, no-slip impermeable walls require

$$\begin{aligned} \phi_{i,j=0} &= 0 \\ \text{and } \phi_{i,j=-1} &= \phi_{i,j=1} \end{aligned} \quad (i=1,3).$$

The properties of the unstable modes, however, are not sensitive to the boundary conditions for eigenfunctions which are well restricted to the basin interior as is the case in many of our simulations.

To cast this problem into standard form, redefine the left-hand sides of (5.4a) and (5.4b) so that

$$Q_{i,j} = \left[\left(\frac{1}{4y^2}\right)\phi_{i,j-1} - \left(\frac{\alpha}{4y^2} + F_1 + k^2\right)\phi_{i,j} + \left(\frac{1}{4y^2}\right)\phi_{i,j+1} + F_1\phi_{3,j} \right] \quad (5.5)$$

and
$$Q_{3,j} = \left[\left(\frac{1}{\Delta y^2}\right) \phi_{3,j-1} - \left(\frac{2}{\Delta y^2} + F_3 + k^2\right) \phi_{3,j} + \left(\frac{1}{\Delta y^2}\right) \phi_{3,j+1} + F_3 \phi_{3,j} \right].$$

On this discrete grid, the relationship between Q_i and ϕ_i is explicitly known to be

$$\underline{Q} = \begin{bmatrix} Q_{3,j=0} \\ Q_{3,j=1} \\ \vdots \\ Q_{3,j=N} \\ Q_{3,j=N} \end{bmatrix} = \underline{M} \begin{bmatrix} \phi_{3,j=0} \\ \phi_{3,j=1} \\ \vdots \\ \phi_{3,j=N} \\ \phi_{3,j=N} \end{bmatrix}$$

with \underline{M} the matrix of coefficients defined by (5.5). Inverting the block tridiagonal matrix \underline{M} yields the $\phi_{3,j}$ as a function of $Q_{3,j}$ on the discrete grid. Then,

$$\frac{d}{dt} \bar{Q} = \underline{H}(\psi, \psi_3) \bar{Q} \quad (5.6)$$

where the functional relationship, \underline{H} , results by substituting for ϕ_i on the right-hand sides of (5.4a, b). Once reduced to this form, the eigenvalues are easily calculable via eigensystem analysis; we have employed EISPACK for this purpose. Note that for a given set of parameters, mean flow conditions, and bottom topography, we need still solve this problem over the range of k to identify the most active wavenumber. In doing so, we regard k as a continuous variable. Insofar as our simulations are enclosed in a bounded domain, however, we do intrinsically restrict the range of admissible x wavelengths to be less than that of the fundamental basin mode. In any case, the most unstable waves generally possess scales much smaller than the basin dimension.

(V.2) The predictions of linearized stability theory

Despite the simplicity of the approach, the methodology outlined in the previous section does predict many quantitative aspects of perturbations arising on the mean flow. These properties can be compared to statistics generated from actual finite-amplitude eddy simulations. From the unstable eigenvalues, if any, we know the expected growth rate of the eddies under the assumed mean flow conditions. The associated eigenvectors and the most unstable x wavenumber, k_{\max} , define the spatial configuration of the eddies and indicate in which region of the y domain they may be expected to appear. This can then be compared with our expectations based on an a priori examination of the profile of mean velocity and potential vorticity, and our knowledge of simple instability theory. Finally, the eigenvectors yield a description of the energy cascade to the growing eddies. We need only multiply (5.3) by ϕ_i^* (ϕ_i conjugate) and combine to construct the two eddy kinetic energy equations

$$\begin{aligned} \sigma_R H_1 [|\phi_{1y}|^2 + k^2 |\phi_1|^2] &= \text{Re} [H_1 \sigma \frac{d}{dy} \{\phi_1^* \phi_{1y}\} - ik H_1 \frac{d}{dy} \{\phi_1^* \phi_{1y} \Psi_{1y}\}] \\ &+ \langle P' \rightarrow K_1' \rangle + \langle \bar{K}_1 \rightarrow K_1' \rangle - \langle K_1' \rightarrow D_H \rangle \end{aligned} \quad (5.7a)$$

and

$$\begin{aligned} \sigma_R H_3 [|\phi_{3y}|^2 + k^2 |\phi_3|^2] &= \text{Re} [H_3 \sigma \frac{d}{dy} \{\phi_3^* \phi_{3y}\} - ik H_3 \frac{d}{dy} \{\phi_3^* \phi_{3y} \Psi_{3y}\}] \\ &+ \langle P' \rightarrow K_3' \rangle + \langle \bar{K}_3 \rightarrow K_3' \rangle - \langle K_3' \rightarrow D_H \rangle - \langle P_3' \rightarrow D_B \rangle \end{aligned} \quad (5.7b)$$

where Re denotes the real part of a complex expression. Similarly, one can easily derive the potential energy equation

$$\sigma_R \left[\left(\frac{\sigma^2 f_0^2}{N^2 H} \right) |\phi_3 - \phi_1|^2 \right] = \langle \bar{P} \rightarrow P' \rangle - \langle P' \rightarrow K_1' \rangle - \langle P_3' \rightarrow K_3' \rangle. \quad (5.7c)$$

The individual flux terms

$$\langle \bar{K}_1 \rightarrow K_1' \rangle = \text{Re} [ikH_1 \phi_1^* \phi_{1y} \Psi_{1yy}]$$

$$\langle P' \rightarrow K_1' \rangle = \left(\frac{2f_0^2}{N^2H} \right) \text{Re} [\sigma \phi_1^* (\phi_3 - \phi_1) - ik \phi_1^* \phi_3 \Psi_{1y}]$$

$$\langle K_1' \rightarrow D_H \rangle = \text{Re} [H_1 K_H \phi_1^* \nabla^4 \phi_1]$$

$$\langle \bar{K}_3 \rightarrow K_3' \rangle = \text{Re} [ikH_3 \phi_3^* \phi_{3y} \Psi_{3yy}]$$

$$\langle P' \rightarrow K_3' \rangle = \left(\frac{2f_0^2}{N^2H} \right) \text{Re} [\sigma \phi_3^* (\phi_1 - \phi_3) - ik \phi_3^* \phi_1 \Psi_{3y}]$$

$$\langle K_3' \rightarrow D_H \rangle = \text{Re} [H_3 K_H \phi_3^* \nabla^4 \phi_3]$$

$$\langle K_3' \rightarrow D_B \rangle = \text{Re} [-H_3 K_B \phi_3^* \nabla^2 \phi_3]$$

and
$$\langle \bar{P} \rightarrow P' \rangle = - \left(\frac{2f_0^2}{N^2H} \right) \text{Re} [ik \phi_2 (\phi_3 - \phi_1)^* (\Psi_3 - \Psi_1)_y]$$

are once again directly comparable to the finite amplitude predictions of the fully nonlinear results.

(VI) The Local Properties of the Unstable Modes and the Prediction of Eddy Statistics

It remains to be seen of course to what extent a highly simplified stability model such as that advanced in Chapter V can reproduce the mean eddy statistics seen in the full numerical simulations. Under the most optimal circumstances, we might find it possible to extract the mesoscale field properties from a stability analysis of selected mean velocity profiles. In such cases, the application of LSA begins to extend beyond the immediate goal of simple model analysis. For instance, one important limitation on making a thorough examination of model behavior under a wide range of parametric conditions is the costliness of the nonlinear simulations described in Chapter IV.¹ Evidently, we cannot expect to do a complete parameter exploration by this means. Consider however the advantages inherent in the LSA. The determination of the most unstable modes from a mean profile and the calculation of the accompanying energetics requires two orders of magnitude fewer computer resources than a full simulation. Thus, if verified, LSA acquires prognostic as well as diagnostic importance in the following ways. First, the effects of small parametric changes can be estimated by studying a range of closely spaced values for fixed mean flow profiles (so long as the functional dependence of the mean fields on the parameters is itself small). Such studies can extend our knowledge of eddy properties into regions of parameter space adjacent to pre-existing nonlinear simulations. We need integrate the quasigeostrophic equations only long

¹Experiment 2R and its accompanying analysis, for instance, required three hours of computer time on the NCAR CDC 7600.

enough to define the approximate interior flow structure and strength; thereupon, LSA predicts the ensuing equilibrium eddies insofar as the modification of the mean fields can be ignored. At the very least, this yields a preliminary estimate of eddy statistics on the basis of which it might be decided, for one reason or another, to terminate the experiment. In such instances, we have saved ourselves the trouble and expense of running the nonlinear code far enough into the equilibrium phase to generate reliable eddy statistics, a savings of nearly 50% in a typical simulation. Meanwhile, the LSA always provides useful diagnostic information, namely the local structure of the unstable modes which, as remarked, is unavailable to us from global energy considerations.

This optimistic evaluation of the uses of the LSA depends on the validity of the predictions it makes, so we proceed now to explore its range of applicability. In particular, we consider the following questions:

- (i) can we qualitatively explain the conclusions of Chapter IV on the basis of linear stability results,
- (ii) can we quantitatively interpret equilibrium eddy statistics from mean or instantaneous velocity profiles which are assumed unidirectional and streamwise invariant,
- (iii) what are the properties of the mean flow primarily responsible for the growth of the unstable modes,
- (iv) how are the instabilities dependent on critical environmental parameters such as R_d and K_H , and,
- (V) what are the most probable signatures for regions of barotropic and baroclinic activity?

(VI.1) A stability analysis of experiment 1

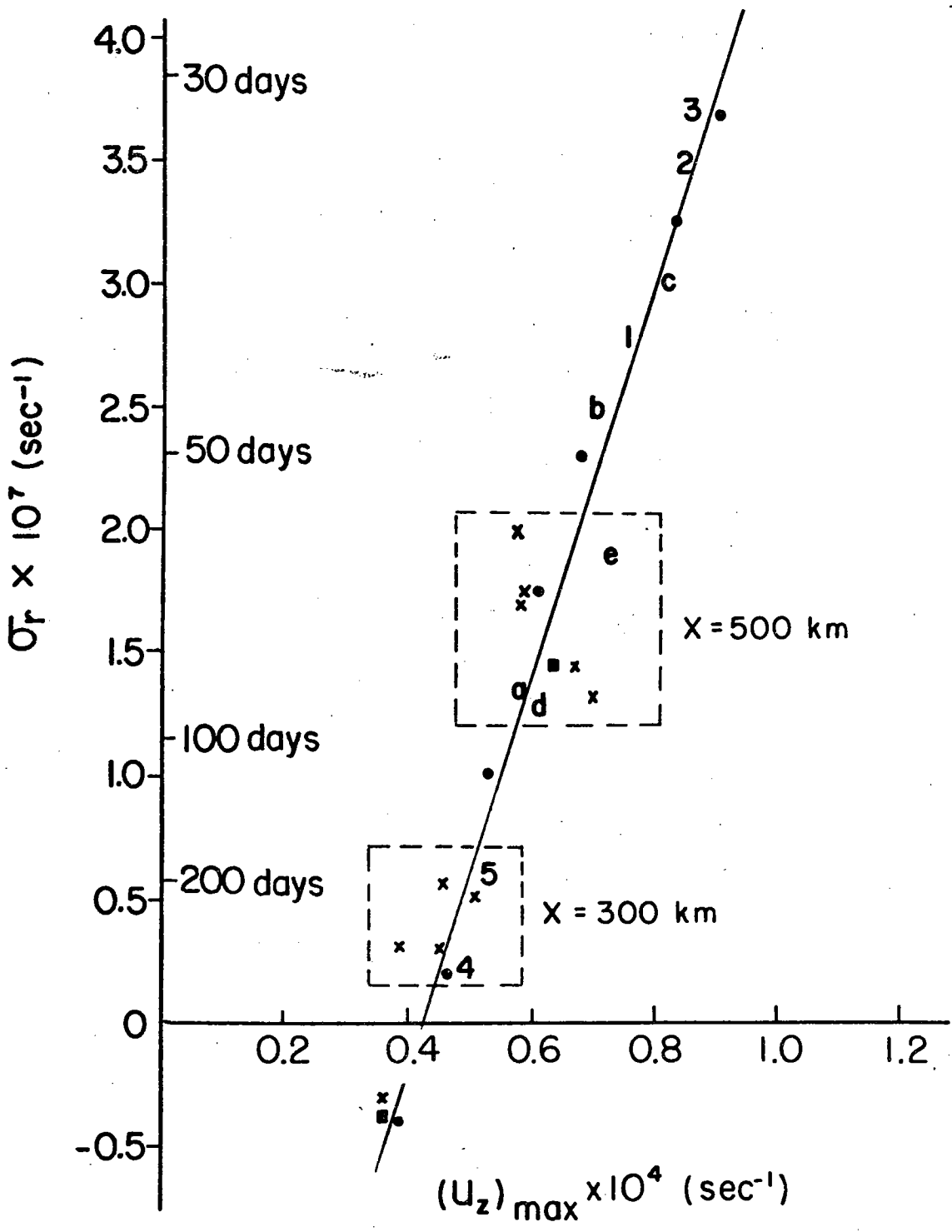
As we recall from Chapter IV, E1 had the cleanest and most uniform eddy field of any of the primary simulations. There is therefore some justification for presuming that E1 will also be the easiest to interpret using LSA. This will be shown to be true. Take, for instance, our initial impression from the boundary layer sensitivity studies that local factors such as (some measure of) circulation intensity affect eddy generation. We can test this hypothesis by considering a succession of E1 velocity profiles including

- (i) mean profiles from the E1 equilibrium phase,
- (ii) instantaneous profiles from the spinup phase, and,
- (iii) instantaneous profiles from the equilibrium phase.

In the experiments to be reported, profiles were typically taken along $x = 300$ km and $x = 500$ km. For each profile, we have used LSA to determine the accompanying unstable modes and their associated statistics. Figure 21 shows the resulting correlation between the growth rate for the maximally unstable modes (baroclinic in this case) and the maximum local value of vertical shear for all the E1 profiles analyzed. Because E1 has a negligible lower layer velocity, vertical shear has been estimated by the maximum upper layer velocity.

The dominant trend in the experimental results is unmistakable; the growth rates of the unstable baroclinic modes vary quasilinearly with the local vertical shear. The e-folding times predicted for the equilibrium phase eddies lie between 50 and 200 days. Note, however, the time evolution of the growth rate, $\sigma_R = \text{Re } \sigma$, during the spinup phase -

- Figure 21: The variation with vertical shear of the growth rate of the baroclinic modes observed in experiment 1.
- × instantaneous profiles taken during the equilibrium phase.
 - mean profiles taken during the equilibrium phase.
 - baroclinic mode scaling experiment (see section VI.5)
 - 1-5 time sequence of instantaneous profiles taken during spinup phase along $x = 300$ km.
 - a-e time sequence of instantaneous profiles taken during spinup phase along $x = 500$ km.



also plotted in Figure 21. As the circulation accelerates, the predicted growth time of the unstable eddies decreases, approaching a minimum of 30 days. Once the eddies, which grow from perturbations of unknown initial amplitude, reach finite amplitude and begin to efficiently extract energy from the mean field, $\text{Re } \sigma$ falls drastically and eventually assumes its more modest equilibrium value. During spinup, the baroclinic modes along $x = 300$ km are more unstable than those along $x = 500$ km; the reverse is true for the equilibrium phase. Since the E1 flow features, at least at the upper level, are dominated by the mean flow and are thus quasisteady, the instantaneous eddy properties do not vary a great deal in time but lie in localized regions in Figure 21. This may arise because of the influence of the northern wall; relaxing this constraint allows a greater range of unstable modes to appear - as we will see in (VI.3). This rather narrow range of flow variability in E1 is translated into the simple quasilinear relation between σ_R and $|u_z|$ which depends, as we supposed, on the fact that north-south profiles taken along any longitude at any time have nearly identical shapes but differing amplitudes; thus, jet structure as such cannot play a significant role in these results.

The predicted substantial eddy growth rate as early as day 500 was initially quite perplexing. The obvious manifestations of finite amplitude eddies do not appear in plots of streamfunction and global kinetic energy until nearer day 900 (Figure 4). Perhaps the assumptions made during the derivation of the LSA have led to overestimates of the growth rate. Assuming a 50-day e-folding time, perturbations would need to begin with an amplitude some 20,000 times smaller than that of the mean

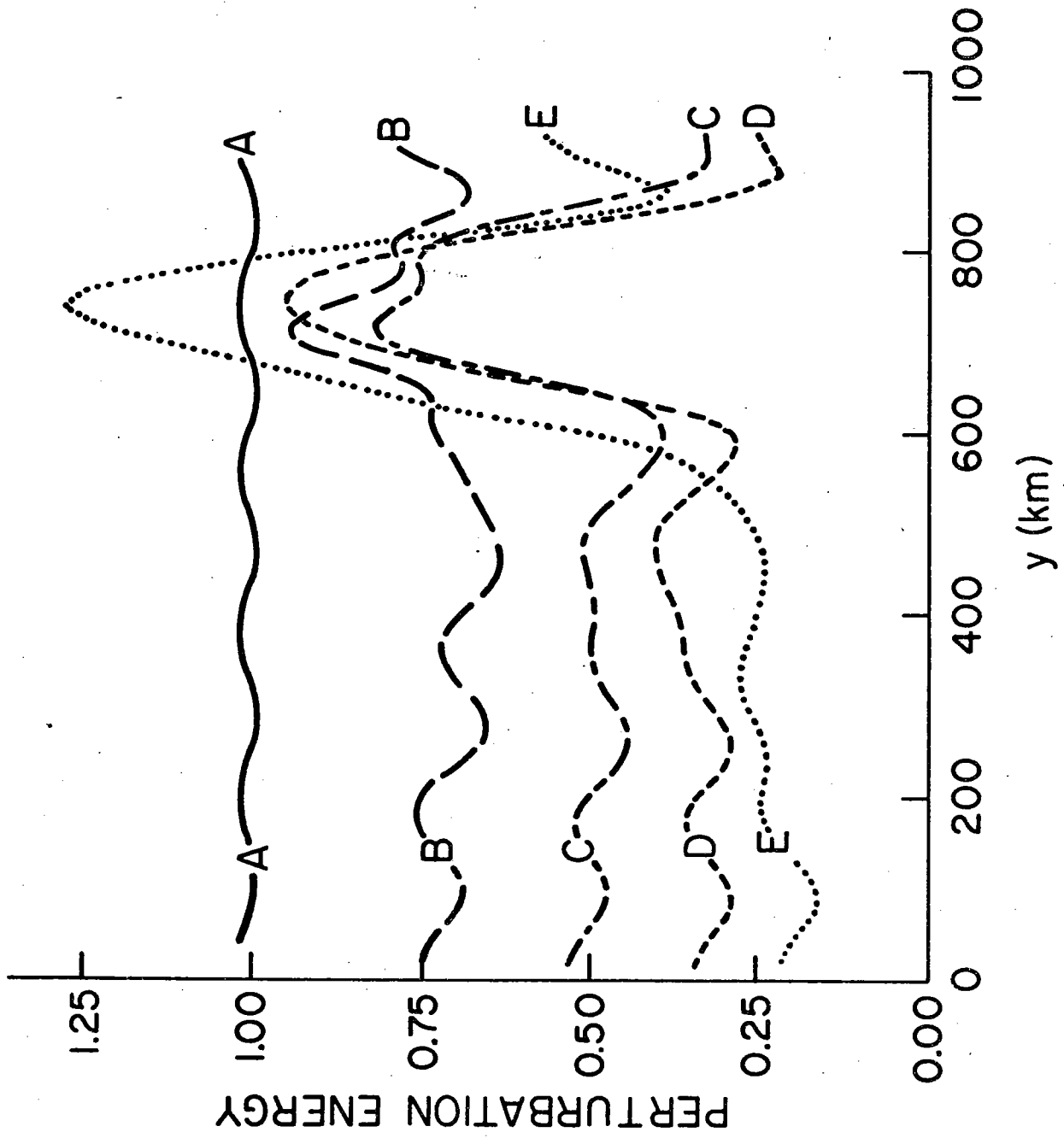
flow in order to grow to a distinguishable magnitude in 500 days. It is unclear whether or not this is a reasonable estimate for error amplitude at this stage in the model calculations. We need another way of verifying the growth rate prediction of the LSA, preferably an unambiguous demonstration of instability at day 500.

To provide such a demonstration, we have devised a perturbation growth test. Beginning from the state of E1 at day 540, a periodic streamfunction "error" field was introduced with an amplitude of approximately $0.1\% |\psi_1|_{\max}$ and a length scale comparable to R_d . The nonlinear equations were then integrated in time and the growth of the eddy field, defined as the difference between the perturbed and unperturbed simulations as a function of time, was monitored. The zonally averaged perturbation energy, $\frac{1}{x_0} \int_0^{x_0} (K_1' + K_3' + P') dx$, shows in Figure 22 that the error energy decays everywhere but in the zonal band where instantaneous instability has been predicted. Aside from an initial tendency for a slight loss of energy even at these latitudes (due to the fact that the eddies are unstable only in about one-half of the basin width), the perturbation energy soon begins to grow in the expected manner. A closer examination of individual eddies in the unstable region confirms that the eddy amplitude increases with a characteristic time of 50-100 days. We are therefore encouraged to put some confidence in the LSA results which in this case have for the first time revealed the instability mechanisms to be operative very early in the numerical simulations; apparently, the onset of instability really begins prior to day 540.

Rather than describe in detail the over 100 profiles examined from all four experiments, we choose instead to discuss only one representative

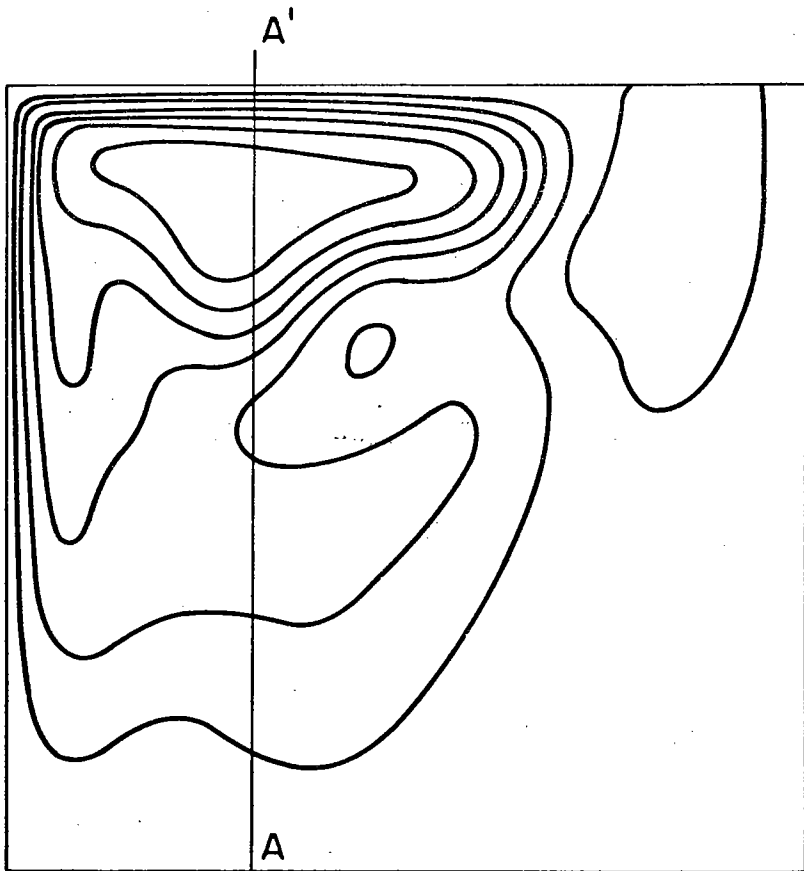
Figure 22: The time evolution of the zonally averaged eddy energy from the experiment 1 perturbation growth test.

A = day 540
B = day 560
C = day 580
D = day 600
E = day 620

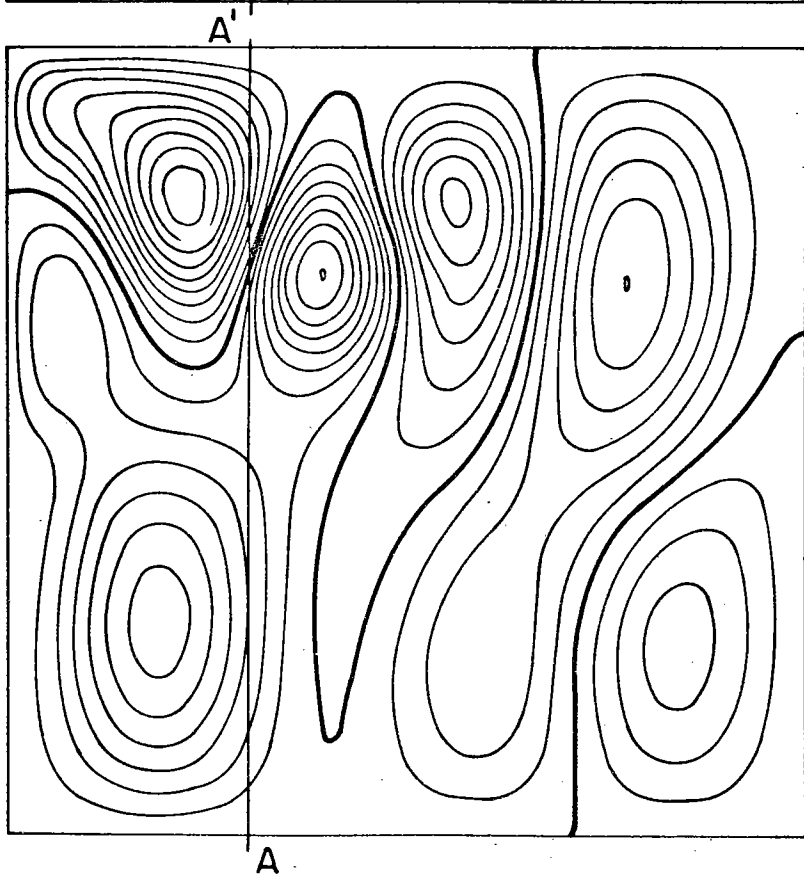


profile and the accompanying eddy statistics for each of E1, E1R, E2 and E2R. In most cases, and this is a primary conclusion of the LSA studies, it is the large-scale features of the mean circulation rather than the higher order properties that indicate whether instability will occur; consequently, even a single profile can give an accurate impression of the instabilities at work in a particular experiment. In examining the E1 equilibrium fields, the situation is very simple (as Figure 21 suggests); there is never more than one instability, a moderately unstable baroclinic mode which occurs in the region of westward return flow. Both the time mean and instantaneous two-dimensional velocity profiles exhibit this instability. Take, for example, the instantaneous profile of Figure 24 which corresponds to cross section AA' in Figure 23. The primary (eastward) and secondary (westward) jets are clear in this diagram, as is the slow westward return flow in the southern half basin. Note that although the upper level streamfunction field in the neighborhood of AA' does satisfy our assumption of x-dependence quite well (since it is dominated by the mean flow rather than the eddy field), the projection of the lower level velocity onto section AA' is quite large; that is, $\left| \frac{\partial \psi_3}{\partial x} \right| > \left| \frac{\partial \psi_3}{\partial y} \right|$. Fortunately, the maximum velocity at level 1 exceeds that at level 3 by more than an order of magnitude and, hence, the local shears will depend most strongly on the upper level circulation. Still, it will be shown presently that even small uncertainties in the value of the shear can, in some instances, cause large uncertainties in the LSA results. Despite these limitations, we shall proceed with the linear analysis bearing in mind that, should our assumptions

Figure 23: Representative instantaneous fields from experiment 1.
(a) upper layer streamfunction (contour interval = 4.0 Sverdrups).
(b) lower layer streamfunction (contour interval = 2.4 Sverdrups).
Profile AA' is replotted in Figure 24.

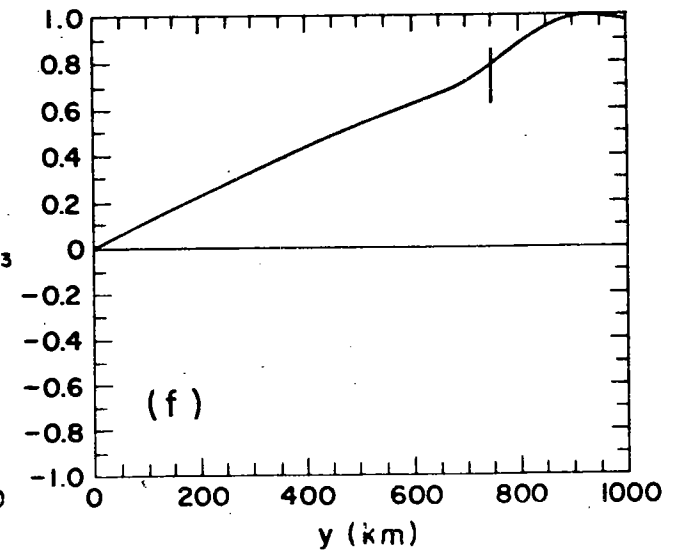
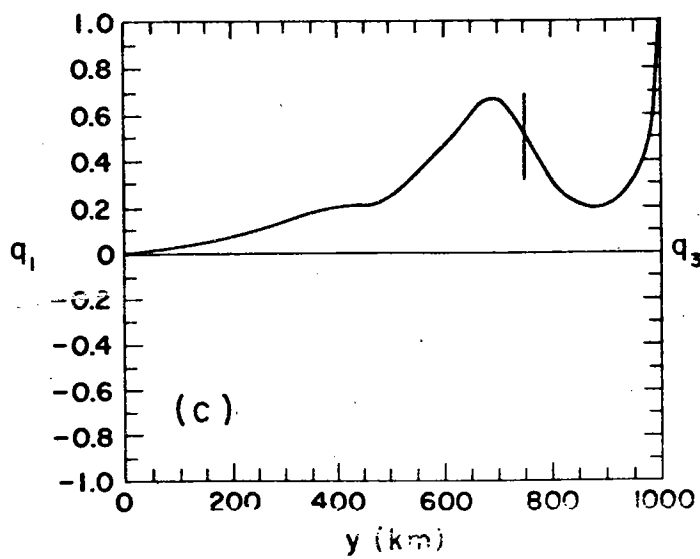
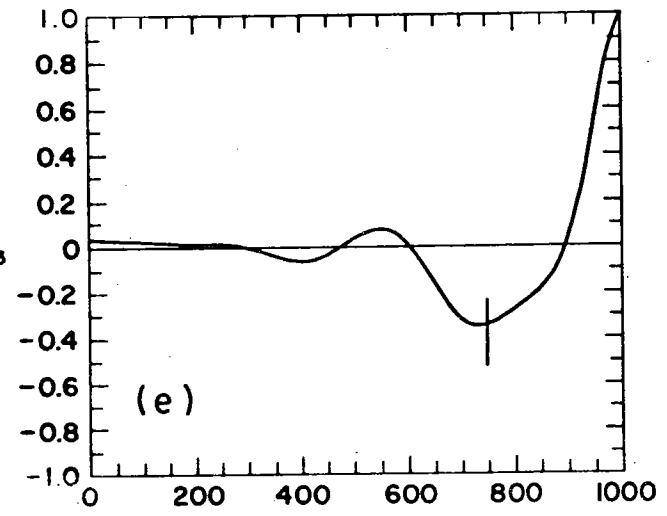
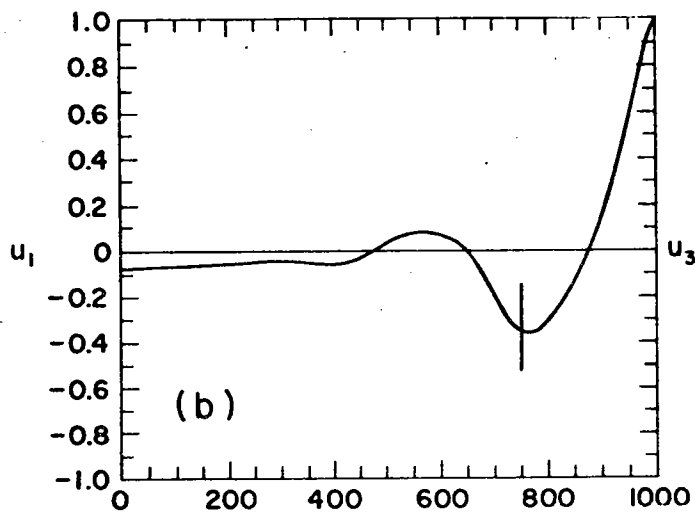
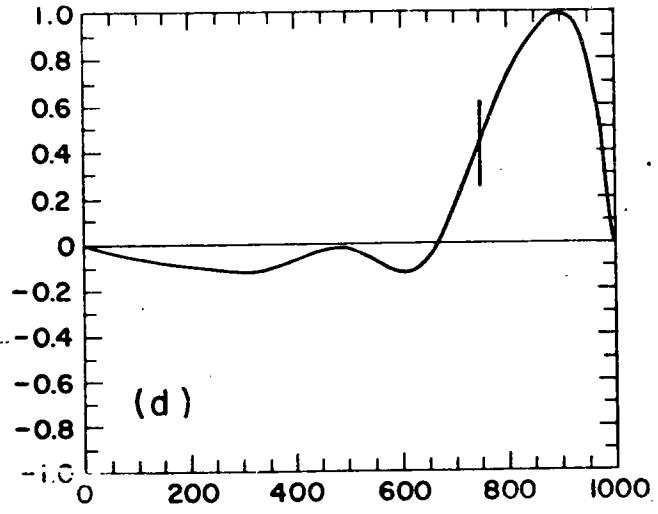
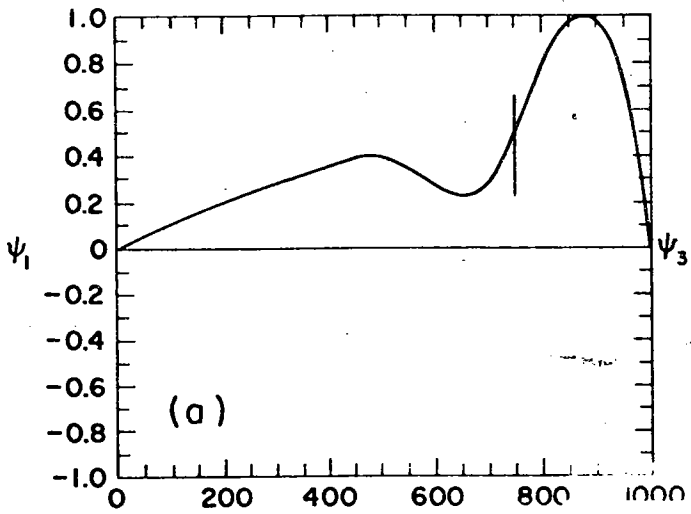


(a)



(b)

Figure 24: Profiles AA' from experiment 1, Figure 23.
(a) upper layer streamfunction ($|\psi_1|_{\max} = 3.2 \times 10^8$).
(b) upper layer velocity ($|u_1|_{\max} = 51.3$).
(c) upper layer potential vorticity ($|q_1|_{\max} = 2.0 \times 10^{-5}$).
(d) lower layer streamfunction ($|\psi_3|_{\max} = 7.9 \times 10^6$).
(e) lower layer velocity ($|u_3|_{\max} = 1.4$).
(f) lower layer potential vorticity ($|q_3|_{\max} = 2.1 \times 10^{-5}$).
Maximal instability occurs at $y = 750$ km.



prove too severe or the two-dimensional results inconclusive, we may wish in future to devise a fully three-dimensional stability theory.

The unstable mode predicted by LSA is centered at $y = 750$ km as denoted by the line drawn through the individual plots of Figure 24. As we expect, the instability aligns with the westward inertial recirculation and lies in a region of opposing potential vorticity gradients at the upper and lower levels (Figures 24c, f), a necessary condition for baroclinic instability (Pedlosky, 1963). The growing eddies - the eigenfunctions of the LSA - appear in Figure 25 both in transect (25a, c) and with the oscillatory x-dependence reintroduced (25b, d). As should be no surprise, the eddies display the telltale 90° phase offset between upper and lower level appropriate for a transfer of mean potential energy to the perturbation field.

In comparison to the results of the E1 nonlinear simulation, the predicted eddies have many of the same statistical properties (Tables 3 and 4). Even by inspection it is obvious that the idealized stability analysis "eddies" have the same spatial scales (Figures 5 and 25) and that they are both preferentially elongated in the meridional direction.¹ Wave radiation into the southern basin and the consequent setup of the barotropic far field can, of course, only occur in the fully nonlinear experiments.

An energy diagram for the growing eddies (Figure 26) confirms the characteristic baroclinic energy transfers. (Note that since these are

¹This feature can also be anticipated theoretically for westward zonal currents (Robinson and McWilliams, 1974).

Figure 25: The most unstable baroclinic mode corresponding to profile AA', Figures 23 and 24.
(a,c) the complex upper and lower layer eigenfunctions ($\text{Re}\phi$ solid, $\text{Im}\phi$ dotted).
(b,d) the real part of the unstable modes with the x-dependence reintroduced.
Lines have been drawn along $x = 480$ km to indicate the phase relationship between the upper and lower layer eddies.

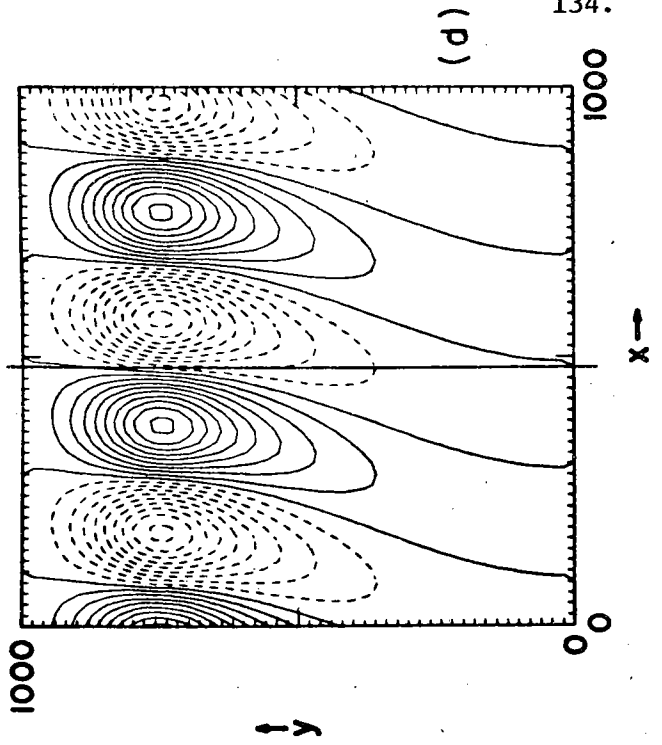
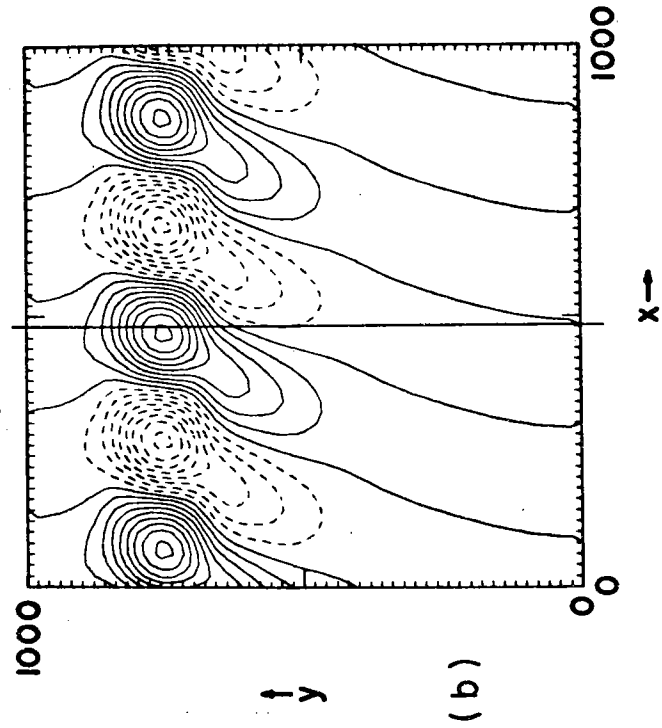
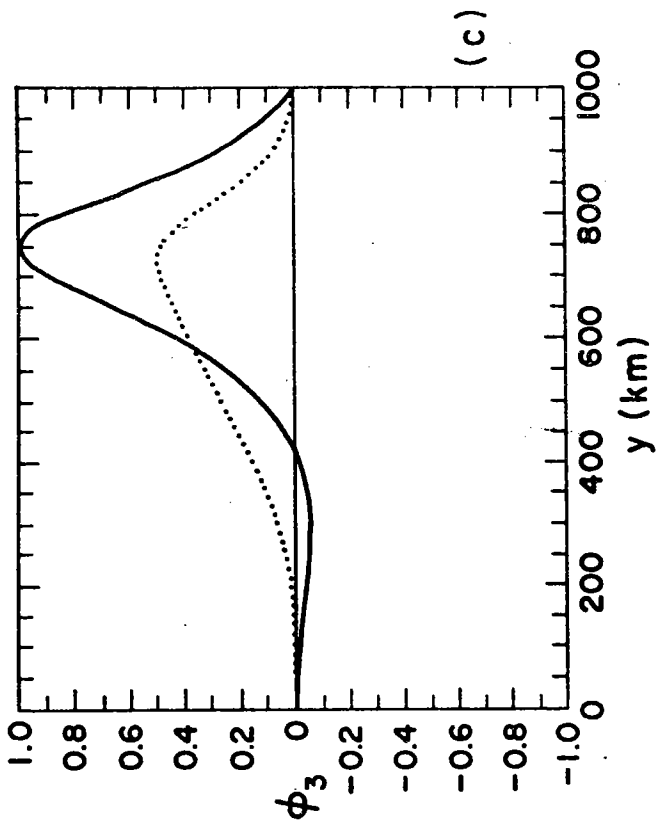
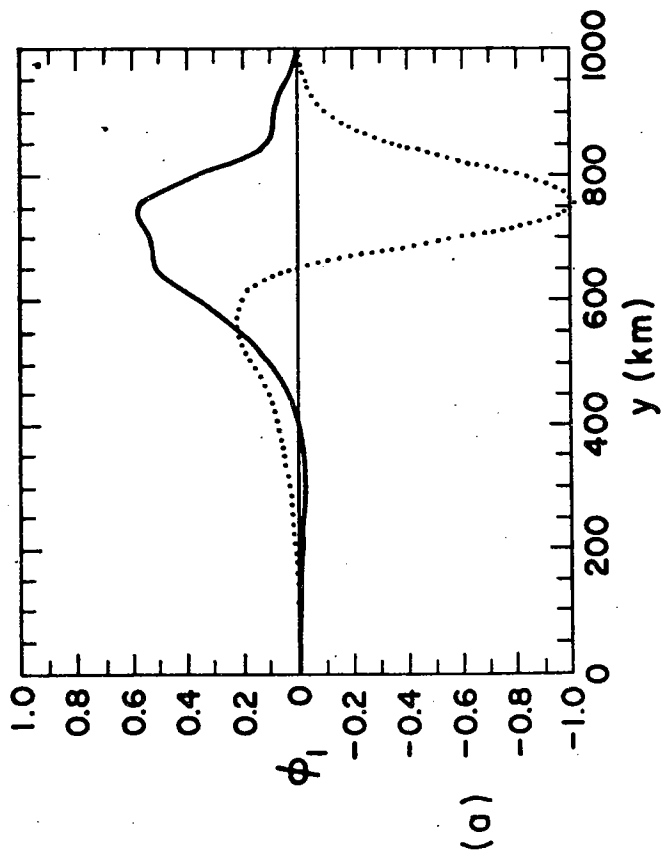
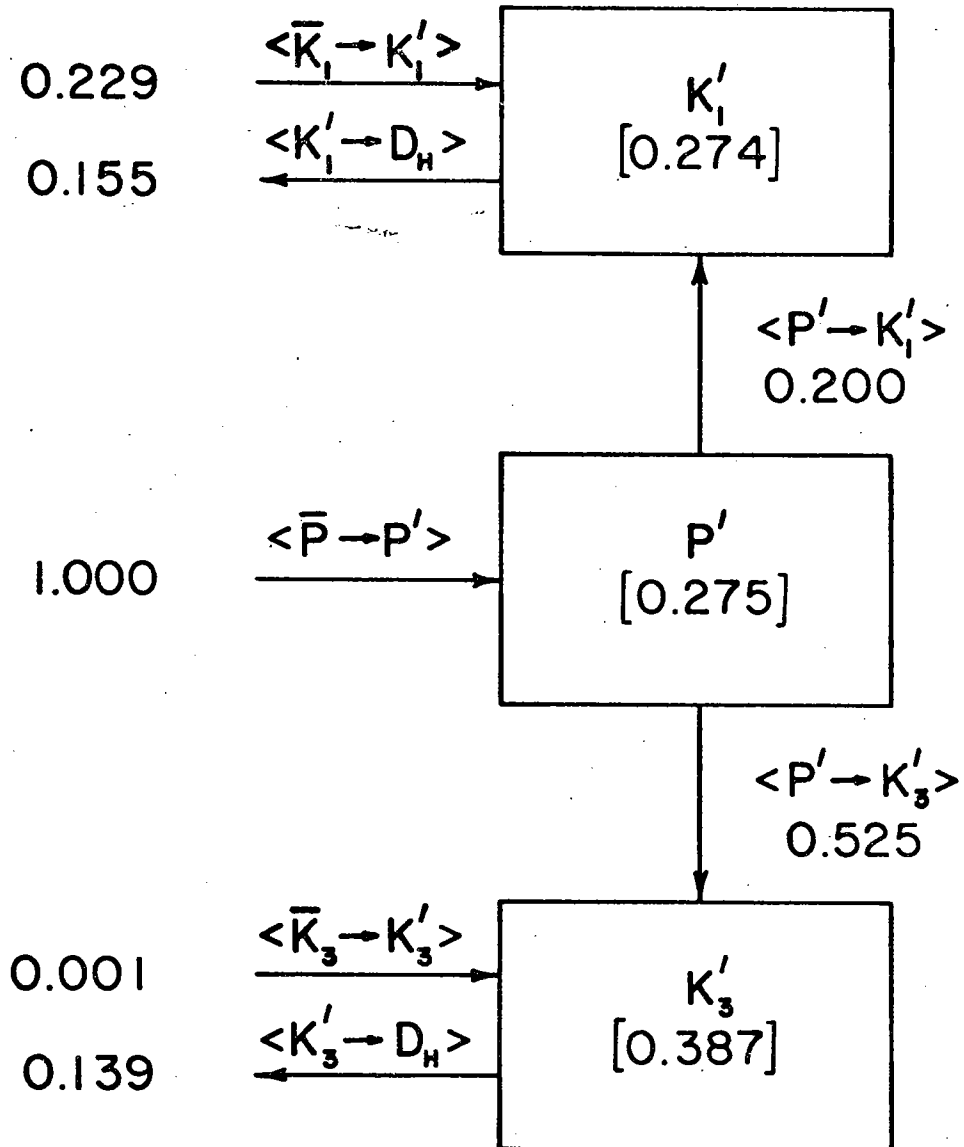


Table 4: The equilibrium eddy statistics from the four primary experiments as predicted by the linear stability analysis.

	E1 baroclinic	E2 baro- / baro- clinic / tropic		E2R baro- / baro- clinic / tropic	
wavelength (km)	370	350/470	420	390	350
period (days)	58	35/490	75	180	67
phase speed (cm sec ⁻¹)	7.4	-12/-0.51	7.9	-2.4	6.1
global energy transfer	baroclinic (FP1)	baro- tropic (FP2)	baro- clinic (FP1)	baro- tropic (FP2)	baro- tropic (FP1)

Figure 26: The normalized global energy budget for the growing perturbation of Figure 25.



growing eddies the energy fluxes to each eddy energy component need not sum to zero.) Individual plots of the energy flux terms as a function of y indicate the localness of the energy transfers (Figures 27 and 28); the band of baroclinic activity is $O(200 \text{ km})$ in width. The global and local fluxes have been normalized by their maximum values which are also listed in the figures. Since the E1 eddy energetics are dominated by this single localized region of instability, the corresponding LSA energy fluxes have the same spatial characteristics as the zonal eddy energy fluxes observed in the nonlinear simulation (Figure 29).

We would like, however, to be able to do better than just a prediction of the primary energy flux paths and their spatial distributions. How might we redimensionalize the predicted energy fluxes so as to provide a quantitative comparison to the experimental results? There are two possible methods. First, we could estimate the equilibrium amplitude of the eddies in E1 and, adopting a similar amplitude for the corresponding LSA eigenfunctions, determine the approximate magnitudes of the various flux terms. Second, we might try the converse tactic and nondimensionalize the global energy fluxes derived in E1; this is most easily accomplished by normalizing by the maximum flux value as we have already implicitly done for the LSA energy diagram. Both types of comparison are risky, however, because no matter how we make our estimates, we are always comparing an equilibrium energy diagram with an inherently non-equilibrium one. We can expect a correspondence between the two only in the fortuitous case that certain energy fluxes and/or paths remain essentially fixed during the onset and equilibrium

Figure 27: Normalized local energy fluxes for the growing perturbations of Figure 25.

Diagram	Flux	Maximum Value
(a)	$\langle \bar{K}_1 \rightarrow K_1' \rangle$	4.7×10^{10}
(b)	$\langle P' \rightarrow K_1' \rangle$	5.6×10^{10}
(c)	$\langle D_H \rightarrow K_1' \rangle$	3.1×10^{10}
(d)	$\langle \bar{K}_3 \rightarrow K_3' \rangle$	3.0×10^8
(e)	$\langle P' \rightarrow K_3' \rangle$	4.9×10^{10}
(f)	$\langle D_H \rightarrow K_3' \rangle$	1.8×10^{10}

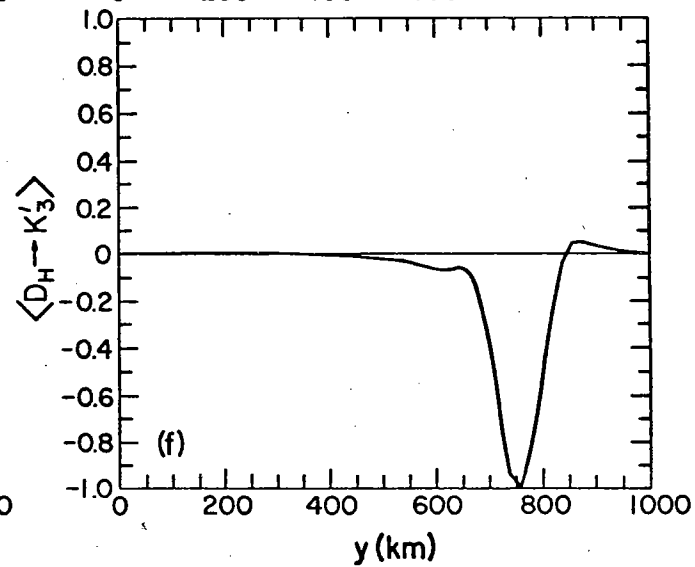
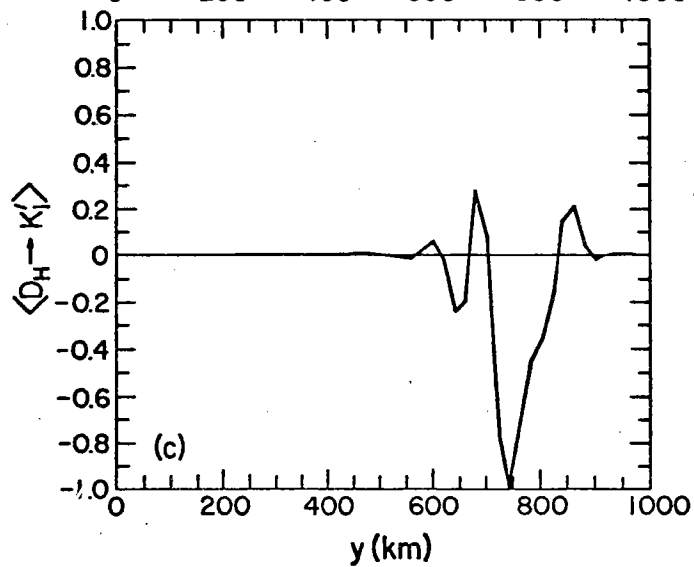
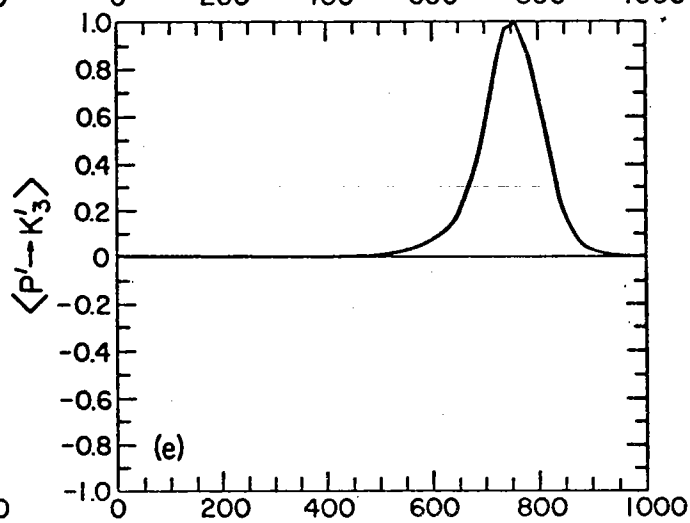
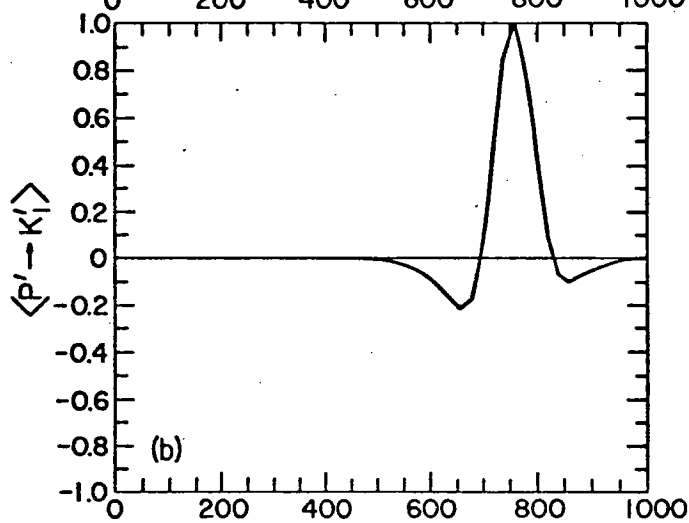
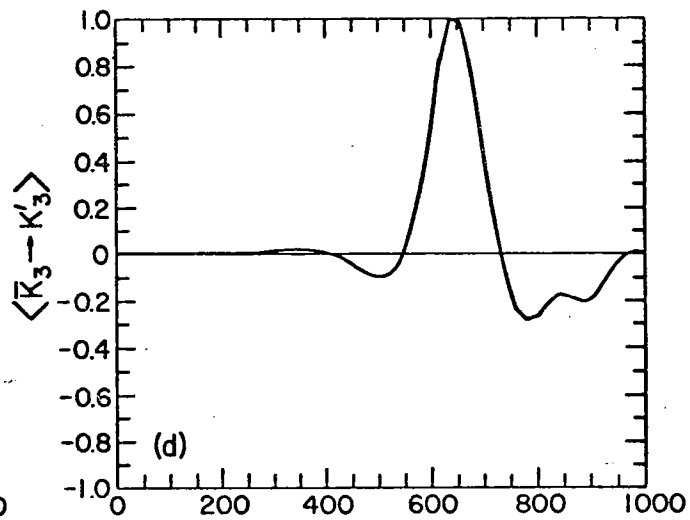
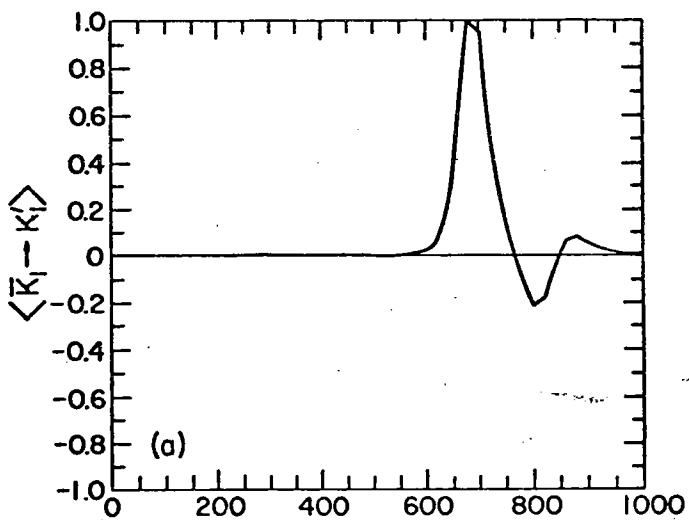


Figure 28: Normalized local energy fluxes for the growing perturbations of Figure 25.

Diagram	Flux	Maximum Value
(a)	Pressure Work on K_1'	2.7×10^{10}
(b)	Total Flux to K_1'	2.2×10^{10}
(c)	$\langle \bar{P} \rightarrow P' \rangle$	1.4×10^{11}
(d)	Pressure Work on K_3'	9.5×10^9
(e)	Total Flux to K_3'	2.2×10^{10}
(f)	Total Flux to P'	3.0×10^{10}

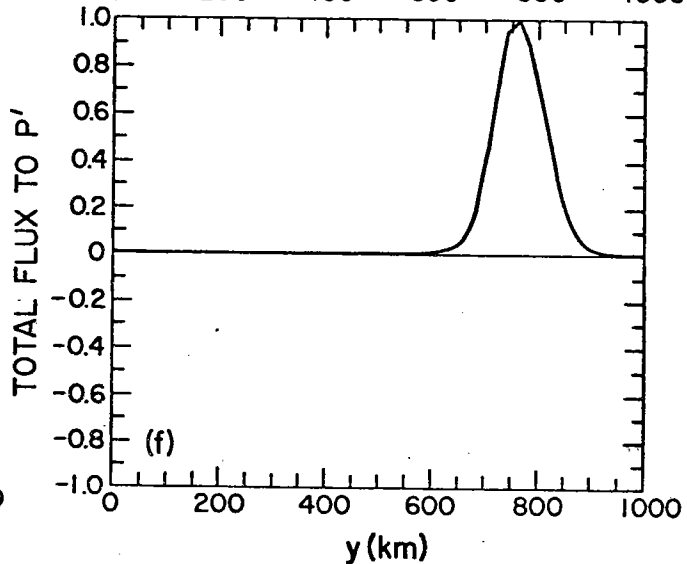
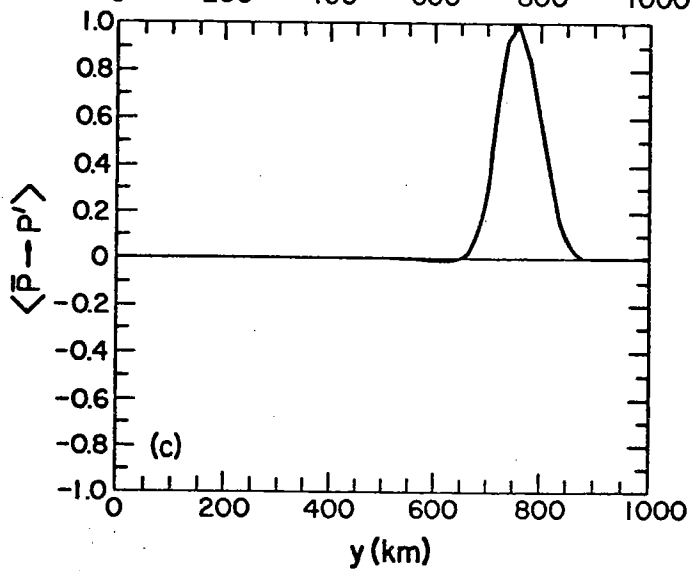
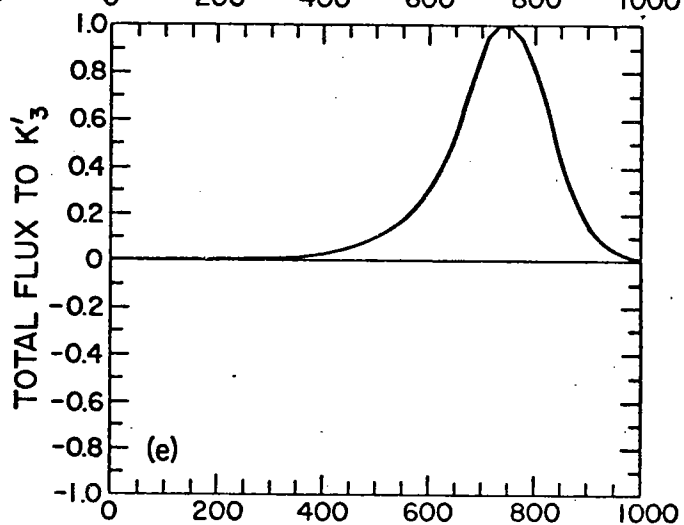
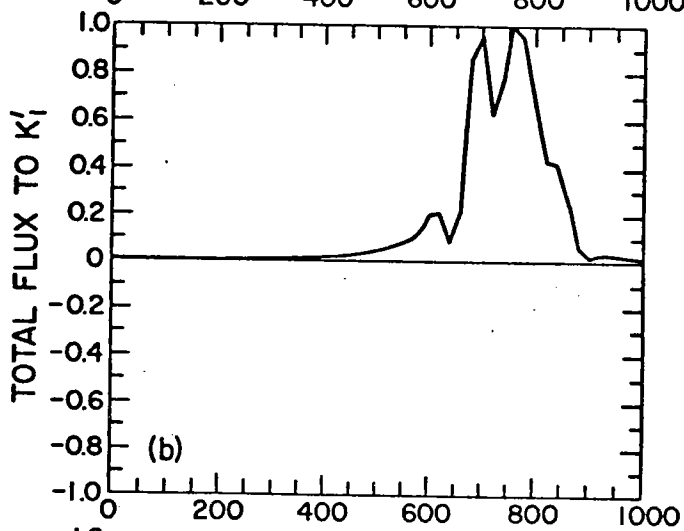
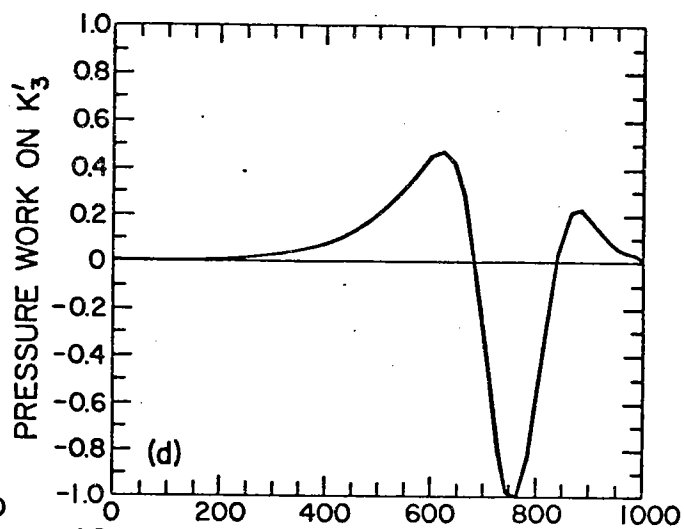
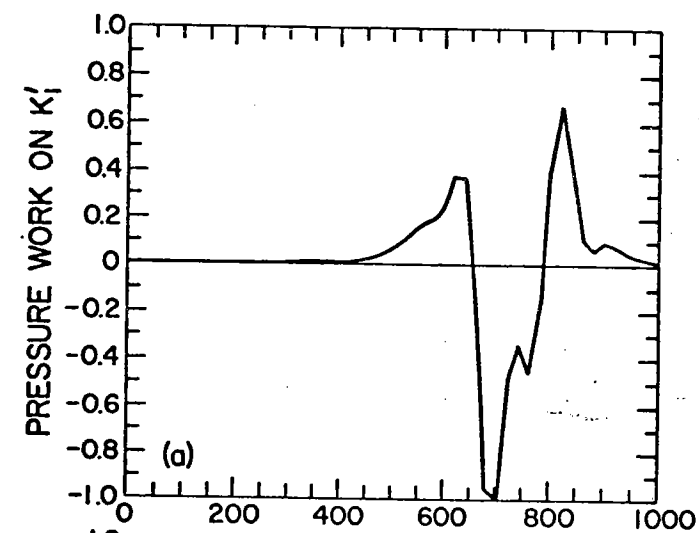
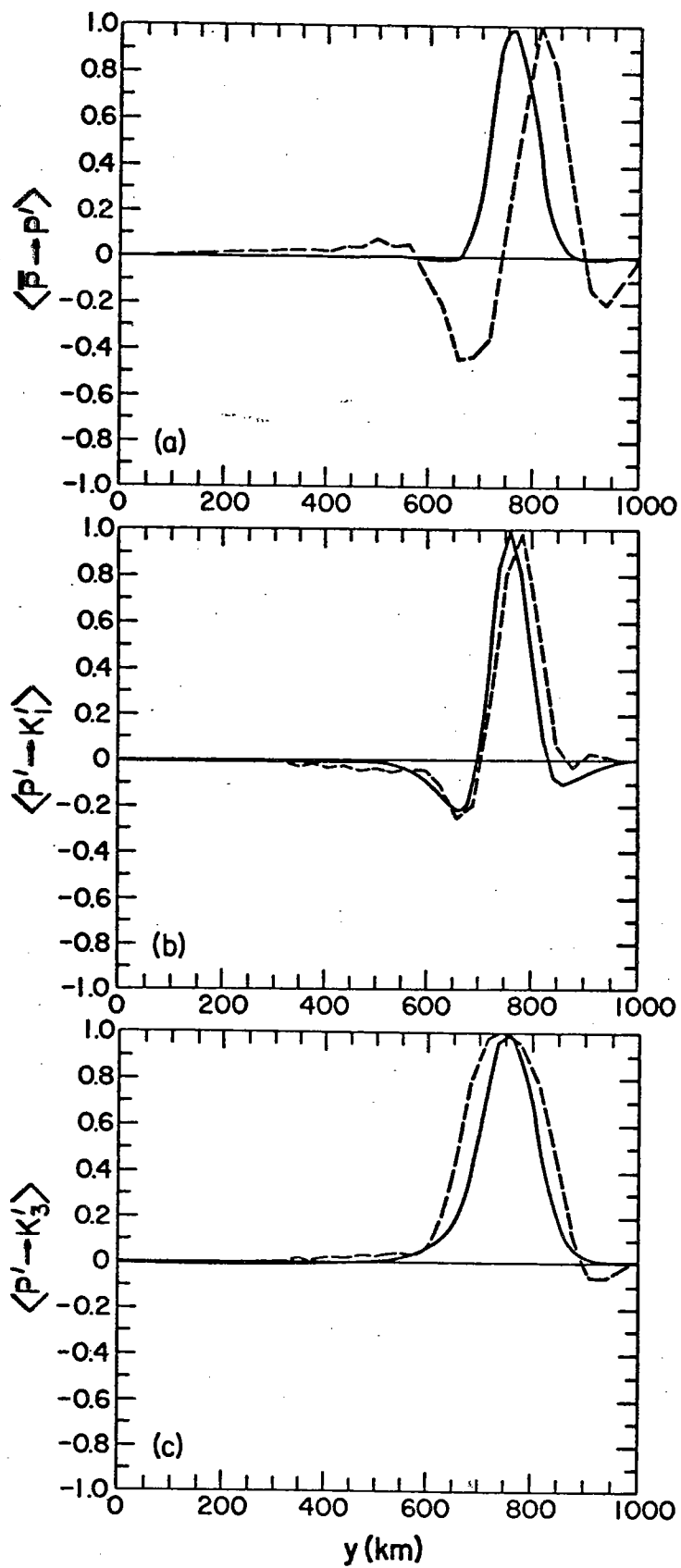


Figure 29: A comparison of the dominant energy fluxes from experiment 1 as observed in the nonlinear simulations (zonal average; dotted line) and as predicted by the linear stability analysis of the profile of Figure 25 (solid line).

(a) $\langle \bar{P} \rightarrow P' \rangle$.

(b) $\langle P' \rightarrow K_1' \rangle$.

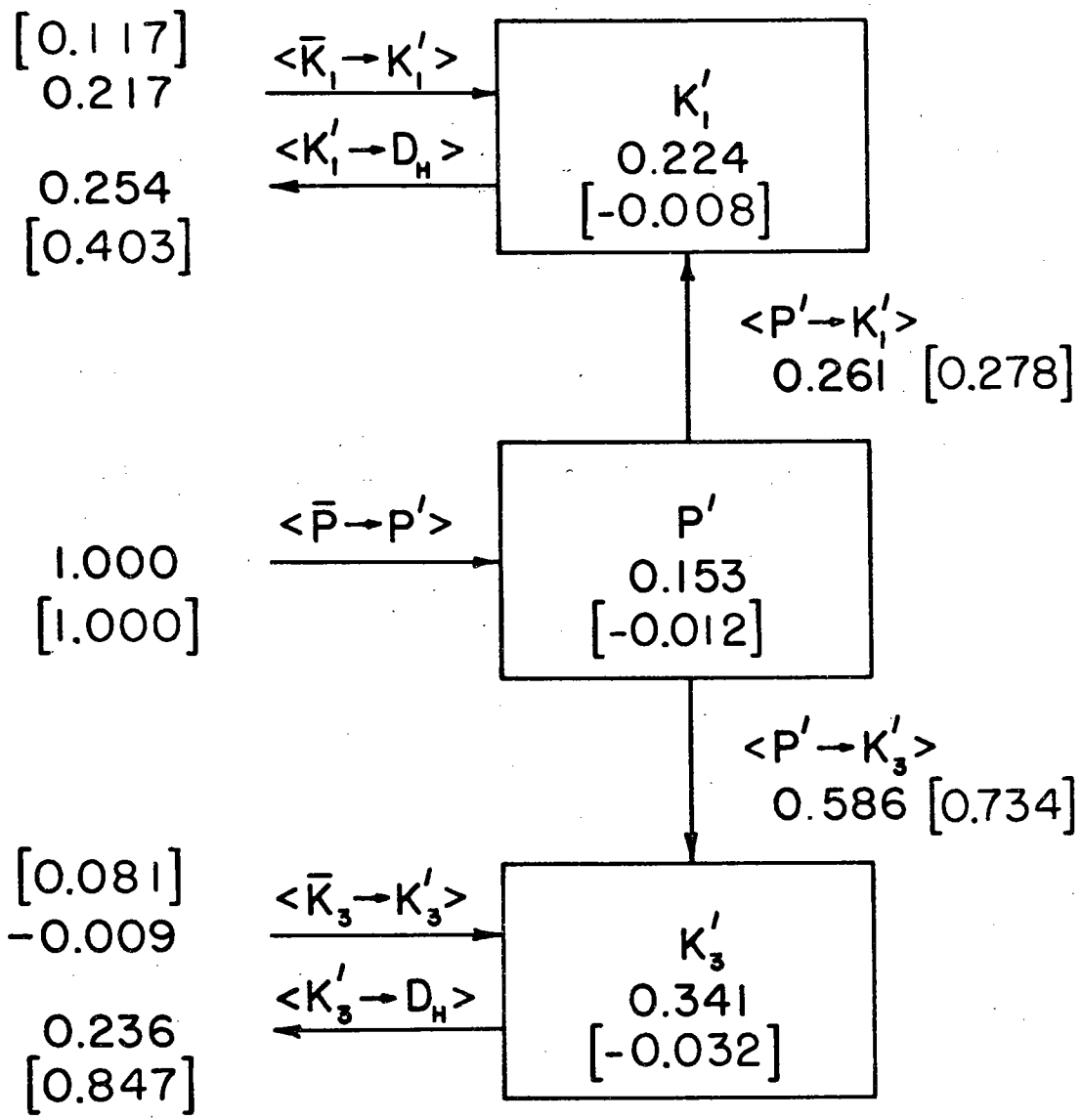
(c) $\langle P' \rightarrow K_3' \rangle$.



phases of these experiments, or, equivalently, where the infinitesimal eddies maintain their structural features as they grow to finite amplitude. There is no reason a priori why this should be true, but with this proviso we proceed to attempt such quantitative comparisons.

Figure 30 shows the normalized energetics derived from an average over five El instantaneous profiles taken 10 days apart (thus covering approximately one eddy cycle) along $x = 500$ km. By assigning to the eigenfunctions an estimate of the eddy amplitude in El over this interval ($\phi_1 = \phi_3 = 4.5 \times 10^7$), we redimensionalize the $\langle \bar{P} \rightarrow P' \rangle$ transfer and get an energy transfer estimate of one erg/cm²/sec. This is too high, in comparison to Figure 8, by a factor of nearly four but the extension of the $x = 500$ km (local) cascade rates uniformly across the basin, an assumption of zonal uniformity, is overly optimistic; actually, $x = 500$ km is a longitude of unusually high activity and some geometric factor of 0(1/2) can be reasonably applied to the LSA energy fluxes to account for lateral inhomogeneities. With this correction, the comparison of the linearized perturbation energy flux $\langle \bar{P} \rightarrow P' \rangle$ to the results of experiment 1 is within a factor of perhaps two. This is a first indication that some of the primary energy transfers from mean to eddy field established during the onset phase may be insensitive to the approach of the system to equilibrium. Adopting our second strategy, let us normalize the El global energy fluxes by the $\langle \bar{P} \rightarrow P' \rangle$ value (Figure 8), producing flux ratios comparable to those associated with the predicted linear modes (Figure 30). Again, we are left with the impression that certain flux ratios, most notably $\frac{\langle P' \rightarrow K'_1 \rangle}{\langle \bar{P} \rightarrow P' \rangle}$, may remain invariant during the establishment of the eddy field. The

Figure 30: A mean normalized global energy budget for the baroclinic instabilities of experiment 1 as predicted by LSA (average over five baroclinic modes). The numbers in brackets are the equivalent flux ratios derived from the experiment 1 global energy diagram (Figure 8) by dividing by $\langle \bar{P} \rightarrow P' \rangle$.



generality of this relationship remains to be established.

It is clear, however, that the predictions of the LSA compare favorably with the exact statistics of the E1 mesoscale field. Growth rates, space and time scales, spatial distribution of eddies, and energy fluxes have been shown to be quantitatively as well as qualitatively accurate. However, E1 is not an overly complex situation. A north-south section through its instantaneous velocity field actually satisfies our assumption of two-dimensionality quite well.¹ A more severe test of the applicability of the LSA will be its accuracy in predicting the statistics of more disordered eddy fields such as those of E2 and E2R.

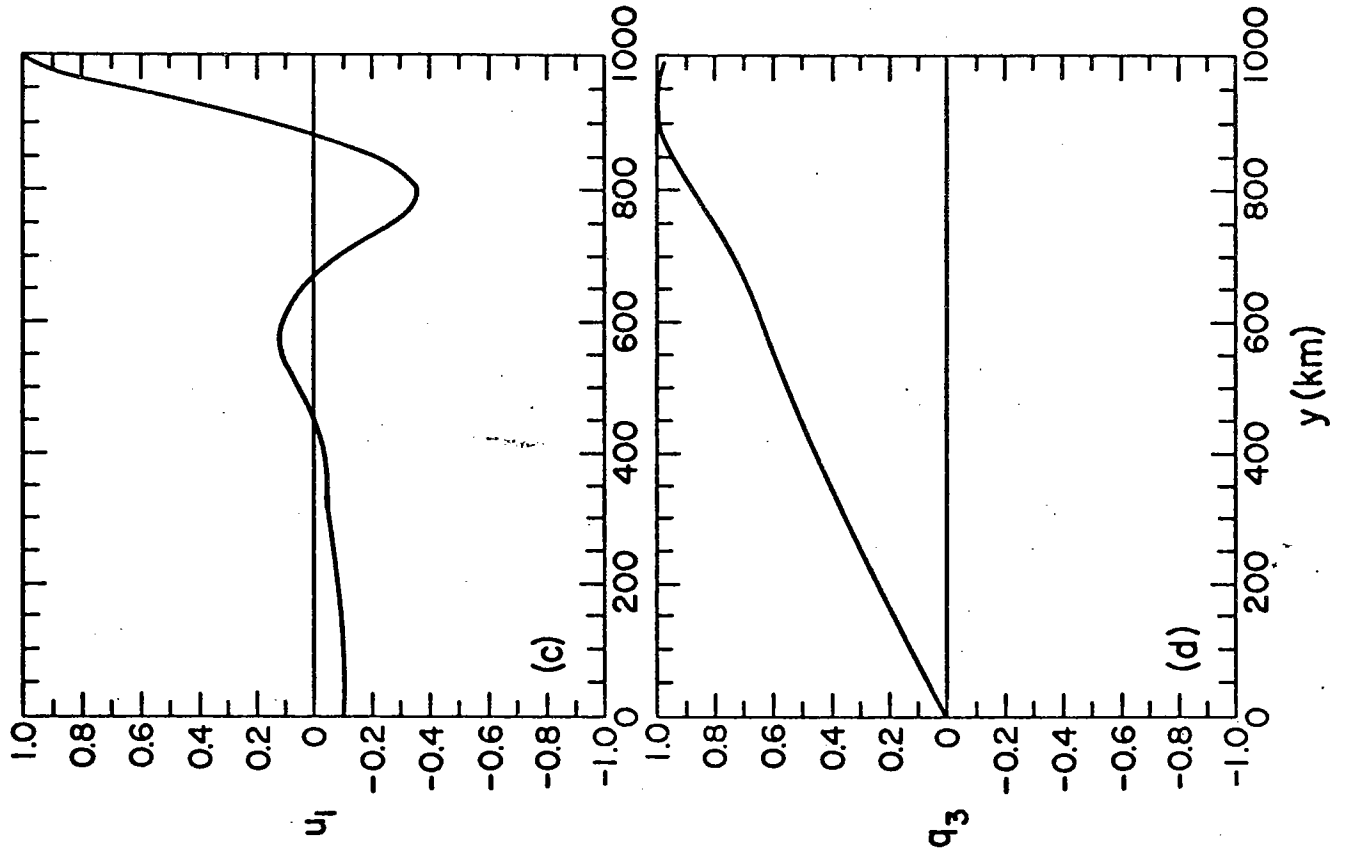
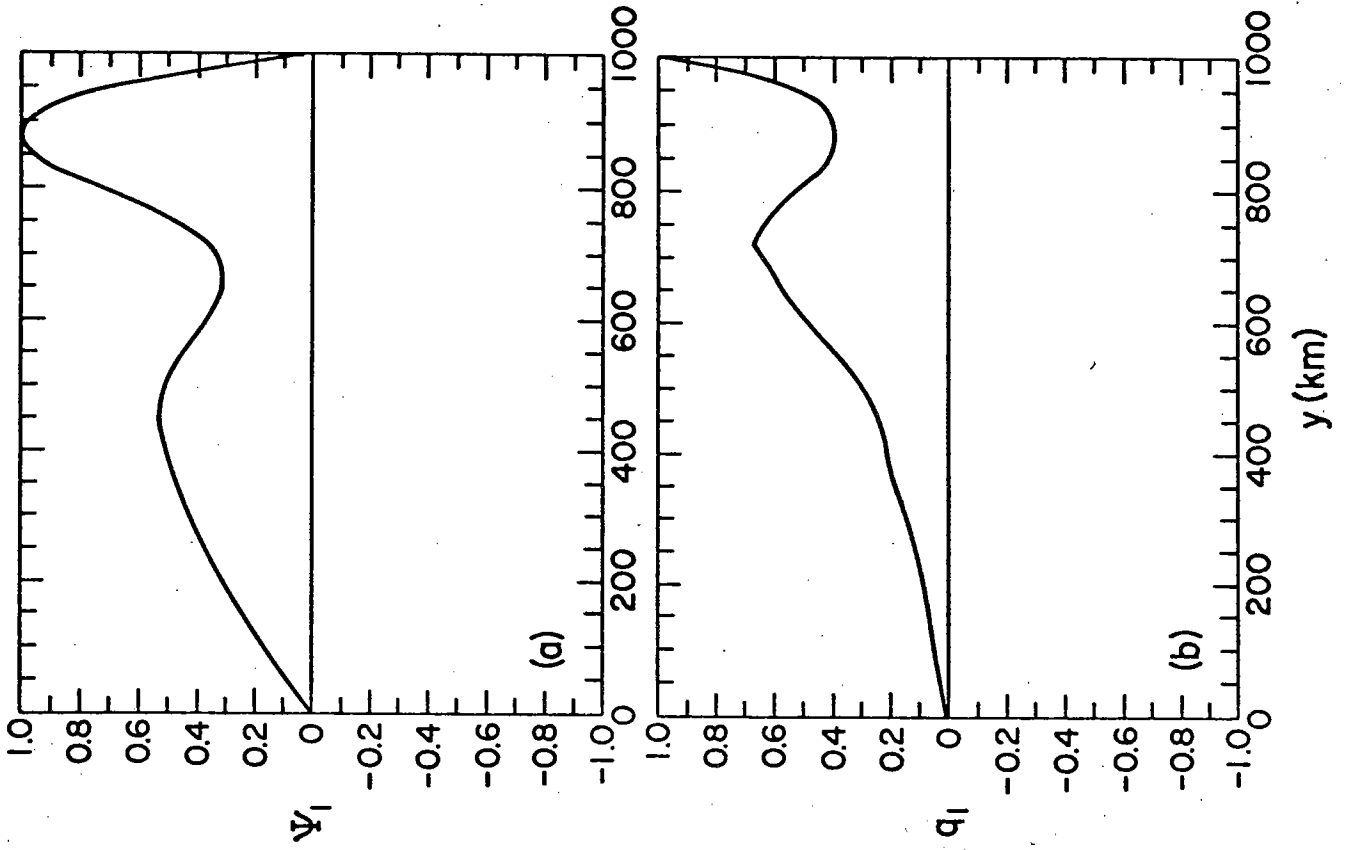
¹When corrections for path curvature are made to the stability analysis of E1, the predictions are altered by less than 5%.

(VI.2) A stability analysis of experiment 1R

As we have noted, the north-south profiles of E1R are nearly identical in structure to those from E1 (Figures 24 and 31). Why then is the equilibrium phase of E1R identified by a stable rather than eddy-ing state? The answer lies in the observation that a sufficient reduction in vertical shear will always stabilize a frictional baroclinic flow. A diminution in the maximum upper level velocity by only 30% will stabilize E1 for example (Figure 21). Such an explanation is clearly indicated in E1R where western boundary layer dissipation has reduced the estimated shear by 31%, or just enough to preclude the unstable growth of small perturbations. For a slightly higher characteristic velocity, the E1R westward return flow would presumably be the site of a mesoscale eddy field comparable to that in E1. In this sense, and as E2 and E2R will demonstrate, rigid boundaries, in the flat bottom limit, impose only weak constraints on the interior.

Figure 31: Profile AA' from experiment 1R, Figure 11.

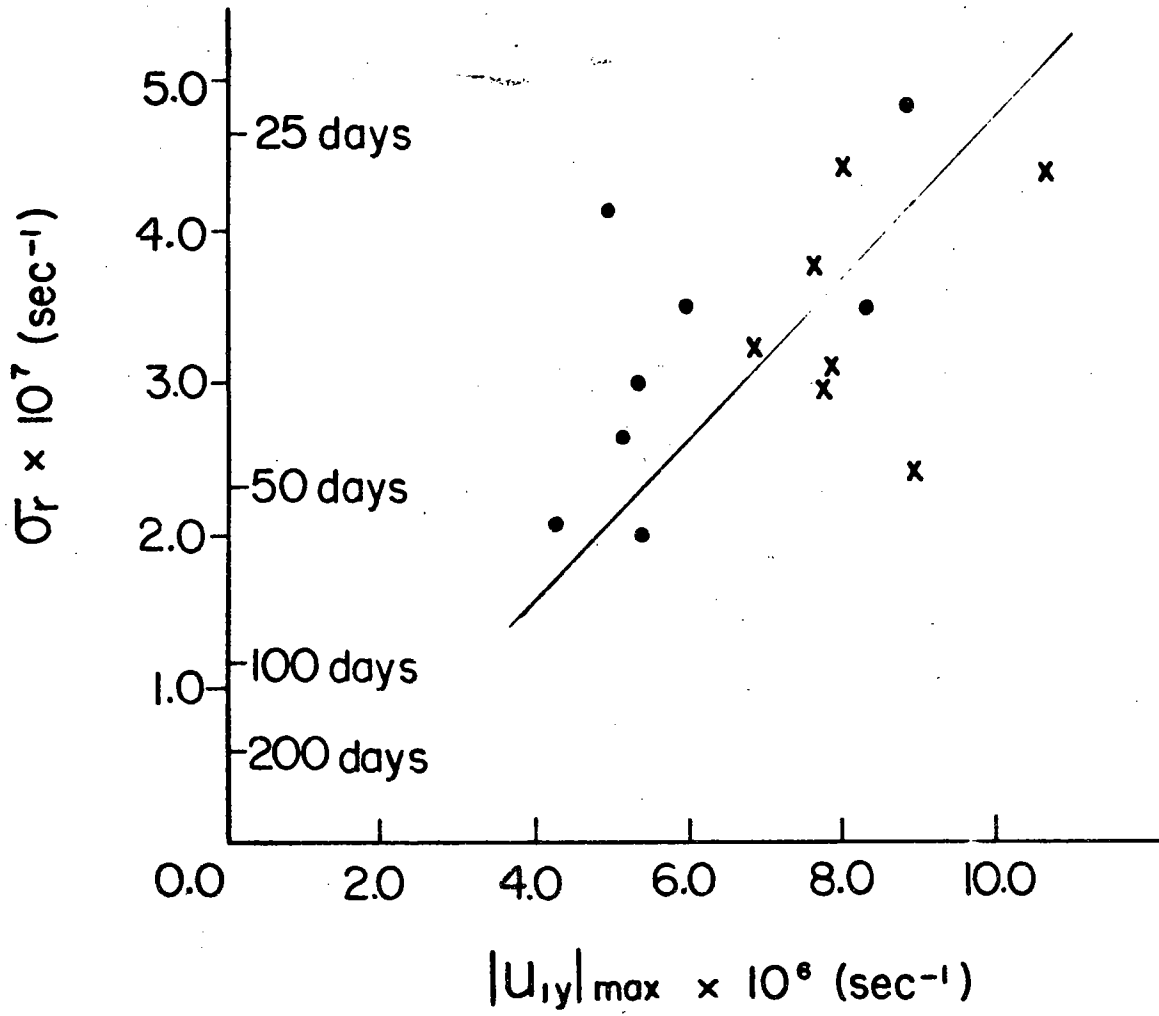
- (a) upper level streamfunction ($|\psi_1|_{\max} = 2.2 \times 10^8$).
- (b) upper level potential vorticity ($|q_1|_{\max} = 2.0 \times 10^{-5}$).
- (c) upper level velocity ($|u_1|_{\max} = 33.1$).
- (d) lower level potential vorticity ($|q_3|_{\max} = 2.0 \times 10^{-5}$).



(VI.3) A stability analysis of experiment 2

The qualitative behavior of the E2 equilibrium fields suggest that at least three instabilities are periodically or continuously active; one barotropic mode in the eastward flowing internal jet, and two baroclinic modes symmetrically disposed in the westward return flows. One of the tests of the LSA, therefore, will be whether or not it can resolve these distinct regions of instability and hence prove to be capable of a truly local analysis. Since the E2 global energetics are dominated by the FP2 energy flux pathway, we know that the barotropic conversion process is the most intense overall; it should be readily distinguishable in almost any profile that transects the internal jet. Surprisingly, however, when a variety of profiles similar to that proposed in (VI.1) were examined for experiment 2, barotropic instabilities could not be detected from any mean velocity profile; only for an instantaneous velocity record did the barotropic mode appear. The associated growth rates depend sensitively, with a certain amount of scatter, on horizontal shear values (Figure 32). (Vertical shear was the crucial environmental parameter in the case of the baroclinic mode.) Thus, the meandering of the internal jet, itself indicative of the presence of the finite-amplitude eddies, tends in the mean to smear out the streamfunction field in the same way as the envelope of the Gulf Stream paths is much broader than any individual trajectory. Our inability to detect the presence of barotropic instabilities from a mean profile is a direct result of this smearing action. The instability acts on the mean flow to weaken the set of conditions which originally favored the instability and ultimately to limit the finite amplitude of the eddies.

Figure 32: The variation with horizontal shear of the growth rate of the barotropic modes observed in experiment 2. The modes denoted by x's were determined from instantaneous profiles taken 600 days later than those used to determine the dotted points(•). The residual differences in the instability properties of the two sets of points indicates that either we have not, as yet, quite attained equilibrium or that there are very long period processes at work in this simulation.



For a representative E2 example, we choose transect AA' through the instantaneous streamfunction fields pictured in Figure 33; the associated profiles are replotted for convenience in Figure 34. The quasisymmetry of the upper level velocity about the mid-latitude (Figure 34b) stands out, with the central jet and two westward recirculations being highly prominent features. The most unstable mode corresponding to this zonal representation of the instantaneous flow occurs in the eastward current as expected (Figure 35). The eddies are distinctly barotropic in both phase relationship (35b, d) and energy transfer characteristics (Figure 36) which now favor the $\langle \bar{K}_1 \rightarrow K'_1 \rangle$ cascade. In general, the growth rates of the instantaneous barotropic modes are predicted to be quite large; Figure 32 suggests a mean e-folding time less than 50 days. This is consistent with the vigorous meandering observed during the course of E2. The individual energy flux profiles demonstrate that narrow, highly structured transfers are involved in the barotropic instability process (Figures 37-38). Note that the LSA predicts the existence of two separate barotropic modes of widely separated scales (Table 4). The long-period barotropic instability may well account for long-term trends observed in the E2 global energy statistics.

The barotropic mode is not, however, the only instability predicted for the Figure 34 profile. LSA also reveals baroclinic activity in the northern branch of the westward return flow (Figure 39). Its growth time, 0(75 days), is much greater than that of the barotropic mode, but the phase and energy flux relationships indicative of baroclinic instability are again present (Figures 39 and 40). The individual energy flux profiles are similar to those of the E1 baroclinic mode and need not be

Figure 33: Representative instantaneous fields from experiment 2.
(a) upper layer streamfunction (contour interval = 4.0 Sverdrups).
(b) lower layer streamfunction (contour interval = 8.0 Sverdrups).
Profile AA' is replotted in Figure 34. Lows (L) and highs (H) indicate cyclonic and anticyclonic flow respectively.

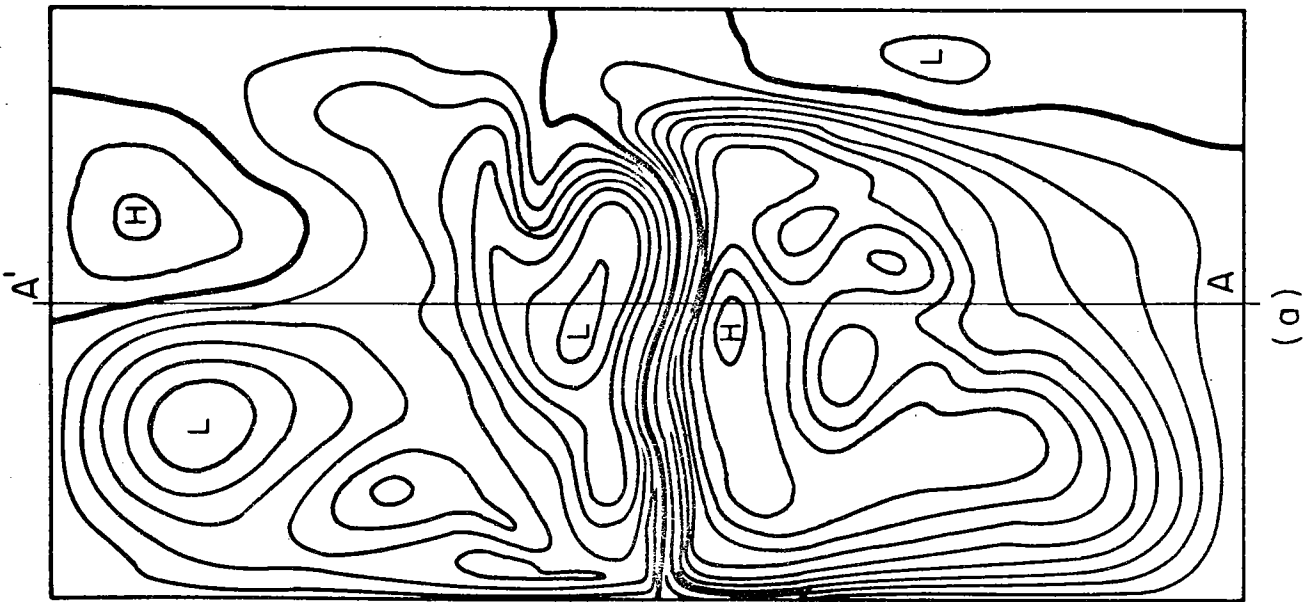
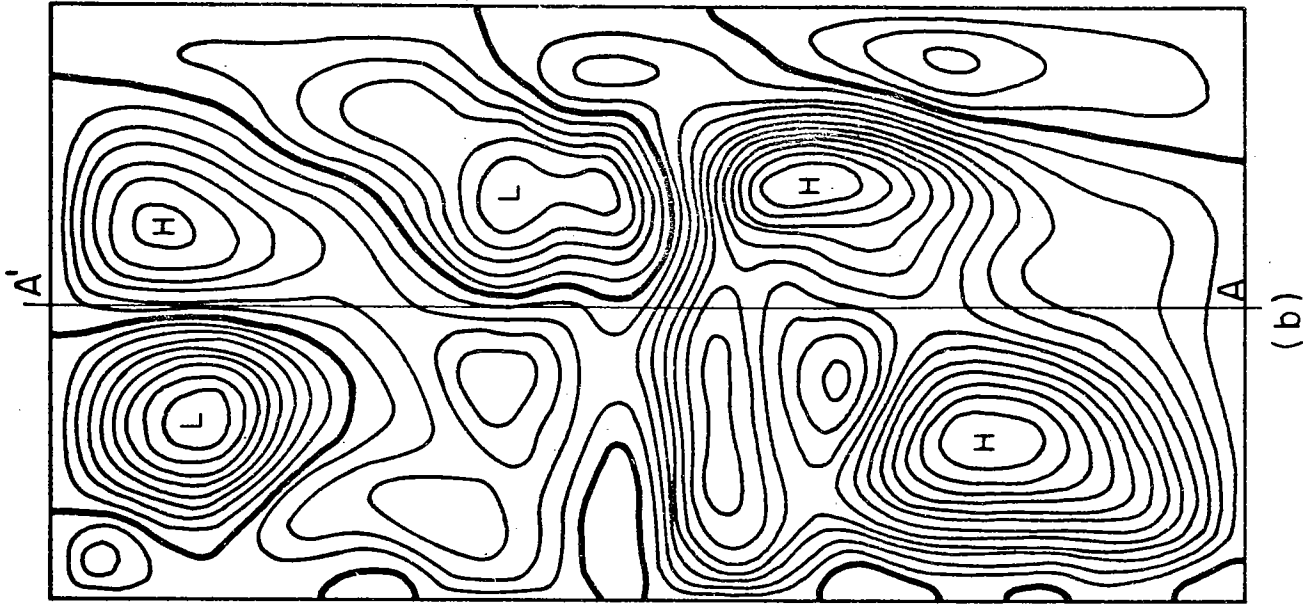


Figure 34: Profile AA' from experiment 2, Figure 33.

- (a) upper layer streamfunction ($|\psi_1|_{\max} = 4.1 \times 10^8$).
- (b) upper layer velocity ($|u_1|_{\max} = 53.0$).
- (c) upper layer potential vorticity ($|q_1|_{\max} = 4.0 \times 10^{-5}$).
- (d) lower layer streamfunction ($|\psi_3|_{\max} = 1.4 \times 10^8$).
- (e) lower layer velocity ($|u_3|_{\max} = 9.8$).
- (f) lower layer potential vorticity ($|q_3|_{\max} = 4.0 \times 10^{-5}$).

Maximal instability occurs at $y = 980$ km (barotropic) and $y = 1230$ km (baroclinic).

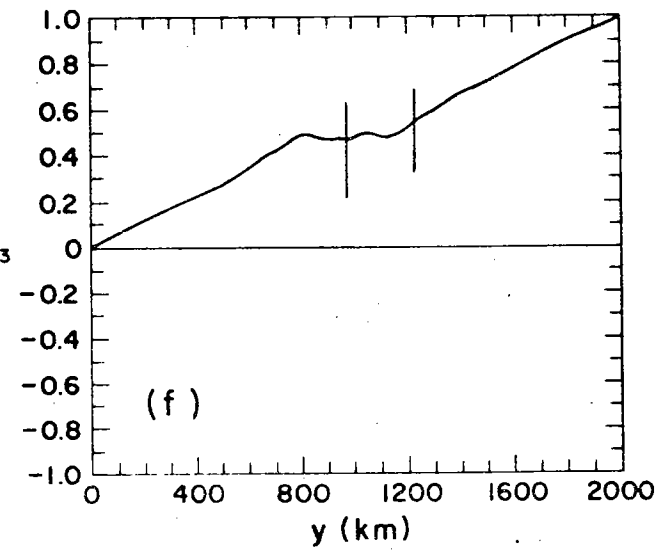
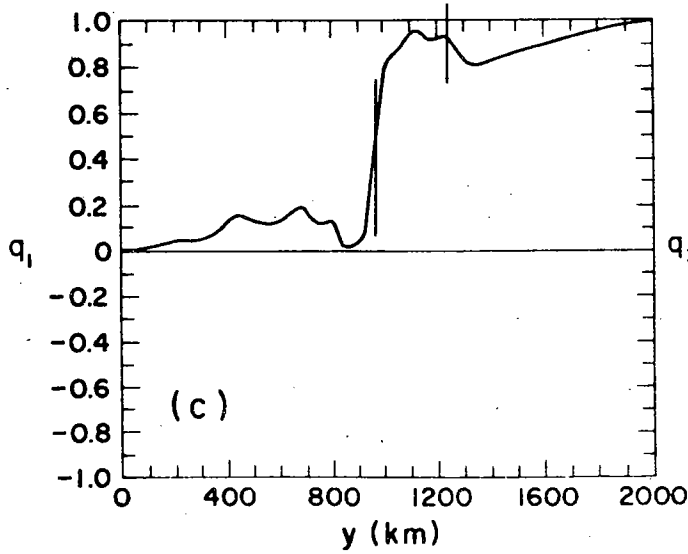
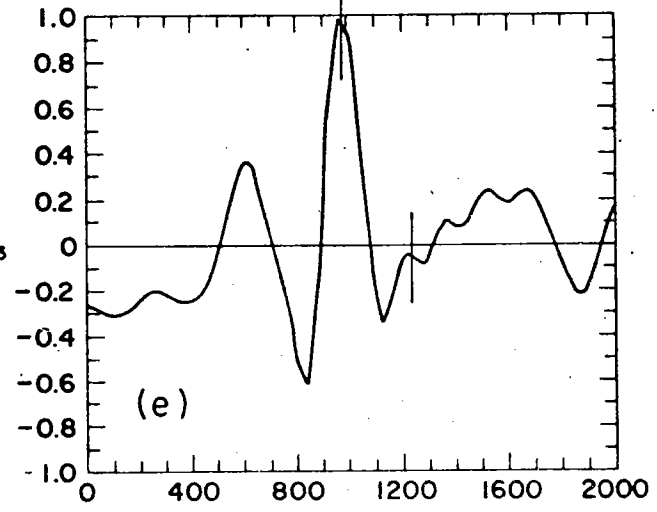
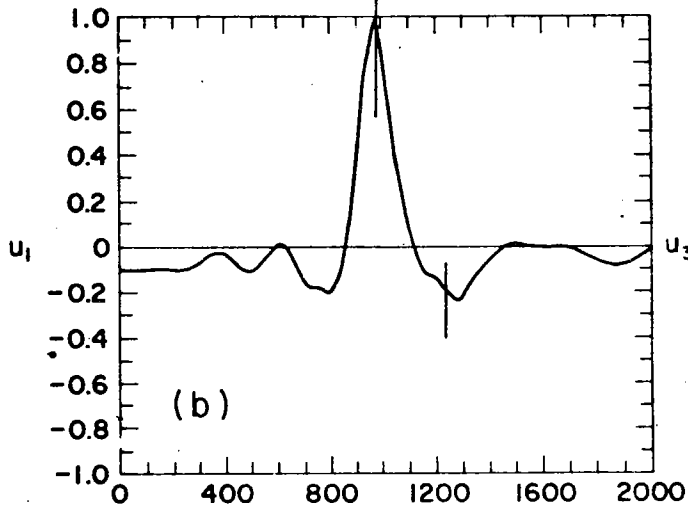
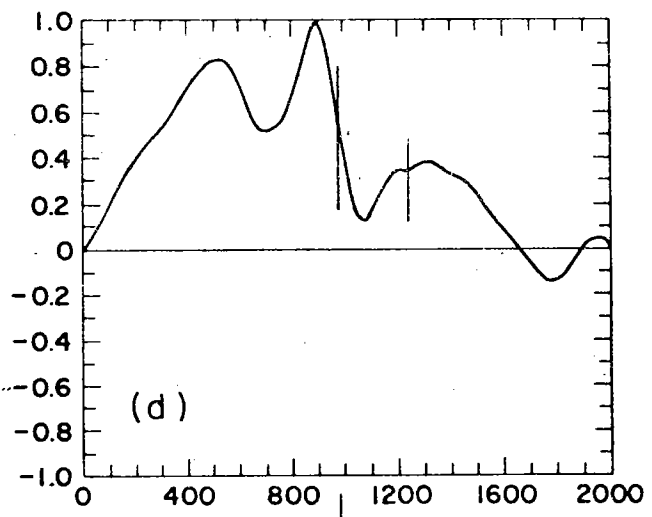
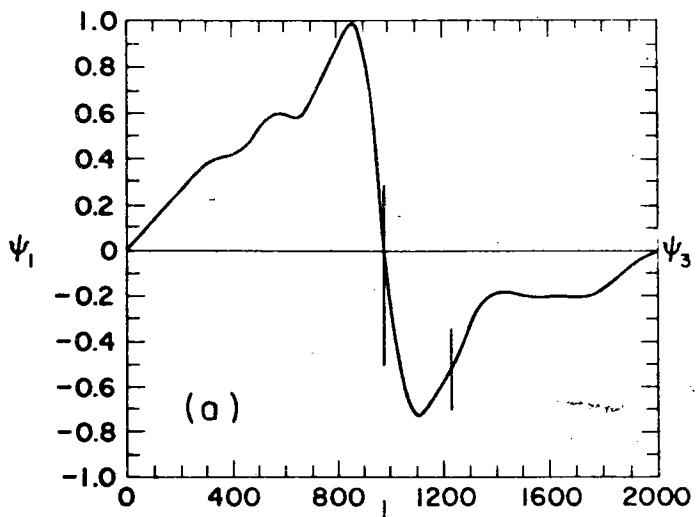


Figure 35: The most unstable barotropic mode corresponding to profile AA', Figures 33 and 34.
(a,c) the complex upper and lower layer eigenfunctions ($\text{Re}\phi$ solid, $\text{Im}\phi$ dotted).
(b,d) the real part of the unstable modes with the x -dependence reintroduced.
Lines have been drawn along $x = 560$ km to indicate the phase relationship between the upper and lower layer eddies.

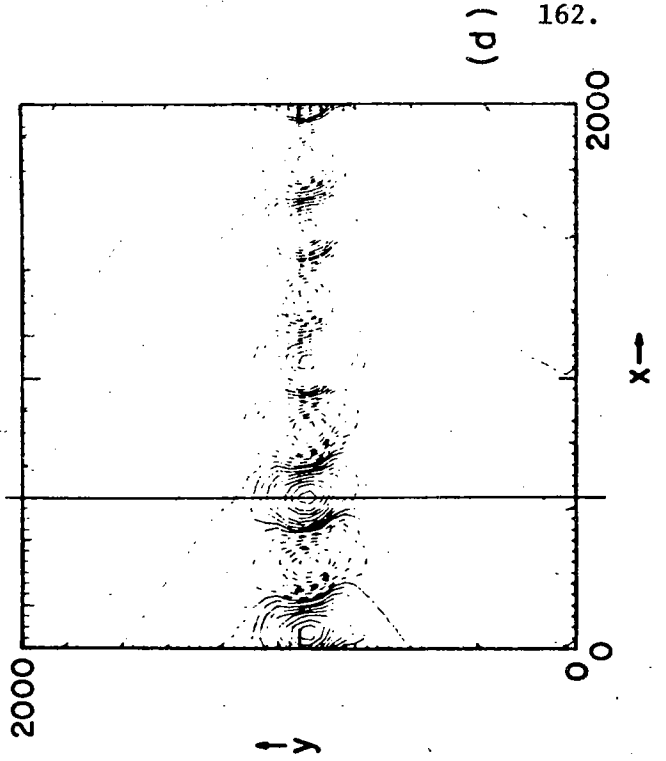
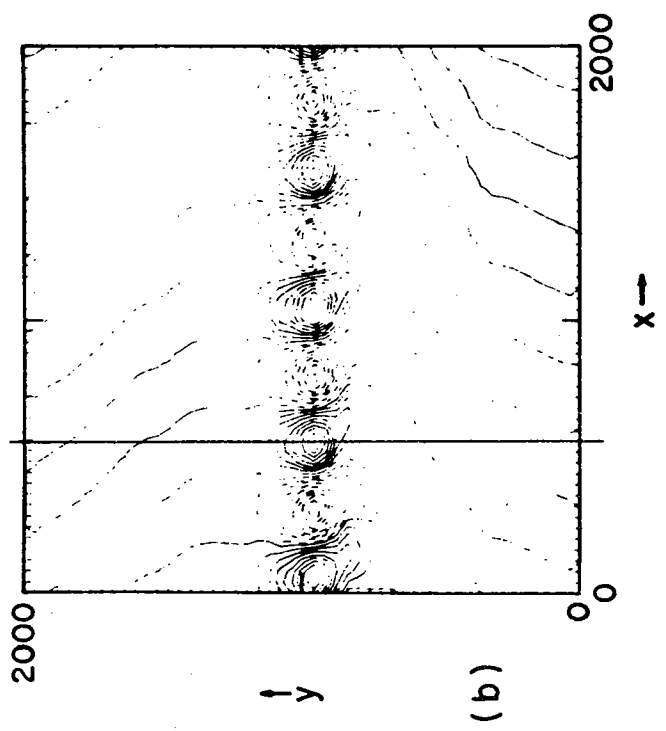
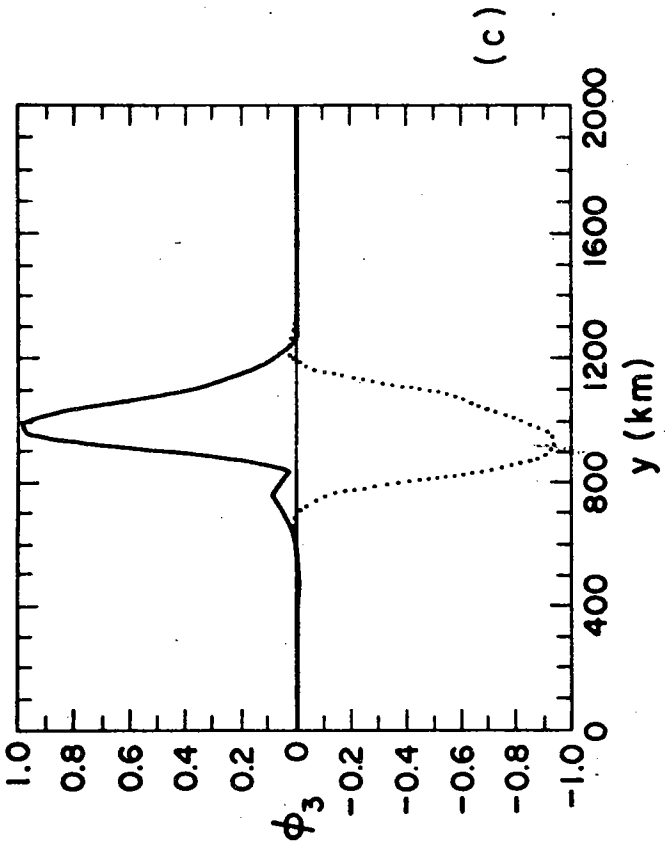
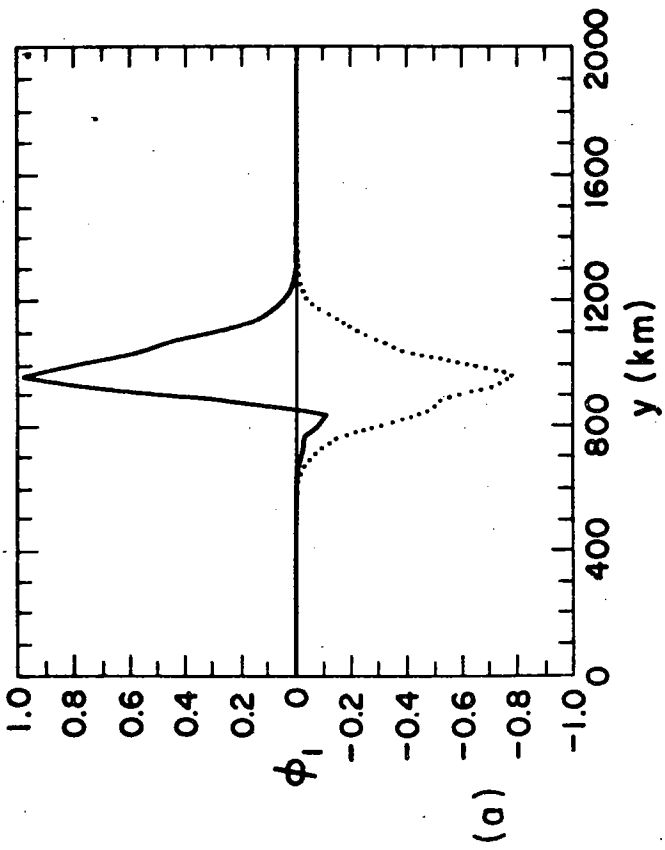


Figure 36: The normalized global energy budget for the growing perturbations of Figure 35.

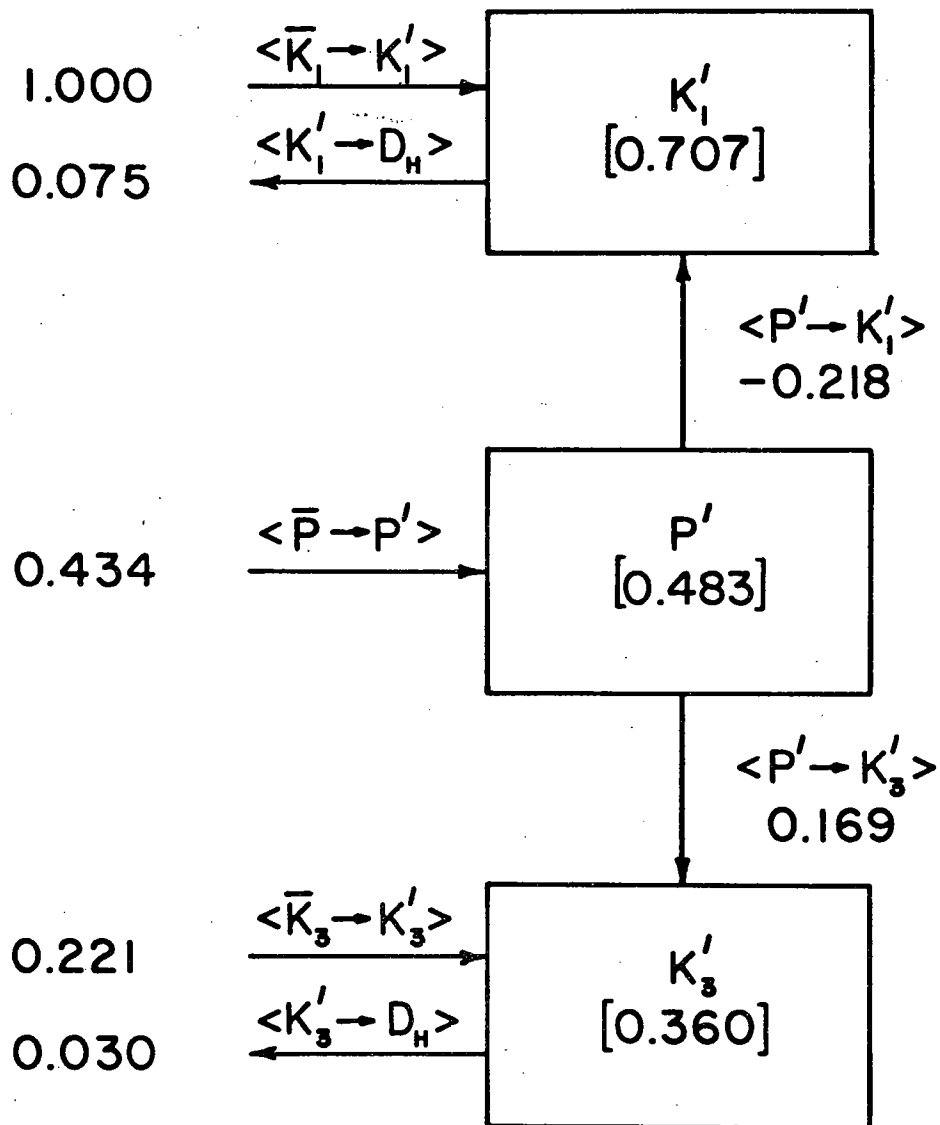


Figure 37: Normalized local energy fluxes for the growing perturbations of Figure 35.

Diagram	Flux	Maximum Value
(a)	$\langle \bar{K}_1 \rightarrow K_1' \rangle$	1.9×10^{12}
(b)	$\langle P' \rightarrow K_1' \rangle$	2.4×10^{11}
(c)	$\langle D_H \rightarrow K_1' \rangle$	2.5×10^{11}
(d)	$\langle \bar{K}_3 \rightarrow K_3' \rangle$	3.1×10^{11}
(e)	$\langle P' \rightarrow K_3' \rangle$	1.5×10^{11}
(f)	$\langle D_H \rightarrow K_3' \rangle$	2.8×10^{10}

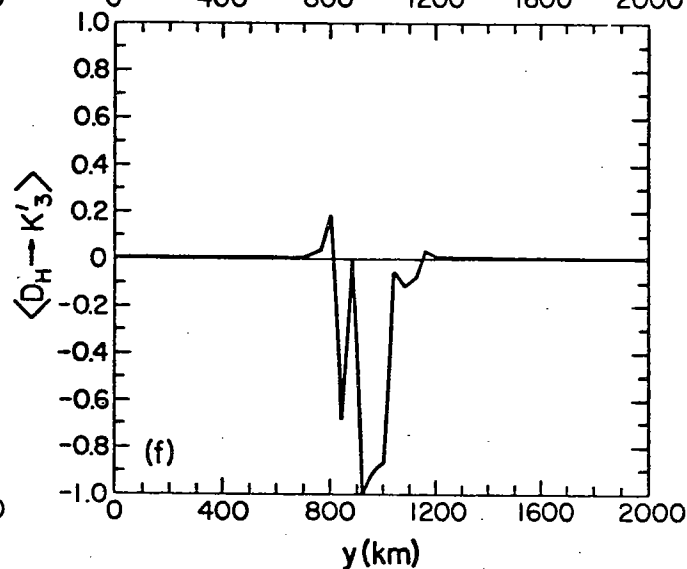
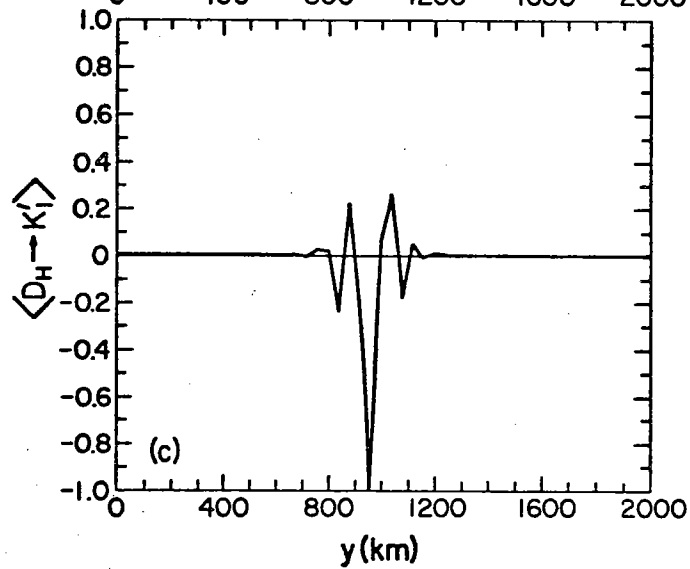
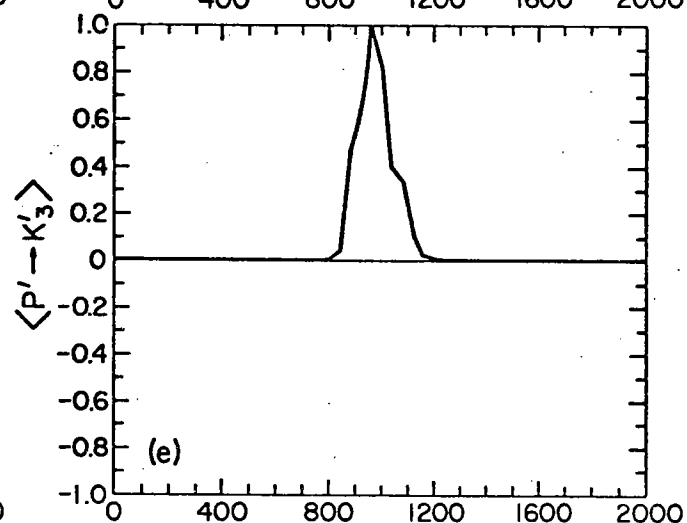
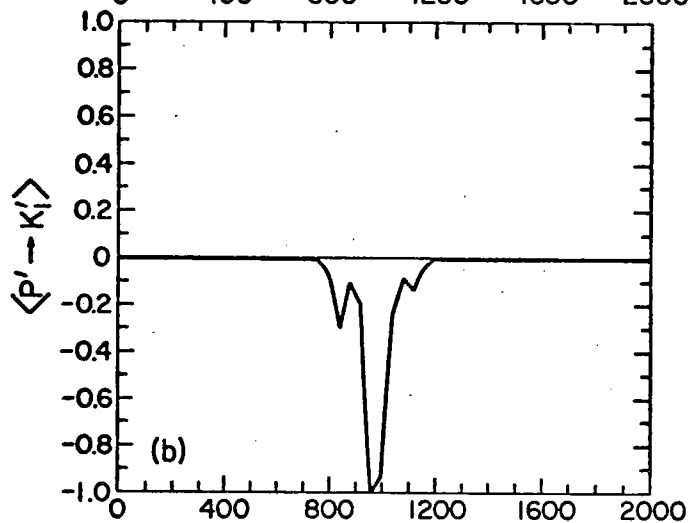
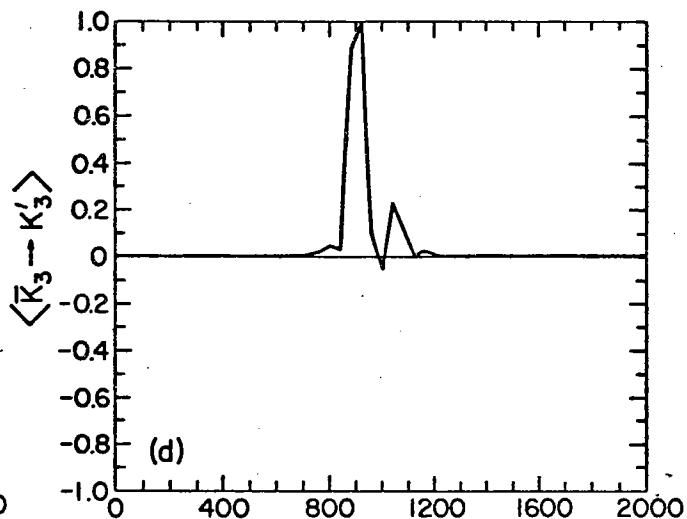
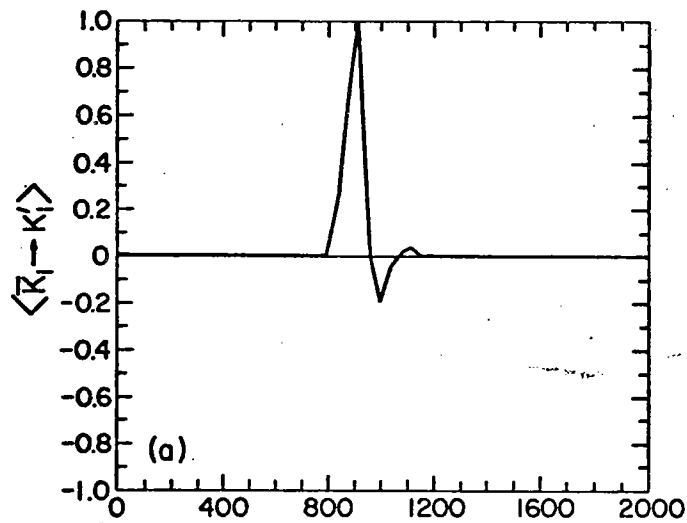


Figure 38: Normalized local energy fluxes for the growing perturbations of Figure 35.

Diagram	Flux	Maximum Value
(a)	Pressure Work on K_1'	1.0×10^{12}
(b)	Total Flux to K_1'	1.1×10^{12}
(c)	$\langle \bar{P} \rightarrow P' \rangle$	4.9×10^{11}
(d)	Pressure Work on K_3'	1.6×10^{11}
(e)	Total Flux to K_3'	2.2×10^{11}
(f)	Total Flux to P'	5.8×10^{11}

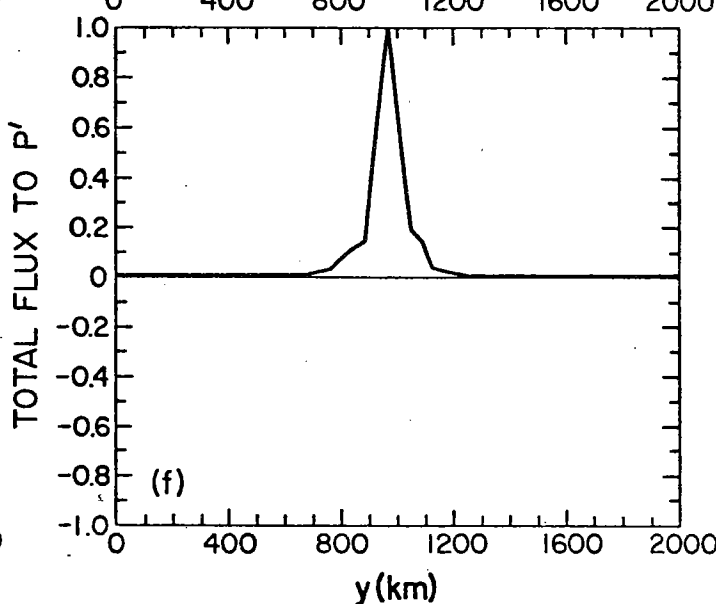
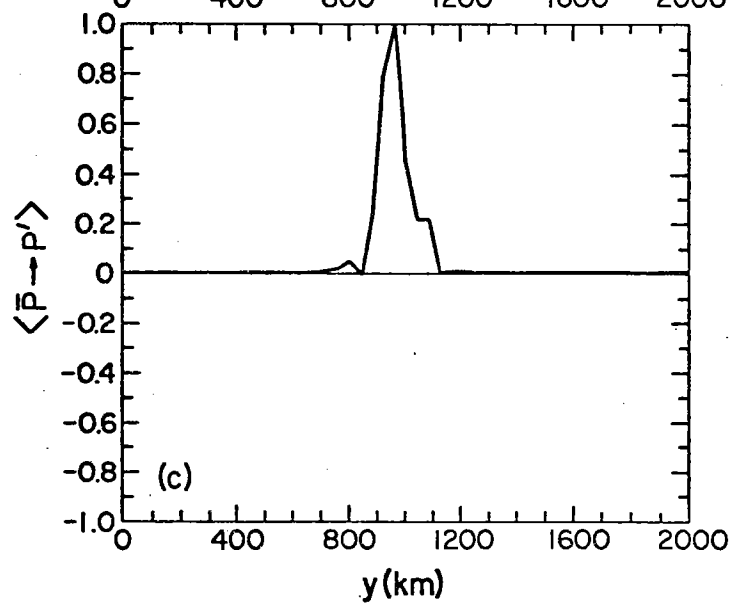
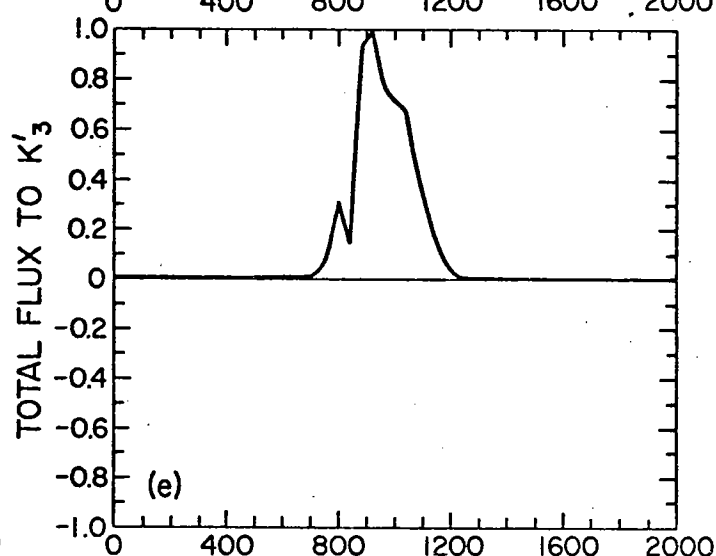
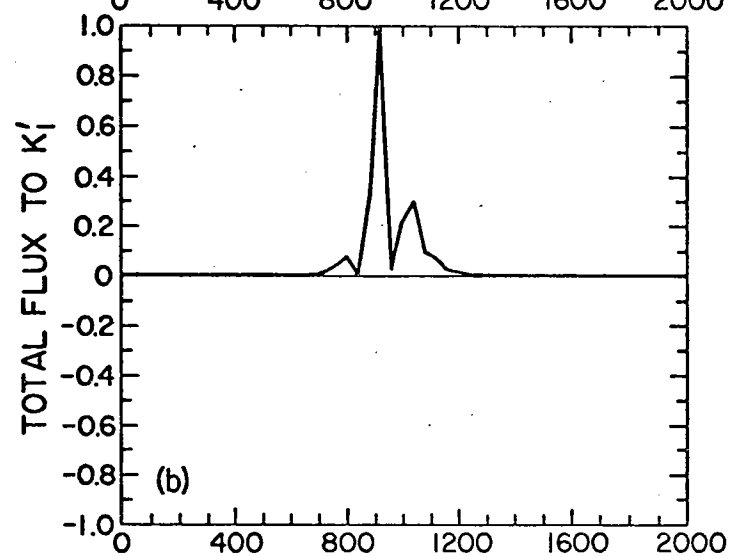
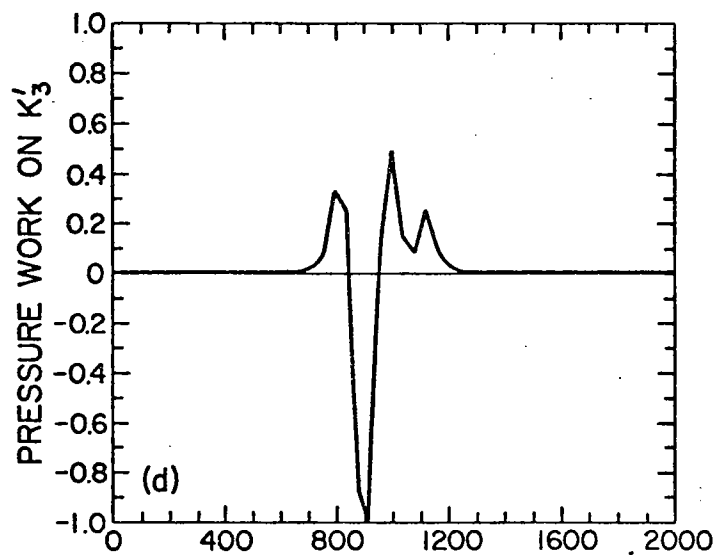
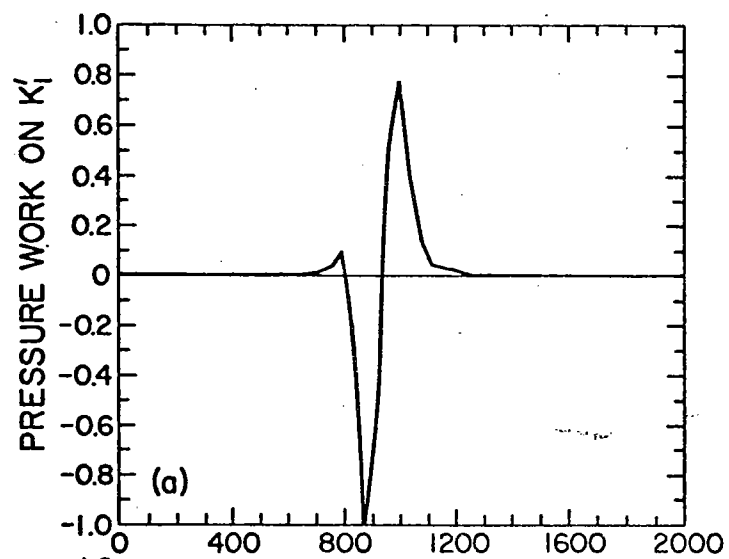


Figure 39: The most unstable baroclinic mode corresponding to profile AA', Figures 33 and 34.
(a,c) the complex upper and lower layer eigenfunctions ($\text{Re}\phi$ solid, $\text{Im}\phi$ dotted).
(b,d) the real part of the unstable eigenfunctions with the x-dependence reintroduced.
Lines have been drawn along $x = 600$ km to indicate the phase relationship between the upper and lower layer eddies.

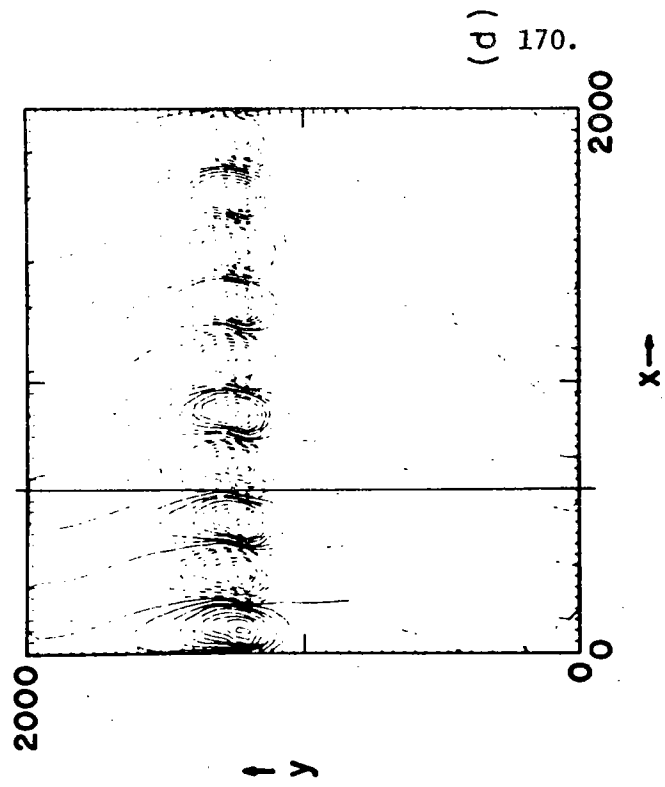
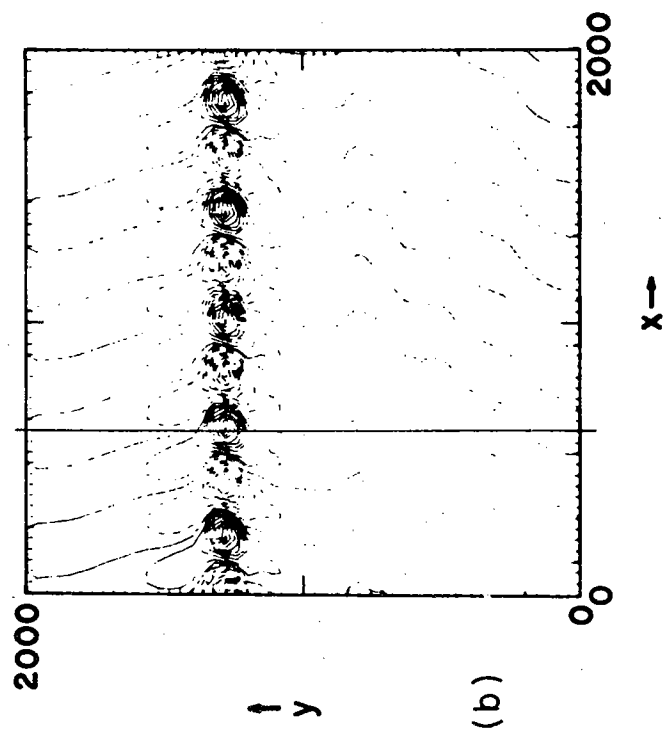
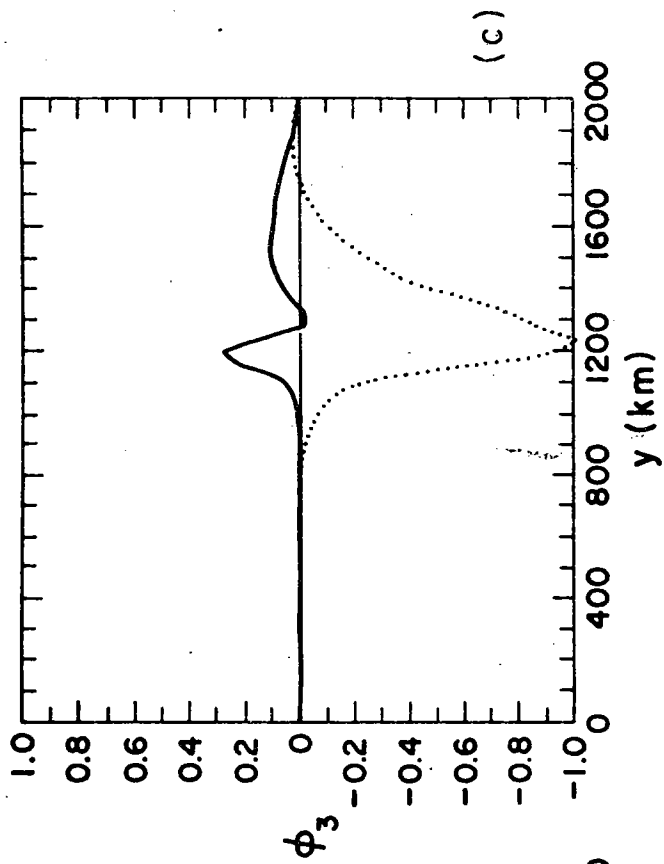
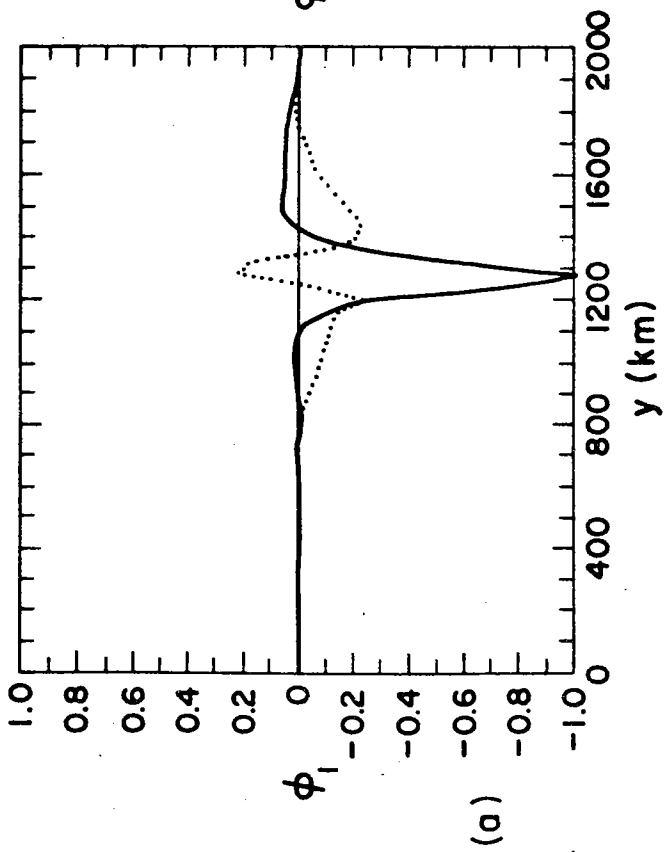
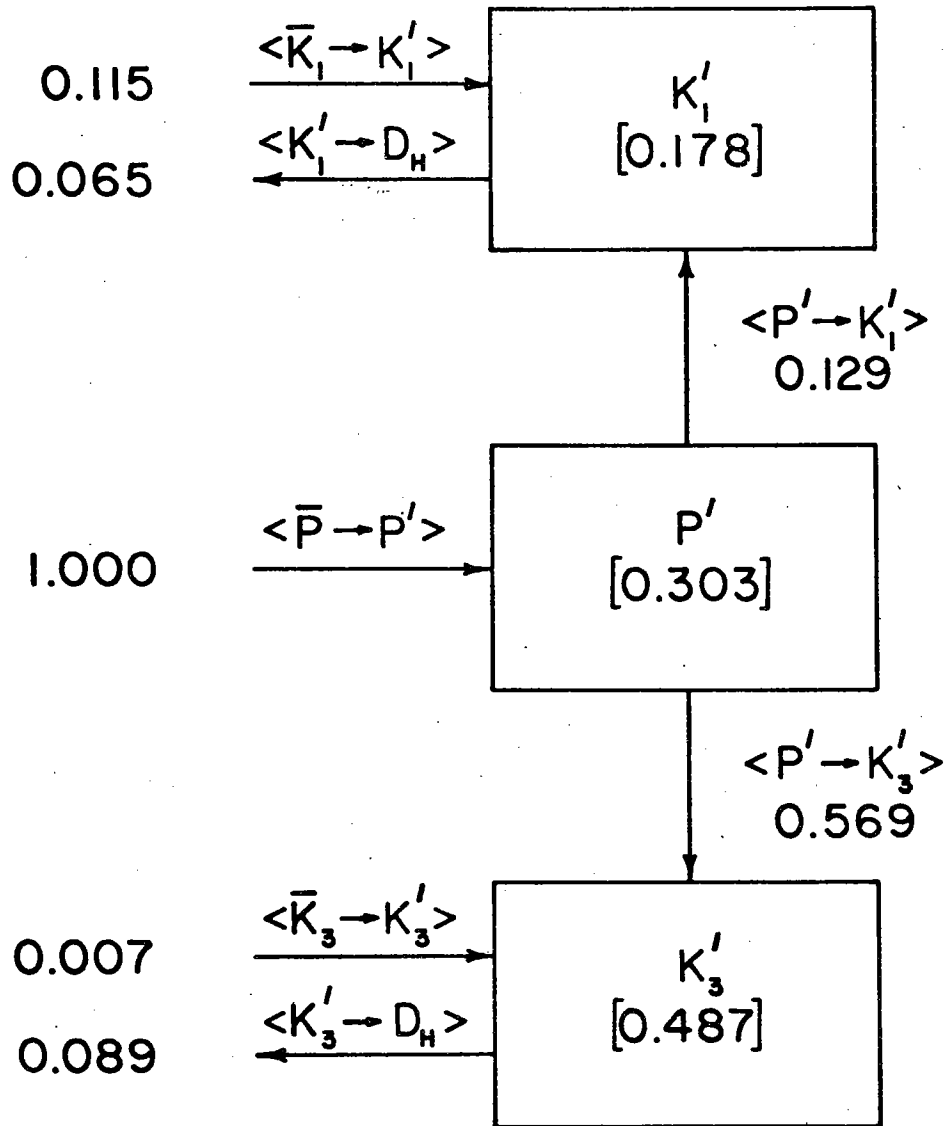


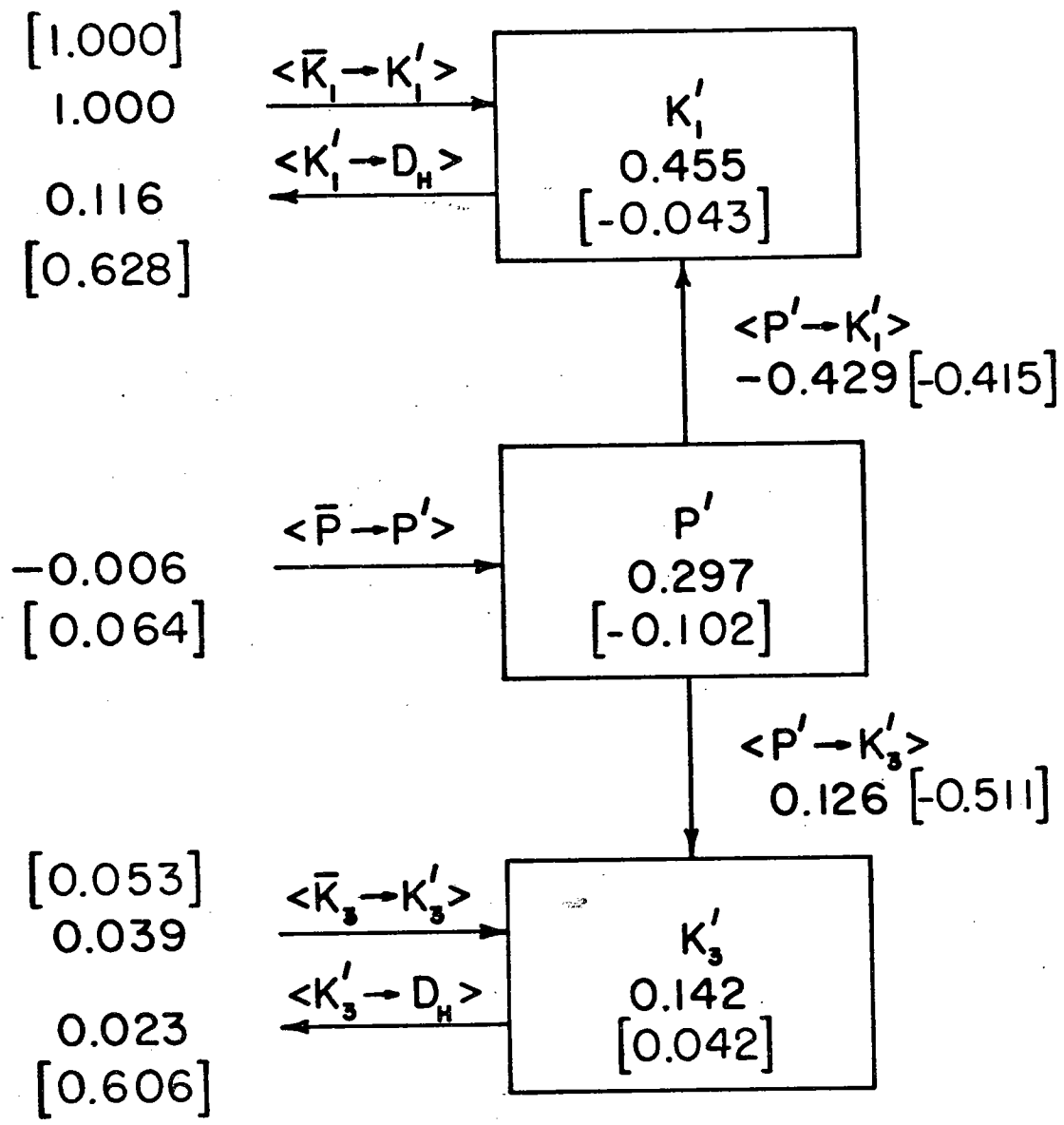
Figure 40: The normalized global energy budget for the growing perturbations of Figure 39.



included here. The ineffectiveness of the baroclinic transfer (FP1) relative to the barotropic (FP2) in the global, long-term energy fluxes (Figure 14) can be explained by observing that the region of westward inertial flow is highly variable in E2 with the consequence that the baroclinic instability is intermittent while the barotropic is continuous.

Because of the difficulty of estimating a representative amplitude for the barotropic eddies from the E2 results, the quantitative comparison of the LSA energy fluxes to the E2 model results can be made most easily by the second of our two methods in which the six-box global energy diagram is normalized by the dominant flux $\langle \bar{K}_1 \rightarrow K_1' \rangle$. The flux ratios for the LSA eddies have been estimated by an average over the results for the barotropic modes from nine separate profiles to give them greater reliability (Figure 41). By comparison to the full model energetics, we note that the flux ratio $\frac{\langle P' \rightarrow K_1' \rangle}{\langle \bar{K}_1 \rightarrow K_1' \rangle}$ is approximately constant for both the growing as well as the equilibrium eddy field. This observation conforms, in a certain sense, to the conclusions of Section VI.1. In both E1 and E2, flux ratios lying on or near the primary flux pathway remain constant throughout the infinitesimal and finite-amplitude eddy phases. This strengthens our belief in an invariance of some understandable sort but the evidence is hardly overwhelming. Thus, though perhaps somewhat less successful than the prediction attempted in (VI.1), the results for E2 do clearly show that the component instabilities of a more complicated equilibrium can be isolated and described. The difficult and unresolved question is how to put the many LSA modes (Table 4) back together to form the best prediction of the equilibrium eddy field (Table 3).

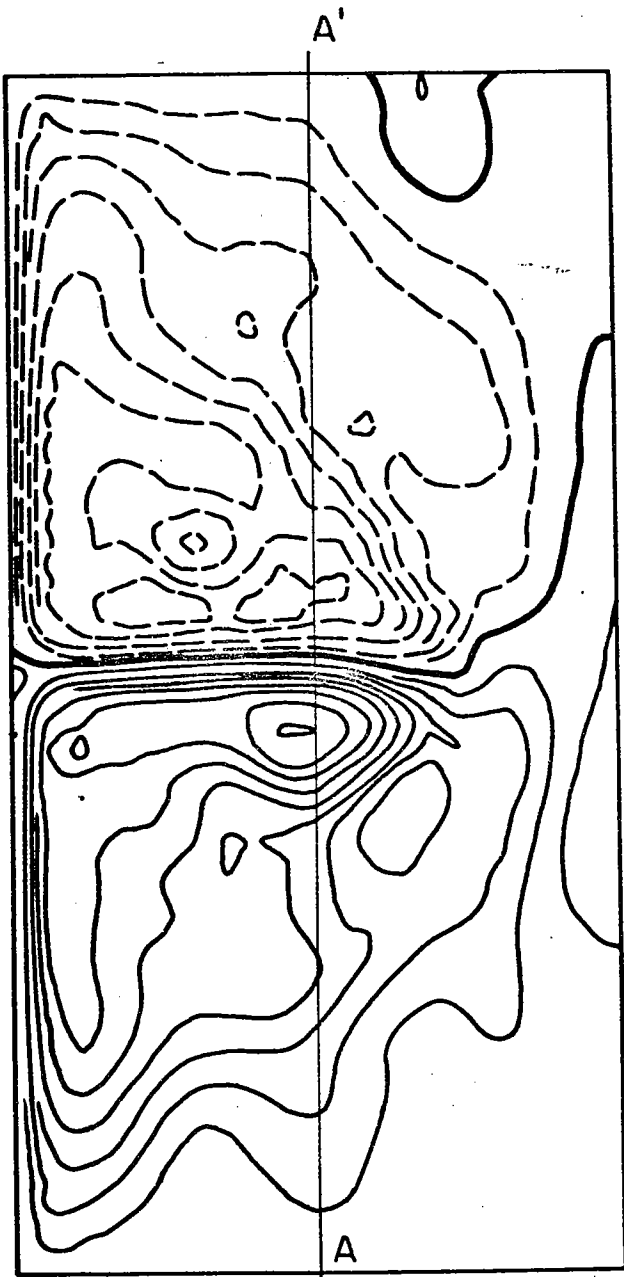
Figure 41: A mean normalized global energy budget for the barotropic instabilities of experiment 2 as predicted by LSA (average over nine barotropic modes). The numbers in brackets are the equivalent flux ratios obtained from the experiment 2 global energy diagram (Figure 14) by dividing by $\langle \bar{K} \rightarrow K' \rangle$.



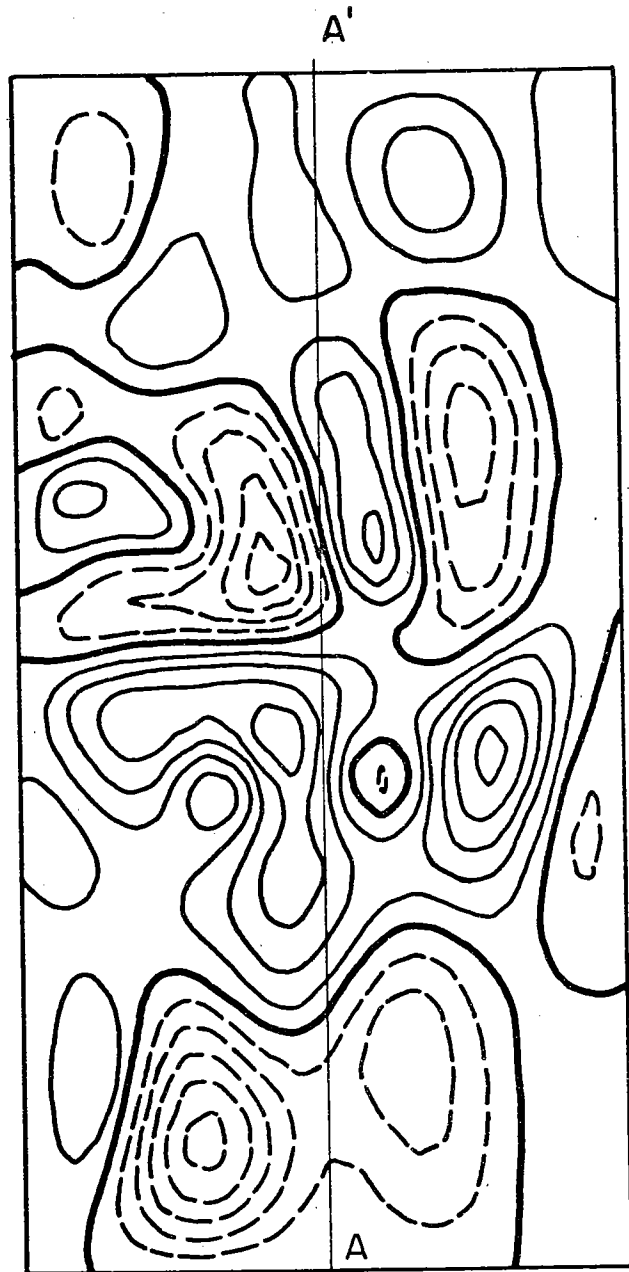
(VI.4) A stability analysis of experiment 2R

The instantaneous north-south velocity profiles collected for analysis from E2R bear many of the features of the E2 sections. A profile taken along the mid-longitude in E2R (Figures 42 and 43) with minor changes could be a scaled version of the transect studied in (VI.3) - Figure 34, the amplitude ratio being about 0.5. We therefore expect the instabilities of both experiments to have comparable properties. Indeed, an examination of the E2R profiles reveals the analogue of the quasi-linear relationship, noted before in E2, between the growth rate, $\text{Re } \sigma$, of the barotropic mode and the local value of horizontal shear in the mid-latitude jet (Figure 44). Because of the lower overall flow speed, however, the mean e-folding time for the barotropic instability is now 0(75 days). Physically, this reduced growth rate is translated into a more quiescent stream which undergoes less meandering and displays less asymmetry between the cyclonic and anticyclonic gyres. The effectiveness of the barotropic mode has been so reduced by the weakening of the current that the baroclinic modes are now equally as energetic as the barotropic, as opposed to E2 where the barotropic clearly dominated. The most unstable eigenfunctions associated with the representative E2R flow profile are shown in Figures 45 (barotropic) and 47 (baroclinic) and align with the regions of greatest local horizontal and vertical shear respectively. The accompanying energy flux diagrams (Figures 46 and 48) clearly identify the instabilities as barotropic and baroclinic in the sense (adopted previously) that the fluxes are dominated by the $\langle \bar{K}_1 \rightarrow K'_1 \rangle$ and $\langle \bar{P} \rightarrow P' \rangle$ transfers.

Figure 42: Representative instantaneous fields from experiment 2R.
(a) upper level streamfunction (contour interval = 2.4 Sverdrups).
(b) lower level streamfunction (contour interval = 4.0 Sverdrups).
Profile AA' is replotted in Figure 43.



(a)



(b)

- Figure 43: Profile AA' from experiment 2R, Figure 42.
- (a) upper level streamfunction ($|\psi_1|_{\max} = 2.1 \times 10^8$).
 - (b) upper level velocity ($|u_1|_{\max} = 30.7$).
 - (c) upper level potential vorticity ($|q_1|_{\max} = 4.0 \times 10^{-5}$).
 - (d) lower level streamfunction ($|\psi_3|_{\max} = 3.0 \times 10^7$).
 - (e) lower level velocity ($|u_3|_{\max} = 3.2$).
 - (f) lower level potential vorticity ($|q_3|_{\max} = 4.0 \times 10^{-5}$).
- Maximal instability occurs at $y = 1020$ km (barotropic) and $y = 760$ km (baroclinic).

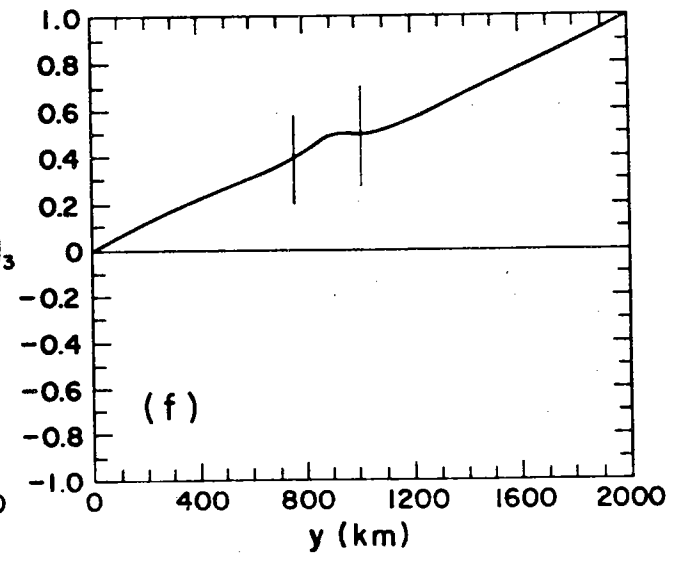
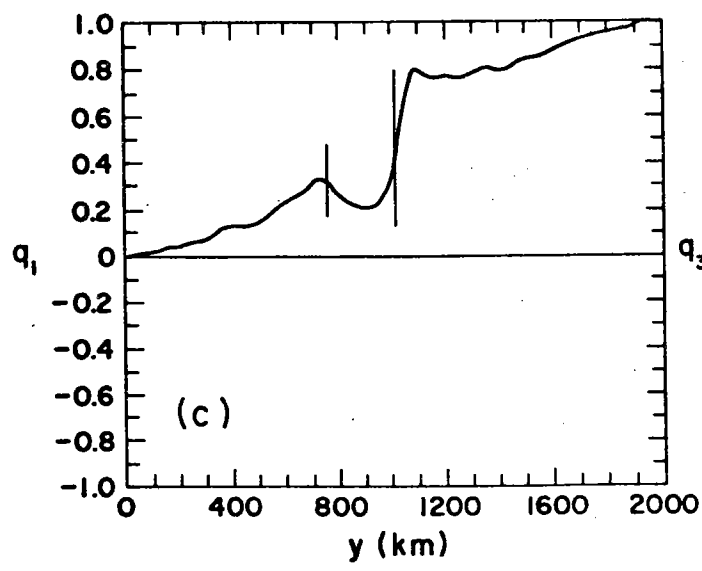
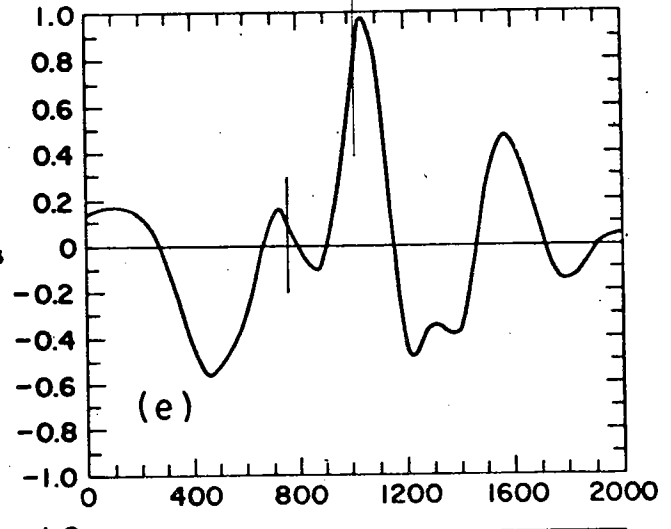
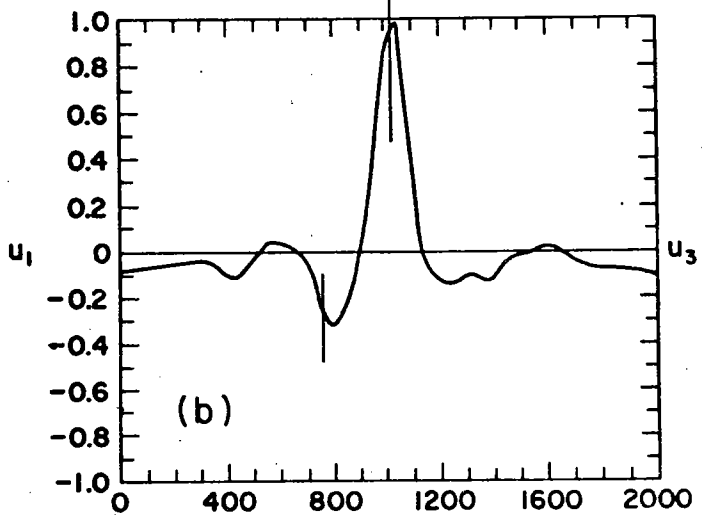
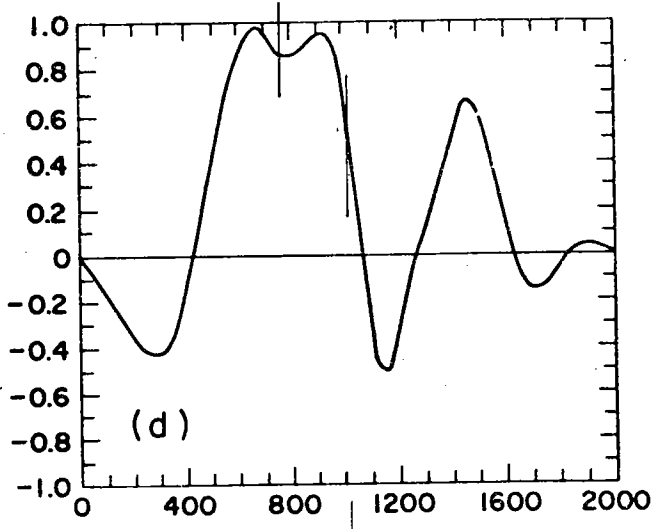
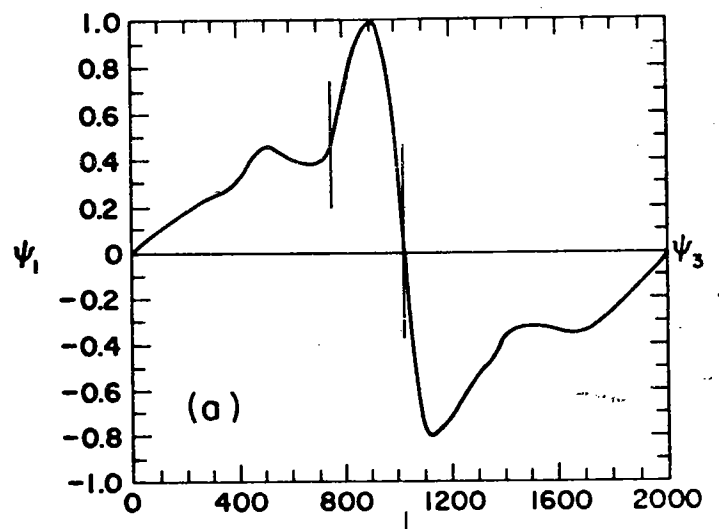


Figure 44: The variation with horizontal shear of the growth rate of the barotropic modes observed in experiment 2R.

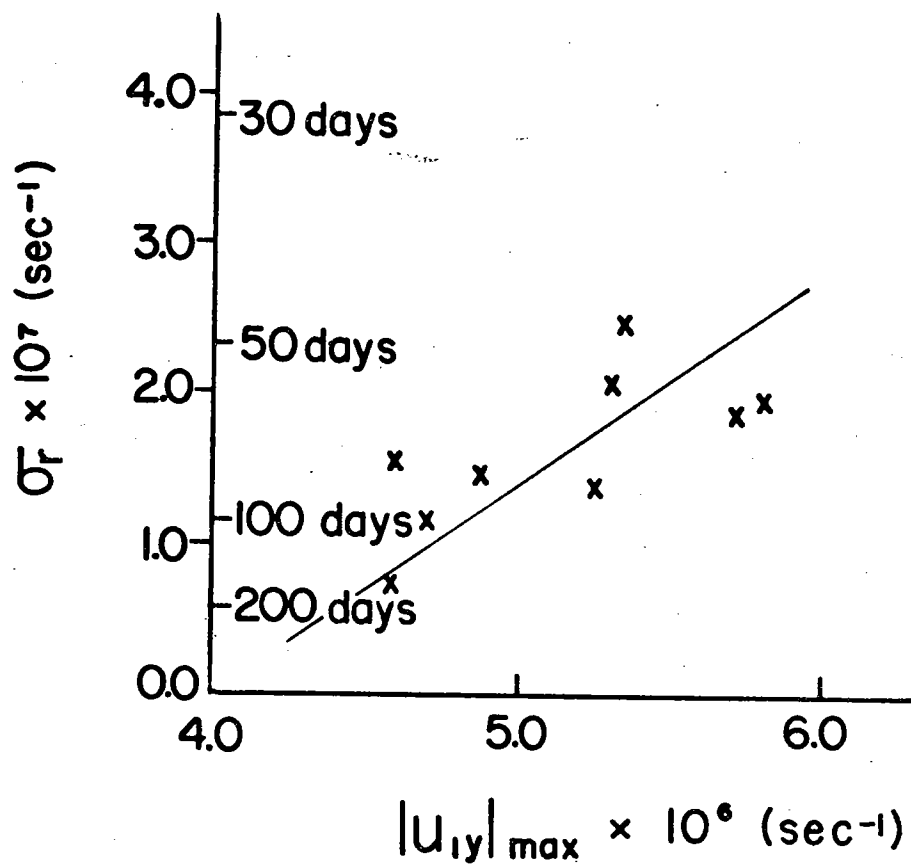
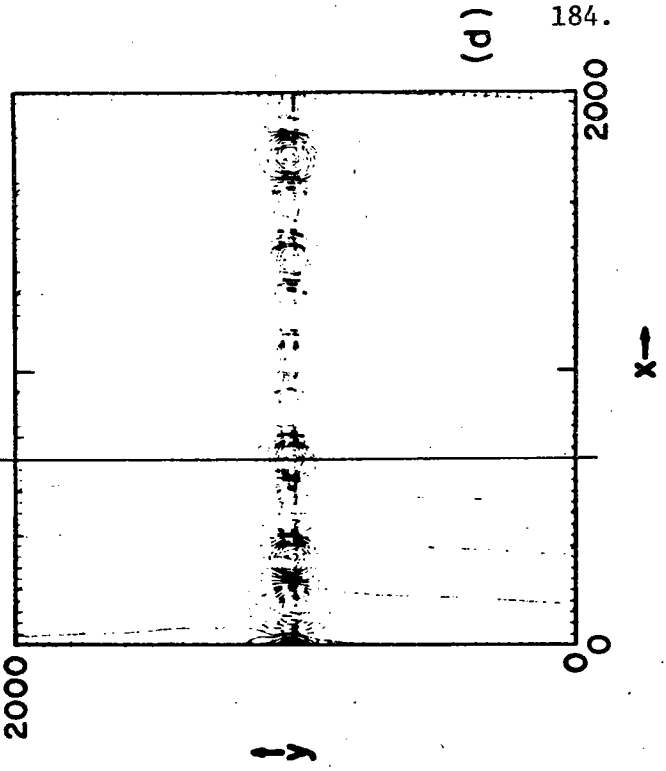
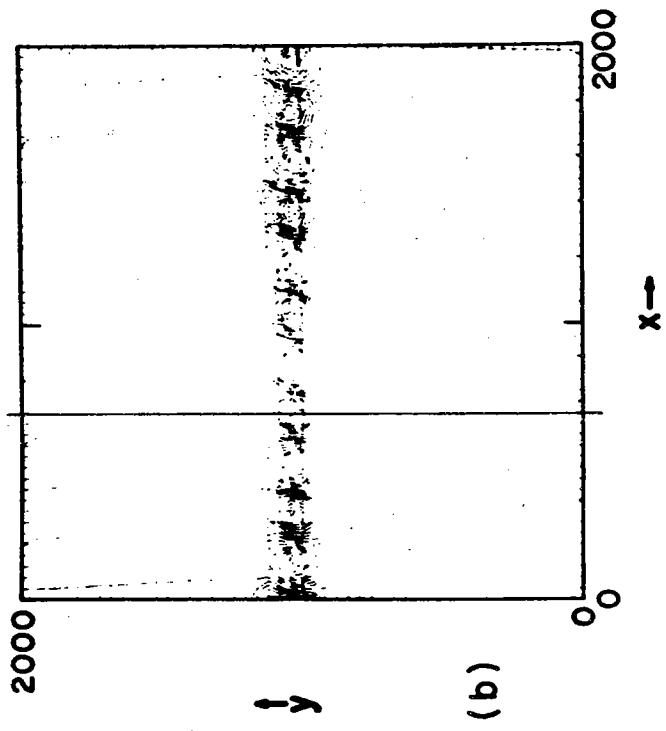
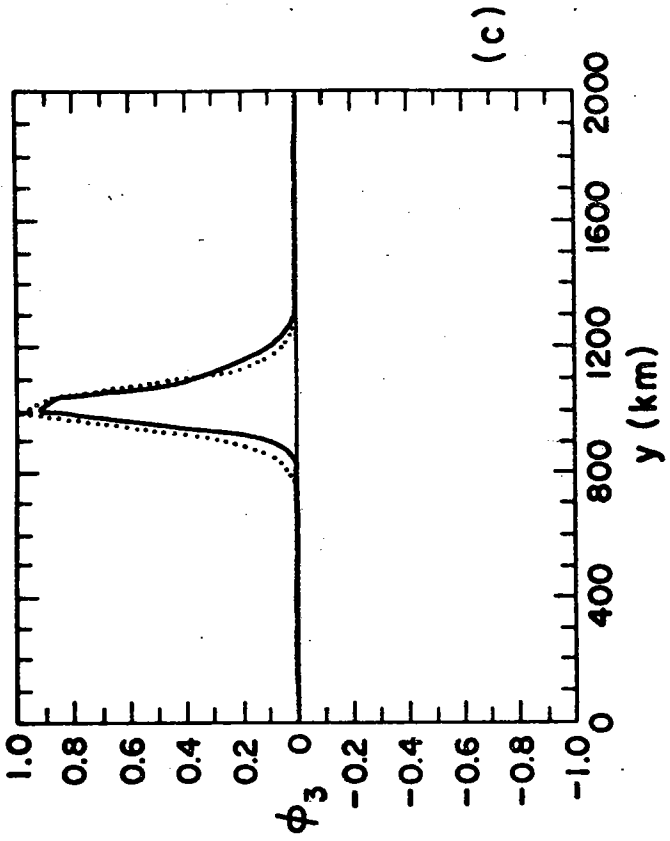
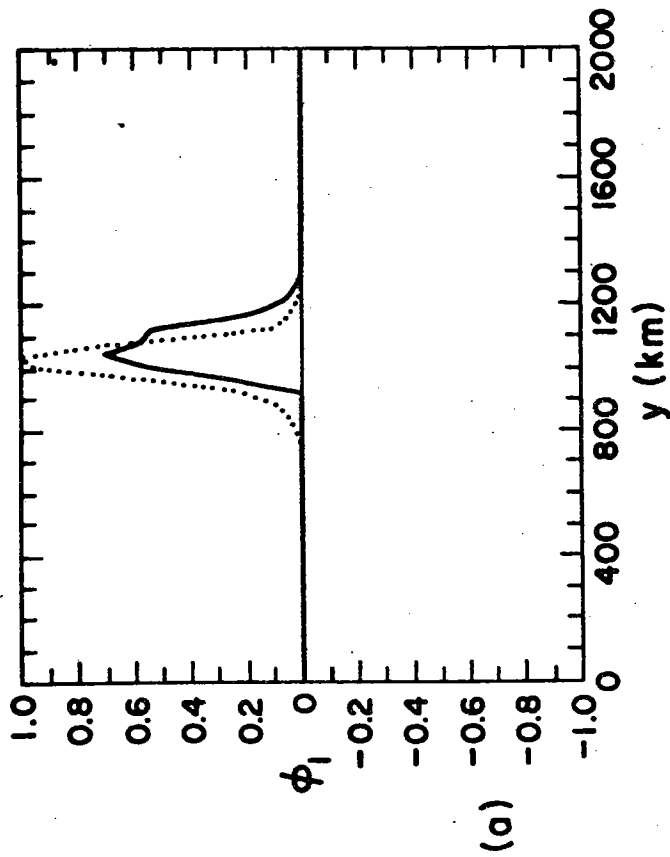


Figure 45: The most unstable barotropic mode corresponding to profile AA', Figures 42 and 43.
(a,c) the complex upper and lower level eigenfunctions ($\text{Re}\phi$ solid, $\text{Im}\phi$ dotted).
(b,d) the real part of the unstable eigenfunction with the x-dependence reintroduced.
Lines have been drawn along $x = 680$ km to indicate the phase relationship between the upper and lower level eddies.



184.

Figure 46: The normalized global energy budget for the growing perturbations of Figure 45.

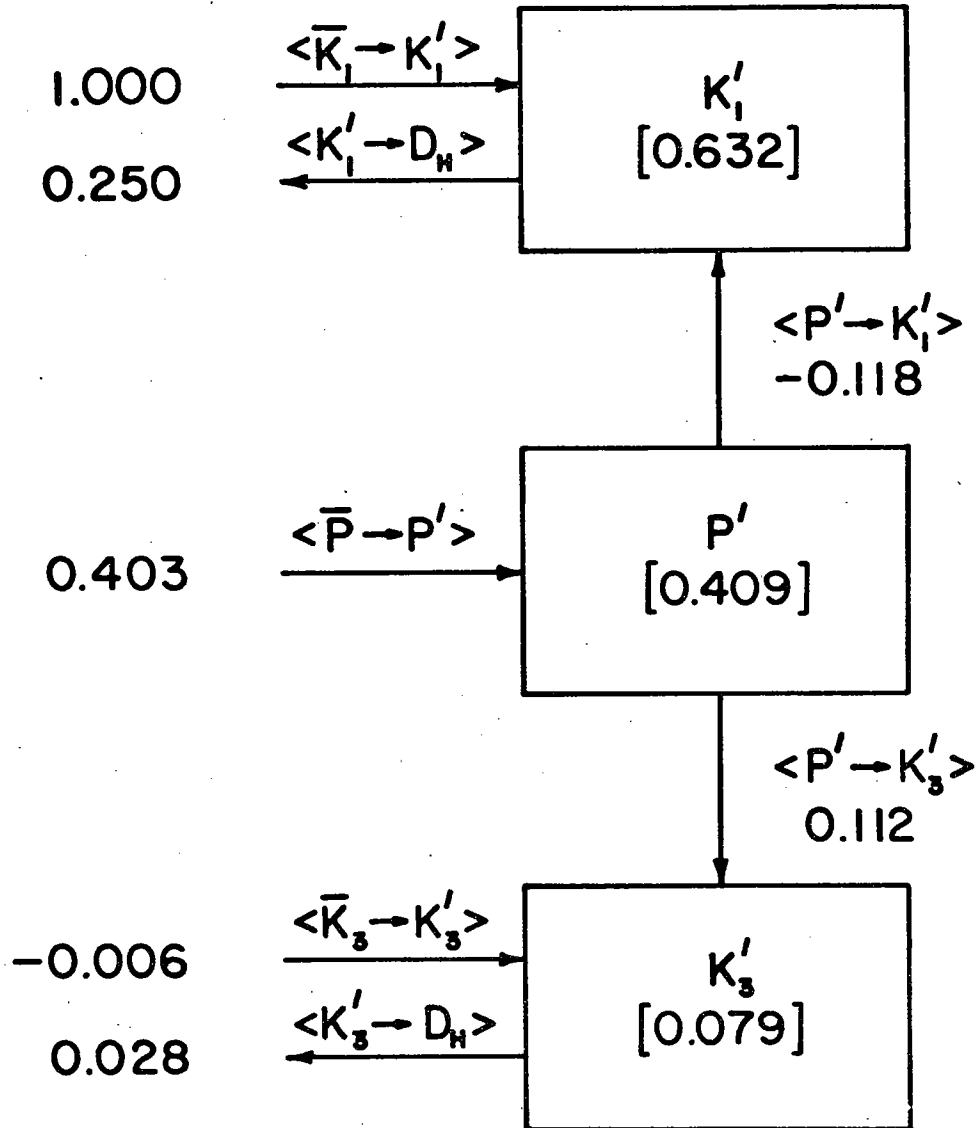


Figure 47: The most unstable baroclinic mode corresponding to profile AA' Figures 42 and 43.
(a,c) the complex upper and lower level eigenfunctions ($\text{Re}\phi$ solid, $\text{Im}\phi$ dotted).
(b,d) the real part of the unstable eigenfunction with x-dependence reintroduced.
Lines have been drawn along $x = 680$ km to indicate the phase relationship between the upper and lower level eddies.

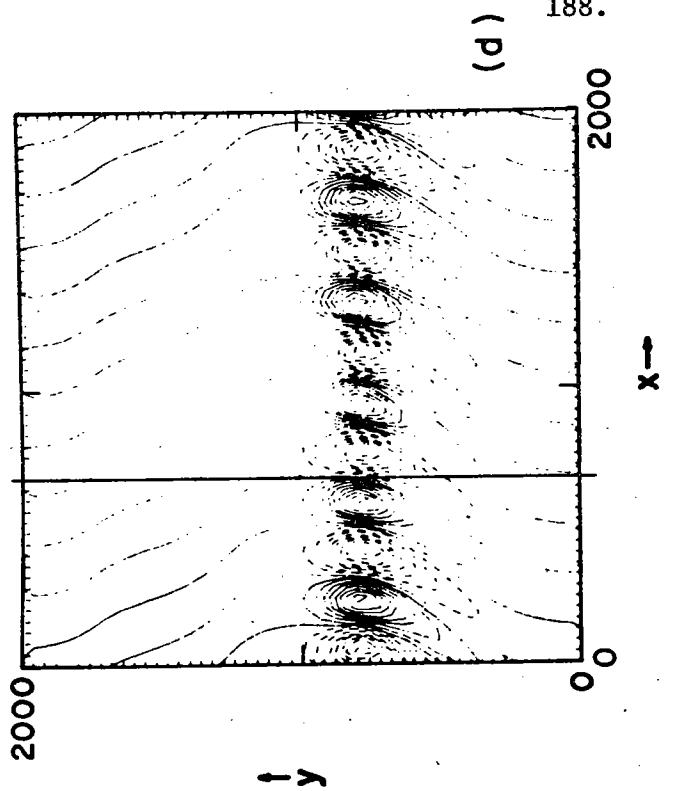
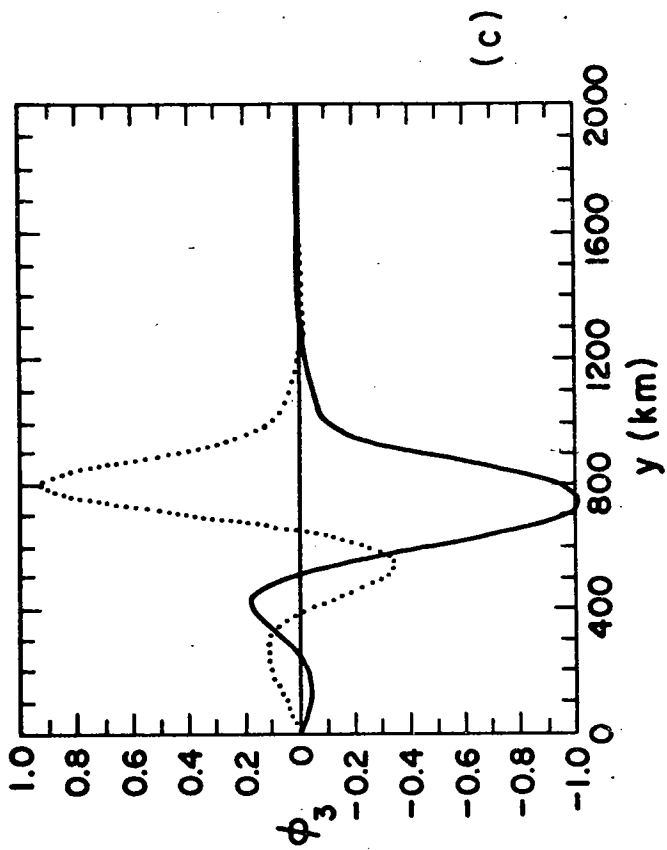
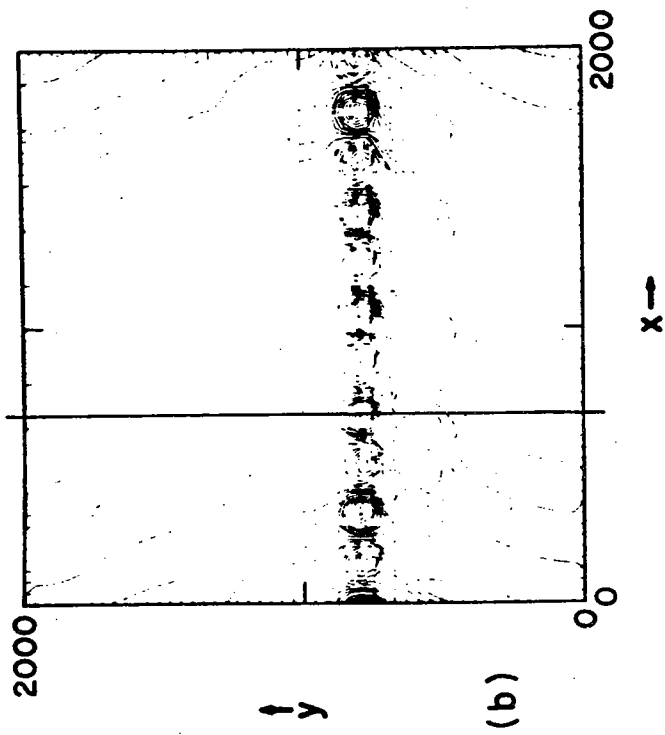
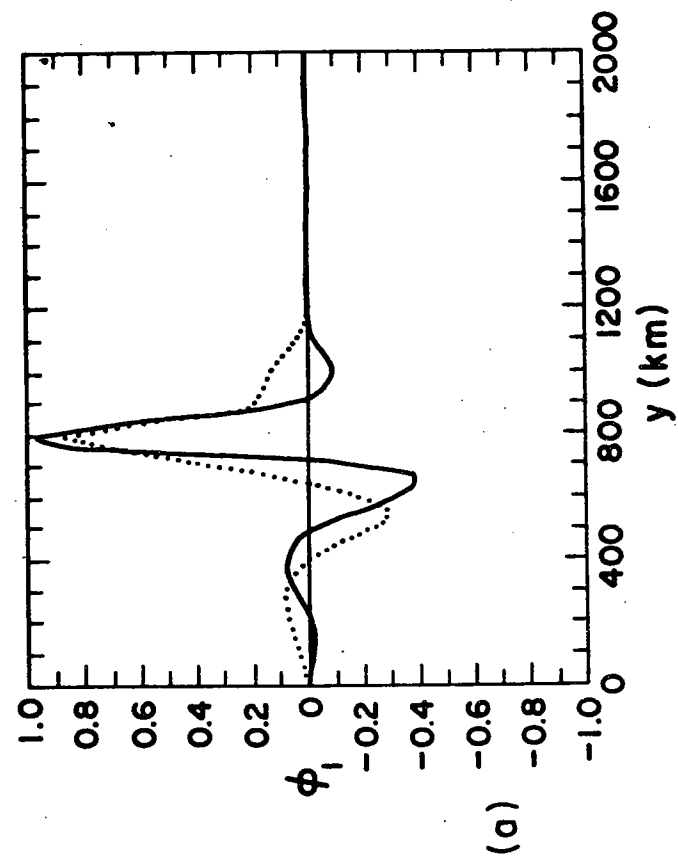
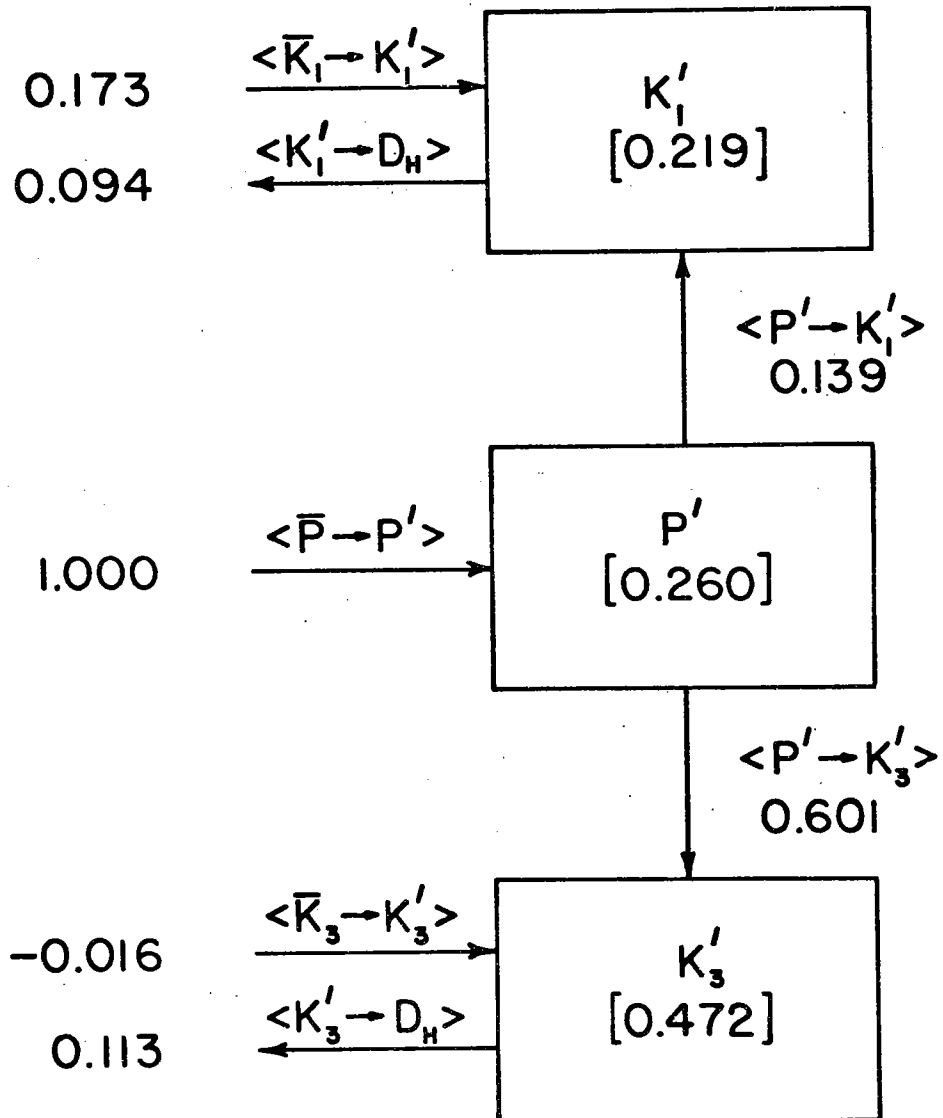


Figure 48: The normalized global energy budget for the growing perturbations of Figure 47.



One might argue that E2R has the most complicated equilibrium of all the primary experiments; although the eddies grow less rapidly than those in E2, and therefore the eddying is less intense, we now have a situation where at least two (and possibly three) unstable modes are continuously active with neither overwhelming the other. Previously, either a baroclinic (E1) or barotropic (E2) mode completely controlled the global energetics even though smaller regions of competing instabilities might have been locally operational. In E2R, both instability processes are in approximate balance, making the overall energy transfer path (FP3) more complex and the mean eddy statistics (Table 4) more difficult to ascertain. Note, however, one very nice confirmation of the E2R nonlinear results by the LSA. Recall that the E2R frequency spectrum has significant content near not only 64, but also 51, days (Figure 17). The 64-day periodicity arises directly from the presence of the baroclinic mode (predicted by LSA to have a 67-day period). There is also a smaller but significant content at a period of 171 days which must be due to the barotropic mode (predicted period 180 days). Now where could the strong 51-day oscillation be originating? Almost certainly it results from the nonlinear coupling of the two primary instabilities which have an interactive period of 49 days.

Unfortunately, attempts to renormalize and compare the predicted LSA energy flux ratios with those from the full experiment are not successful; they fail because now the energy cascade cannot be adequately modelled by a simple flux pathway. Presumably, a local energetic analysis of the individual regions of instability in E2R would reconfirm (over limited areas) the invariance of the flux ratios identified in Sections VI.1 and VI.3.

(VI.5) Generalized properties of the baroclinic mode

In studying our four primary experiments, certain characteristics of the unstable modes have become clear, specifically the strong relationship between local velocity shear and the efficiency of the instability process. But have we learned enough about the conditions under which the eddies arise to be able to construct analytic profiles with given instabilities? To do so, we first need to know whether other profile features and environmental parameters affect eddy generation. If we are then successful in making unstable flows to order, we are also much closer to generalizing our deductions to the real world.

Consider first the profiles of Figure 49 in which we have constructed a smooth mean flow consisting of two strong internal jets, one eastward and the other westward. Now, we perform an experiment by solving for the unstable modes as a function of maximum jet velocity. As will emerge later, the breadth of the jets is such that we are always in the baroclinic regime so that vertical shear, u_z , should be the appropriate measure of instability. Figures 50 and 51 show the results of this baroclinic mode scaling experiment. A gently curving relationship exists between growth rate, $Re\sigma$, and the local maximum vertical shear. The westward flowing jet is always more unstable than the eastward, and the threshold value for instability occurs for a velocity difference of 5-10 cm/sec across the thermocline; both observations conform to the predictions of baroclinic instability theory (Robinson and McWilliams, 1974). However, the systematic variation of the most unstable wavenumber, k_{max} , with shear amplitude is in the opposite sense - decreasing

Figure 49: An idealized mean circulation consisting of two oppositely directed internal jets of equal strength.

- (a) upper level streamfunction ($|\psi_1|_{\max} = 6.0 \times 10^8$).
- (b) upper level velocity ($|u_1|_{\max} = 22.7$).
- (c) upper level potential vorticity ($|q_1|_{\max} = 4.9 \times 10^{-5}$).
- (d) lower level potential vorticity ($|q_3|_{\max} = 4.0 \times 10^{-5}$).

The lower level is at rest.

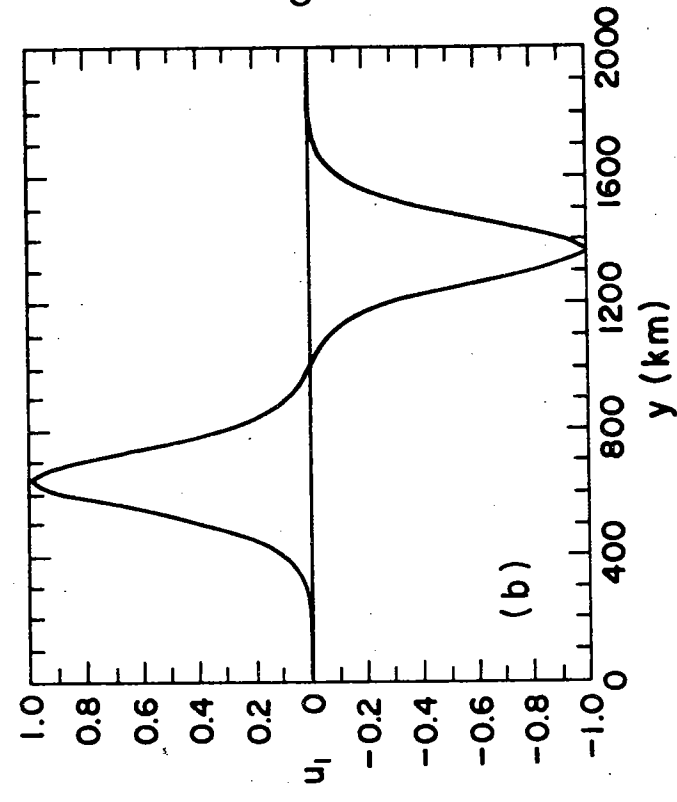
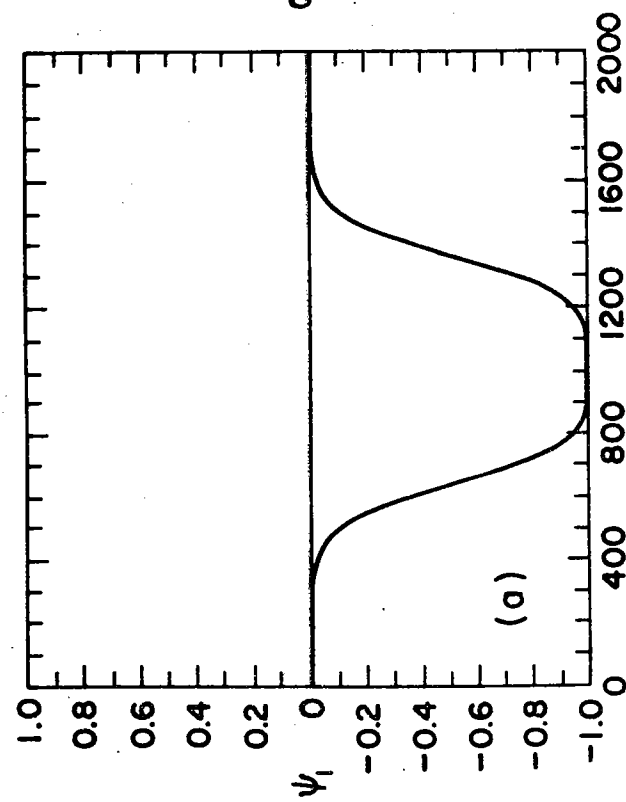
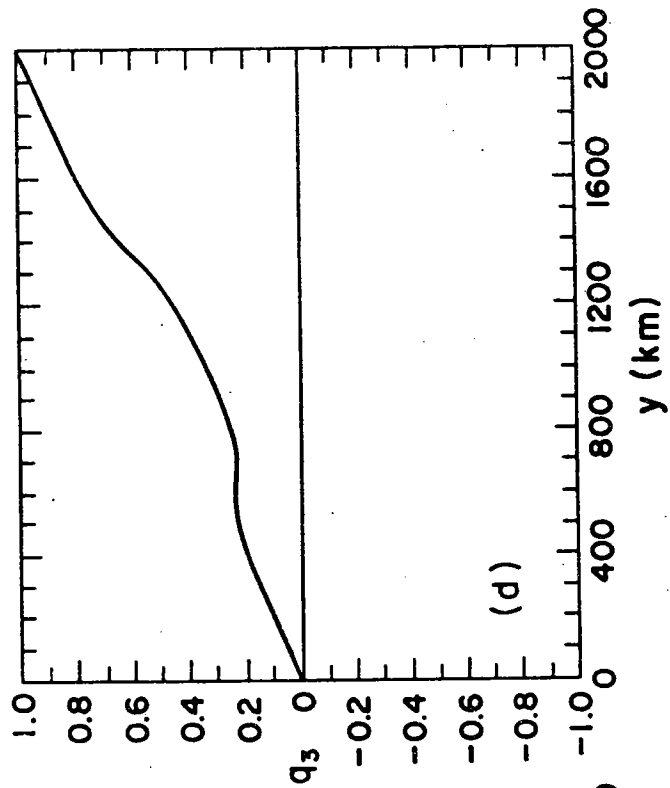
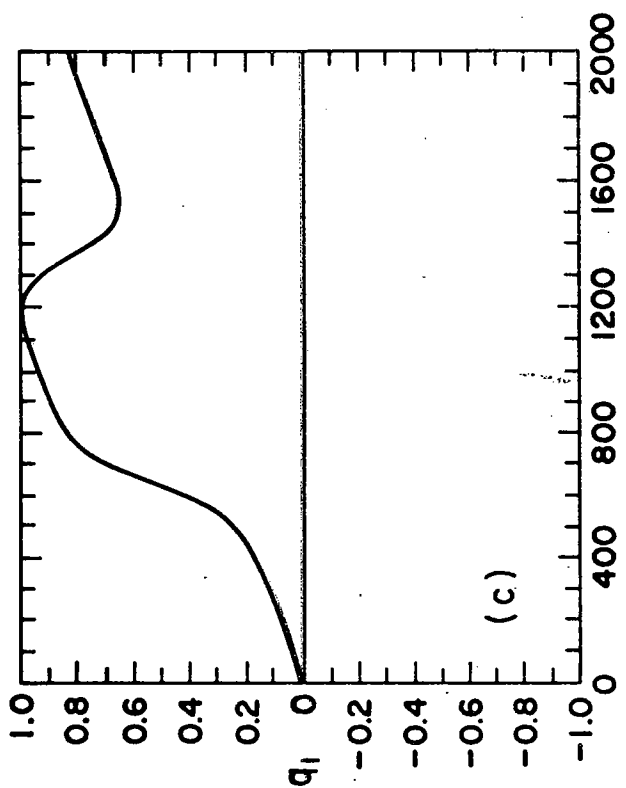


Figure 50: The variation with vertical shear of the growth rate of the baroclinic modes associated with the analytic circulation of Figure 49.

- ✕ unstable modes in the westward flowing jet.
- unstable modes in the eastward flowing jet.

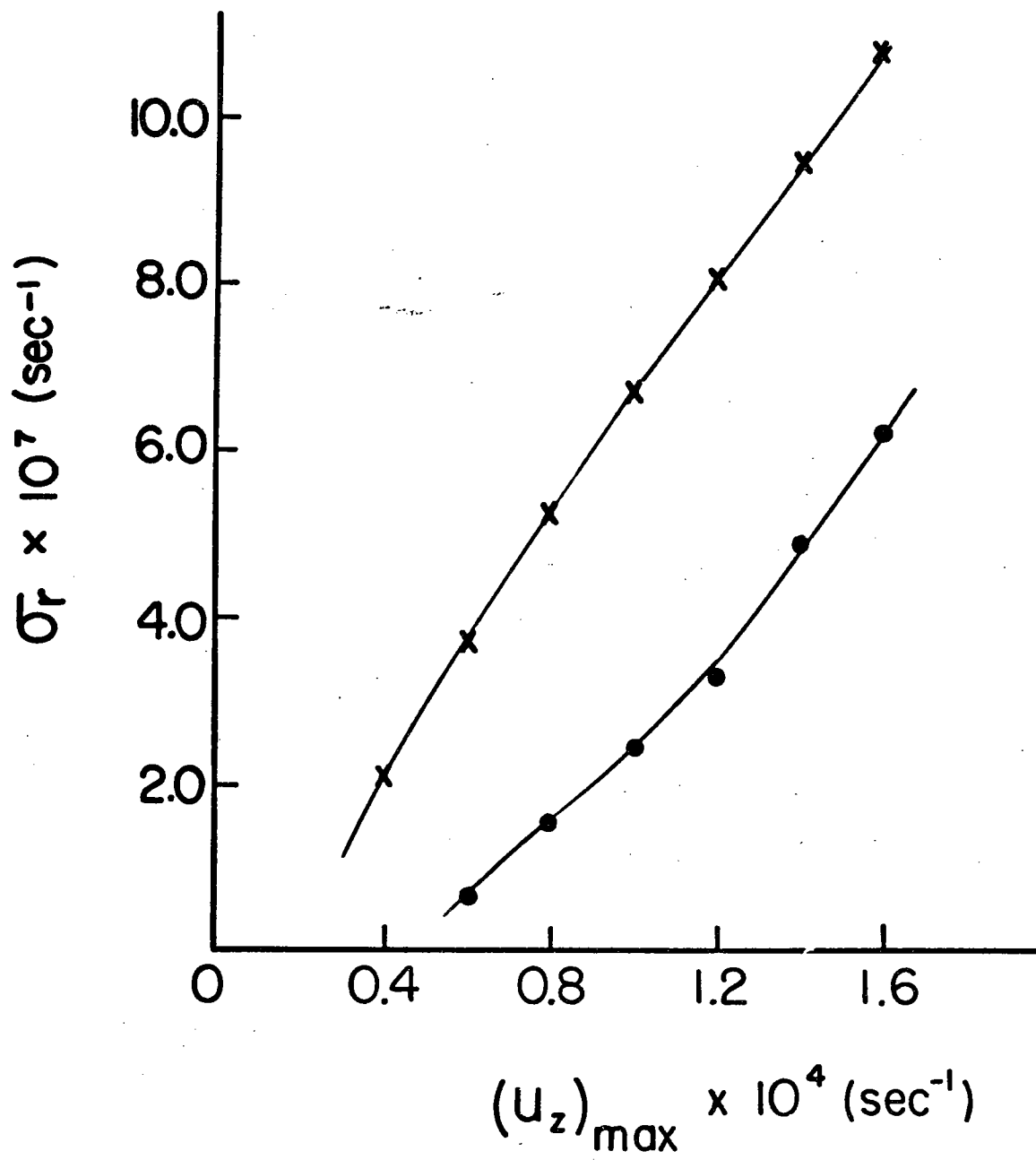
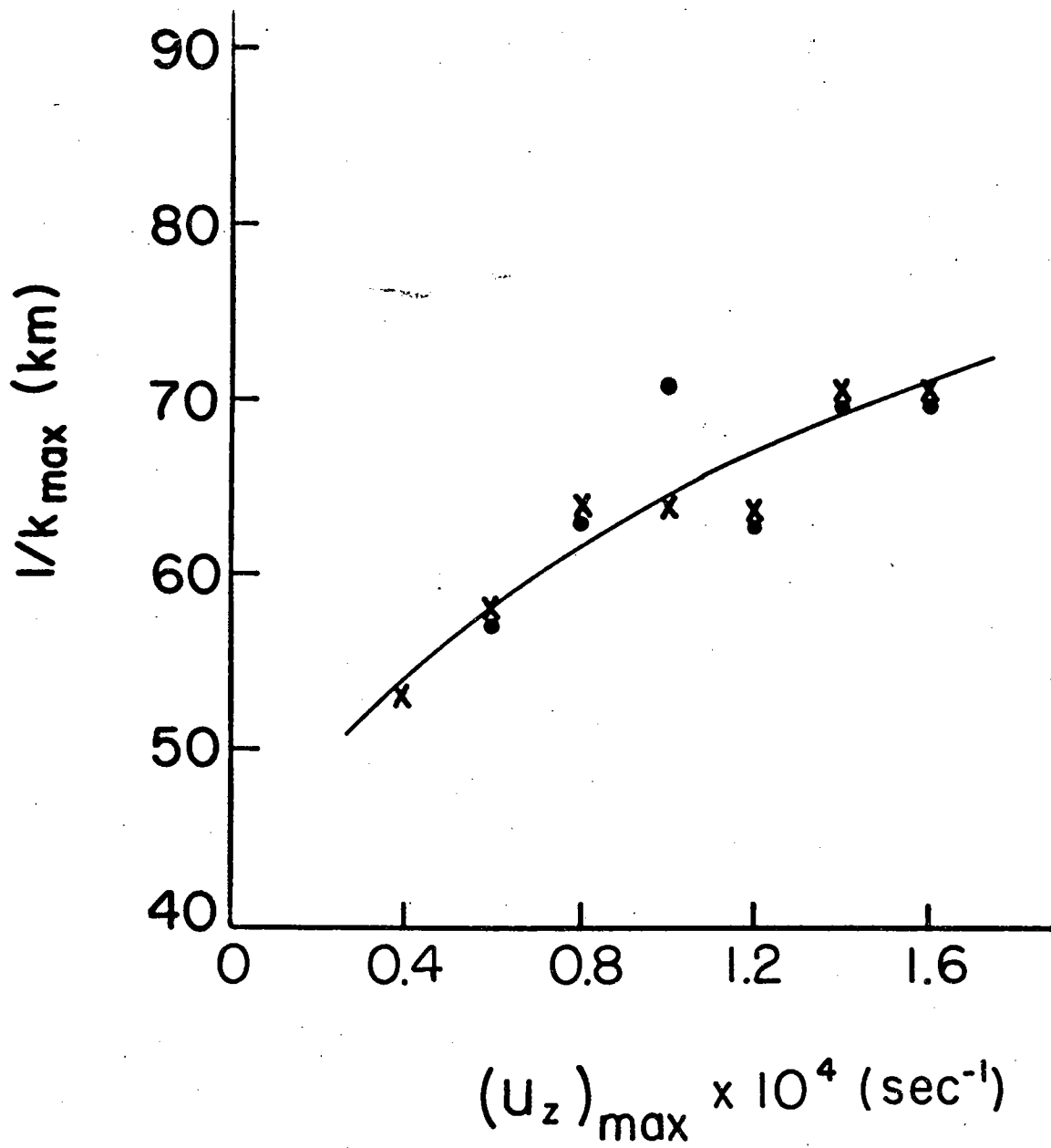


Figure 51: The variation with vertical shear of the most unstable wavenumber, k_{\max} , associated with the analytic circulation of Figure 49.

- ✕ unstable modes in the westward flowing jet.
- unstable modes in the eastward flowing jet.



with increasing vertical shear (Figure 51) - to that suggested by the same theories. This conflict, which has not been adequately resolved, is however the only point of contention between mid-ocean stability theories and the LSA results.

The quasilinear trend of σ_R with u_z is very reminiscent of the cumulative results of E1 plotted in Figure 21. This is expected if, as we suppose, local amplitude variabilities are primarily responsible for the time-dependence of the instabilities. An additional experiment confirms this explanation. Taking an instantaneous velocity profile from E1, i.e., a model-generated rather than an analytic profile, we perform a similar scaling experiment and overlay the results onto Figure 21. The coincidence of the two sets of points justifies our assigning a primary role to variations in the amplitude of the local shear.

Of course, we hold other potentially important environmental parameters fixed during these nonlinear simulations so we have no way of gauging the sensitivity of the results to other factors. Assume for the moment, however, that the strategy outlined at the beginning of the chapter can be used. That is, let us fix the profiles under consideration and vary the interesting parameters without worrying about the fact that the profiles, if model generated, would themselves depend on the same parameters. (Alternatively, we could just consider this a study of the instability properties of generalized current profiles.) We have done this for the Rossby radius of deformation, R_d , which has been varied for the idealized jet profile of Figure 49a.¹ The variation

¹A systematic study of the effects of frictional parameterization is underway; the results will be reserved for future elaboration.

in $Re\sigma$ with R_d is smooth, monotonic, and inverse, with larger growth rates associated with smaller deformation scales (Figure 52). The wave-scale of the most unstable eddies is always slightly larger than and varies linearly with R_d (Figure 53).

The effects of jet structure - including their width and separation - on the baroclinic mode have also been studied. The results indicate that over a wide range of values the width of the jet has little effect on its stability properties so long as the ratio of vertical to horizontal shear remains large. Similarly, a sequence of jet pairs separated by successively larger and larger distances (Figures 54 and 55) shows that a separation of only one or two jet widths (or equivalently one or two deformation wavelengths) is sufficient for the eastward and westward flowing regions to be independent (Figure 56).

A last experiment underscores the sensitivity of the instability mechanisms to the exact levels of local shear. Figure 57 shows an isolated jet with strong horizontal as well as vertical shear. If the lower layer is taken to be at rest, the energetics are dominated by the $\langle \bar{P} \rightarrow P' \rangle$ flux (FP1); this is a baroclinic instability in our terminology. Now, consider adding successively to the strength of the lower layer flow by setting $\psi_3 = \alpha\psi_1$ and varying α from 0.0 to 1.0, thereby slowly reducing the vertical but not the horizontal shear. Such a test shows that setting ψ_3 to the 15% level completely eliminates the dominance of the baroclinic transfer, yielding a mixed mode (FP3). Adding 30% of ψ_1 to ψ_3 , we have a heavily barotropic transfer (FP2). These results are summarized in Figure 58. On the basis of the analytic profile experiments, then, there is little reason to doubt that the

Figure 52: The variation with R_d of the growth rate of the baroclinic modes associated with the analytic circulation of Figure 49.

- × unstable modes in the westward flowing jet.
- unstable modes in the eastward flowing jet.

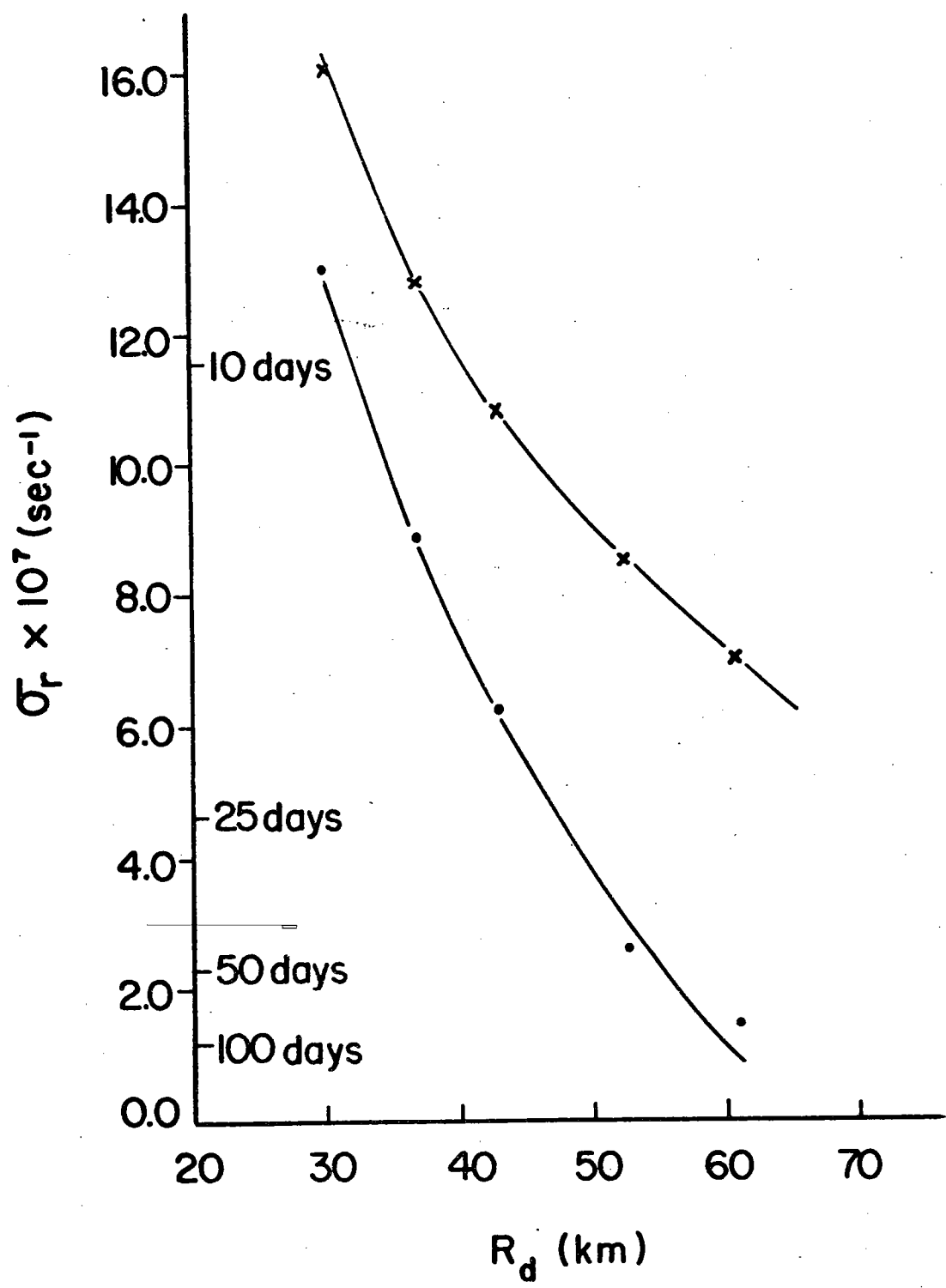


Figure 53: The variation with R_d of the most unstable wavenumber, k_{\max} , associated with the analytic circulation of Figure 49.

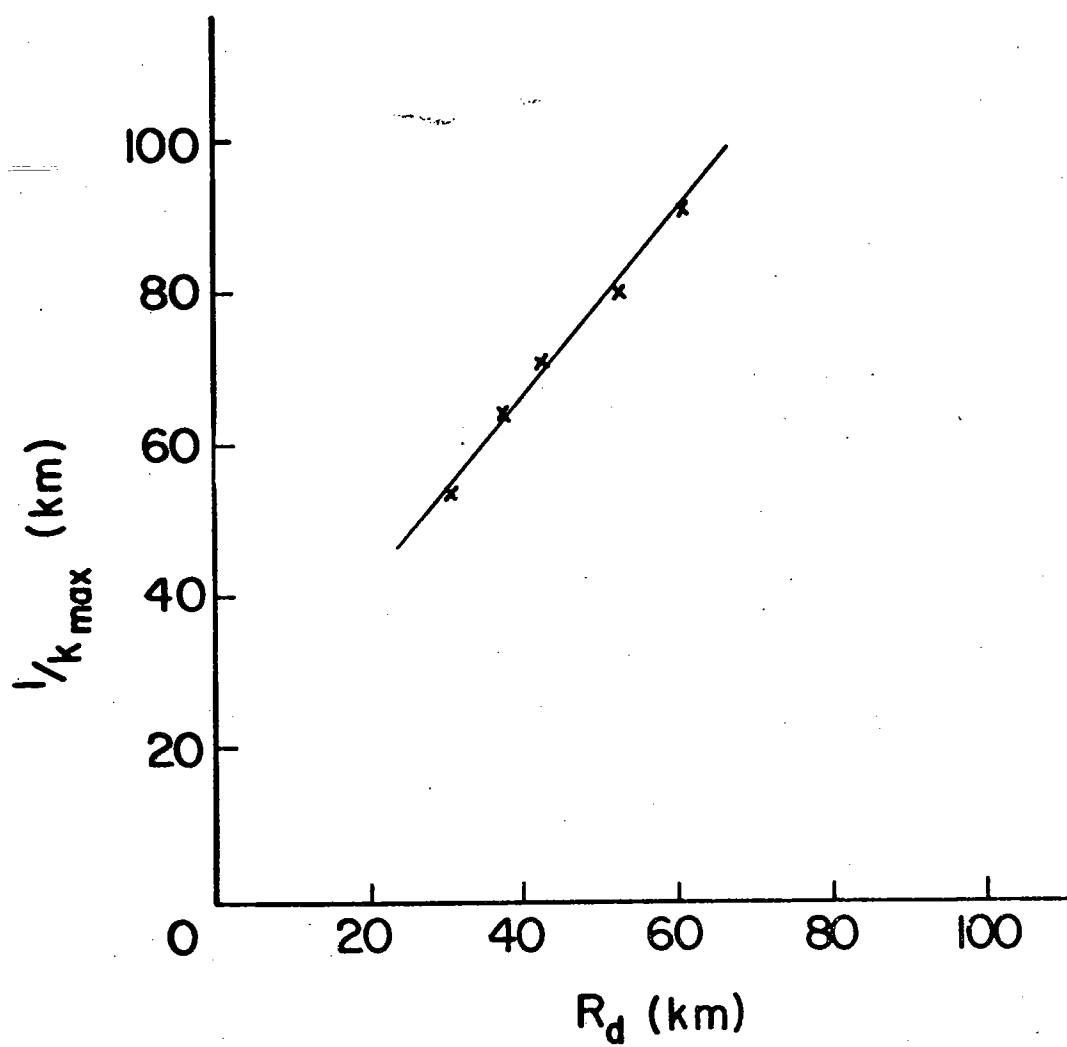


Figure 54: A sequence of idealized mean circulations consisting of two oppositely directed internal jets of equal strength separated by succeeding greater distances.

<u>Diagram</u>	<u>Jet Separation</u>
(a)	120 km
(b)	180
(c)	240
(d)	360

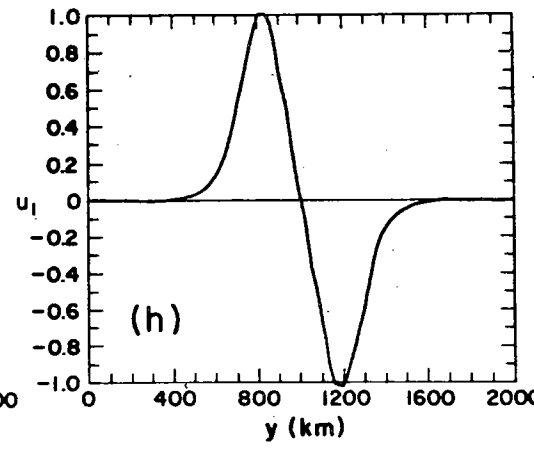
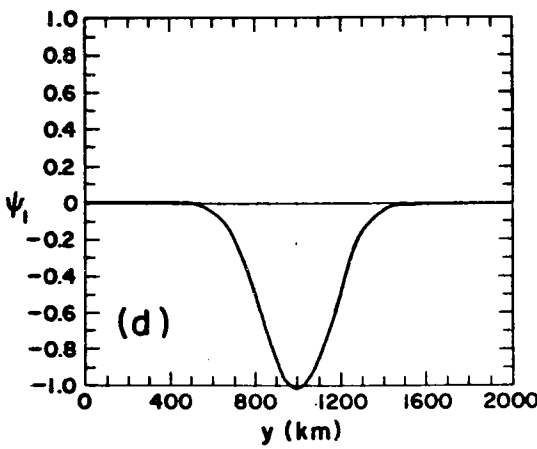
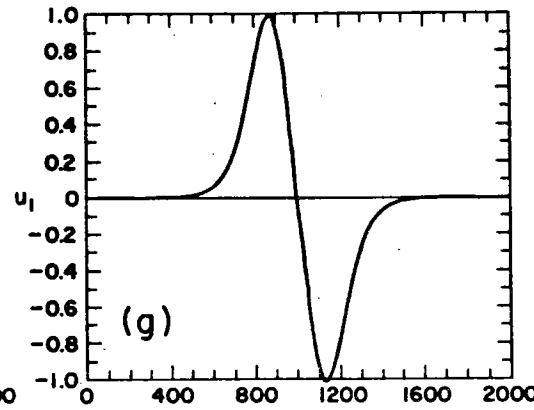
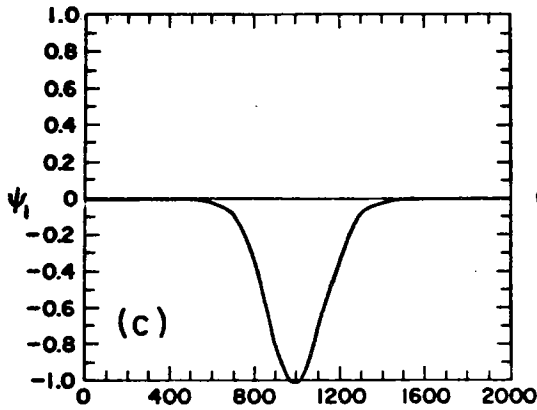
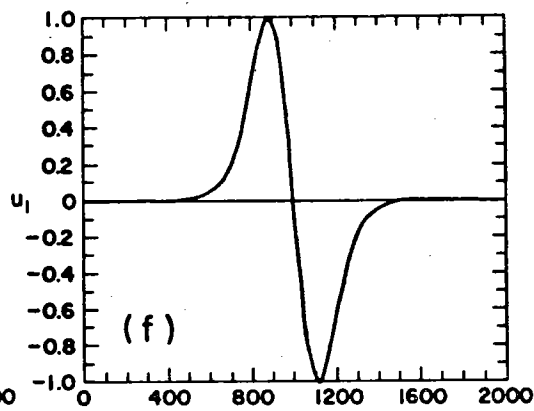
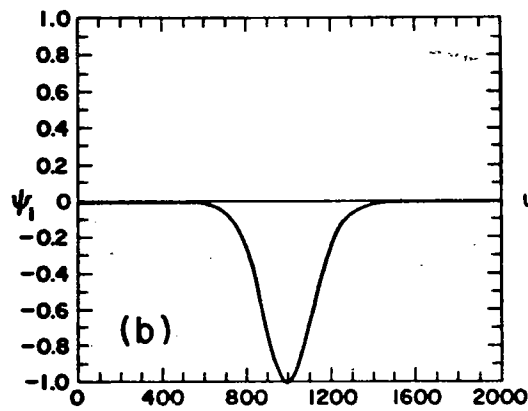
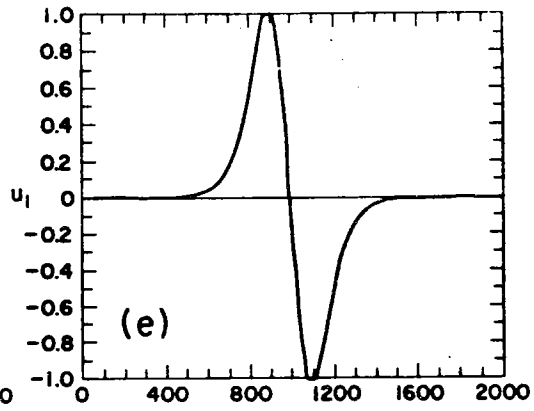
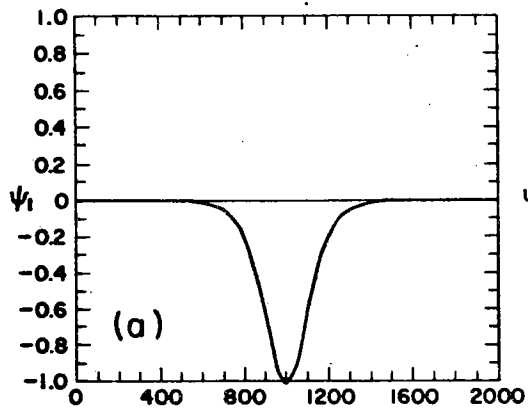


Figure 55: A continuation of the sequence of analytic jets from Figure 54.

<u>Diagram</u>	<u>Jet Separation</u>
(a)	480 km
(b)	720
(c)	960
(d)	1200

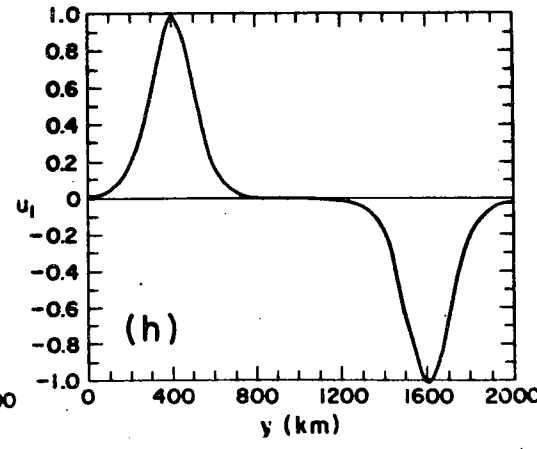
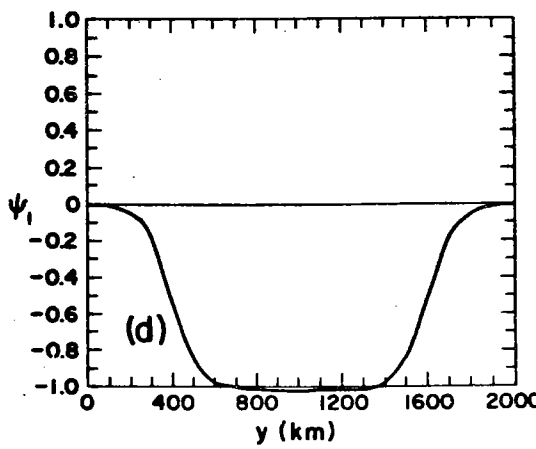
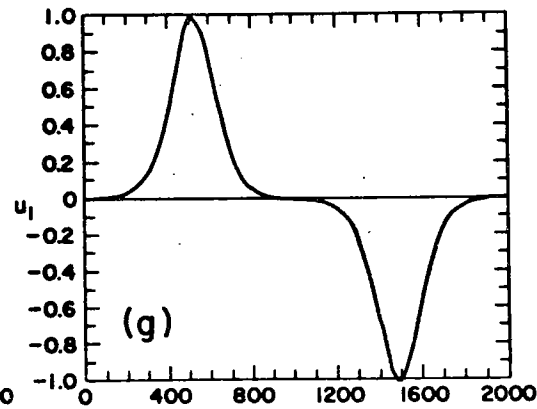
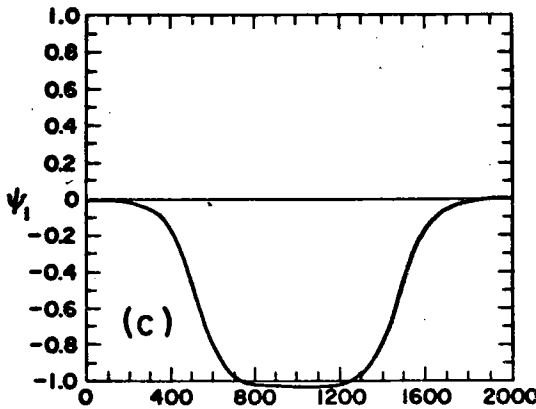
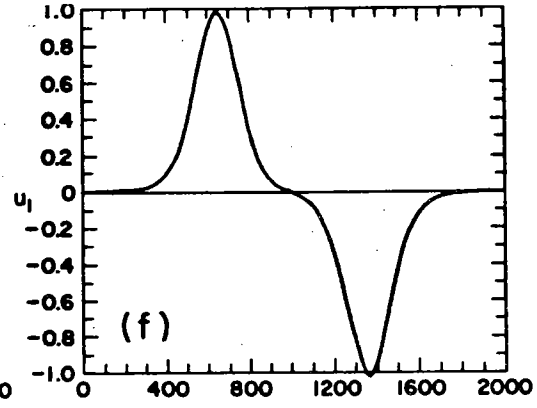
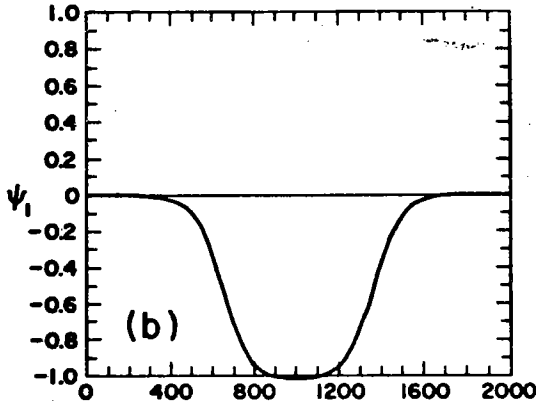
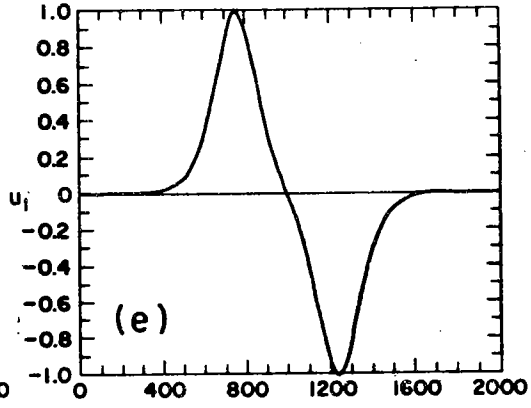
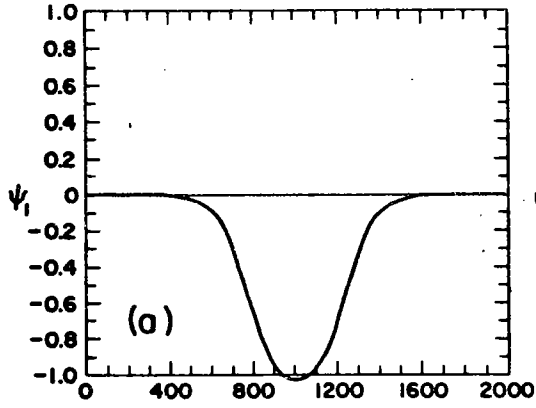


Figure 56: The variation with jet separation of the baroclinic modes associated with the analytic circulations of Figures 54 and 55.

- × unstable modes in the westward flowing jet
- unstable modes in the eastward flowing jet

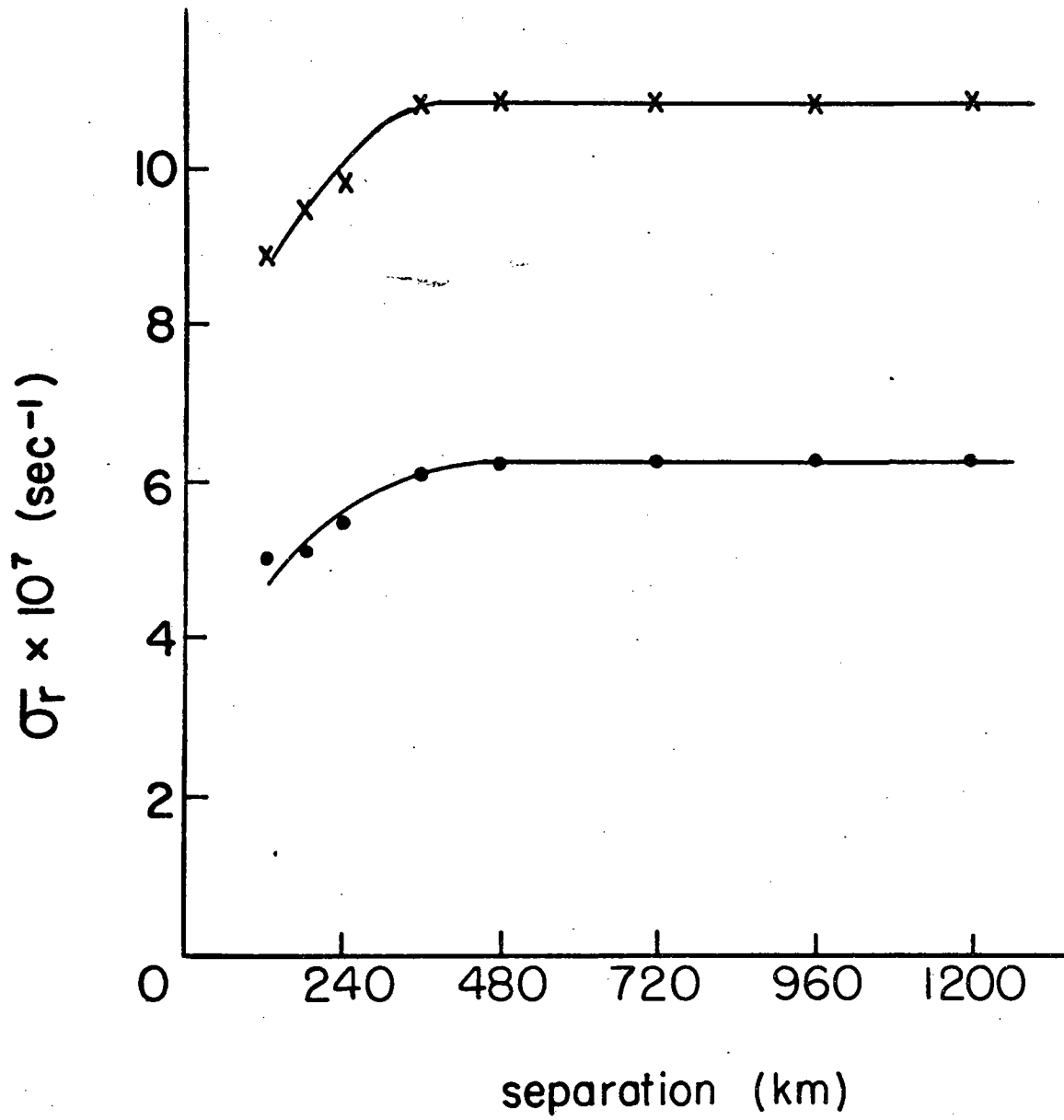


Figure 57: An idealized mean circulation consisting of a single eastward jet and a slow uniform westward return flow.
(a) upper level streamfunction ($|\psi_1|_{\max} = 2.5 \times 10^8$).
(b) upper level velocity ($|u_1|_{\max} = 42.0$).
(c) upper level potential vorticity ($|q_1|_{\max} = 4.0 \times 10^{-5}$).
(d) lower level potential vorticity ($|q_3|_{\max} = 4.0 \times 10^{-5}$).
The lower level is at rest.

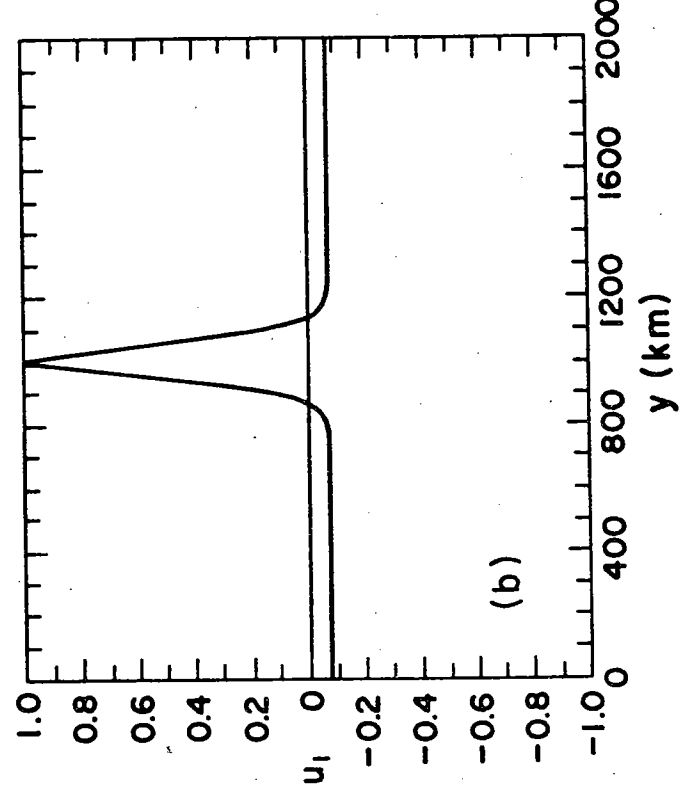
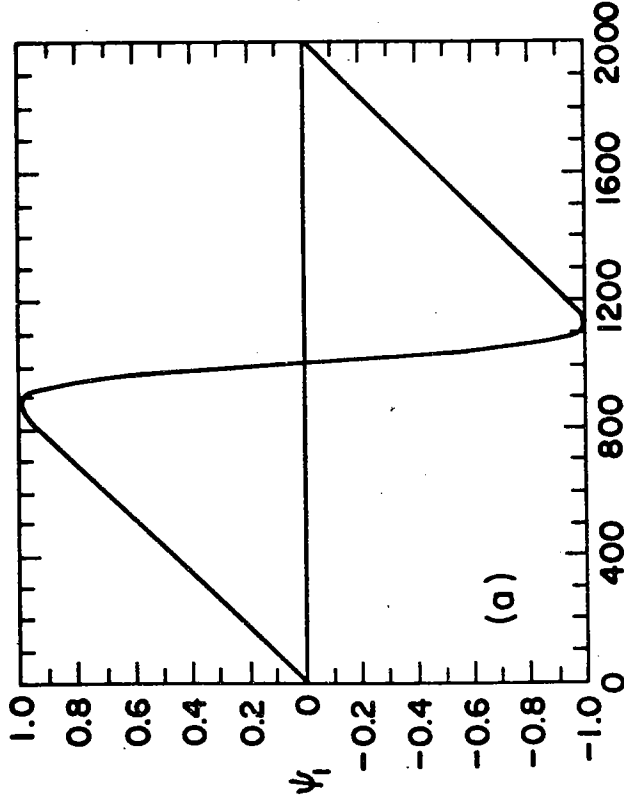
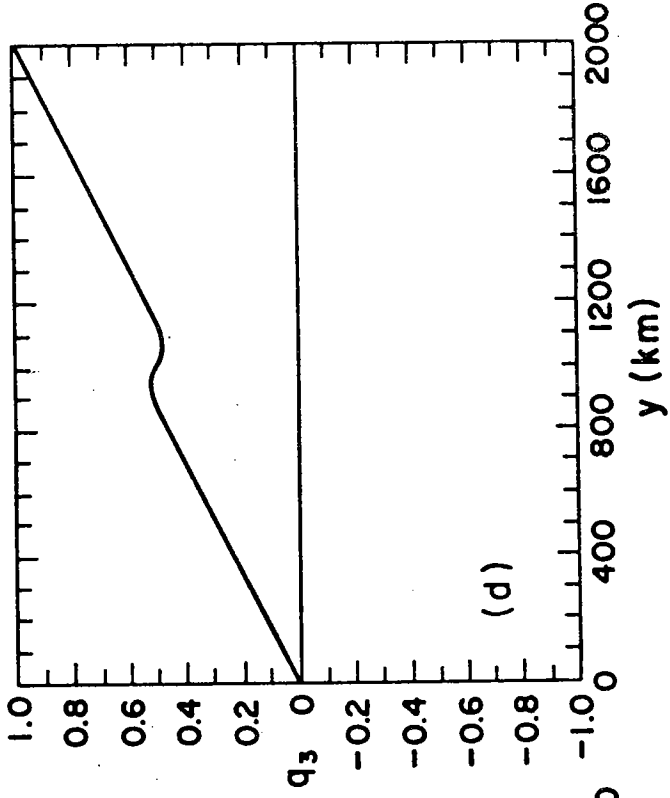
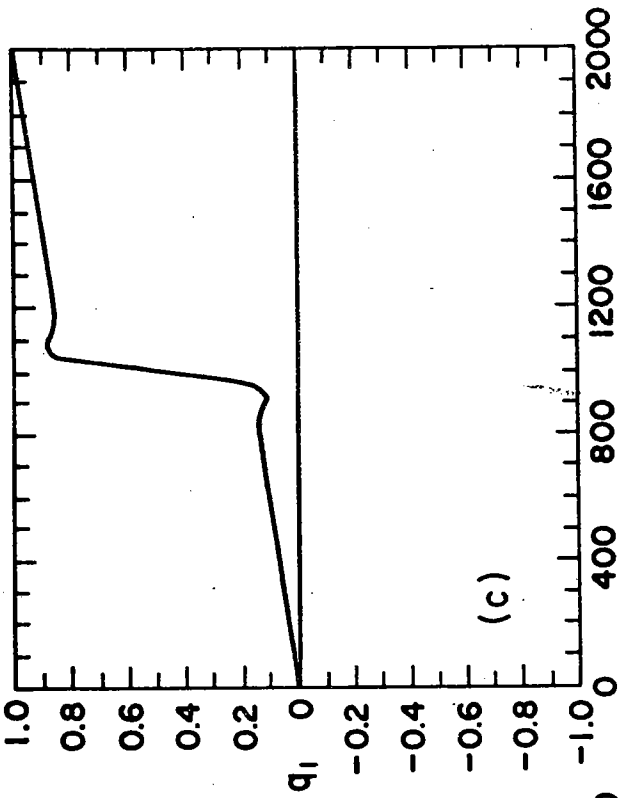
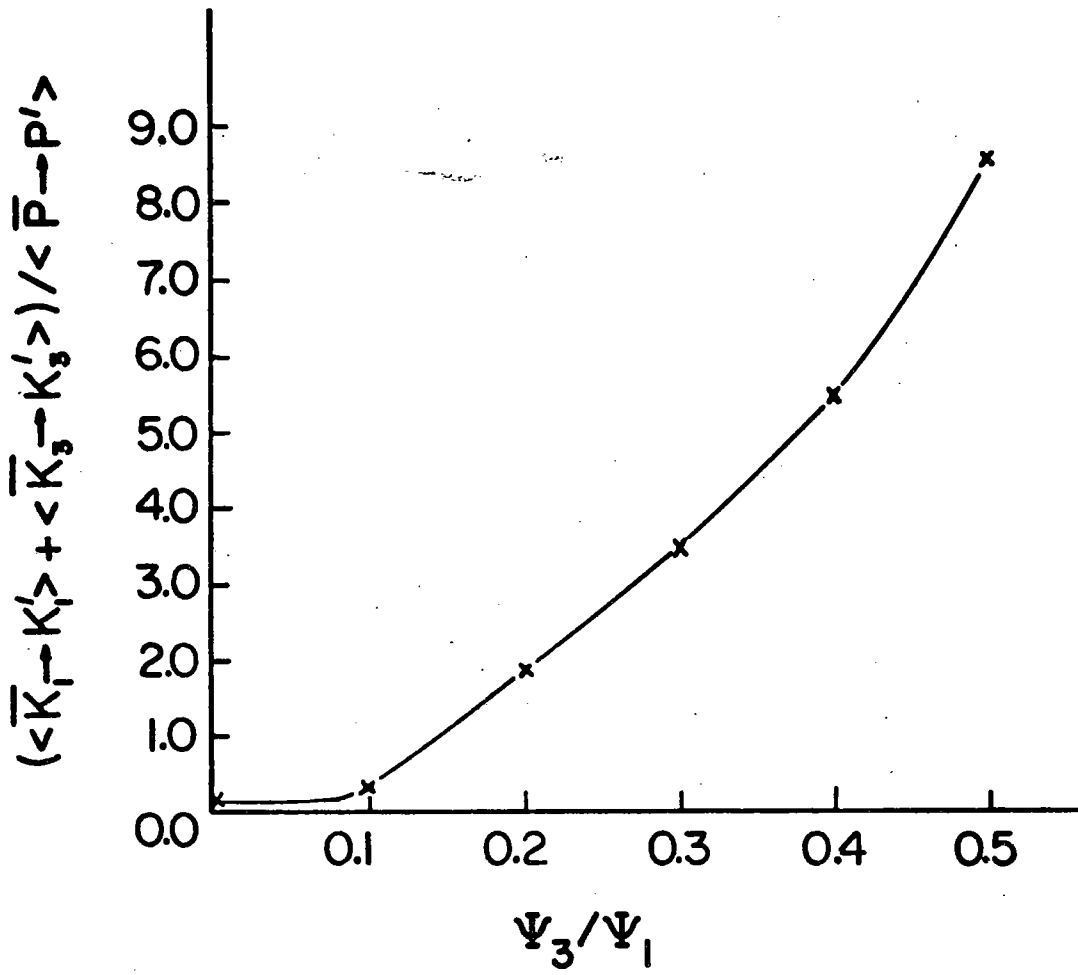


Figure 58: The variation with the strength of the lower layer circulation, ψ_3/ψ_1 , of the energy flux ratio

$$\frac{\langle \bar{K}_1 \rightarrow K_1' \rangle + \langle \bar{K}_3 \rightarrow K_3' \rangle}{\langle \bar{P} \rightarrow P' \rangle}$$

for the unstable mode corresponding to Figure 57.



baroclinic instabilities, though rather insensitive to certain features of the jets such as width and separation, depend critically on the local ratio of horizontal to vertical shear. The transition from a baroclinic to a barotropic instability can therefore be quite rapid if we use as a measure the accuracy with which we can make velocity measurements in the field.

(VI.6) Generalized properties of the barotropic mode

As indicated in the previous section, a jet with a sufficiently intense horizontal velocity gradient will be barotropically unstable. Such a current is shown in Figure 59; we have made it very narrow to insure the predominance of the barotropic over the baroclinic instability mechanism. Using this idealized jet profile in a scaling experiment similar to that conducted for the baroclinic mode, LSA yields the variation of $\text{Re}\sigma$ with horizontal shear. The trend is once again quasi-linear (Figure 60) with a threshold value of approximately $2 \times 10^{-6} \text{ sec}^{-1}$. This scaling behavior roughly explains the observed distribution of σ_R versus $|u_{1y}|$ in E2 (Figure 32) and E2R (Figure 44). However, as opposed to the baroclinic modes of E1, the time-dependence of the solutions clearly involves more than just amplitude changes. This is indicated not only by the scatter in the correlation between growth rate and horizontal shear but by the fact that the linear regressions from three complementary experiments have slightly different slopes and intercepts (Figure 32, 44, and 60). Perhaps barotropic activity is a function of some higher order profile feature? Without further tests, we have no indication what this additional dependence might be. It is known, however, that, as opposed to the strong role of the radius of deformation in determining the vigorousness of a baroclinic mode, R_d seems to have only a slight effect on the growth rate and wavenumber characteristics of the barotropic eddies. This suggests that the missing functional dependence might involve velocity profile features that we have not as yet considered.

Figure 59: An idealized mean circulation consisting of a single eastward jet and a slow uniform westward return flow.

- (a) upper level streamfunction ($|\psi_1|_{\max} = 2.7 \times 10^8$).
- (b) upper level velocity ($|u_1|_{\max} = 62.7$).
- (c) upper level potential vorticity ($|q_1|_{\max} = 4.6 \times 10^{-5}$).
- (d) lower level potential vorticity ($|q_3|_{\max} = 4.0 \times 10^{-5}$).

The lower level is at rest.

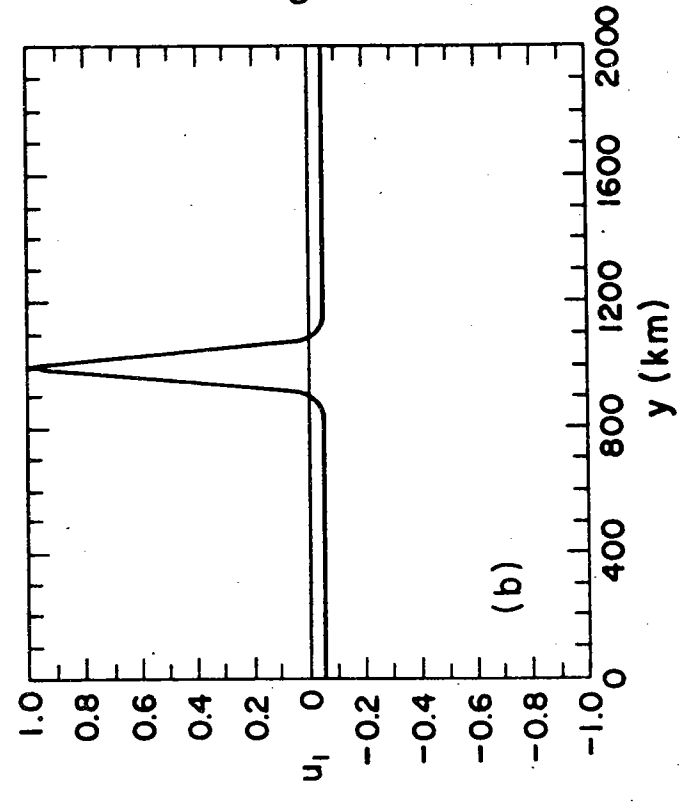
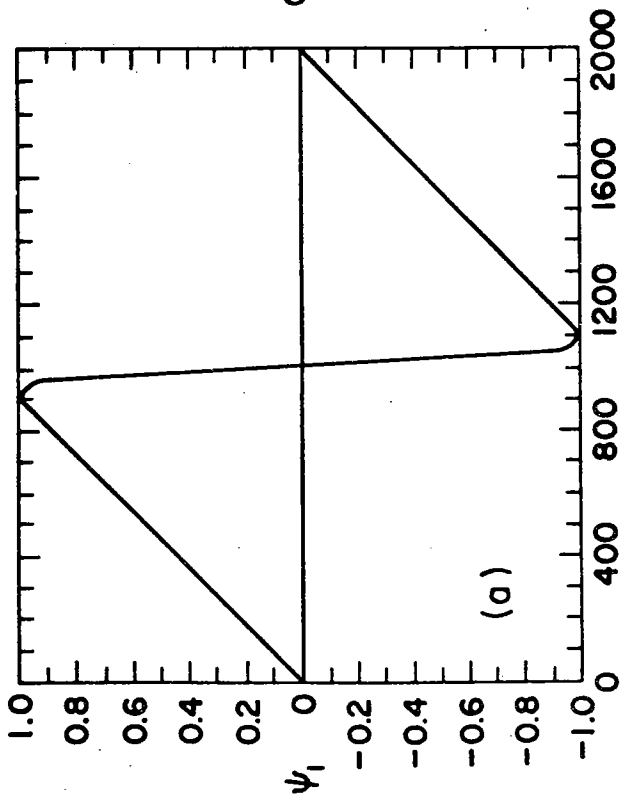
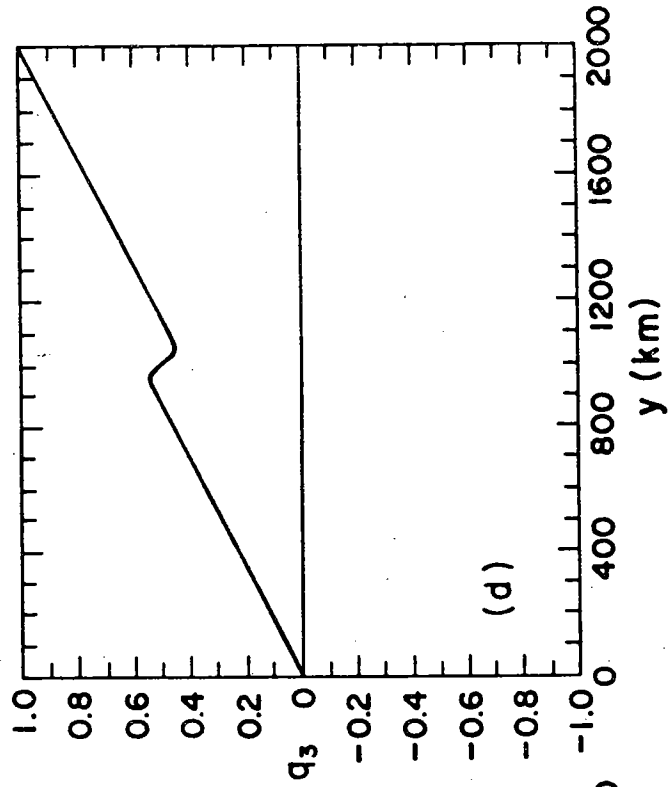
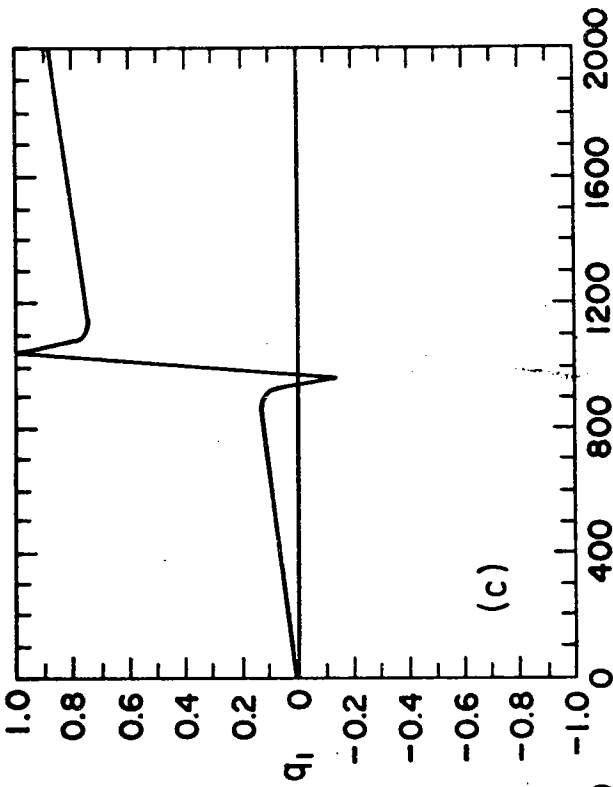
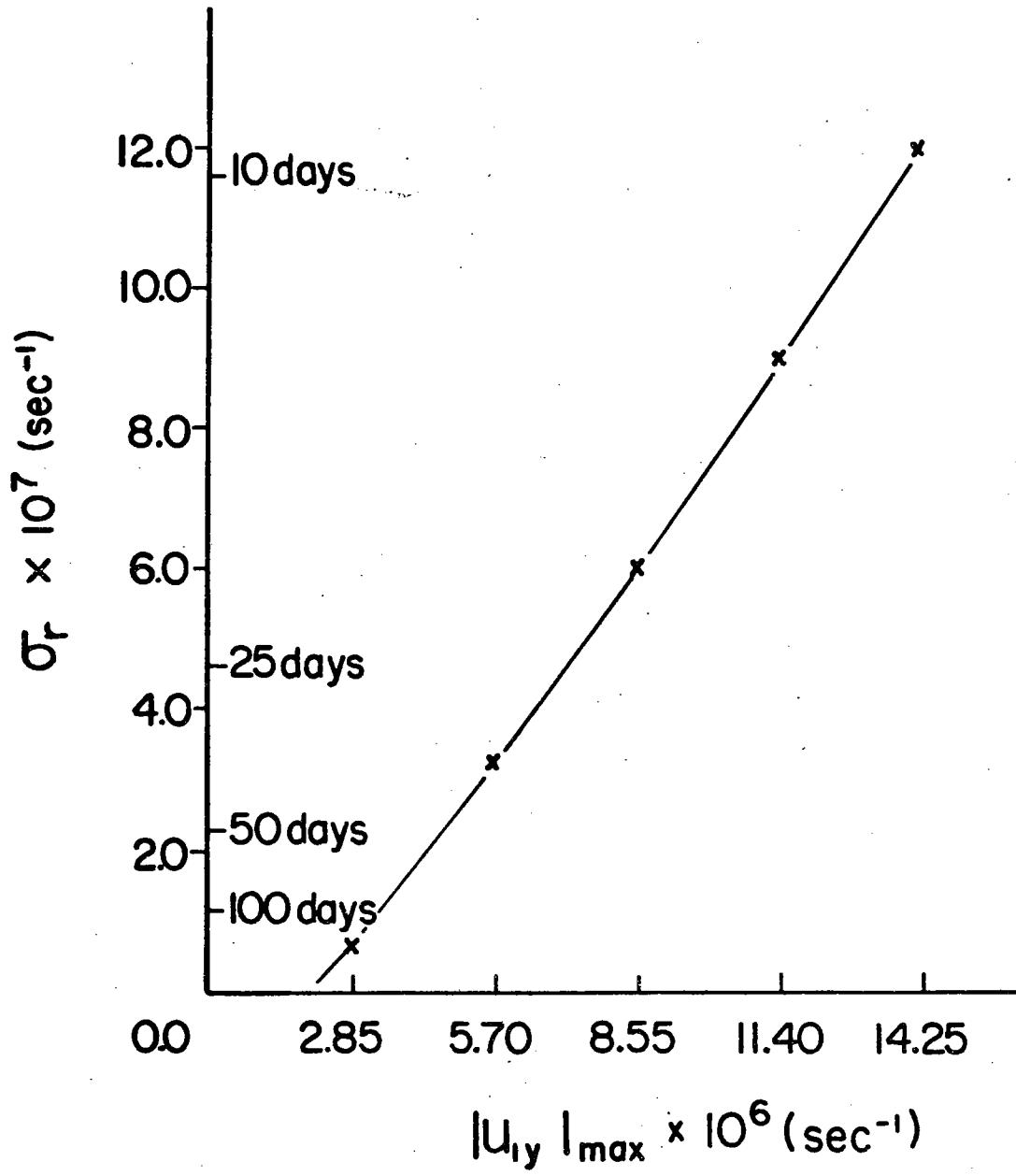


Figure 60: The variation with horizontal shear of the growth rate of the barotropic mode associated with the analytic circulation of Figure 59.



(VII) Conclusions

We have described two numerical procedures for simulating quasi-geostrophic mesoscale eddies under a variety of conditions. The first, a global nonlinear model, uses a pseudospectral technique whose accuracy, efficiency and resolution make it well suited to the study of boundary layer phenomena of which these highly asymmetric beta-plane flows are an example. The application of this formulation was to an investigation of the effects on the mid-ocean equilibrium circulation of variations in western boundary layer structure; two pair of primary simulations, including both single and double-gyred mean flows, were conducted in this context. Second, in an attempt to explore the local dynamic processes at work in eddy generation regions, a quasisteady linear stability theory was advanced and used to interpret the simulated eddy statistics on the basis of mean and instantaneous velocity profiles.

We will not dwell at length on the primary conclusions of the previous chapters; they were

- (i) the closed basin Chebyshev-sine model can be made at least as accurate and efficient as other current finite-difference two-layer box models though it has a definite superiority in its resolution of boundary layer processes and adaptability to rather arbitrary boundary conditions;
- ~~(ii) in the absence of topography, no-slip western boundaries tend to promote a more efficient diffusion of vorticity than free-slip walls; they thus affect the quantitative, though not the qualitative, properties of the interior flow field;~~
- (iii) a linear stability analysis (LSA) can, in most cases, accurately reproduce the statistics of the equilibrium eddy field given pairs of one-dimensional velocity profiles;
- (iv) the LSA has an advantage over global analysis techniques in that it yields accurate information on the local dynamics of the eddies; thus, relatively less unstable regions that may be masked in the global statistics can be explored via LSA;

- (v) the growth rates of the individual barotropic and baroclinic modes scale directly with the local magnitude of the horizontal and vertical shears respectively;
- (vi) the immediate effect of infinitesimal eddies on the mean flow is to reduce the horizontal and vertical shear fields whose extreme values originally induce the instabilities; the finite-amplitude modification of the mean flow by the eddies - that is, $\langle \bar{K} \rightarrow K' \rangle \ll 0$ - is not predicted by the LSA;
- (vii) in the presence of barotropic disturbances, horizontal shears, and consequently the existence of unstable modes, can be severely underestimated on the basis of mean velocity profiles; instantaneous velocity records, although unaveraged in time and therefore not quasisteady as required by the theory, are barotropically unstable to linear perturbations which bear some resemblance to the eddies of the nonlinear double-gyred experiment;
- (viii) very small relative errors of 0(10%) in the measurement of vertical and horizontal shears can lead to completely erroneous predictions as to the existence and type of instability operative in a local region; and
- (ix) the general properties of the baroclinic modes - phase relationships, parametric dependencies, and spatial characteristics - conform in most cases to the predictions of mid-ocean baroclinic stability theory.

Many of these points can be summarized very nicely in one scatter diagram - Figure 61 - in which all the unstable modes we have calculated from all of the four primary experiments (E1, E1R, E2, E2R) are plotted as a function of u_z and $|u_{1y}|$. The corresponding instabilities, deduced via LSA, are classified as either barotropic, baroclinic or mixed and are each represented by a different symbol. The resulting dependence of the instabilities on the ratio of horizontal to vertical shear is obvious; the $u_z - |u_{1y}|$ half-infinite plane can be divided into three distinct regions: one region of stability, and two of barotropic and baroclinic activity. The transition from one to another of these regions can be quite abrupt as was verified using a sequence of analytic profiles

Figure 61: A scatter diagram of the barotropic and baroclinic instabilities observed in the four primary experiments as a function of local horizontal and vertical shear strengths.

- × barotropic modes
- baroclinic modes
- △ mixed modes

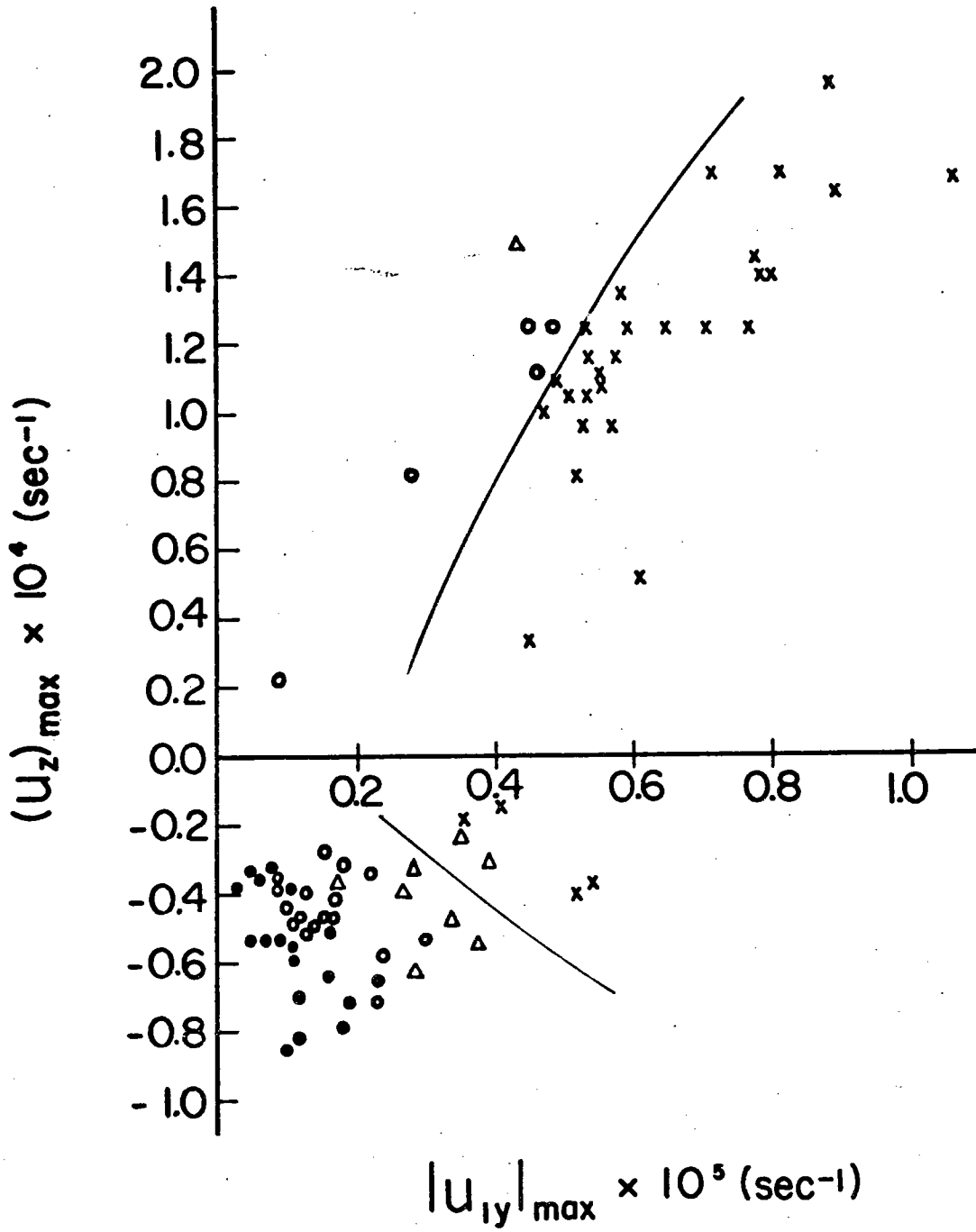


(Figure 62) whose horizontal to vertical shear ratio passes from the predicted barotropically to the baroclinically unstable region of Figure 61. The LSA was applied to this series of profiles to ascertain exactly what type(s) of energy transfer predominated, either FP1 (baroclinic instability), FP2 (barotropic instability), or FP3 (mixed instability). The seven points determined in this way have been added to Figure 61; they lie along $(u_z)_{\max} = 1.25 \times 10^{-4} \text{ sec}^{-1}$ and again reestablish the existence of a very rapid transition from barotropic to baroclinic instability.

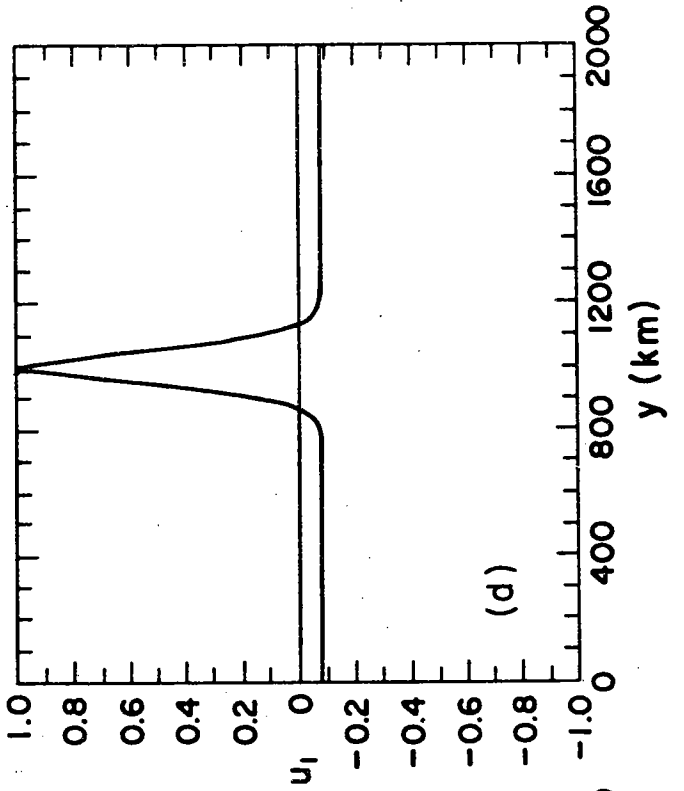
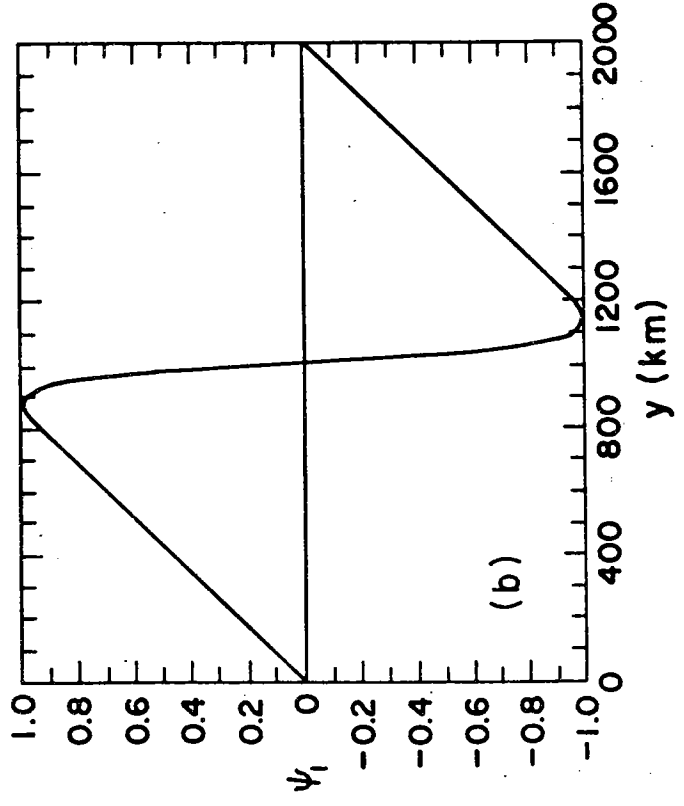
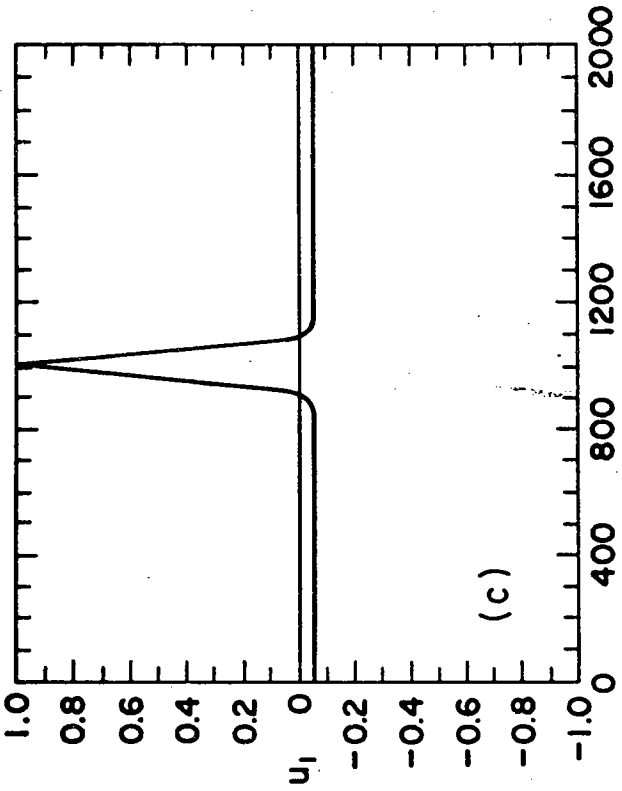
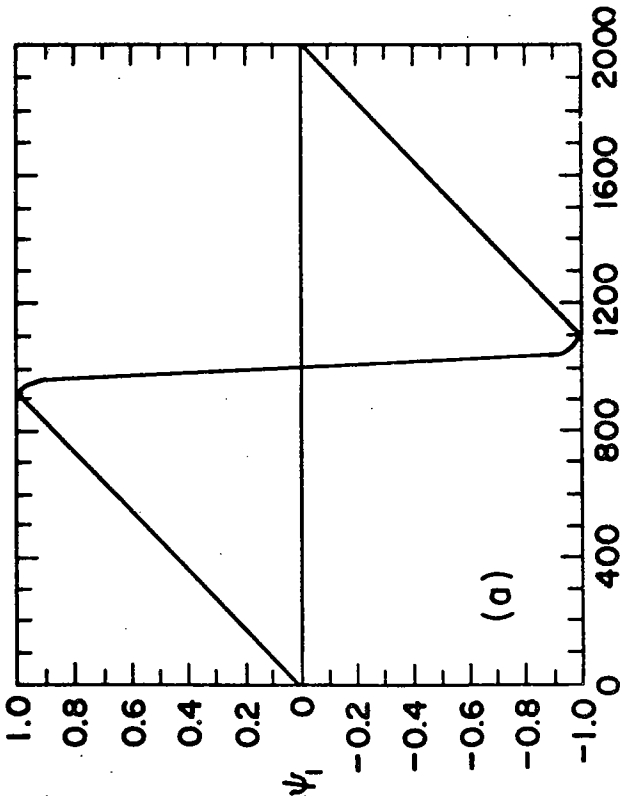
Of course, other important parameters have been held invariant during our four simulations. The scatter diagram of Figure 61 represents, therefore, only one two-dimensional slice through a many-dimensional space of parameters; under other conditions, quite different behavior can be expected. Hart (1974), for instance, has pointed out the dependence of the mixed instability problem on the eddy Froude number ($F_e = \frac{f_0^2 L_e^2}{N^2 H_3}$) and the layer depth ratio ($\delta = H_1/H_3$) in a two-layer quasigeostrophic model on an f-plane. For sufficiently small δ and moderate F_e , mean current distributions representative of an isolated eddy embedded in the mid-ocean can be stabilized. For our experiments, $F_e \approx 1$ and $\delta = 0.25$. According to Hart, these conditions allow a wide range of unstable behavior which depends on the width of the shear zone. Our simulations, in which the ratio of vertical to horizontal shear varies, support this conclusion. As in related contexts (see Owens, 1975, for instance), therefore, the mesoscale eddies are characterized by a competition between many physical processes. Even under the very modest range of flow structures and strengths studied in our experiments, a variety of

Figure 62: Representative profiles taken from a sequence of analytic single-jet circulations whose horizontal to vertical shear ratio passes from the predicted barotropically to the baroclinically unstable region of Figure 61.

(a,c) the most barotropically active streamfunction and velocity profiles ($|\psi_1|_{\max} = 2.7 \times 10^8$, $|u_1|_{\max} = 62.7$).

(b,d) the most baroclinically active streamfunction and velocity profiles ($|\psi_1|_{\max} = 3.8 \times 10^8$, $|u_1|_{\max} = 62.7$).

The lower layer is at rest.



instabilities are evident. As Hart pointed out, the ocean's eddy field seems to occupy a unique position in the space of available nondimensional parameters, lying very near the "triple point" where the stable, and barotropically and baroclinically unstable regions coincide.

The last conclusion to be drawn from Figure 61 concerns the conditions necessary for instability. On the one hand, approximately a 5 cm sec^{-1} velocity difference across the thermocline can lead to vigorous baroclinic activity in the two-level model; this corresponds to an amplitude of $2-3 \text{ cm sec}^{-1}$ for the first baroclinic mode in an equivalent two-mode dynamical model (Flierl, 1975a). Persistent vertical shears in the mid-ocean probably do not reach this level and, indeed, there is no strong evidence for baroclinic instability in either the Polygon or MODE field results (McWilliams and Robinson, 1974; McWilliams, 1975). On the other hand, a horizontal shear greater than $2-3 \times 10^{-6} \text{ sec}^{-1}$ seems to be large enough to promote barotropic instabilities. This value is equivalent to a 12.5 cm sec^{-1} velocity gradient over a horizontal distance of 50 km. Such relatively small shears are certainly attained instantaneously, if not in the mean, in the Gulf Stream (Robinson, Luyten, and Fuglister, 1974). These numerical experiments therefore support the contention, long held by observationalists, that intense current systems such as the Gulf Stream or the North Equatorial Current, and not the mid-ocean, are the primary sites of eddy generation and growth.

Appendix A - Fast sine/cosine transforms

The implementation of spectral methods depends primarily on the ability to construct efficient spectral transform routines. In the present applications, the variable fields can be expanded in a discrete Fourier series. However, we have even more information about these fields; not only are they real, but they must be either odd or even functions (see section III.1). Armed with these extra bits of information, conventional discrete fast Fourier transforms can be modified to provide even more efficient transform programs. A gain in execution time of four can be achieved.

(A.1) FFST

Following Orszag (1971a), let us consider a string of $(N+1)$ uniformly spaced points, a_n ($0 \leq n \leq N$), such that

$$(i) \quad a_n^* = a_n \quad (a_n \text{ real}) \quad (a.1)$$

$$(ii) \quad a_n = a_{N-n} \quad (a_n \text{ antisymmetric}) \quad (a.2)$$

and $(iii) \quad a_0 = a_N = 0.$

The Fourier transform of such a series must be conjugate-symmetric, that is, for $0 \leq j \leq N-1$,

$$(iv) \quad A_j = A_{N-j}^* \quad (a.3)$$

where the discrete transform

$$A_j = \sum_{n=0}^N a_n e^{2\pi i n j / N} \quad 0 \leq j \leq N-1.$$

Now, let $\hat{a}_n = ia_n$,

so that if $b_n = \hat{a}_{2n} + i(\hat{a}_{2n+1} - \hat{a}_{2n-1}) \quad 0 \leq n \leq M-1$
 $= ia_{2n} - (a_{2n+1} - a_{2n-1}) \quad M = N/2$

then
$$B_j = \sum_{n=0}^{M-1} \hat{a}_{2n} e^{2\pi i j (2n)/N} + [ie^{-2\pi i j/N}] \sum_{n=0}^{M-1} \hat{a}_{2n+1} e^{2\pi i j (2n+1)/N}$$

$$- [ie^{2\pi i j/N}] \sum_{n=0}^{M-1} \hat{a}_{2n-1} e^{2\pi i j (2n-1)/N}$$

$$= \sum_{n=0}^{M-1} \hat{a}_{2n} e^{2\pi i j (2n)/N} + [2 \sin(\frac{2\pi j}{N})] \sum_{n=0}^{M-1} \hat{a}_{2n+1} e^{2\pi i j (2n+1)/N}$$

and

$$B_{M-j} = \sum_{n=0}^{M-1} \hat{a}_{2n} e^{-2\pi i j (2n)/N} - [2 \sin(\frac{2\pi j}{N})] \sum_{n=0}^{M-1} \hat{a}_{2n+1} e^{-2\pi i j (2n+1)/N}$$

$$= - \sum_{n=0}^{M-1} \hat{a}_{2n} e^{2\pi i j (2n)/N} + [2 \sin(\frac{2\pi j}{N})] \sum_{n=0}^{M-1} \hat{a}_{2n+1} e^{2\pi i j (2n+1)/N}$$

Therefore, for $0 \leq j \leq M-1$,

$$\hat{A}_j = \sum_{n=0}^{M-1} \hat{a}_{2n} e^{2\pi i j (2n)/N} + \sum_{n=0}^{M-1} \hat{a}_{2n+1} e^{2\pi i j (2n+1)/N} \quad (a.4)$$

$$= \frac{1}{2} [B_j - B_{M-j}] + \frac{1}{4 \sin(\frac{2\pi j}{N})} [B_j + B_{M-j}]$$

In addition, from (a.1) and (a.2),

$$b_n^* = -ia_{2n} - (a_{2n+1} - a_{2n-1})$$

$$= ia_{N-2n} + (a_{N-2n-1} - a_{N-2n+1})$$

$$= b_{M-n}$$

The conjugate symmetry of b suggests that we set

$$c_n = (b_n + b_{K+n}) + i e^{2\pi i n/N} (b_n - b_{K+n}) \quad \begin{matrix} 0 \leq n \leq K-1 \\ K = N/4 \end{matrix}$$

from which, for $0 \leq j \leq K-1$,

$$\begin{aligned} C_j &= \sum_{n=0}^{K-1} (b_n + b_{K+n}) e^{2\pi i (2j)n/M} + i \sum_{n=0}^{K-1} (b_n - b_{K+n}) e^{2\pi i (2j+1)n/M} \\ &= \left[\sum_{n=0}^{K-1} b_n e^{2\pi i (2j)n/M} + \sum_{n=K}^{M-1} b_n e^{2\pi i (2j)n/M} \right] \\ &\quad + i \left[\sum_{n=0}^{K-1} b_n e^{2\pi i (2j+1)n/M} + \sum_{n=K}^{M-1} b_n e^{2\pi i (2j+1)n/M} \right] \\ &= \beta_{2j} + i \beta_{2j+1}. \end{aligned} \quad (a.5)$$

In other words, the N -point transform A_j can be obtained from the $K (=N/4)$ point transform C_j and the relations (a.3), (a.4), and (a.5).

(A.2) FFCT

Similarly, consider a set of $(N+1)$ points a_n such that

$$(i) \quad a_n^* = a_n \quad (a_n \text{ real})$$

$$(ii) \quad a_n = A_{n-n} \quad (a_n \text{ symmetric})$$

and, as before, for $0 \leq j \leq N-1$,

$$(iii) \quad A_j = A_{N-j}^* \quad (a.6)$$

Then, let

$$b_n = a_{2n} + i(a_{2n+1} - a_{2n-1}) \quad \begin{matrix} 0 \leq n \leq M-1 \\ M = N/2 \end{matrix}$$

from which, by considerations of symmetry,

$$b_n^* = b_{M-n}$$

232.

and

$$A_j = \frac{1}{2} [B_j + B_{M-j}] + \frac{i}{4 \sin(\frac{2\pi j}{N})} [B_j - B_{M-j}]. \quad (\text{a.7})$$

Since the b field is once again conjugate-symmetric, define

$$c_n = (b_n + b_{K+n}) + i e^{2\pi i n/N} (b_n - b_{K-n})$$

whence,

$$C_j = B_{2j} + i B_{2j+1}. \quad (\text{a.8})$$

The results (a.7) and (a.8) may be obtained by retracing the steps of section (A.1). The N -point cosine transform A_j can again be retrieved from the K -point discrete Fourier transform of the array c_n ($0 \leq n \leq K-1$) via equations (a.6), (a.7), and (a.8).

Appendix B - Some properties of Chebyshev series

Consider the one-dimensional discrete Chebyshev expansion

$$A(x) = \sum_{n=0}^N a_n T_n(x) \quad -1 \leq x \leq +1 \quad (\text{b.1})$$

where $T_n(x) = T_n(\cos \theta) = \cos(n\theta)$

and $A(x)$ is some unspecified scalar function. Then the series expansions for the first and second derivatives of $A(x)$ are given by

$$\frac{dA}{dx} = A'(x) = \sum_{n=0}^N a_n T_n'(x) = \sum_{n=0}^N a_n' T_n(x) \quad (\text{b.2})$$

and $\frac{d^2A}{dx^2} = A''(x) = \sum_{n=0}^N a_n T_n''(x) = \sum_{n=0}^N a_n'' T_n(x) \quad (\text{b.3})$

where

$$a_n' = \frac{2}{c_n} \sum_{\substack{p=n+1 \\ p+n \text{ odd}}}^N p a_p$$

$$a_n'' = \frac{1}{c_n} \sum_{\substack{p=n+2 \\ p+n \text{ even}}}^N p(p^2 - n^2) a_p$$

and $c_0 = 2, \quad c_n = 1 \quad (n > 0).$

These relations can be expressed more compactly as

$$(2n) a_n = c_{n-1} a_{n-1}' - a_{n+1}' \quad (\text{b.4})$$

and $(2n) a_n'' = c_{n-1} a_{n-1}'' - a_{n+1}'' \quad (\text{b.5})$

By considering (b.1) and (b.2), one can also show that the Chebyshev series has the following properties:

$$A(x=\pm 1) = 0 \quad \Rightarrow \quad \sum_{\substack{n=0 \\ n \text{ odd}}}^N a_n = \sum_{\substack{n=0 \\ n \text{ even}}}^N a_n = 0 \quad (\text{b.6})$$

and

$$\frac{dA}{dx}(x=\pm 1) = 0 \quad \Rightarrow \quad \sum_{\substack{n=0 \\ n \text{ odd}}}^N a'_n = \sum_{\substack{n=0 \\ n \text{ even}}}^N a'_n = 0$$

or

$$\sum_{\substack{n=0 \\ n \text{ odd}}}^N n^2 a_n = \sum_{\substack{n=0 \\ n \text{ even}}}^N n^2 a_n = 0. \quad (\text{b.7})$$

These are the equivalent series statements of the analytic boundary conditions adopted in Chapter III.

Appendix C - A modified Adams-Bashforth method

Consider the partial differential equation

$$\frac{d\eta}{dt} = A + B \quad (c.1)$$

where $\eta = \eta(x, y, t)$ is some scalar function. In analogy to our quasigeostrophic vorticity equations, we may think of η as representing potential vorticity. It is convenient to consider the right-hand side of (c.1) as including two expressions, A and B, the former containing the advective and forcing effects and the latter the diffusive terms. Now, for considerations of viscous stability as well as those numerical constraints mentioned in Chapter III, we wish to treat B semi-implicitly. By modifying the traditional Adams-Bashforth approximation, we therefore derive the following appropriate scheme

$$\eta^{k+1} = \eta^k + \left(\frac{\Delta t}{2}\right) B^{k+1} + \left(\frac{3\Delta t}{2}\right) A^k + \left(\frac{\Delta t}{2}\right) (B^k - A^{k-1}). \quad (c.2)$$

As usual, verification of (c.2) follows directly from a Taylor series expansion of the A and B terms; thus,

$$\begin{aligned} \eta^{k+1} &= \eta^k + \left(\frac{\Delta t}{2}\right) \left[B + \Delta t \frac{dB}{dt} + O(\Delta t^2) \right]^k + \left(\frac{3\Delta t}{2}\right) A^k \\ &\quad + \left(\frac{\Delta t}{2}\right) \left[B - A + \Delta t \frac{dA}{dt} + O(\Delta t^2) \right]^k \\ &= \eta^k + \Delta t (A + B) + \frac{\Delta t^2}{2} \left(\frac{dA}{dt} + \frac{dB}{dt} \right) + O(\Delta t^3) \\ &= \eta^k + \Delta t \left(\frac{d\eta}{dt} \right)^k + \frac{\Delta t^2}{2} \left(\frac{d^2\eta}{dt^2} \right)^k + O(\Delta t^3) \end{aligned}$$

from which the second-order validity of the modified Adams-Bashforth method is established.

Appendix D - Constructing pseudospectral analogues of Arakawa conservative schemes

In many applications, it is considered advantageous for the discretized version of the nonlinear equations to retain some of the conservative properties they have in their continuous form. In particular, the discrete representation of the advective terms must have rather specific integral properties if conservation is to be maintained. A variety of possible finite-difference formulations which conserve some or all of the quadratic moments was originally noted by Arakawa (1966). As we now show, the extension of these results to the pseudospectral or spectral approximation is quite trivial. Consider, for instance, the energy-conserving, second-order finite-difference representation of the Jacobian term:

$$\begin{aligned}
 J_{i,j}(\psi, \xi) &= \frac{1}{4d^2} \left[-S_{i+1,j}(\psi_{i+1,j+1} - \psi_{i+1,j-1}) + S_{i-1,j}(\psi_{i-1,j+1} - \psi_{i-1,j-1}) \right. \\
 &\quad \left. + S_{i,j+1}(\psi_{i+1,j+1} - \psi_{i-1,j+1}) - S_{i,j-1}(\psi_{i+1,j-1} - \psi_{i-1,j-1}) \right] \\
 &= \frac{1}{2d} \left[-S \frac{\partial \psi}{\partial y} \Big|_{i+1,j} + S \frac{\partial \psi}{\partial y} \Big|_{i-1,j} + S \frac{\partial \psi}{\partial x} \Big|_{i,j+1} - S \frac{\partial \psi}{\partial x} \Big|_{i,j-1} \right] + O(d^2) \\
 &= \left\{ \frac{\partial}{\partial x} \left[S \frac{\partial \psi}{\partial y} \right] - \frac{\partial}{\partial y} \left[S \frac{\partial \psi}{\partial x} \right] \right\}_{i,j} + O(d^2).
 \end{aligned}$$

Recasting the expression into its equivalent derivative forms shows that the Arakawa second-order, energy-conserving scheme involves nothing more than setting

$$J_{i,j}(\psi, \xi) = \nabla_{i,j} \cdot (\xi \psi) \quad (\text{d.1})$$

that is, using the well known conservative representation of the

advective terms. Now the analogous pseudospectral energy-conserving approximation follows immediately; it consists of making the identical assumption (d.1) although now the relative error in the calculation of the Jacobian term is of course much reduced in the pseudospectral approximation.

The conservative properties of representation (d.1) follow from the fact that the corresponding flux terms in the energy equation can be integrated by parts; thus,

$$\begin{aligned}
 \iint_{\Sigma} \psi \mathcal{J}(\psi, \rho) dx dy &= \iint_{\Sigma} \left\{ \psi \frac{d}{dx} \left[\rho \frac{d\psi}{dy} \right] - \psi \frac{d}{dy} \left[\rho \frac{d\psi}{dx} \right] \right\} dx dy & (d.2) \\
 &= \iint_{\Sigma} \left\{ \frac{d}{dx} \left[\psi \rho \frac{d\psi}{dy} \right] - \rho \frac{d\psi}{dx} \frac{d\psi}{dy} - \frac{d}{dy} \left[\psi \rho \frac{d\psi}{dx} \right] + \rho \frac{d\psi}{dy} \frac{d\psi}{dx} \right\} dx dy \\
 &= \iint_{\Sigma} \left\{ \frac{d}{dx} \left[\psi \rho \frac{d\psi}{dy} \right] - \frac{d}{dy} \left[\psi \rho \frac{d\psi}{dx} \right] \right\} dx dy \\
 &= 0
 \end{aligned}$$

where Σ is the boundary of our closed domain through which no mass or energy transport is allowed. We therefore see that the requirement of energy conservation is satisfied by assuming (d.1) only if our discrete formulation maintains the property of being integrable by parts so that the advective energy flux terms can be identically cast into the form of a global divergence (which clearly sums out in the appropriate manner). The pseudospectral technique does, in fact, have the required property. To prove this, it is sufficient to show that, in general,

$$\sum_{n=0}^{N-1} \frac{d}{dx} (f_n g_n) = \sum_{n=0}^{N-1} \left(\frac{df_n}{dx} g_n + f_n \frac{dg_n}{dx} \right) = 0. \quad (d.3)$$

For instance, choose a generalized Fourier expansion for the functions

f_n and g_n :

$$f_n = \sum_{p=-K}^{K-1} f_p e^{ipx_n}$$

and

$$g_n = \sum_{p=-K}^K g_p e^{igx_n}$$

$$\begin{aligned} 0 \leq n \leq N-1 \\ K = N/2 \\ x_n = 2\pi n/N \end{aligned}$$

Then,

$$\frac{df_n}{dx} = \sum_{p=-K}^{K-1} ip f_p e^{ipx_n}$$

and

$$\frac{dg_n}{dx} = \sum_{p=-K}^{K-1} ig g_p e^{igx_n}$$

(d.4)

so that

$$\sum_{n=0}^{N-1} \frac{d}{dx} (f_n g_n) = \sum_{n=0}^{N-1} \left(\frac{df_n}{dx} g_n + f_n \frac{dg_n}{dx} \right)$$

(d.5)

$$= \sum_{n=0}^{N-1} \sum_{p=-K}^{K-1} \sum_{q=-K}^{K-1} i(p+q) f_p g_q e^{i(p+q)x_n}$$

Note, however, that

$$\sum_{n=0}^{N-1} e^{i(p+q)x_n} = \begin{cases} 0 & (p+q) \neq 0 \pmod{N} \\ N & (p+q) = 0 \pmod{N} \end{cases}$$

Hence, contributions to the summation (d.5) can occur only for $p = q = -K$.

In order to obtain the cancellation required by (d.3), we must modify the derivative relations (d.4) to become

$$\frac{df_n}{dx} = \sum_{p=-K+1}^{K-1} ip f_p e^{ipx_n}$$

and

$$\frac{dg_n}{dx} = \sum_{q=-K+1}^{K-1} iq g_q e^{igx_n}$$

(d.6)

from which integration by parts and our conservative properties are insured. Relations (d.6) therefore define the appropriate method for taking derivatives in the pseudospectral approximation.

This derivation only holds for a set of expansion functions - like the Fourier series - which are orthonormal with respect to a unit weight function over the interval under consideration. (Therefore, this result applies equally well to a summation of sine modes or Legendre polynomials.) However, the Chebyshev series adopted in Chapter III does not satisfy this orthogonality condition; its weight function - $w(x) = (1-x^2)^{-1/2}$ - is quite different. Consequently, if we let

$$f_n = \sum_{p=0}^N f_p T_p(x_n)$$

$$x_n = \cos\left(\frac{m\pi}{N}\right)$$

and

$$g_n = \sum_{q=0}^N g_q T_q(x_n)$$

then

$$\sum_{n=0}^N \left(\frac{df_n}{dx} g_n + f_n \frac{dg_n}{dx} \right) = \sum_{p=0}^N \sum_{q=0}^N (f_p' g_q + f_p g_q') \sum_{n=0}^N T_p(x_n) T_q(x_n)$$

which cannot in general sum to zero for any arbitrary fields f_n and g_n . Indeed, this is the price we must pay for the convenience, efficiency, and increased boundary layer resolution of the Chebyshev transform method. It is operationally possible to guarantee strict conservation even with a Chebyshev series if one is willing to modify some of the higher order dynamic equations as was done in (III.3) to satisfy the

boundary conditions. However, tests have shown that the nonconservation associated with the Chebyshev series technique rarely exceeds one part in 10^5 for well behaved fields such as those of the primary experiments. This error is relatively much less than the errors arising from the physical and numerical approximations of Chapters II and III and can be safely ignored.

REFERENCES

- Arakawa, A. (1966) Computational design for long-term numerical integration of the equations of motion: two-dimensional incompressible flow. Part I. J. Comp. Phys., 1, 119-143.
- Bernstein, R. L., and W. B. White (1975) Time and length scales of baroclinic eddies in the central North Pacific Ocean. J. Phys. Ocean., 4, 613-624.
- Blandford, R. R. (1971) Boundary conditions in homogeneous ocean models. Deep-Sea Res., 18, 739-751.
- Bretherton, F. P., and D. B. Haidvogel (1976) Two-dimensional turbulence above topography. Submitted to the Journal of Fluid Mechanics.
- Byran, K. (1963) A numerical investigation of a non-linear model of a wind-driven ocean. J. Atm. Sci., 20, 594-606.
- Bryden, H. L., Jr. (1975) Momentum, Mass, Heat, and Vorticity Balances from Oceanic Measurements of Current and Temperature. Doctoral Dissertation, Massachusetts Institute of Technology and the Woods Hole Oceanographic Institution.
- Charney, J. G. (1955) The Gulf Stream as an inertial boundary layer. Proc. Nat. Acad. Sci., 41, 731-740.
- Crease, J. (1962) Velocity measurements in the deep water of the western North Atlantic. J. Geophys. Res., 67, 3173-3176.
- Flierl, G. R. (1975a) Models of vertical structure of oceanic motions and the calibration of the two layer models. Unpublished manuscript.
- Flierl, G. R. (1975b) Gulf Stream Meandering, Ring Formation, and Ring Propagation. Doctoral Dissertation, Harvard University.
- Fofonoff, N. P. (1954) Steady flow in a frictionless homogeneous ocean. J. Mar. Res., 13, 517-537.
- Fox, D. G., and S. A. Orszag (1973) Pseudospectral approximation to two-dimensional turbulence. J. Comp. Physics, 11, 612-619.
- Gill, A. E., J. S. A. Green, and A. J. Simmons (1974) Energy partition in the large-scale ocean circulation and the production of mid-ocean eddies. Deep-Sea Res., 21, 499-528.
- Gould, W.J., W. J. Schmitz, Jr., and C. Wunsch (1974) Preliminary field results for a Mid-Ocean Dynamics Experiment (MODE-I). Deep-Sea Res., 21, 911-931.

- Hart, J. E. (1974) On the mixed stability problem for quasi-geostrophic ocean currents. J. Phys. Ocean., 4, 349-356.
- Holland, W. R. (1966) Wind-Driven Circulation in an Ocean with Bottom Topography. Doctoral Dissertation, University of California, San Diego.
- Holland, W. R. (1973) Baroclinic and topographic influences on the transport in western boundary currents. Geophys. Fluid Dyn., 4, 187-210.
- Holland, W. R., and L. B. Lin (1975a) On the generation of mesoscale eddies and their contribution to the ocean general circulation. I. A preliminary numerical experiment. J. Phys. Ocean., 5, 642-657.
- Holland, W. R., and L. B. Lin (1975b) On the generation of mesoscale eddies and their contribution to the ocean general circulation. II. A parameter study. J. Phys. Ocean., 5, 658-669.
- Holland, W. R., and L. B. Lin (1976) Numerical experiments with a quasigeostrophic eddy-resolving oceanic general circulation model. In preparation.
- Kim, K. (1975) Instability and Energetics in a Baroclinic Ocean. Doctoral Dissertation, Massachusetts Institute of Technology and the Woods Hole Oceanographic Institution.
- Koshlyakov, M. N., and Y. M. Grachev (1973) Mesoscale currents at a hydrophysical polygon in the tropical Atlantic. Deep-Sea Res., 20, 507-526.
- Lorenz, E. N. (1955) Available potential energy and the maintenance of the general circulation. Tellus, 7, 157-167.
- Lorenz, E. N. (1972) Barotropic instability of Rossby wave motion. J. Atm. Sci., 29, 258-264.
- McWilliams, J. C., and A. R. Robinson (1974) A wave analysis of the Polygon array in the tropical Atlantic. Deep-Sea Res., 21, 359-368.
- McWilliams, J. C. (1975) Baroclinic instability and the MODE observations. Dynamics and the Analysis of MODE-I: Report of the MODE-I Dynamic Group, 94-112.
- Munk, W. H. (1950) On the wind-driven ocean circulation. J. Meteorology, 7, 79-93.
- Orlanski, I. (1969) The influence of bottom topography on the stability of jets in a baroclinic fluid. J. Atm. Sci., 26, 1216-1232.
- Orlanski, I., and C. Cox (1973) Baroclinic instability in ocean currents. Geophys. Fluid Dyn., 4, 297-332.

- Orszag, S. A. (1971a) Numerical simulation of incompressible flows within simple boundaries. I. Galerkin (spectral) representations. Stud. App. Math., 50, 293-327.
- Orszag, S. A. (1971b) Numerical simulation of incompressible flows within simple boundaries: accuracy. J. Fluid Mech., 49, 75-112.
- Orszag, S. A. (1972) Comparison of pseudospectral and spectral approximation. Stud. App. Math., 51, 253-259.
- Owens, W. B. (1975) A Numerical Study of Mid-Ocean Mesoscale Eddies. Doctoral Dissertation, Johns Hopkins University.
- Parker, C. E. (1971) Gulf Stream rings in the Sargasso Sea. Deep-Sea Res., 18, 981-993.
- Pedlosky, J. (1963) Baroclinic instability in two layer systems. Tellus, 15, 20-25.
- Phillips, N. A. (1951) A simple three-dimensional model for the study of large-scale extratropical flow patterns. J. Meteorology, 8, 381-394.
- Phillips, N. A. (1966) Large-scale eddy motion in the western Atlantic. J. Geophys. Res., 71, 3883-3891.
- Rhines, P. B. (1973) Observations of the energy-containing oceanic eddies, and theoretical models of waves and turbulence. Boundary-layer Met., 4, 345-360.
- Rhines, P. B. (1975) The dynamics of unsteady currents. To appear in The Sea, Volume VI.
- Robinson, A. R. (1963) Wind-Driven Ocean Circulations. Blaisdell Publishing Company, 161 pp.
- Robinson, A. R., J. R. Luyten, and F. C. Fuglister (1974) Transient Gulf Stream Meandering. Part I: An observational experiment. J. Phys. Ocean., 4, 237-255.
- Robinson, A. R., and J. C. McWilliams (1974) The baroclinic instability of the open ocean. J. Phys. Ocean., 4, 281-294.
- Starr, V. P. (1968) Physics of Negative Viscosity Phenomena. McGraw-Hill Book Company, 256 pp.
- Stommel, H. (1948) The westward intensification of wind-driven ocean currents. Trans. Amer. Geophys. Union, 29, 202-206.
- Sverdrup, H. U. (1947) Wind-driven currents in a baroclinic ocean; with application to the equatorial currents of the eastern Pacific. Proc. Nat. Acad. Sci., 33, 318-326.

Veronis, G. (1966) Wind-driven ocean circulation - part 2. Numerical solutions of the non-linear problem. Deep-Sea Res., 13, 31-55.

Webster, F. (1965) Measurements of eddy fluxes of momentum in the surface layer of the Gulf Stream. Tellus, 17, 239-245.

BIOGRAPHY

The author was born on January 26, 1949, in Buffalo, New York, where he completed his secondary education at The Nichols School in 1967. Four years later, he received the degree of Bachelor of Science from the Massachusetts Institute of Technology where he graduated Phi Beta Kappa. Since that time the author has been enrolled in the Woods Hole/M.I.T. Joint Program in Physical Oceanography. He currently holds membership in the Society of the Sigma Xi and the American Meteorological Society.

Publications:

Bretherton, F. P. and D. B. Haidvogel (1976) Two-dimensional turbulence above topography. Submitted to the Journal of Fluid Mechanics.

Haidvogel, D. B. (1973) The rectified response of a two-layer model ocean to a time-dependent forcing. Summary Reports - Fellowship in Scientific Computing. NCAR-TN/PROC-90, 57-93.